From Single Atoms to Clusters

Measuring Catalytic Activity for Energy Conversion

Ph.D. Thesis

Johannes Novak Hansen

Supervisor: Professor Ib Chorkendorff
Co-supervisor: Associate Professor Jakob Kibsgaard

Surface Physics and Catalysis (SurfCat)
Department of Physics
Technical University of Denmark

Abstract

Developing active, selective and stable catalysts to drive key reactions is essential for a future sustainable energy landscape. Catalysts in the size range of single atoms to clusters show interesting possibilities in this regard. In this thesis, the challenges and opportunities of such small entities, as well as more general issues in measuring catalytic activity, are discussed. The thesis starts out by briefly outlining the climate crisis and motivating the need for catalysts to drive eletrochemical reactions for energy conversion and storage. Subsequently, a brief introduction is given to some fundamentals on catalysis, electrochemistry and the experimental methods used for the work herein. The following chapters present three studies within the field of electrocatalysis:

Oxygen Reduction Reaction (ORR): The two-electron ORR provides a sustainable way to synthesize H_2O_2. A study of a single atom palladium catalyst is presented, demonstrating high selectivity (80% faradaic effieciency) and activity toward H_2O_2. Using various characterization techniques and density functional theory (DFT), the geometric effect of the single atom site and the surrounding coordination environment of nitrogen species was rationalized to be the cause of this.

Hydrogen Evolution Reaction (HER): Geometric current densities are often reported for novel HER catalysts, without consideration for the applied loading of the catalyst. To address this issue as well as other common pitfalls, a benchmark study of HER was conducted using 3.8 nm mass-selected Pt nanoparticles and commercial Pt/C. It was demonstrated that platinum has an intrinsic activity at least three orders of magnitude larger than earth-abundant catalyst, however, the true activity of platinum is still underestimated.

Developing a Model System for Small Entities: To gain fundamental insight into small entities, a model system of Pt_{1-3} on nitrogen-doped highly oriented pyrolytic graphite (HOPG) was investigated. It was shown that the system displays HER activity correlating with the presence of Pt species and that atomic nitrogen-defects can be created in the HOPG lattice by NH_3-sputtering and subsequent annealing. Furthermore, the possibilities for further developing the model system and elucidating the active site structure are discussed.

Resumé

Udviklingen af aktive, selektive og stabile katalysatorer til at drive en række vigtige reaktioner er essentielt for et fremtidigt bæredygtig energisystem. Katalysatorer i størrelsesordenen fra enkelte atomer til små klynger er særligt interessante i denne sammenhæng. Denne afhandling beskriver, hvilke udfordringer og muligheder disse små enheder har, samt nogle mere generelle aspekter af at måle katalytisk aktivitet. Afhandling starter med kort at opridse klimakrisen og motivere behovet for katalysatorer til at drive elektrokemisk konvertering of lagring af energi. Derefter gives en kort introduktion til nogle grundlæggende begreber inden for katalyse, elektrokemi samt de anvendte eksperimentelle metoder. De efterfølgende kapitler præsenterer tre studier inden for området elektrokatalyse:

Oxygenreduktion (ORR): to-elektron ORR er en bæredygtig måde at fremstille H_2O_2 på. Her præsenteres et studie af en enkelt-atom palladium-katalysator, som demonstrerer høj selektivitet (80% faradisk effektivitet) og aktivitet for H_2O_2. Grunden til dette findes, ved brug af en række karakteriseringsteknikker og densitets-funktionale-teori (DFT), at være den geometriske effekt af enkelt-atomerne og koordineringen til omkringliggende nitrogen.

Hydrogenudvikling (HER): Geometrisk strømdensitet rapporteres ofte for nye HER-katalysatorer, uden hensyntagen til den anvendte mængde af katalysator. For at adressere dette, samt andre almene faldgruber, blev der foretaget et benchmarkstudie af HER ved brug af 3.8 nm masse-selekterede nanopartikler samt kommerciel Pt/C. Det blev vist at platins intrinsiske aktivitet er mindst tre størrelsesordener højere end mere rigeligt tilgængelige katalysatorers, selvom platins sande aktivitet stadig er underestimeret.

Udviklingen af et modelsystem til små enheder: For at opnå grundlæggende indsigt i små enheder blev et modelsystem bestående af Pt_{1-3} på nitrogen-doteret, ordnet pyrolytisk grafit (HOPG) undersøgt. Det blev vist, at systemet har HER-aktivitet som er koblet med tilstedeværelsen af Pt enheder, og at atomare N-defekter af HOPG kan skabes ved beskydning med NH_3 og efterfølgende varmebehandling. Mulighederne for videreudvikling af modelsystemet samt belysning af den aktive struktur bliver diskuteret.

Preface

This thesis is submitted in partial fulfillment of the requirements for the Ph.D. degree from the Technical University of Denmark. The work presented in this thesis was conducted under the supervision of Professor Ib Chorkendorff and Associate Professor Jakob Kibsgaard in connection to the CLUNATRA project, funded by the European Research Council under the European Union's Horizon 2020 research and innovation program. The work took place from April 2018 until April 2021 at the Surface Physics & Catalysis (SurfCat) group, Department of Physics, Technical University of Denmark.

Firstly, I want to thank Ib Chorkendorff and Jakob Kibsgaard for sharing insights, giving constructive feedback and for enabling me to work with such exciting and challenging projects. I have truly enjoyed working at SurfCat, and for that I owe thanks to all who have contributed to the collaborative and social environment. A special thanks goes to Niklas Mørch Secher and Karl Krøjer Toudahl, whom I have had a good time and a constructive collaboration with, even when our projects did not go as expected. I would also like to thank Hector Prats and Karen Chan for our collaboration and the many interesting discussions on mass-transport and hysteresis. I have also enjoyed working with Jens-Peter B. Haraldsted and Degenhart Hochfilzer as well as sharing some good laughs in the lab. I am also grateful to Jacqueline McAnulty, Brian Peter Knudsen and Patrick Strøm-Hansen for their always friendly and helpful attitude. Furthermore, I have had the pleasure of sharing an office with Tomas Hugh Youngman and Olivia Fjord Sloth, whose company has brightened my mood even when experiments kept failing. Thank you all.

Last but not least, I want to thank my fiancée Camilla Hartmann, for her support and patience with me - particularly during the intensive process of writing this thesis.

Johannes Novak Hansen

List of Symbols

Symbol	Description	Usual Unit
A	area	cm^2
a_i	activity of species i	
B	Levich constant	C m mol^{-1} $\mathrm{s}^{-1/2}$
C_i	concentration of species i	mol L^{-1}
C_d	double layer capacitance	μF cm^{-2}
D_i	diffusion coefficient of species i	cm^2 s^{-1}
e	elementary charge	1.602177×10^{-19} C
E	potential	V
E^0	standard potential	V
$E^{0'}$	formal potential	V
η	overpotential	mV
F	Faraday's constant	96485.332 C mol^{-1}
f	F/RT	V^{-1}
f_EIS	frequency in EIS	Hz
ΔG	Gibbs free energy (difference)	kJ mol^{-1}
i	(a) current	mA
	(b) index of parameter	
i_f	faradaic current	mA
i_nf	non-faradaic current	mA
j	current density	mA cm^{-2}
j_d	current density of diffusion	mA cm^{-2}
	(or concentration) overpotential	
j_i	current density normalized	mA cm^{-2}
	by area of i: geo, ECSA, disk	
j_k	kinetic current density	mA cm^{-2}
j_mass	mass activity	A g^{-1}
j_0	exchange current density	mA cm^{-2}

Symbol	Description	Usual Unit
k_i	rate constant of i	$\mathrm{cm}^1\ \mathrm{s}^{-1}$
m	mass	ng
n	stoichiometric number of electrons	
n_i	number of species i	
N	RRDE collection efficiency	
N_A	Avogadro's number	$6.022141 \times 10^{23}\ \mathrm{mol}^{-1}$
ν	(a) scan speed	$\mathrm{mV\ s}^{-1}$
	(b) kinematic viscosity	$\mathrm{cm}^2\ \mathrm{s}^{-1}$
O	(a) oxidized form of redox couple	
	(b) atomic oxygen	
ω	rotational speed	$\mathrm{rad\ s}^{-1}$ or rpm
Q, q	charge	C
R	(a) resistance	Ω
	(b) gas constant	$8.31446\ \mathrm{J\ mol}^{-1}\ \mathrm{K}^{-1}$
R	reduced form of redox couple	
r	radius	mm
σ	surface charge density	$\mu\mathrm{C\ cm}^{-2}$
T	temperature	K
t	time	s
Z	impedance	Ω
$\varnothing$	diameter	mm
$*$	(a) surface site	
	(b) bulk value of e.g. C^* or D^*	

List of Abbreviations & Acronyms

Abbreviation	Meaning
amu	atomic mass unit
BV	Butler-Volmer
CA	chronoamperometry
CE	counter electrode
COF	covalent-organic framework
CP	chronopotentiometry
CV	cyclic votammogram
	(or cyclic voltammetry)
CVD	chemical vapor deposition
DFT	density functional theory
DOS	density of states
ECSA	electrochemically active surface area
EC-MS	electrochemical - mass spectrometry
EIS	electrochemical impedance spectroscopy
EXAFS	extended X-ray absorption fine structure
FE	faradaic efficiency
GC	glassy carbon
GCE	glassy carbon electrode
GDE	gas diffusion electrode
geo	geometric
HDI	human development index
HER	hydrogen evolution reaction
HOPG	highly oriented pyrolytic graphite
HOR	hydrogen oxidation reaction
ICP-MS	inductively coupled plasma mass spectrometry

Abbreviation	**Meaning**
ISS	ion scattering spectroscopy
LCoE	levelized cost of electricity (energy)
MOF	metal-organic framework
OCV	open circuit voltage
OER	oxygen evolution reaction
ORR	oxygen reduction reaction
PCTFE	polychlorotrifluoroethylene
PEEK	polyetheretherketone
PEM	polymer electrolyte membrane
	(or proton exchange membrane)
PEMFC	polymer electrolyte membrane fuel cell
PTFE	polytetrafluoroethylene
QMS	quadrupole mass spectrometer
REF	reference electrode
RDE	rotating disk electrode
RRDE	rotating ring disk electrode
RHE	reversible hydrogen electrode
SAC	single atom catalyst
SHE	standard hydrogen electrode
STEM	scanning transmission electron microscope
STM	scanning tunneling microscopy
STS	scanning tunneling spectroscopy
TOF	(a) turnover frequency
	(b) time-of-flight
UHV	ultra high vacuum
UPD	under potential desorption
WE	working electrode
XANES	X-ray absorption near edge structure
XPS	X-ray photo-electron spectrocopy

Appended Papers

Paper I:

Highly active, selective, and stable Pd single-atom catalyst anchored on N-doped hollow carbon sphere for electrochemical H_2O_2 synthesis under acidic conditions
Jiangbo Xi, Sungeun Yang, Luca Silvioli, Sufeng Cao, Pei Liu, Qiongyang Chen, Yanyan Zhao, Hongyu Sun, Johannes Novak Hansen, Jens-Peter B. Haraldsted, Jakob Kibsgaard, Jan Rossmeisl, Sara Bals, Shuai Wang, Ib Chorkendorff
Journal of Catalysis, Volume 393, 2021, Pages 313-323

Paper II:

Is There Anything Better Than Pt for HER?
Johannes Novak Hansen, Hector Prats, Karl Krøjer Toudahl, Niklas Mørch Secher, Karen Chan, Jakob Kibsgaard, Ib Chorkendorff
ACS Energy Letters, Volume 6, 2021, Pages 1175-1180

Contents

Chapter 1

Introduction

In this chapter, a brief summary of the climate crisis is given and put in the context of energy consumption. The challenges of replacing fossil fuels is discussed and put in relation to the intermittency of renewable energy sources as well as the challenge regarding applications which cannot directly use these renewable energy sources. This motivates the ability to convert and store sustainable energy by the means of electrochmical processes. Building on this concept, a future energy landscape is presented as a way to cut the emission of CO_2, hence addressing the crux of the climate crisis. In this context, hydrogen is brought up as an example of a sustainable fuel and chemical. This motivates the need for catalysts to drive the reactions producing hydrogen as well as other fuels and chemicals necessary in the effort to combat climate change.

1.1 Stop Burning Dinosaurs!

The evidence of widespread global climate change is overwhelming. Decades of extensive research, model predictions and a broad varieties of experimental observation point the same way and the general scientific consensus is unequivocal: the large emission of green house gasses into the atmosphere leads to a cascade of detrimental effects on the global scale including temperature anomalies, rising sea levels, eroding shoreline, more frequent and intense natural disasters (droughts, heatwaves, hurricanes etc.), just to name a few. It will have severe consequences for humans, animals and entire eco-systems. The cause of the problem is the large-scale emission of green house gasses, and in particular CO_2-emission stemming from the burning of fossil fuels.[1–12]. The atmospheric CO_2 content has since the industrial revolution increased rapidly to a level significantly higher than it has been in at least 800,000 years![13] In figure 1.1 the atmospheric CO_2 level is shown, focusing on the past millennium. The current level of $\approx$ 420 parts per million (ppm) constitutes a significant increase above any fluctuations and natural variations over time and the upward trajectory is alarming. In a historical perspective carbon based fuels have been predominant,

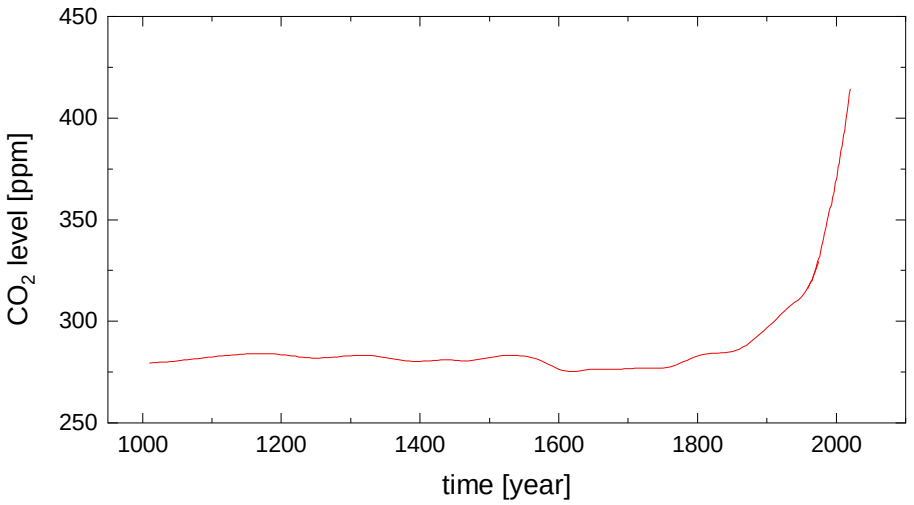

Figure 1.1: Atmospheric CO_2 levels for the last millennium. Since the industrial revolution the CO_2 content of the atmosphere has rapidly increased above it's former stable, albeit fluctuating level. Data adapted from [14] and [15].

but within the last century, the consumption of fossil fuels like coal (and later oil and gas too) has exploded, explaining the drastic increase in CO_2 levels.[16] Fossil fuels have been essential for the technological boom following the industrial revolution and in turn for our way of life. An increasing standard of living (measured by the human development index, HDI) generally correlates with a higher rate of CO_2 emission per capita and as HDI generally increases over time (particularly in developing countries), emissions will too.[17] Another driver for CO_2 emissions is the growing population, whose net energy consumption is unlikely to decrease - on the contrary. The United Nations predict that the population will grow to 9.7 billion already in 2050 and 10.9 billion by the end of the century[18]. By extension the levels of green house gasses will continuously rise unless viable alternatives to fossil fuels are found.

1.1.1 What is the Alternative?

Currently, the global energy consumption is predominantly based on fossil fuels, while renewable energy sources account for a relatively small amount, as seen in figure 1.2. A substantial part of global energy consumption is directly related to the generation of electricity.[19] While this demand is primarily met by the use of fossil fuels, hydropower and nuclear technologies are already used to generate low-emission electricity(grey and purple slivers, respectively, in the figure). Hydropower is, however, geographically limited in applicability and nuclear power has the added challenges of nuclear-waste handling, safety of operation etc. On the other hand, sustainable technologies, such as wind and solar power, are readily available and adaptable on the global scale. These technologies are highly

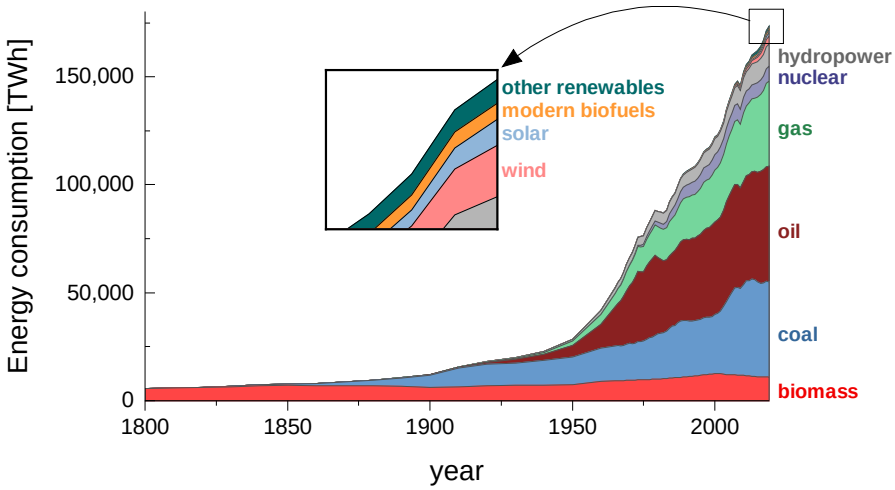

Figure 1.2: Global energy consumption by source. The overall energy consumption has drastically increased in less than a century and is almost exclusively covered by fossil-based sources, in particular coal, oil and gas. The inset shows the small fraction of renewable energy sources. Data adapted from [16].

mature and their levelized cost of electricity (LCoE) is competitive with that of fossil fuels.[20] That is to say, considering all relevant costs and subsidies, these technologies are on par with or cheaper than conventional fossil fuels. This begs the question why these technologies only account for a minuscule part of our energy landscape instead of being it's main constituents. The answer is twofold. Firstly, solar and wind power are intermittent in nature. Secondly, some applications are not electrifiable. Given the intermittency of solar and wind, these technologies cannot be relied upon alone to deliver a steady supply of electricity (or energy). As an example, figure 1.3 shows the net electrical power demand of Denmark during January 2021 and the generated wind power for the same period. While the demand follows a somewhat regular pattern, the generated wind power fluctuates significantly. At times the entire demand may be covered by wind power, other times the wind power falls short and the supply is balanced by e.g. coal and gas[21]. The fraction of the demand covered by wind (or solar for that matter) could naturally be somewhat increased by increasing the overall capacity. On the other hand, the capacity would have to be highly over-dimensioned, which presumably would affect the LCoE negatively to a substantial degree. Even so, there are times where effectively no wind (or solar) power can be generated, given the fluctuating weather conditions. No amount of capacity scaling can make up for this. If, however, a surplus of energy may be stored and instead used in a time of deficit, the intermittent power supply can be dimensioned accordingly and the need for fossil fuels to balance the tab can be eliminated. Thereby, the main obstacle lies in converting and storing energy generated by the renewable resources.

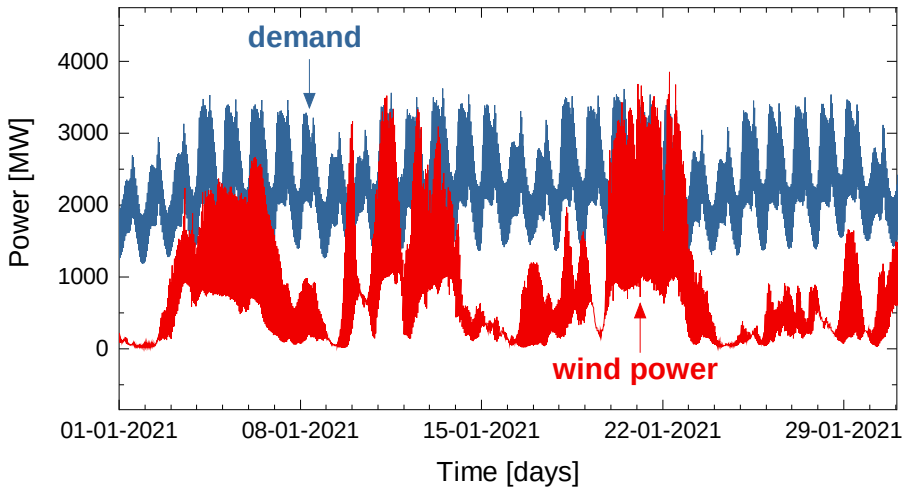

Figure 1.3: Total electrical power demand (blue) and total wind power available (red, sum of onshore and offshore) in Denmark, for January 2021. At peak wind power production the total demand can be met but in the absence of wind, not even a scale-up of capacity will cover the demand. Data from [21].

1.2 Energy Conversion & Storage

Just like fossil fuels, sustainable fuels contain energy in the form of chemical bonds. Wind and solar power can be used to drive electrochemical reactions in which the electrical power is used to convert suitable precursors into more energetic products. Simply put, the idea is that electricity may be converted into *sustainable fuels* at times where wind turbines and solar panels produce energy in excess. At a time when wind and sun fall short, the electricity may then be regained from the fuels. Returning to the global energy consumption, it was mentioned that a large part goes into generating electricity - another large part does not. While, for example, solar and wind power generates sustainable energy in the form of electricity, some technologies are not readily electrifiable, such as aviation[22], and some processes may even *require* fossil fuels as precursors.[19] Renewable energy may also be used to power electrochemical reactions synthesizing these chemicals and materials, given the right precursors. A schematic of this envisioned energy landscape can be seen in figure 1.4. From a few essential building blocks (H_2O, CO_2 and N_2) electricity may drive the production of fuels, fertilizer, chemicals and more[22]. The details and inter-dependencies of such a future energy landscape are intricate, but may be summarized in a few key points. The capacity for sustainable production of electricity, e.g. solar and wind, should be ramped up and electrification should be applied whenever possible. The problem of intermittency should be solved by appropriate technologies for energy conversion and storage, a key element being electrochemical processes powered by renewable electricity. Applications and syntheses which cannot be directly electrified should be replaced with alternatives using sus-

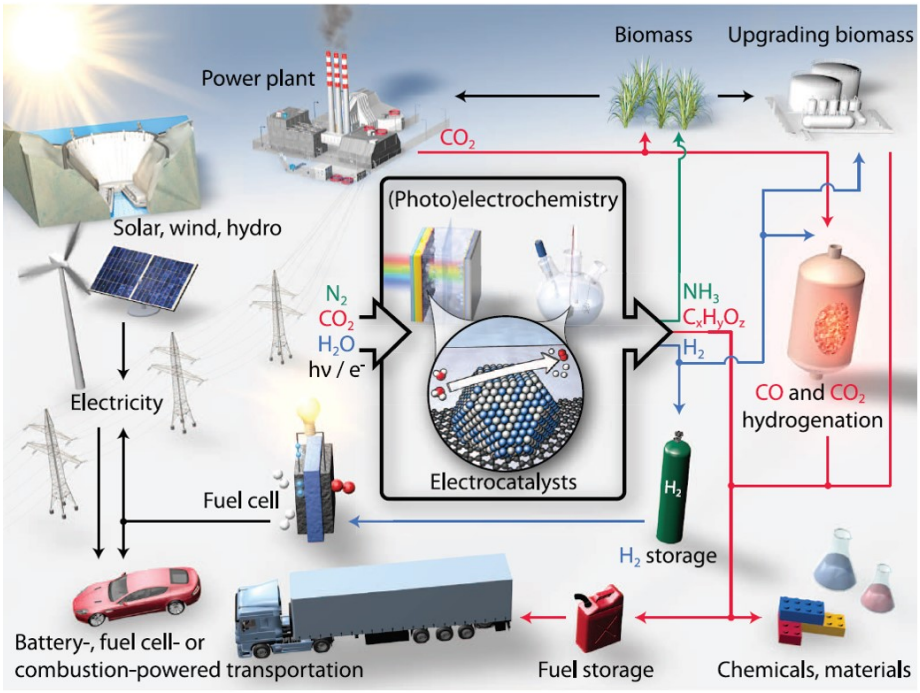

Figure 1.4: Schematic of a sustainable energy landscape: Fuels and chemicals are produced via electrocatalysis using renewable energy and the essential compounds N_2, CO_2 and H_2O. From [22]. Reprinted with permission from AAAS.

tainable energy and renewable chemical building blocks - here electrochemical processes may also come in play. Thereby the emission of green house gasses may be eliminated all together (or at least drastically decreased). Take the electrochemical water-splitting reaction as an example. By applying electrical power, water (H_2O) can be split into it's constituents: hydrogen (H_2) and oxygen (O_2), in which case the electrical energy is converted and stored in chemical bonds, a process called *electrolysis*. The hydrogen may then be consumed again together with oxygen, releasing energy in the form of electricity and nothing but pure water as a by-product. For instance, hydrogen may be used as a sustainable fuel in a so called *fuel cell*, where the electrical energy generated can power a vehicle in a sustainable way, in contrast to a fossil based internal combustion engine emitting CO_2. Note, however, that CO_2 may play a useful role in the energy landscape of the future. The CO_2 reduction reaction (CO_2RR) may be used in to synthesize plastics, chemicals and high energy density fuels. The combustion of carbon based fuels naturally emit the CO_2, but provided that CO_2 is efficiently re-captured, the carbon cycle is sustainable and there is no *net* emission. In the following, hydrogen will be used as an example to further motivate the use of electrochemical processes in general, and highlight the prerequisite for doing so, namely *electrocatalysis*. It is essentially electro-

catalysis that enables the desired reactions of the future energy landscape to run, and it is therefore instrumental in tackling the climate crisis. The concept of electrocatalysis will be introduced further in the following chapter and is in fact the pivotal point for all following chapters.

1.3 Hydrogen as Example

Hydrogen is poised a central role for decarbonizing industry e.g. steel production, as a feedstock component and as a sustainable fuel for transport, domestic purposes etc.[22–25]. A scalable hydrogen production is a prerequisite for these advances and the advent of cheap and renewable electricity from solar and wind power makes the electrolysis of water a promising path for hydrogen production[26]. The water-splitting process is made up of two half-reactions, namely hydrogen evolution reaction (HER) and oxygen evolution reaction (OER). These reactions take place in an electrolysis cell (EC) also called an electrolyzer. Similarly, the reverse reaction releasing energy and water, is also constituted by two half-reactions, which take place in a fuel cell (FC). All of these reactions require efficient *catalysts* to proceed at any rate relevant for industrialization. The nature of such catalysts as well as the details of the half-reaction will be introduced later. Only the overall function of FC and EC devices is relevant for now.

1.3.1 Fuel Cells & Electrolyzers

The polymer electrolyte membrane (PEM) electrolysis cells and fuel cells, working in acidic conditions, can operate at a higher power density than alkaline water electrolyzers as well as a higher pressure and a shorter start-stop time.[27–29] Therefore, only the principles of PEMECs and PEMFCs will be discussed here. Likewise, the rest of this thesis is centered around reactions in acidic conditions. The overall water splitting reaction proceeds like equation (1.1) and requires 237 kJ per mole of hydrogen produced. In other words 237 kJ is stored in each mole of H_2. This is ideal upper limit value given by thermodynamics.

$$2\,H_2O \longrightarrow 2\,H_2 + O_2 \qquad \Delta G^0 = 237\,\mathrm{kJ/mol_{H_2}} \tag{1.1}$$

Actual PEMECs will not have unity power efficiency when splitting water and thus the electrical power spent will be larger than the chemical power stored. Likewise, when consuming H_2 in a PEMFC, not all the stored energy will effectively translate into electrical power. These losses are among other factors due to non-ideal catalysts. Finding suitable catalysts to achieve high efficiency and power density is thus a key goal in order for the technology to be viable. The storage of hydrogen also poses limitations on the achievable power density of the entire system, but this is beyond the scope of this thesis to dive into. The

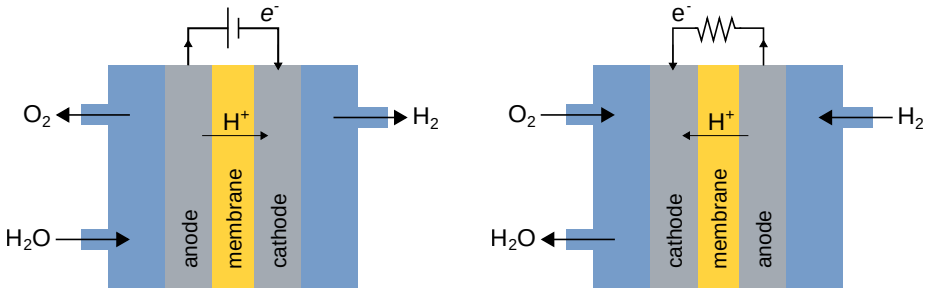

(a) Electrolysis cell (b) Fuel cell

Figure 1.5: (a) PEM elctrolysis cell running the water-splitting reaction to store energy in chemical bonds, forming H_2 and O_2. (b) PEM fuel cell converts H_2 and O_2 to H_2O while releasing excess energy. The PEM membrane separates the two half reactions but allows proton transport.

OER and HER half-reactions of eq. (1.1) are shown in eqs.(1.2)

$$\begin{aligned} H_2O &\longrightarrow \frac{1}{2}\,O_2 + 2\,H^+ + 2e^- \qquad \text{(OER)} \\ 2\,H^+ + 2e^- &\longrightarrow H_2 \qquad \text{(HER)} \end{aligned} \tag{1.2}$$

The two half-reaction are physically separated and involves the transfer of charge, i.e. a current. The schematic of a PEMEC is seen in figure 1.5a. By applying a sufficient voltage between the two electrodes denoted anode and cathode and supplying water (H_2O) to the system the reaction proceeds: at the anode H_2O is split into O_2 via the OER process. Protons (H^+) travel through the PEM membrane while electrons (e^-) go through the external circuit. This enables the HER reaction to proceed at the cathode, thereby producing H_2. Both the cathode and anode are hosts for a catalyst facilitating each reaction. Under acidic conditions platinum and iridium based catalysts are commonly used to drive the HER and OER reactions, respectively.[22,29] In order to take hydrogen production to the terawatt scale it is imperative to find an OER catalyst to replace the extremely scarce iridium. Although less critical, it is highly desirable to find alternatives to the scarce platinum for catalyzing the HER reaction.[23,30,31] Figure 1.5b shows the schematic of a PEMFC, where H_2 and O_2 (e.g. from air) is supplied to the system. The hydrogen oxidation reaction (HOR) takes place at the anode, splitting H_2 into electrons and protons. On the cathode side the oxygen reduction reaction takes place, producing H_2O. The reaction is spontaneous, and now the device can deliver energy in the form of an electric current in a load. Also in this case suitable catalyst are needed to facilitate the reactions. The same is true for many other processes of interest and thus *electrocatalysis* is a cornerstone in the energy landscape needed for a sustainable future.

1.4 Thesis Outline

I have now given a brief outline of the climate crisis and the relation to burning of fossil fuels. Replacing fossil fuels requires a new energy landscape, in which electrochemical energy conversion and storage plays a key role. Developing suitable catalyst to drive these reactions is instrumental for the advancements of these technologies. Accurately measuring catalytic activity, and understanding the factors affecting it, is an essential step in the development.

Thereby, the aim of the work presented in this thesis is to develop a better understanding of active site structures, mass-transport phenomena and other effects relevant for assessing catalytic activity. As already alluded to, single atom catalysts (SACs) and other small entities display particularly interesting catalytic properties. This theme is also reflected in two of the projects presented here. While the third study was not directly related to SACs, the findings might be relevant to the field nonetheless. The main results are presented in three of the following chapters. These studies are the product of collaborative efforts with several colleagues, both from SurfCat and elsewhere. While emphasis will be on the experimental work, to which I have contributed, a more complete picture will be given by drawing on the works of others too.

Chapter 2 gives a brief introduction to electrocatalysis. First, the general concept of catalysis is introduced. Then, some key points regarding electrochemistry is given. These fundamental concepts acts as a frame of reference for later discussions.

Chapter 3 introduces the standard experimental equipment which has been used for most of my work, namely the rotating disk electrode (RDE) and the three-electrode setup. Furthermore, the main types of electrochemical experiments performed are introduced, along with some general experimental procedures.

Chapter 4 revolves around the challenges of catalyzing the oxygen reduction reaction (ORR), in particular the issue of linear scaling relations and product selectivity. The two-electron pathway of ORR, producing hydrogen peroxide, will be the main point of focus. The electrochemical synthesis of hydrogen peroxide via ORR is compared to other methods, highlighting it's technological advantages. The promising prospect of using single atom catalyst for driving the reaction is discussed. In connection with this, a study of a palladium single atom catalyst will be discussed. This chapter is based on paper I.

Chapter 5 is on the hydrogen evolution reaction (HER). While platinum is an excellent HER catalyst, there is an ongoing effort to find cheap, earth-abundant alternatives. In literature, novel catalysts are often reported to be suitable in this regard, but the experimental procedures are often flawed. These common pitfalls are addressed and the impact of mass-transport limitations during HER

is discussed. These topics also prompted our benchmark study of HER on platinum, which is presented here. This chapter is based on paper II.

Chapter 6 deals with the intriguing possibilities and the significant challenges of small entities such as single atoms, dimers etc. as catalysts. The main focus is on the development of a model system for small catalytic entities, specifically platinum single atoms, dimers and trimers anchored by nitrogen defects on highly oriented pyrolytic graphite (HOPG). A brief motivation for the topic is given and preliminary results are presented. The work draws on lessons learned from both the Pd SAC-project and the Pt HER benchmark study (discussed in chapters 4 and 5, respectively) as well as the effort of a number of collaborators. The project is still at an early stage, however, results of various experiments, electrochemical and otherwise, have shown interesting results. The chapter is ended with a brief outlook on the further development of the model system.

Chapter 7 summarizes the main results of the studies presented in the previous chapters. Furthermore, an outlook is given.

Chapter 2

Electrocatalysis

This chapter serves as a very general introduction to electrocatalysis. I will start out with the "catalysis" part by, in broad strokes, describing what a catalyst is and what constitutes a good catalyst. The brief introduction of these main points serve as a primer for the later, more in depth, discussions in the following chapters. Turning to the "electro" part, I outline some fundamentals of electrochemistry. The Butler-Volmer model is then introduced, providing a simplistic framework for understanding electrochemical measurements in the context of catalytic processes. The effects of mass-transport limitations are also included, provinding the foundation for later discussions.

2.1 Catalysis

A catalyst is a facilitator of a reaction. A catalyst drives the transformation of reactants into products, while the catalyst itself is preserved. By lowering the energy barriers associated with the reaction, the catalysts enables a higher reaction rate. Essentially, a catalyst provides the location for the involved species to adsorb, react and desorb. A schematic of a generic reaction is shown in figure 2.1, where reactants a and b undergo a catalyzed process to form a product p. Reaction barriers may still have to be overcome in this case, but the energy required is substantially less than for the un-catalyzed pathway (stipulated line). Ideally, the energy profile of the catalyzed pathway (full line) would go monotonically between the initial and final states, i.e. no intermediate energy barriers. This is generally not the case. Note that the catalyst does *not* change the initial nor final state - the overall thermodynamics of the reaction is the same, the catalyst merely promotes a more favorable path. A catalyst facilitates a reaction by binding the intermediates, and the strength of this bond is determining for how favorable the reaction step becomes. If a reaction intermediate binds too weak, the ability to get said intermediate onto the catalyst will limit the reaction. If, on the other hand, the intermediate binds too strong, the further reaction to form the product will be impeded. Thus, the highest *activity*, i.e. re-

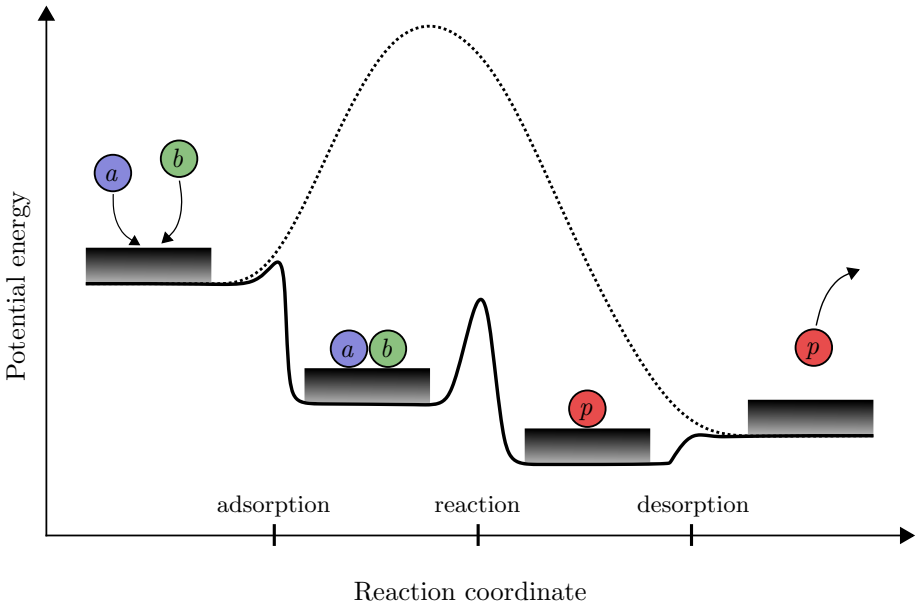

Figure 2.1: Energy diagram of a reaction where reactants a and b form a product p. The stipulated line shows the *un*-catalyzed reaction. The catalyzed reaction (solid line) has significantly smaller energy barriers to overcome. The sumperimposed gray boxes and colored spheres display the catalyst surface and reactants/products, respectively, between each reaction step.

action rate, will be achieved for a catalyst which binds the intermediate neither too weak nor too strong, known as *Sabatier's Principle*. For instance, in the case of the hydrogen evolution reaction (HER), the only intermediate is hydrogen adsorbed on the catalyst (H*) where * denotes a catalytic *site*. Therefore, an optimal catalyst should have an adsorption free energy $\Delta G_{\mathrm{H}^*} \approx 0$. This qualitatively agrees with what is observed in figure 2.2(a). The blue points represent experimental estimates of HER activity for various transition metals and the black line shows a kinetic model calculated via density functional theory (DFT). Qualitatively a so-called volcano trend emerges, with and optimum around $\Delta G_{\mathrm{H}^*} \approx 0$. The case of the oxygen reduction reaction (ORR) is more complex, since the reaction has multiple intermediates, whose binding energies are related to one another. Due to these *scaling relations*, the binding energies cannot be optimized independently[32]. This issue is the limiting factor in the performance of ORR catalyst[33]. This topic will be discussed further in chapter 4. Nevertheless, the activity-dependence can be simplified to a one dimensional volcano plot as well, as seen in figure 2.2(b), where the oxygen binding strength is used as descriptor. The binding characteristics of the catalyst, and the performance in general, is not solely defined by the catalyst material, but also by the nature of the catalytic sites - the place where the reaction takes place. Tuning the properties of catalytic sites is essential for improving the intrinsic

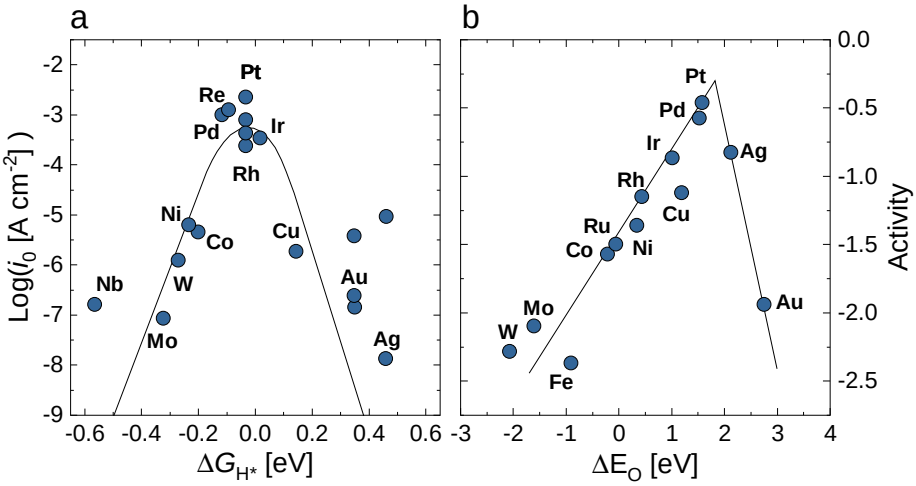

Figure 2.2: Volcano plots: (a) HER activity trend with free energy of H-adsorption as descriptor. Adapted with permission from [34]. Copyright 2010 American Chemical Society (b) Trend in ORR activity: The binding energy of oxygen acts as a descriptor for the overall activity of the reaction. Adapted with permission from [33]. Copyright 2004 American Chemical Society.

activity of a catalyst, but extrinsic factors also contribute to the net activity: Since catalysis occurs at the surface, the overall reaction rate is proportional to the area on which the reaction may occur (neglecting intrinsic effects for now), hence it is desirable to maximize the available surface area of the catalyst, i.e. the umber of active sites. For this reason, catalysts generally have the form of nanoparticles (i.e. particles with a typical size scale of 1-10 nanometers) or structures on the similar size scale, which are then dispersed over larger structures[35]. Decreasing particle size increases the surface-to-bulk ratio and thereby the effective material utilization. This is important as many catalysts are based on scarce and expensive materials, e.g. platinum (Pt) or iridum (Ir). The use of such catalyst material may present a bottleneck in scaling technologies to the desired terawatt level.[23,30] In addition to material utilization, the size of the particle may also affect the intrinsic electronic and geometric properties, e.g. the binding strength of reaction intermediates, the exposed facets and the available sites. Figure 2.3 shows an example of a nanoparticle exposing the low index facets. The kinks and edges are more *under-coordinated* than the energetically favorable low index planes, that is, they have fewer nearest neighbors. The interaction with reaction intermediates may thus be radically different for these sites compared to e.g. the low index planes, which can lead to significant particle-size effects. For example, particle-size effects have been observed for ORR on Pt_xY[36], OER on RuO_2[37], CO-oxidation on Au[38,39] and CO2RR on Cu[40]. For particles less than $\approx$ 2 nm, often called *clusters*, quantum mechanical effects may arise, significantly altering catalytic properties.[41,42] Clusters of a few atoms (from one to some tens of atoms) have shown significant size ef-

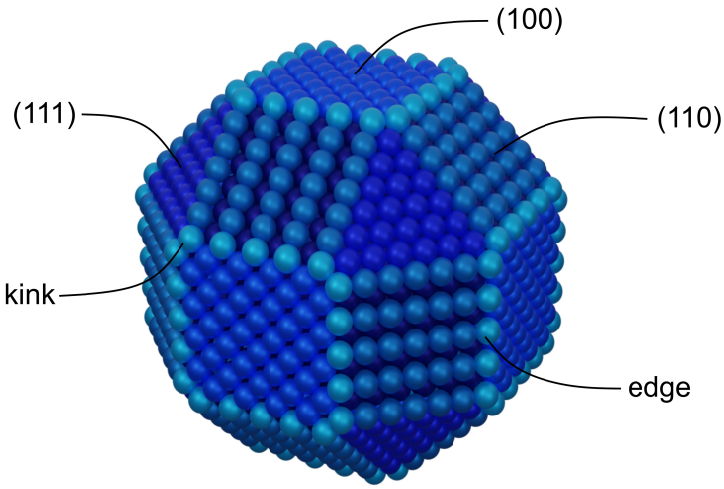

Figure 2.3: Wulff construction of a Pt nanoparticle showing kinks, edges and three low index planes. Generated using the ASE package with ≈ 3900 Pt atoms. Blue color scale corresponds to coordination number where lighter colors represent more under-coordinated sites. The kink and edge sites (light teal blue) are the most under-coordinated sites having only 6 nearest neighbors.

fects in terms of selectivity and activity of various reactions - even to the point where one atom more or less might significantly change the activity and selectivity.[43–46] Thus going to the ultimate limit of the sizes scale - small clusters or single atoms, dimers, trimers and so on - may hold great potential both in terms of maximal material utilization as well as unique geometric and electronic effects, which may possibly allow circumventing the linear scaling relations.

2.2 Electrochemistry

Electrochemistry revolves around reactions in which a chemical change is related to a charge transfer across an interface of differing chemical phases. Generally, the charge is transferred between an electronic conductor (electrode) and an ionic conductor (electrolyte). Conservation of charge dictates that one such reaction at an electrode, e.g. reduction is counterbalanced by an oxidation at another electrode (or vice versa). These electrodes are separated by at least one electrolyte phase. Electrochemical reactions are thus heterogeneous reduction-oxidation (redox) reactions, where the reduction and oxidation are physically separated, although linked.[47]

2.2.1 Redox & Potentials

A generic redox reaction takes the form of equation (2.1), in which a species O gets reduced (going right) or R is oxidized (going left), where n is the stoichio-

metric number of electrons.

$$\mathrm{O} + ne^- \rightleftharpoons \mathrm{R} \tag{2.1}$$

Such a reaction is associated with an equillibrium potential, denoted the *standard potential* (E^0), at which the net reaction rate is zero. The tendency for either the reduction or oxidation to be favored is directly related to the potential of the electrode with respect to this formal potential. An electrode at which a net reduction takes place is called a *cathode*, whereas an electrode at which a net oxidation takes place is called an *anode*. This comes about by driving the potential away from the equilibrium. By decreasing the potential of an electrode (in negative or *cathodic* direction), the energy level of the electrons increase. This thermodynamically favors transferring electrons into the lower energy state of the reduced species, hence favoring reduction. Conversely, increasing the potential (toward positive or *anodic* direction) lowers the energy of electrons, making electron transfer away from R favorable, i.e. oxidation. Note, that the redox couple is in a dynamic equillibrium, so at a zero net reaction rate, the reaction proceeds at equal rates in opposing directions. The potential (E) of an electrode at equilibrium is given by E^0 and the activities a_i of the involved species O and R, via the Nernst equation (2.2)

$$E = E^0 + \frac{RT}{nF} \ln \frac{a_\mathrm{O}}{a_\mathrm{R}} \tag{2.2}$$

where R, T and F are the universal gas constant, temperature and Faradays constant, respectively. However, activities are rarely known, so eq. (2.2) may be reformulated more practically as equation (2.3), by introducing the *formal potential* $E^{0'}$, which incorporate the standard potential and activity coefficients.[47]

$$E_\mathrm{eq} = E^{0'} + \frac{RT}{F} \ln \frac{C^*_\mathrm{O}}{C^*_\mathrm{R}} \tag{2.3}$$

Now the potential is given in terms of the bulk concentrations $C^*_\mathrm{O}, C^*_\mathrm{R}$ of the species, which may be controlled in experiments. On the other hand the standard potentials of redox couples are the ones most often referred to, and not the formal potentials. The discrepancy is, however, not essential for the points discussed in the following so the distinction will not be made. Importantly, either formulations indicate that the equilibrium potential of a redox pair is dependent on the presence of the partaking species. For instance, if the concentration (or activity) of the reduced compound (R) is decreased, the equilibrium potential will become more positive (anodic), making the reduction more favorable with respect to a reference potential. By applying a potential E to an electrode the reaction may be driven away from equilibrium, thus favoring one direction relative to the other. The driving force is the *overpotential* (η), defined by equation (2.4).

$$\eta = E - E_\mathrm{eq} \tag{2.4}$$

Consequently $\eta < 0$ favors reduction while $\eta > 0$ favors oxidation. So far the actual *potential scale*, to which these values refer, has not been discussed.

The *difference* between potentials, is what drives reactions and is therefore more important for present discussion. Nevertheless, potential scales will be discussed in section 3.4.4.

2.2.2 Thermodynamics

The points discussed above lay the foundation for understanding redox reactions at an electrode, though these are only *half-reactions*. As already suggested, the overall reaction taking place in an actual *electrochemical cell* is made up of two half-reactions, each taking place at separate electrodes, according to the potential of and chemical environment around each electrode. One is commonly concerned with studying one half-reaction at a time, but understanding an overall reaction is crucial in the context of real applications. Generally, two electrodes in an electrochemical cell may be at different potentials, one acting as cathode, the other as anode in the overall reaction. The potential difference between the cathode and the anode is then the potential of the cell reaction E_{rxn}. This is associated with the net work available from the cell reaction, i.e. the difference in Gibbs free energy (ΔG), via equation. (2.5)

$$\Delta G = -nFE_{\text{rxn}} \tag{2.5}$$

or in the case of unit activity of all substances the standard potential of the cell reaction E^0_{rxn} gives the standard Gibbs free energy:

$$\Delta G^0 = -nFE^0_{\text{rxn}} \tag{2.6}$$

Convention thus dictates that a positive E_{rxn} is associated with a spontaneous reaction ($\Delta G < 0$). For the overall reaction of X,Y,Z with the corresponding stoichiometric coefficients x, y, z, seen in eq. (2.7)

$$x\text{X} + y\text{Y} \rightleftharpoons z\text{Z} \tag{2.7}$$

thermodynamics states that the free energy is given via eq. (2.8)

$$\Delta G = \Delta G^0 + RT \ln \frac{a_{\text{Z}}^z}{a_{\text{X}}^x a_{\text{Y}}^y} \tag{2.8}$$

Combining this with equations (2.5) and (2.6), the potential of the cell reaction (2.7) is then given by (2.9).

$$E_{\text{rxn}} = E^0_{\text{rxn}} - \frac{RT}{nF} \ln \frac{a_{\text{Z}}^z}{a_{\text{X}}^x a_{\text{Y}}^y} \tag{2.9}$$

It is worth returning to the water-splitting reaction introduced in eq. (1.1) and rewriting the appropriate half-reactions and their standard potentials:

$$2\text{H}_2\text{O} \underset{\text{ORR}}{\overset{\text{OER}}{\rightleftharpoons}} \text{O}_2 + 4\,\text{H}^+ + 4e^- \qquad E^0 = 1.23\ \text{V} \tag{2.10}$$

$$2\,H^+ + 2e^- \underset{\text{HOR}}{\overset{\text{HER}}{\rightleftharpoons}} H_2 \qquad E^0 = 0\ \text{V} \tag{2.11}$$

The overall water-splitting reaction is made up of the two half reactions (left to right direction) in equations (2.10) and (2.11). It is now apparent that $E_{\text{rxn}} = -1.23$ V for water-splitting under standard conditions, meaning that 1.23 V (or more) must be applied for driving the HER and OER half-reactions, producing H_2 and O_2. The reverse reactions (right to left direction), ORR and HOR, are the ones driving a hydrogen fuel cell. Note that the anode and cathode are now "switched", so that $E_{\text{rxn}} = +1.23$ V under standard conditions. Therefore, the fuel cell will (ideally) deliver 1.23 V at equilibrium. Be that as it may, an overpotential (η) is needed to drive the cell at any rate beyond equilibrium. This means that the actual obtainable voltage output E_{cell} of a fuel cell is less while the potential that must be applied to drive an electrolyzer $|E_{\text{cell}}|$ is higher, as seen in eq. (2.12). In both cases this constitutes a loss of efficiency.

$$E_{\text{cell}} = E_{\text{rxn}} - (\eta + \eta_\Omega + \eta_{\text{MT}}) \tag{2.12}$$

Driving the highest possible reaction rate for the lowest possible η is essentially the role of an efficient catalyst. The relation between reaction rate and overpotential will be explored in the following section. Furthermore, the Ohmic resistance of a cell causes a potential drop (η_Ω), which can in some cases be significant. Slow rates of mass transport of reactants and products may also limit the overall reaction rate. This can also be regarded as an overpotential or potential drop, η_{MT}. Although dealing with these effects to some extent is an engineering challenge, they also influence the investigations of half-cell reactions, including those presented throughout this thesis.

2.3 Kinetic Model System

The reaction rate of an electrochemical reaction is characterized by a current i or current density j (current per area) given the charge transfer associated with the reaction. The current and overpotential are essentially the two primary performance descriptors of an electrochemical system, be it an experimental cell, or a commercial electrolyzer or fuel cell. A simple understanding of their interdependence is therefore necessary. The Butler-Volmer (BV) model offers a simple kinetic description, based on the more general *current-overpotential equation*. The BV model assumes a one-step, one-electron ($n = 1$) reaction with no consideration for coverage effects of reaction intermediates or reaction mechanics. Moreover, the model pertains to a purely kinetically limited system i.e. infinitely fast mass transport. In practice this means that the mass transport should be *much* faster than the reaction kinetics, i.e. the mass transport rate constants of all species (i) are much faster than the heterogeneous reaction rate constant ($k_{\text{MT},i} \ggg k$). At the end of this section, the BV model will be expanded to include finite mass transport rates. The model can also be generalized to multi-step reactions for some cases, but this will not be discussed. This

highly idealized model is for most cases not an accurate description of the reactions investigated, but it does give a framework for qualitatively understanding reaction kinetics.

The Butler-Volmer equation (2.13) is given here in terms of current density (j, j_0) rather than reaction rate constants (k, k^0), since the former is more easily comparable with experimental measurements.

$$j = j_0 \left\{ \exp\left[\frac{\alpha F}{RT}\left(E - E_{\mathrm{eq}}\right)\right] - \exp\left[-\frac{(1-\alpha)F}{RT}\left(E - E_{\mathrm{eq}}\right)\right] \right\} \tag{2.13}$$

By once again using $\eta = E - E_{\mathrm{eq}}$ and introducing the shorthand notation $f = F/RT$ the equation can be rewritten in a more compact form (2.14). The transfer coefficient $\alpha \in [0 : 1]$ is a dimensionless parameters describing the symmetry of the energy barrier of the charge transfer. The prefactor j_0 is known as the *exchange current density*.

$$j = j_0 \left[e^{\alpha f \eta} - e^{-(1-\alpha) f \eta} \right] = j_{\mathrm{a}} + j_{\mathrm{c}} \tag{2.14}$$

In essence, the BV equation consists of two terms of exponential dependence on the applied overpotential. This indicates that the total current density j is the sum of two contributions, an anodic and cathodic part, j_{a} and j_{c} respectively, reflecting that the electrochemical reaction is in a dynamic equilibrium where both the oxidation and reduction takes place simultaneously and the overpotential determines which one is dominating. In the case of equilibrium at $\eta = 0$ then $j = 0$, however, j_{a} and j_{c} are equal in magnitude and of opposite in sign. While an overpotential is needed to drive the reaction in either direction, j_0 determines the intrinsic rate of the reaction. A facile reaction is therefore characterized by a high j_0, yielding a high reaction rate, $j(\eta)$, when perturbed. This is where *electro* meets *catalysis*: A catalyst that readily facilitates a reaction is characterized by a high intrinsic activity (e.g. j_0). Finding materials that have high j_0 for the desired reactions is at the heart of electrocatalysis. Current density has only been vaguely defined here as i/A. While i is a measurable current, the area (A) used for normalization depends on the context. Several definitions (and other activity metrics) are used throughout this thesis as well as in literature, and will be introduced when appropriate (note the exception of mass activity (j_{mass}) where catalyst loading (mass) rather than area is used for normalization). In figure 2.4 a Butler-Volmer curve is plotted. In figure (a) the anodic and cathodic contributions are shown as green and blue stipulated lines and the net current density is denoted by the black line. At $\eta = 0$ the net current density is zero as j_{a} and j_{c} are equal in magnitude and opposite in sign. Increasing η (positive direction) shifts the reaction favoring oxidation and the j_{a} becomes the dominating term. Conversely, the reduction is favored when η becomes negative and thus the magnitude of j_{c} dominates. Note that j_0, the parameter of interest, is not directly measurable. The right figure, a so called Tafel plot, shows the current on a logarithmic scale. At large overpotentials, where either j_{a} or j_{c} dominate j completely, the Tafel plot becomes linear.

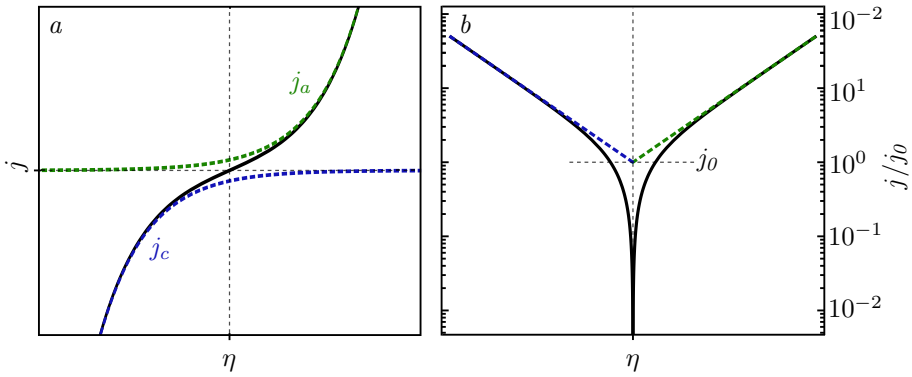

Figure 2.4: Current density vs. potential in case of ideal Butler-Volmer behavior (with $\alpha = 0.5$).(a) Full black lines represent the net current, stipulated green lines the anodic component and stipulated blue lines the cathodic component. (b) a so-called Tafel plot shows the log-scaled $|j|$ (black) and the back extrapolation to $\eta = 0$ of both the anodic and cathodic branch intersecting at j_0.

By back extrapolation from either the anodic or cathodic branch to $\eta = 0$ the exchange current density j_0 is found. In practice, however, a finite mass transport rate and more complex reaction mechanisms make this extrapolation more tricky or even misleading. Using more elaborate formulations of the BV equations, the slope of such a Tafel plot (Tafel slope) may hold information of the reaction mechanism investigated. Fitting experimental data with this approach may however be complicated by the same issues as the back-extrapolation. The highly idealized Butler-Volmer model may not accurately fit real experiments, but it is worth considering the concept nonetheless.

2.3.1 Mass Transport Considerations

As already implied, ohmic resistance and mass-transport limitations may affect the potential measured during an experiment, thus preventing a correct assessment of the kinetic parameters of interest like e.g. $j(\eta)$ or j_0. Frequently the ohmic resistance can be evaluated and compensated for quite easily. The same is not necessarily true for the influence of mass transport. Therefore, a few comments about mass-transport limitations are in order.

The current-overpotential equation (2.15) is a generalized version of the BV equation, where the concentrations of reactants and products at the catalyst surface (C_i^s) and in the bulk electrolyte (C_i^*) are included.

$$j = j_0 \left[\frac{C_{\mathrm{R}}^s}{C_{\mathrm{R}}^*} e^{\alpha f \eta} - \frac{C_{\mathrm{O}}^s}{C_{\mathrm{O}}^*} e^{-(1-\alpha) f \eta} \right] \tag{2.15}$$

In the limit of concentration equilibrium between the catalyst surface and the bulk electrolyte the equation simplifies to the BV equation. On the other hand, the partial current densities may be limited when reactant concentrations at the

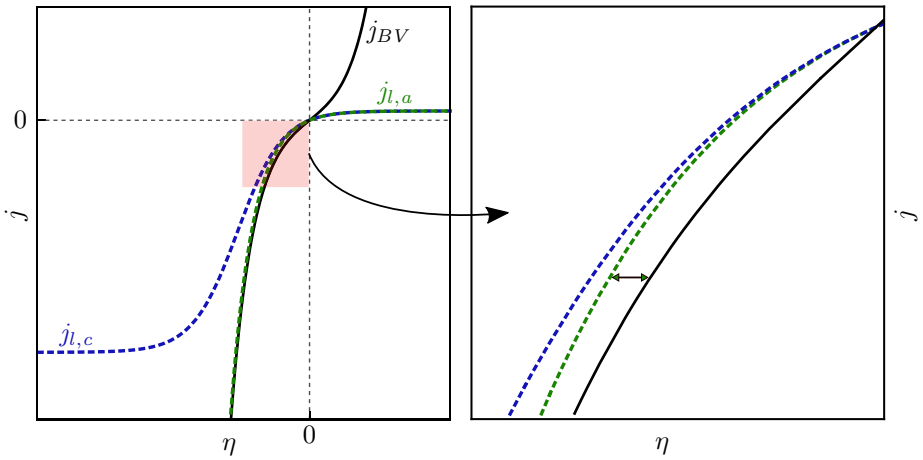

Figure 2.5: Examples of mass transport limitations on Butler-Volmer curves: Limited anodic current density (green stipulated line), both anodic and cathodic limitation (blue stipulated line) and the case of no mass transport limitation (solid black line). Left figure shows a plateau when reaching either the anodic or cathodic limiting current density, $j_{\mathrm{l,a}}$ and $j_{\mathrm{l,c}}$ respectively. Right figure shows a significant deviation from an ideal Butler-Volmer curve even at currents well below the limiting case.

surface drop. Generally, reactants and products are transported to and from the catalyst via diffusion due to a concentration gradient. The difference between C_i^s=0 and C_i^* sets the maximal gradient possible of diffusing reactants to the surface. For example, if $C_{\mathrm{R}}^{\mathrm{s}}$ tends toward zero, the anodic reaction cannot proceed any faster since the delivery of reactants has reached it's maximum rate. Interestingly, a deficiency of reactants is not the only source of limitation. In principle an excess of products can limit the net reaction rate, since a larger surface concentration promotes the reverse reaction. Instead of the concentrations dependence, equation (2.15) may in fact be re-written in terms of limiting current densities - which in some cases may be calculated or experimentally determined. This gives equation (2.16) where the net current density is a function of both the kinetic contribution and the mass-transport limitation, namely the limiting anodic ($j_{l,a}$) and cathodic ($j_{l,c}$) current densities.

$$j = \frac{e^{\alpha f\eta} - e^{-(1-\alpha)f\eta}}{\frac{1}{j_0} + \frac{e^{\alpha f\eta}}{j_{\mathrm{l,a}}} - \frac{e^{-(1-\alpha)f\eta}}{j_{\mathrm{l,c}}}} \tag{2.16}$$

Note, that if $j_0 \ggg j_{\mathrm{l,a}}, j_{\mathrm{l,c}}$, the mass-transport limited current densities completely dominate j. This special case is named the *concentration-overpotential*, which is to say that if the kinetics are sufficiently facile, no kinetic information may be obtained. Conversely, if $j_{\mathrm{l,a}}$ or $j_{\mathrm{l,c}}$ are sufficiently large they have no practical impact on the measured j. Three cases of j vs. η are plottet in figure 2.5. In the left plot the black curve shows the simple BV-behavior, whereas the green line is limited by $j_{l,a}$ at which the curve flattens out. The blue line is

limited both by $j_{l,a}$ and $j_{l,c}$, hence the plateau in both the anodic and cathodic region. The right plot shows the extra overpotential encountered as a consequence of the slow mass-transport compared to the purely kinetic case, even way before the limiting current densities are reached.

Chapter 3

Experimental Methods

In this chapter I give an overview of the experimental methods and setups used for the projects presented in the following chapters. I will limit the discussion here to electrochemical techniques, which is what I primarily have been working with. Several other experimental techniques have been essential for the projects presented in the following chapters, so I will include the main results of these throughout, without diving into the details of the methods. The one exception is the cluster source system, which deserves a brief introduction - this will be given in chapter 6 where the small-entity project, for which the cluster source is the prerequisite, is discussed. First the experimental equipment will be described, in particular the three-electrode setup. Following this, some common experimental preparations will be discussed, such as cleaning procedures and sample preparation. Finally the experimental procedures, data acquisition and treatment will be discussed in brief.

3.1 The Three-Electrode Setup

The three-electrode setup is constituted by a working electrode (WE), counter electrode (CE) and a reference electrode (REF). This allows studying half-reactions taking place at the working electrode. The WE potential is measured with respect to the REF, whereas the current runs between WE and CE. The electrodes are connected to a potentiostat which is controlled using a computer. Describing a potentiostat in any detail is beyond the scope of this thesis but the main parameters and settings will be discussed when relevant. With this basic setup a large variety of experiments may be conducted. The standard setup primarily used for the work presented in this thesis is based on the three-electrode configuration, and is depicted in figure 3.1. A glass cell, which is closed except for five openings with tapered slots contains the electrolyte. Through the center opening the tip of a rotating disk electrode (RDE) may be submerged into the electrolyte and function as WE. The purpose and function of the RDE will be discussed in the following section. Via another opening the CE is inserted into

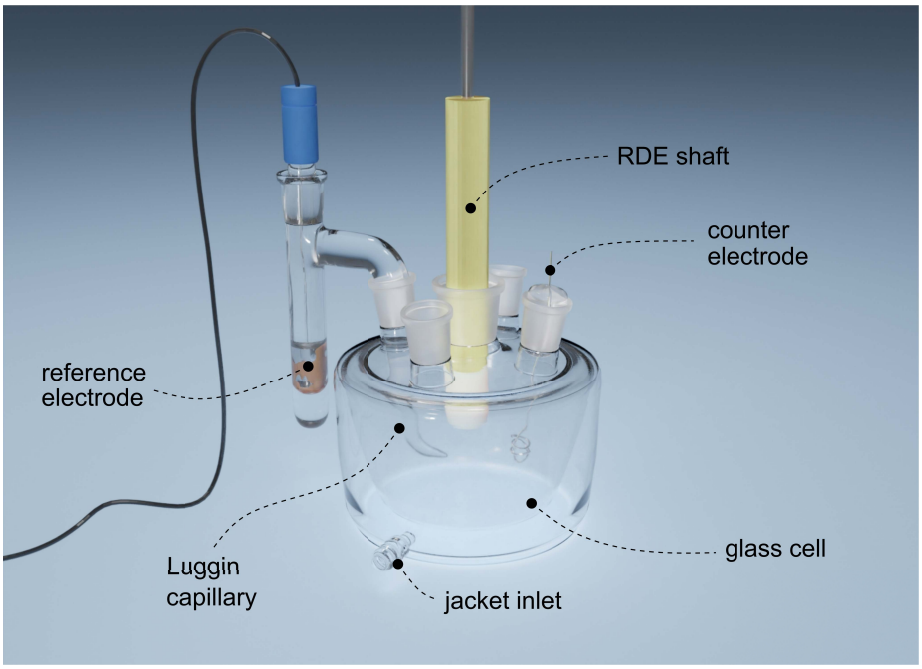

Figure 3.1: Three-electrode setup in glass cell with an RDE as WE, a wire as CE and the REF electrode placed in a Luggin capillary. The gas bubbler and dummy electrode have been left out of the sketch for simplicity, but are inserted in the two available slots in the top of the glass cell. The internal electrolyte volume is encased by a cell-jacket allowing a water flow for heating or cooling through the inlet (outlet on opposite side of cell is not shown).

the electrolyte through a tapered glass plug fitting the slot. A gas bubbler and a dummy electrode (not shown in figure) are mounted in two of the other slots. The bubbler is a glass tube with a porous frit in the end submerged in electrolyte, while the other end connects to the external gas supply. The bubbler thus disperses the supplied gas into the electrolyte as fine bubbles. The dummy electrode, a Pt wire, is used for inserting sample under potential control and calibrating the REF potential as described later. Finally, the Luggin capillary is filled with electrolyte and holds the REF (Hg/Hg_2SO_4), however, only the capillary tip is placed in the cell. The purpose is two-fold: The capillary tip gives a small and well-defined point at which the REF potential is measured. This small point can thus be placed close to the WE, thereby minimizing the Ohmic resistance between WE and REF without significantly obstructing the mass transport to the WE. Furthermore, the long and narrow tip minimizes the rate of diffusion from the REF into the cell, thereby minimizing the amount of possible contaminants. By comparing used electrolyte solutions from the Luggin capillary and cell using inductively coupled plasma mass spectrometry (ICP-MS), the advantage of a Luggin capillary is apparent: Figure 3.2 shows the difference in ICP-MS signal intensities for the two electrolyte samples, nor-

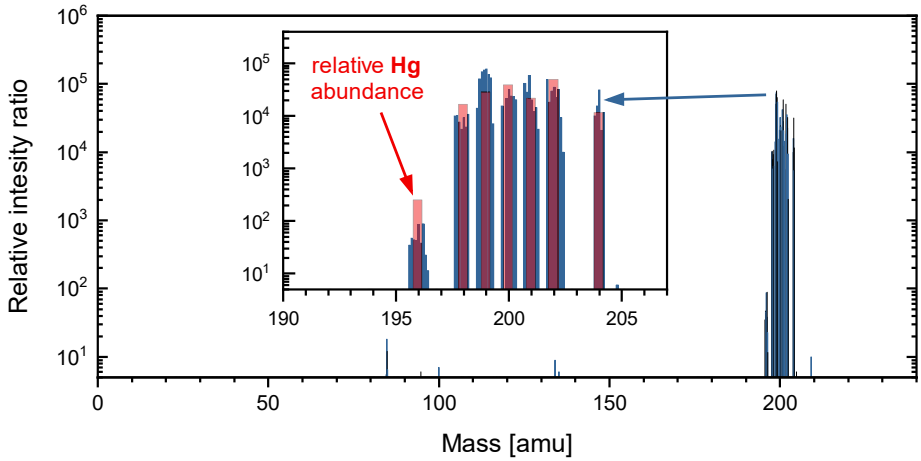

Figure 3.2: Post experiment ICP-MS test of Luggin-electrolyte. Electrolyte (0.5 M Suprapur H_2SO_4) was collected from the Luggin capillary and the cell after an experiment and compared with the blank electrolyte from flask. The difference between ICP-MS intensities of the Luggin capillary and the cell relative to the blank is plotted vs. element mass, that is: $(I_{\text{Luggin}}$-$I_{\text{cell}})/I_{\text{blank}}$. The transparent red bars in the inset show the relative isotope abundance of Hg scaled so that the most abundant isotope ($^{202}_{80}$Hg) matches the measured intensity at same mass.

malized to the signal of a unused aliquot of same electrolyte. The result is a qualitative picture of which chemical elements are present in the electrolyte volume from the Luggin capillary beyond what can be expected. The overall mass-spectrum shows no major features except for at $\approx$ 200 amu, where a set of relatively intense peaks are found. As seen in the inset, the fingerprint of relative isotope abundance for Hg fits the measured peaks reasonably well. The presence of trace amounts of Hg can be attributed to the Hg/Hg_2SO_4 reference electrode. A more rigorous procedure employing calibration via standard solutions is needed if quantitative estimates are desired, but the qualitative indication is already straightforward: Trace Hg impurities due to the REF are practically prevented from entering the cell due to the Luggin capillary. On a more general note, it is important to minimize such trace contaminants by using high purity materials and solutions as well as cleaning glass ware, substrates etc. These points will be elaborated after a brief introduction of the rotating disk electrode.

3.2 The Rotating Disk Electrode (RDE)

The rotating disk electrode (RDE) is a setup used to ensure a controllable and well-defined rate of mass-transport. Figure 3.3 shows a sketch of the basic components and the working principle of an RDE. An exchangeable disk electrode, for instance a glassy carbon electrode (GCE), is mounted in a Teflon (PTFE) RDE-tip so that it is flush with the surface. A leak tight fit is ensured by a

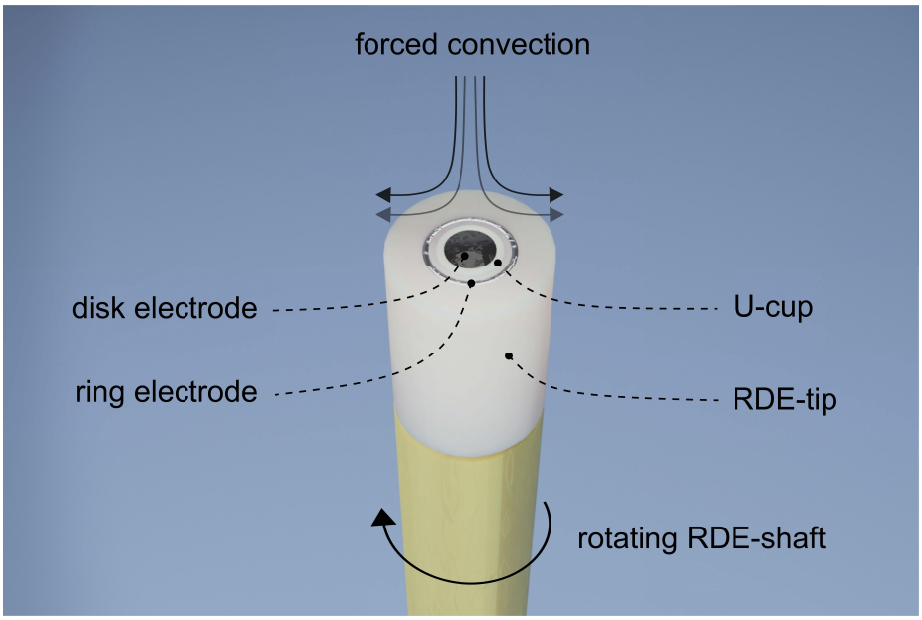

Figure 3.3: Rotating (ring)-disk electrode assembly. A disk electrode is inserted via a U-cup into the RDE-tip. Encircling the disk is a Pt ring electrode. Both electrodes have separate electrical contacts running internally through the RDE shaft. Upon rotating the shaft a convective flow of electrolyte impinges the RDE-tip.

Teflon U-cup assembly sealing the gap between RDE-tip and disk. Optionally, the tip may also have an embedded ring electrode making it a rotating ring disk electrode (RRDE). The RDE-tip is attached to a shaft which connects to an external rotator, including the electrode contacts. When the RDE-tip is immersed in electrolyte and rotated via the shaft, forced convection results in a flow of electrolyte species toward the disk surface and radially out across the tip.

By solving the hydrodynamic and convective-diffusion equations, the current in the case of limiting mass-transport may be found.[47] The Levich equation (3.1) gives the limiting current density (e.g. cathodic, $j_{\mathrm{l,c}}$) from the kinematic viscosity (ν), diffusion coefficient (D_{O}) and bulk concentration (C^*_{O}) of the reactant species (in this case O) - and of course the RDE rotation speed (ω), here in unit of rounds per minute (rpm). The constants can be lumped together into B, known as the Levich constant. A plot of a measured j vs. $\omega^{1/2}$ then gives a straight line with a slope of B when completely limited by mass-transport.

$$j_{\mathrm{l,c}} = 0.201 n F D_{\mathrm{O}}^{2/3} \nu^{-1/6} C^*_{\mathrm{O}} \omega^{1/2} = B C^*_{\mathrm{O}} \omega^{1/2} \tag{3.1}$$

Often it is desirable to estimate kinetic information from measurements under *partial* mass-transport limitation. To this end the Koutecký-Levich equation (3.2) provides a means to extract the kinetic current density (j_{k}) from the measured one (j) by either experimentally measuring or calculating the limiting

current density (j_l) via. (3.1).

$$\frac{1}{j} = \frac{1}{j_k} + \frac{1}{j_l} \tag{3.2}$$

3.2.1 The Rotating Ring-Disk Electrode (RRDE)

The rotating ring-disk electrode (RRDE) is a modification of the RDE with a separate ring electrode encircling the disk as seen in figure 3.3. Using a bi-potentiostat, the ring potential (or ring current) can be controlled independently of the disk, giving extra experimental possibilities. In particular, the ring may be used for product detection of electrochemically active species. For example a reduction reaction may take place at the disk, after which a fraction of the product (R) passes over the ring due to the diffusive/convective flow. If the ring is at an appropriate potential, the reverse reaction may proceed, as in equation (3.3).

$$\mathrm{O} + ne \underset{\text{ring}}{\overset{\text{disk}}{\rightleftharpoons}} \mathrm{R} \tag{3.3}$$

This is particularly useful if multiple reactions take place simultaneously at the disk but only of these reactions take place (in reverse) at the ring. If the collection efficiency (N) of the ring is known, the partial current density toward one of the disk reactions may be then found. This is a valuable tool in studying the selectivity of the oxygen reduction reaction, as discussed in chapter 4. The collection efficiency N is given by the fraction of moles produced at the disk which reach the ring - or in terms of currents by eq. (3.4).

$$N = \frac{-i_R}{i_D} \tag{3.4}$$

Ideally N is independent of experimental parameters such as ω, ν, $C_{O,R}$ etc. and can be analytically derived solely from the disk radius (r_1), inner (r_2) and outer (r_3) radii of the ring[47]. Alternatively N can be measured experimentally as discussed in section 3.4.1.

3.3 General Experimental Preparations

Primarily a VMP-2 potentiostat (BioLogic) was used with channel boards supporting electrochemical impedance spectroscopy (EIS). For RRDE-measurements a bi-potentiostat cable box was used in conjunction with two channels on the VMP-2. The shortest possible ($\approx$ 1 m) potentiostat cables were used (in particular when performing EIS) to minimize inductance. Since the projects were to some degree overlapping, different glass cells, RDE-tips etc. were used for each project to limit cross contamination from differing electrolytes and samples. A Hg/Hg_2SO_4 reference electrode (ScienceLine, Schott Instruments) has been used for all projects reported here. The REF was rinsed in H_2O-mQ before and after every use and calibrated versus the reversible hydrogen electrode (RHE).

RDE-tips with PTFE shrouds (E6R1 ChangeDisk, Pine Research) have been used for the RDE and RRDE experiments reported here. An Ir wire (⌀=0.5 mm, 99.9%, Goodfellow) was used as CE in both the HER benchmark project (chapter 5) and the Pt small entities-project (chapter 6). A graphite rod (grade 1, Ted Pella) was used as CE for the ORR project with Pd single atoms (chapter 4) and also initially on the small entities-project. All dummy electrodes used were Pt wire (⌀=0.5 mm, 99.995%, Mateck).

3.3.1 Cleaning of Glassware

The procedure for cleaning glassware and miscellaneous items (Teflon tweezers, U-cups etc.) generally follows three steps: Cleaning in *piranha*, cleaning in *aqua regia* and finally heat assisted desorption.

The items were submerged in or filled with piranha solution, which is a 3:1 volumetric ratio of H_2SO_4 (98% Emsure, Merck) and H_2O_2 (30% Emsure, Merck), typically for $\approx$ 24 hours. The piranha solution is highly oxidizing and primarily used for removing organic residues. After this, the items were rinsed at least three times with Milli-Q ultra pure water (H_2O-mQ, 18.2 MΩ cm, Merck Millipore) and then cleaned with aqua regia (if applicable) or heat assisted desorption.

A similar procedure was used for cleaning items in aqua regia, consisting of a 3:1 volumetric ratio of HCl (69%, Supelco) and HNO_3 (69% Emsure, Merck). Aqua regia has the ability to dissolve noble metals such as Au and Pt, and was therefore typically used to clean glassware and Teflon parts from trace metal contaminants.

Heat assisted desorption was used subsequent to the chemical cleaning procedures to remove residual adsorbates from the used solutions, e.g. sulfur containing compounds stemming from piranha. In essence, items were rinsed and then filled with ultra pure H_2O-mQ, which was boiled or heated close to the boiling point for at least 20 minutes before emptying out the water, rinsing and restarting the process. This was repeated at least 3 times. Small items were heated using clean beakers on a hot-plate. For electrochemical glass cells a combined heater-and-pump system was used (TC-120, Grant): De-ionized water heated to 90 °C was continuously circulated into the cavity surrounding the cell (the "jacket") via the inlet (seen in fig. 3.1) and via the outlet back to the heater-pump water reservoir. All items were cleaned periodically following this procedure and also before first usage (i.e. new items). Glass cells etc. were rinsed and filled with H_2O-mQ and capped before storage.

3.3.2 Preparation of Samples & Substrates

Glassy carbon electrode (GCE) disks (⌀ = 5.0 mm, Sigradur G, HTW) have been used as the primary substrate in two of the projects reported in this

thesis. For the ORR project the GCEs were cleaned in the following way prior to dropcasting of catalyst ink:

(i) polishing with using suspension of 0.3 μm alumina particles

(ii) rinsed and then sonicated in isopropanol and subsequently H_2O-mQ

(iii) polishing with using suspension of 0.05 μm alumina particles

(iv) three repetitions of step (ii)

For the HER benchmark study some samples were deposited with very low catalyst loadings and generally a clean, well-defined system was desired, thus new GCE's were used for every sample. The GCEs were cleaned in the following way prior to dropcasting of catalyst ink or deposition of mass-selected nanoparticles.

(i) 10 minutes sonication is isopropanol

(ii) 3 times rinse, then 10 minutes sonication, then 3 times rinse in H_2O-mQ

(iii) immersion in HNO_3 (65%, Suprapur, Merck) for one hour

(iv) one repetition of step (ii)

For the small entities-project (chapter 6), highly oriented pyrolytic graphite (HOPG) was used as substrate after failed attempts with other approaches. The HOPG was cleaved several times immediately before deposition of small entities with the cluster source or dropcasting of catalyst ink (for reference samples with Pt nanoparticles). Catalyst inks for dropcasting were prepared as outlined in refs. [48] and [49] and dropcasted on cleaned substrates. Dropcasting on GCE disks mounted in a rotating RDE-tip (turned upside down) was attempted in order to obtain a more homogeneous catalyst distribution by applying rotation. No significant improvement could be observed and hence this approach was not pursued any further.

3.4 Measurement Techniques

The main electrochemical measurement techniques used will briefly be discussed in the following section. In general the experimental procedures may combine several of such techniques in sequence if desired. In particular experiments based on cyclic voltammetry using RDEs have been used to study catalyst activity for the projects described throughout this thesis, hence a few general points will be made on this technique. A so called CO-stripping techniques has been used to estimate the number of active sites on some of the studied catalysts. The general procedure for this will be described. Measurements of impedance spectra and open-circuit voltages have furthermore been used for ohmic drop compensation and potential scale calibration, respectively, of cyclic voltammograms, and will be discussed too.

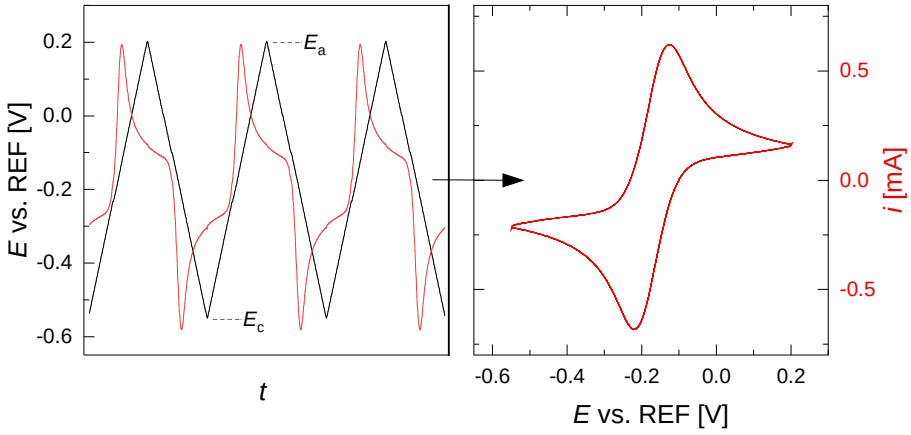

Figure 3.4: Cyclic voltammogram of ferricyanide-ferrocyanide redox couple. The right axis (i) applies for both figures. The CVs were recorded with a GCE disk as WE in Ar-saturated electrolyte consisting of 10 mM $K_3[Fe(CN)_6]$ in 1 M KNO_3 using ν = 200 mV/s and ω=0.

3.4.1 Cyclic Voltammetry (CV)

In cyclic voltammetry (CV) the potential on the working electrode E is swept over a range of interest while the current is measured. Upon reaching a vertex potential, the direction of the potential scan reverses, continuing like this in cycles. The data is usually plotted as i or j vs. E, called a cyclic voltammogram (also CV). The scan speed of the potential (ν), i.e. $\mathrm{d}E/\mathrm{d}t$ and the vertex potentials, that is the cathodic and anodic limits of the scan (E_c, E_a), are controlled and may be altered dynamically. As an example, the ferricyanide-ferrocyanide redox couple seen in equation (3.5) is investigated. Figure 3.4 (left) shows the linear potential sweep during three cycle and the current measured simultaneously. The corresponding CV is shown in fig. 3.4 (right).

$$[Fe(CN)_6]^{3-} + e^- \leftrightharpoons [Fe(CN)_6]^{4-} \tag{3.5}$$

When the potential is swept in the anodic direction, a postive current kicks in near E^0 due to the oxidation reaction. The current peaks when the maximum gradient of the reactant concentration occurs, after which the current decreases due depletion of reactants. When the current has nearly flattened out, the potential is reversed at E_a. Now the opposite reaction (reduction) occurs, since the oxidized species is in vicinity of the electrode, giving a similar peak before flattening out. Under these diffusion-limited conditions a set of redox peaks may occur as seen in figure 3.4, rather than an exponential behavior of i vs. E as in the case of kinetically dominated Butler-Volmer behavior. Such a redox reaction may indeed be reversible (*Nernstian*), but under these conditions a steady state response is not obtained. By using an RDE-setup to enhance the mass transport, a steady state CV may be obtained. As seen in figure 3.5 an increase in rotation rate (ω) makes the redox peak transition into a S-shaped

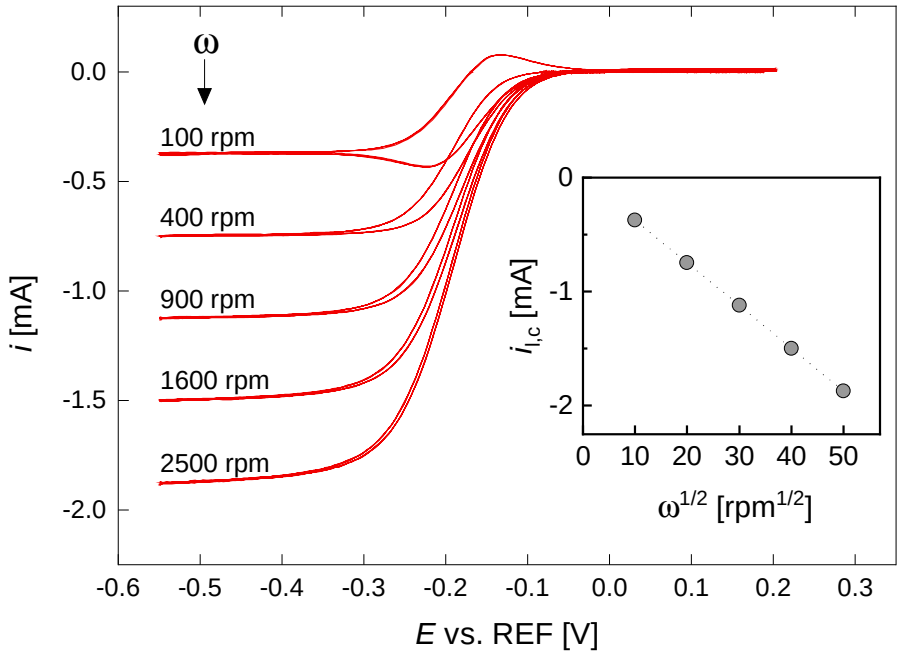

Figure 3.5: Limiting current density of ferricyanide-ferrocyanide redox couple at varying rotation speed. The redox peaks gradually turn into S-shaped waves with plateaus at gradually higher $j_{l,c}$ as ω increases. The inset shows that $j_{l,c}$ scales linearly with $\omega^{1/2}$, in agreement with the Levich equation. The CVs were recorded with a GCE disk as WE in an Ar-saturated electrolyte consisting of 10 mM $K_3[Fe(CN)_6]$ in 1 M KNO_3 using ν = 50 mV/s and ω=100, 400, 900, 1600, 2500 rpm.

curve characteristic of a steady state. A higher ω effectively shortens the diffusion layer thickness (and the hydrodynamic boundary layer), allowing a higher concentration gradient between the bulk and the electrode surface, hence the current response increases. Nevertheless, the current reaches a plateau, indicating a complete mass-transport limitation. By plotting the limiting current density or simply the limiting current ($i_{l,c}$) versus $\omega^{1/2}$ a linear trend is observed, as predicted by the Levich equation (3.1). An important observation to note is that i varies with ω well before $i_{l,c}$ is reached, indicating a partial limitation already here.

General Procedure

The procedure for conducting CV experiments varies depending on the purpose and samples studied, but mostly follow the same overall pattern: Prior to starting experiment, the reference electrode is calibrated and the electrolyte is purged with the desired gas for sufficiently long time to achieve saturation. When studying HER/HOR the electrolyte is saturated with H_2 while O_2 is used for ORR experiments, to ensure standard conditions. When performing

CO-stripping (further explanation in the following) or measuring base CVs, Ar-saturation is used. For HER/HOR 0.5 M H_2SO_4 electrolyte is used, whereas 0.1 M $HClO_4$ is used for ORR to avoid sulfur compounds from adsorbing in the potential range of interest studied in this reaction. Typically ω= 1600 rpm is used for activity measurements, consistent with literature. The sample is inserted under potential control to avoid possible degradation. This is achieved by holding the dummy electrode at the desired potential, essentially a chronoamperometry (CA) step (which may be integrated in a CV technique). The real WE is then electrically shorted to the dummy and subsequently immersed in the electrolyte. The dummy is then disconnected and the experiment may commence. Since the non-faradaic charging current scales linearly with scan speed ($i_{\mathrm{nf}} = AC_{\mathrm{d}}\nu$), typically ν is kept to 50 mV/s or 10 mV/s, depending on sample roughness (which correlates with the double layer capacitance, C_{d}). Depending on the stability range of the sample and the reaction studied, E_{a} and E_{c} are chosen appropriately. In general, several experiments with various parameters are conducted in a row, while keeping potential control in between. This is often combined with a CO-stripping experiments, as described in the following. Typically EIS measurements are conducted to evaluate the ohmic resistance, and compensate for it during data treatment.

RRDE Procedure

For experiments using the RRDE capability, the general procedure and parameters are quite similar to the ones described above. A key difference is that a bi-potentiostat is used to control the ring-electrode and disk-electrode - in practice two synchronized channels connecting to a bi-potentiostat cable box. The experimental technique used is a simultaneous CV-CA measurement, in that the disk performs CVs while the ring runs CA. To get a useful measurement, E_{ring} is set sufficiently high so that there is no kinetic limitation for the ring reaction, so that all reactants reaching the ring react promptly.

For RRDE-experiments, the ring electrodes collection efficiency N is important for an accurate determination of selectivity. It is dependent on the disk and ring dimensions, and may be determined experimentally: by choosing a system with only one redox couple the only possible faradaic process is oxidation or reduction of these species. Figure 3.6 shows a disk CV and ring CA experiment plotted versus E_{disk} for the ferrocyanide-ferricyanide redox couple. It is found from the $i_{\mathrm{disk}}/i_{\mathrm{ring}}$ ratio that only around 20% of the ferricyanide reduced to ferrocyanide at the disk is captured and oxidized back to ferricyanide at the ring. Thereby the collection efficiency of the RRDE-tip used is $N \approx 20\%$.

3.4.2 CO-stripping

Platinum and platinum-like metals bind CO strongly, leading to a surface coverage of a CO ad-layer, which effectively blocks surface sites. For instance, HER on Pt may be virtually blocked by adsorbed CO, known as CO-poisoning. At

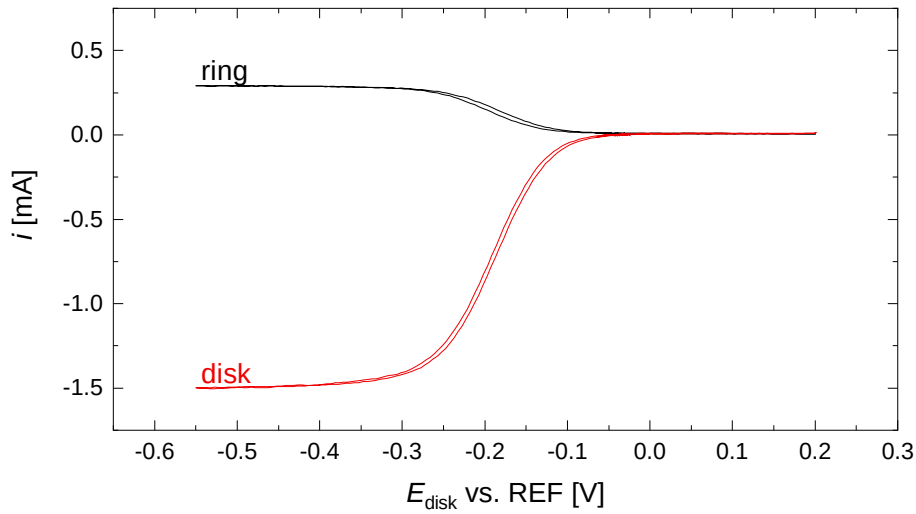

Figure 3.6: CV of the ferrocyanide/ferricyanide redox couple obtained by a GCE disk and Pt ring in an RRDE. The ratio between disk current (red) and ring current (black) gives the collection efficiency $N \approx 20\%$. The CV was recorded in an Ar-saturated electrolyte consisting of 10 mM $K_3[Fe(CN)_6]$ in 1 M KNO_3 using $\nu = 50$ mV/s, $\omega = 1600$ rpm and E_{ring}=0.58 V vs. REF.

more anodic potentials, however, the CO can be electrochemically oxidized to CO_2, leaving the surface. Many parameters influence the process such as CO-adsorption potential, electrolyte, material composition, surface morphology etc. and also the details of reaction mechanism has given rise to some debate.[50–56] The electrochemical oxidation of CO is generally believed to take place in two steps, as seen in equation (3.6): Adsorption of OH from the oxidation of water (1) and the reaction of adsorbed CO with adsorbed OH (2)

$$\begin{aligned} H_2O + {}^* &\longrightarrow {}^*OH + H^+ + e - \qquad (1) \\ {}^*CO + {}^*OH &\longrightarrow CO_2 + H^+ + e - + 2^* \qquad (2) \end{aligned} \tag{3.6}$$

The net process is hence a 2-electron transfer per CO-molecule. This knowledge can be employed when performing a so-called *CO-stripping* experiment, where the electrochemical oxidation of CO can be measured as a current. By appropriate integration a net CO-strip charge ($Q_{\text{CO,tot.}}$) may be found. This charge is directly proportional to the number of active sites on the surface. Such a measurement may be used to estimate the *intrinsic* activity of a catalyst. A typical CO-strip experiment is shown in figure 3.7 and proceeds as follows: The electrolyte is saturated with Ar and a few CV's are performed in the potential-range of interest (typically from +50 mV to 1.0 V vs. RHE). After a stable CV is verified, a potential-hold period is applied (e.g. +50 mV for 15 minutes) during which CO is purged in stead of Ar for the first 2 minutes. This allows CO to adsorb on the working electrode. After dosing CO, the Ar purging is

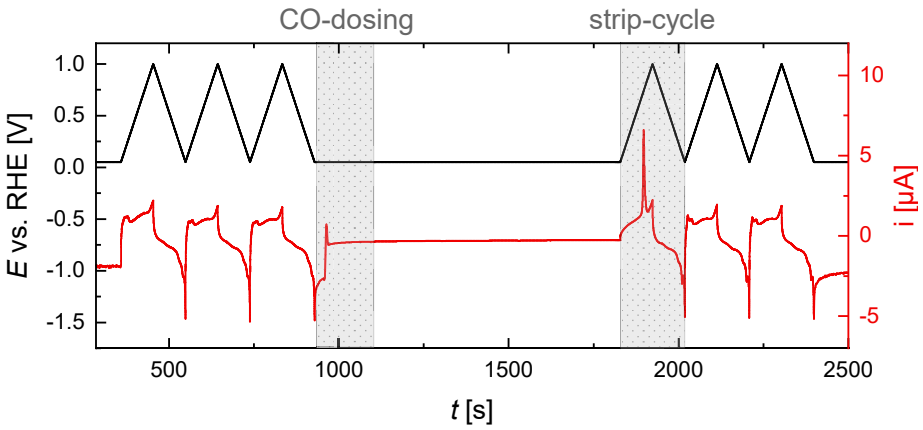

Figure 3.7: Experimental procedure for a typical CO-strip showing (in chronological order): Initial cycles in Ar saturated electrolyte, potential hold period (CA) for 15 minutes (900 s) at -50 mV vs. RHE, where CO is dosed during the first 2 minutes, after which Ar purging is switched on again. The potential sweep is started again and CO is striped off during the first cycle. A few additional cycles are obtained to ensure a stable CV before going to potential-hold again. Then the same procedure is repeated with no CO-dosing, giving a base CV for background subtraction. This experiment was performed on 3.8 nm Pt nanoparticles on a GCE disk in 0.5 M H_2SO_4 using $\nu = 10$ mV/s and $\omega = 200$ rpm.

switched back on for the remainder of the experiment, allowing all excess CO to be purged away. At the end of the potential-hold time, the potential cycling recommences. On the first anodic sweep the CO is stripped off, resulting in a distinct peak of the current, often around 0.7-0.8 V. Additional features (e.g. a pre-peak) may exist in this strip cycle as evidence of the more complex mechanisms[50,52,55]. If the amount of sites is sufficient, a so called displacement current may be observed during the CO-dosing. The phenomenon is associated with CO displacing and oxidizing hydrogen adsorbed on Pt in the H_{upd} potential region. In figure 3.7 this anodic current is seen as the small peak at $t = 965$ s. A few cycles are recorded after the strip cycle and then the procedure shown in figure 3.7 is repeated, this time *without* dosing CO. The purpose of this is to get a base CV after the samples has experienced the same potential hold time but without CO-poisoning. This "blank" measurement is used for background subtraction of the strip cycle to minimize the effect of measuring currents unrelated to the CO-stripping. Similar approaches have also been reported in the literature[57]. The CV from a typical CO-strip experiment can be seen in figure 3.8 (left), where the strip cycle is shown in red along with the cycle used for background subtraction shown in black. Despite applying a background subtraction, the resulting peaks are generally not ideal. For instance the region to the anodic side of the peak might not go to i=0 as expected or the strip current might be less than the background current (cathodic side) leading to an ambiguity in defining at which potential the peak starts. The cause of this

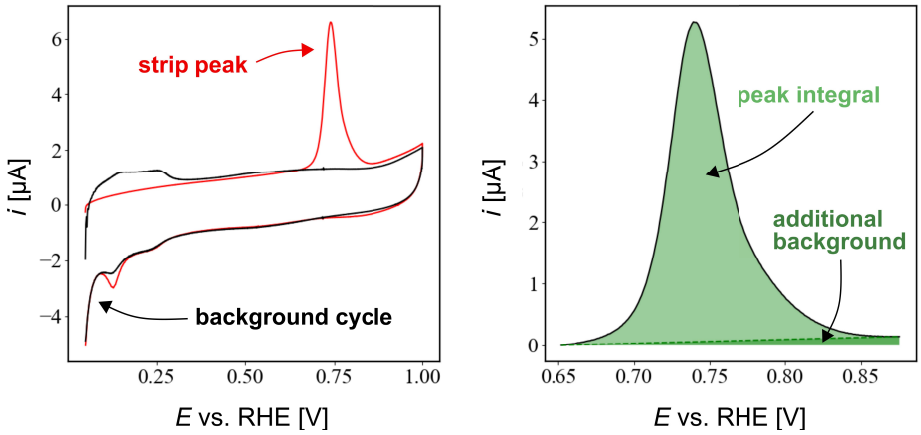

Figure 3.8: CV and data treatment of typical CO-strip. (left) CV of strip cycle (red line) showing a distinct peak and cycle (black line) used for background subtraction. (right) The black curve denotes the strip peak after background subtraction. The light green area under the curve represents the peak integral where an additional linear background (dark green area) has been subtracted. This experiment was performed on 3.8 nm Pt nanoparticles on a GCE disk in 0.5 M H_2SO_4 using $\nu = 10$ mV/s and $\omega = 200$ rpm.

could be surface reconstruction, an artifact of double layer capacitance, a difference in the OH-adsorption and so on. This, however, is somewhat speculative. Dealing with this in a consistent manner for a set of different samples is tricky. This can practically be addressed by defining the end points of a peak by a threshold value of e.g. $\mathrm{d}i/\mathrm{d}E$ or i. Furthermore, a linear background might be drawn between these end points if appropriate. An example of this is shown in figure 3.8 (right) where the small, dark green sliver represents the additional background being subtracted and hence the peak integral is represented by the light green area. The difference in the resulting integration is modest for most cases, but for samples of very low loading, say a few percent of a monolayer, the discrepancy might be significant. An example of this will be shown in chapter 5.

$$Q_{\mathrm{CO,tot.}} = \frac{1}{\nu}\int_{E_{\mathrm{p,c}}}^{E_{\mathrm{p,a}}} i\,\mathrm{d}E \tag{3.7}$$

By simply integrating i over the timespan of the peak, $Q_{\mathrm{CO,tot.}}$ is found. Using that $\nu{=}\mathrm{d}E/\mathrm{d}t$, the integral may alternatively be formulated as equation (3.7) where $E_{\mathrm{p,c}}$ and $E_{\mathrm{p,a}}$ are the cathodic and anodic potential limits of the peak, respectively. In both cases i represents the current after the appropriate background subtraction(s).

3.4.3 Chronoamperometry (CA)

Chronoamperometry (CA) is a technique concerned with monitoring current as a function of time, as the name implies. The technique has not been predominant for the work presented here, but is brought up a few times, hence a

few key points are called for. In CA experiments the potential is set at constant value (and perhaps changed in steps or pulses) and the system response is recorded. Upon changing the potential, non-faradaic currents are significant on a short time scale, but decay exponentially, unlike in potential-sweep methods such as cyclic voltammetry. This means that after just a very short time (e.g. ms timescale) the current becomes completely dominated by faradaic processes. For a steady state measurement the current should then be constant in time, and therefore CA is a relatively simple approach for gauging catalyst stability under reaction conditions. A deviation from constant current may indicate catalyst degradation but not the underlying cause. A deviation may also be due to other experimental artifacts, and thus CA should not solely be relied on for accurately assessing stability. Anyhow, some CA measurements will be discussed in chapter 4. Lastly, CA procedures may implicitly be incorporated in other measurement for practical reasons, e.g. as a potential control step.

3.4.4 Potential Scales

The standard potential scale widely accepted is the *standard hydrogen electrode* (SHE) defined by the equilibrium of $2H^+ + 2e^- \leftrightharpoons H_2$ on a Pt electrode and unit activities, $a_{H^+}=1$, $a_{H_2}=1$. By definition $E^0 = 0$ V at all temperatures. The *reversible hydrogen electrode* (RHE) furnishes a potential scale which depends on pH with respect to SHE. This has the practical advantage that the RHE scale can be used for different electrolytes and that reactions involving proton-electron transfers will not be pH-dependent on the RHE scale and are thus more easily compared between measurements. First the Nernst relation for the HER/HOR is given on the SHE scale in equation (3.8):

$$E_{\mathrm{SHE}} = E^0_{\mathrm{SHE}} + \frac{RT}{2F} \ln \frac{a^2_{H^+}}{a_{H_2}} \tag{3.8}$$

Given the definition of the pH-scale and that $a_{H_2} = 1$, $E^0_{\mathrm{SHE}}=0$ V and $n=2$, this may at room temperature be written as:

$$E_{\mathrm{SHE}} = -59[\mathrm{mV}]\ \mathrm{pH} \tag{3.9}$$

The RHE scale is also defined with $a_{H_2}=1$ but with $E_{\mathrm{eq,RHE}}=0$ for all a_{H^+} (equivalently all pH values), meaning that:

$$E_{\mathrm{RHE}} = E_{\mathrm{SHE}} + 59[\mathrm{mV}]\ \mathrm{pH} \tag{3.10}$$

The activity of a gas is given by the partial pressure of the gas with regards to the standard pressure (1 bar). Thus the RHE scale is defined by a 1 bar H_2 partial pressure. An actual RHE may be used as a reference electrode, but for experiments it is often more practical to use another REF electrode, which is then calibrated against RHE. Given a difference in equilibrium potential between the REF and SHE of ΔE_{REF}, then, E vs. RHE is given by eq. (3.11).

$$E_{\mathrm{RHE}} = E_{\mathrm{REF}} + \Delta E_{\mathrm{REF}} + 59[\mathrm{mV}]\ \mathrm{pH} \tag{3.11}$$

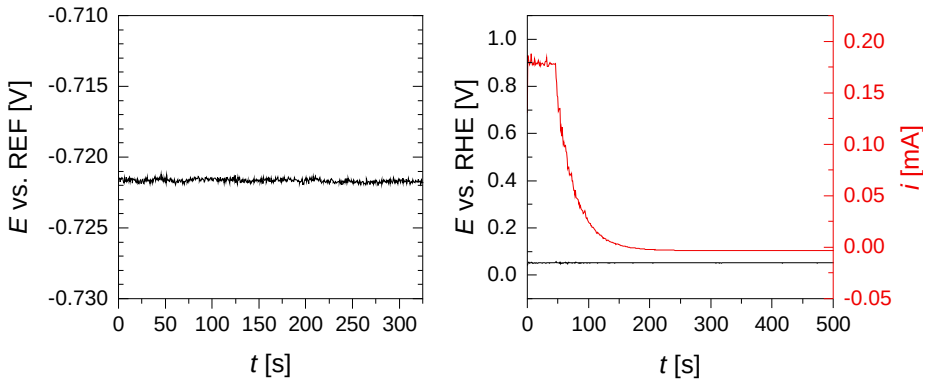

Figure 3.9: REF calibration and characteristic gas saturation time. (left) OCV of Pt dummy in H_2-saturated 0.5 M H_2SO_4 used for calibrate potential scale. Noise level is within ≈1 mV and $dE/dt \approx 0$ indicating a stable equilibrium. (right) Chronoamperometry at $E = 50$ mV vs. RHE where the purging gas is changed from H_2 to Ar at $t = 50$ s. WE: Pt nanoparticles on a GCE disk (5000 ng cm^{-1}), electrolyte: 0.5 M H_2SO_4, ω=200 rpm.

The reference electrode may be calibrated versus RHE using a Pt electrode while saturating the electrolyte with 1 bar H_2. For this purpose a dummy electrode (a Pt wire) is used as WE. By letting the WE go to the open circuit voltage (OCV), i.e. where i=0, the equilibrium potential of HER/HOR (which is 0 V vs. RHE) is measured versus the REF and hence eq. (3.11) is solved. Figure 3.9(left) shows a typical OCV measurement used for calibration, showing fluctuations no larger than ≈1 mV and dE/dt practically zero. A similar calibration could also be obtained via cyclic voltammetry under the same conditions. Here the CV should intersect (E_{RHE}, i)=(0,0), with a minimal spread of the anodic and cathodic scan (hence a sufficiently slow scan speed is required to minimize i_{nf}). Throughout this thesis, all potentials are referring to the RHE scale unless noted otherwise.

Ensuring complete saturation of the electrolyte is not only important for REF calibration but for experiments in general. Since the gas used may sometimes be changed during a sequence of experiments, e.g. when going from a base CV to HER activity tests or during a CO-strip procedure, it is worth knowing the typical time it takes for the system to equilibrate with a new gas. Figure 3.9 (right) shows a simple CA experiment investigating this. Initially a working electrode consisting of Pt nanoparticles dispersed on a GCE is held at +50 mV vs. RHE while being purged with H_2 and hence a steady HOR current is sustained. At $t \approx 50$ s the H_2 purge is exchanged with Ar. As H_2 is oxidized at the WE or otherwise leaves the electrolyte and is not replenished, the HOR current drops. Within ∼5 minutes the current has stabillized to a new equilibrium: A slight cathodic current attributable to HER due to the Nernst shift of the HER/HOR equilibrium potential. This characteristic time scale is not necessarily expected to hold for other gasses, electrolytes and cells, but similar

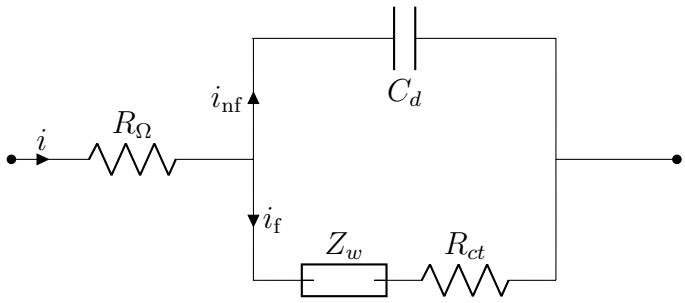

Figure 3.10: Randles equivalent circuit.

experiments tend to yield roughly the same time scale. Hence at least 5 minutes saturation, and most often longer, has been used when changing gas for the experiments presented throughout this thesis.

3.4.5 Impedance Spectroscopy

Several processes can take place simulateneously at the working electrode studied, both faradaic and non-faradaic. Furthermore, uncompensated resistance may influence the potential measured. It is therefore desirable to deconvolute the various effects to aid the analysis. One method for doing so is electrochemical impedance spectroscopy (EIS). The electrode processes may be modeled by circuit elements with some characteristic impedance (Z), i.e. a generalized (complex) resistance, which is frequency dependent. The EIS technique is used to probe the response of such systems by using pertubations of varying frequencies in order to analyze the constituents of the circuit. This is done by setting E at a point of interest and then varying this potential with a small sinusoidal pertubation, $\pm\delta E$, at series of frequencies (f_{EIS}) starting from high to low. A range of interesting properties may in principle be examined using this technique, for instance kinetic information such as i_0 could be extracted. This does, however, require a well-defined and well-known system which can be represented by a meaningful circuit model. For the present work the technique has only been used to estimate R_Ω, although the more generalized use of EIS is interesting. The diagram in figure 3.10 shows the *Randles equivalent circuit*, describing a simple model electrode where both faradaic and no-faradaic currents are contributing. The uncompensated ohmic resistance (R_Ω) is an ideal resistor, through which the total current (i) runs. The faradaic and non-faradaic processes are running in parallel, and hence the diagram shows two partial currents, the faradaic (i_{f}) and the non-faradaic (i_{nf}, charging current), which run in parallel. Ideally, the double layer charging behaves as a capacitor (C_d) being charged/discharged. The *charge-transfer resistance* (R_{ct}) models the kinetic barrier associated with the charge transfer process and can be related to the ex-

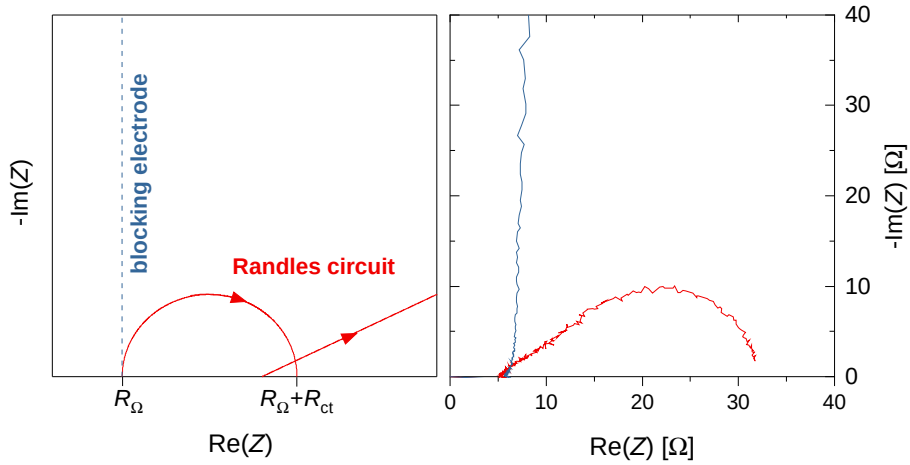

Figure 3.11: Nyquist plots of a blocking electrode, Randles equivalent circuit model and experimental data: (left) The blue line denotes a blocking electrode, the red lines denote the ideal behavior of an electrode described by a Randles equivalent circuit, where the semi circle is valid for high frequencies and the linear region is the solution for low frequencies. (right) Experimental spectra of Pt nanoparticles on a GCE disk (5000 ng cm^{-1}) at ω = 1600 rpm in 0.5 M H_2SO_4. Blue curve behaves like a blocking electrode and was obtained at E=0.2 V vs. RHE, δE=10 mV with a range of f_{EIS}=[200 kHz; 10 Hz] in Ar-saturated electrolyte. The red curve is slightly skewed and more compressed than an ideal high-frequency response (semi-circle) expected from a Randles circuit. The measurement does not extend all the way to the linear, low-frequency response. The red curve was obtained at E=0 V vs. RHE, δE=5 mV with a range of f_{EIS}=[200 kHz; 0.2 Hz] in H_2-saturated electrolyte.

change current (i_0). The *Warburg impedance* (Z_w) represents the "resistance" of mass-transport. The data obtained from EIS measurements are often presented in Nyquist plots, where the imaginary vs. real components of Z are plotted. The frequency response of a Randles circuit may be derived analytically either in the range of very high or very low frequencies. As seen in figure 3.11(left), the high-frequency response of a Randles circuit gives rise to a semi-circle of radius $R_{ct}/2$ which goes to -Im(Z)=0 at the points R_Ω and R_Ω+R_{ct}. The low frequency range has a linear solution, where the intersection with the real axis depends on the magnitude of the Warburg impedance (not shown here). If E is set in a region where no faradaic processes occur, only double layer charging contributes to the EIS spectrum, equivalent of only having the part of the circuit where i_{nf} runs, a so-called blocking electrode. This results in a vertical line going up form R_Ω. In case of a less ideal behavior, the response of a blocking electrode is slightly slanted, like that of a constant phase element. An example of this can be seen as the blue line in figure 3.11(right). Here EIS was performed on a GCE disk with Pt nanoparticles at E= 0.2 V vs. RHE in an Ar-saturated electrolyte, where double layer charging is expected to dominate. It should be noted that the Ar-saturation gives a Nernst-shift of the HER/HOR equilibrium potential and that underpotential deposition of hydrogen also may occur at this potential, which may contribute to charge transfer. That being said, the

curve is almost like that of an ideal double layer capacitance. The figure also shows a plot of the same sample but at E= 0 V vs. RHE in H_2-saturated electrolyte, i.e. at the (dynamic) equilibrium of HER/HOR. This gives a spectrum somewhat similar to a Randles circuit, however, the high frequency region is more linear than circular (perhaps another semi-circle is overlapping), showing a more complex behavior. Given the rotation and the potential the linear region is not seen within the frequency window of the experiment. Nonetheless both measurements approach the -Im(Z) at nearly identical points, namely R_Ω=5 Ω. This underlines that the ohmic drop may be estimated from EIS data at the high frequency limit regardless of complexities of the equivalent circuit model.

$$E = E_{\text{measured}} - i\, R_\Omega \tag{3.12}$$

The uncompensated resistance (R_Ω) gives a potential drop of the measured potential (E_{measured}). This may then simply be post-corrected using eq. (3.12), giving E.

Chapter 4

Oxygen Reduction Reaction (ORR)

The electrochemical oxygen reduction reaction (ORR) can follow two overall pathways, involving a total transfer of either four or two electrons per O_2 reduced. The four-electron reaction ($4e^-$-ORR) reduces oxygen to water, as seen in eq. (4.1), whereas the two-electron reaction ($2e^-$-ORR) reduces oxygen to hydrogen peroxide, seen in eq. (4.2).

$$O_2 + 4\,H^+ + 4\,e^- \longrightarrow 2\,H_2O \qquad E^0 = 1.23\ \text{V} \tag{4.1}$$

$$O_2 + 2\,H^+ + 2\,e^- \longrightarrow H_2O_2 \qquad E^0 = 0.7\ \text{V} \tag{4.2}$$

The two reactions are closely linked and may happen in parallel on a catalyst. In fact, the issue of *selectivity*, meaning preferentially catalyzing one and not the other, is of great interest in the studies of these reactions. The challenges of catalyzing these reactions and their applications will be discussed in the following two sections: Firstly, the $4e^-$-ORR will briefly be discussed alluding to it's relevance in fuel cells and the challenges posed by scaling relations, which also sets the stage for later discussions. In the second section, the $2e^-$-ORR will be in focus. The applications of hydrogen peroxide and alternative synthesis methods will be touched upon, leading up to a discussion of the electrochemical synthesis via $2e^-$-ORR, and in particular the catalysis of this reaction. The main focus here will be on the interesting prospects of single atom catalysts and especially the interplay between geometric and electronic effects. This section is largely based on the paper[48] titled *Highly active, selective, and stable Pd single-atom catalyst anchored on N-doped hollow carbon sphere for electrochemical H_2O_2 synthesis under acidic conditions*, which was recently published in *Journal of Catalysis*. This was the product of an international collaboration, where the electrochemical tests took place at SurfCat, DTU. I worked together with Sungeun Yang and Jens-Peter B. Haraldsted on these experiments. I mainly focused on RRDE-measurements, and contributed to revision of the manuscript. The full manuscript is included in appendix A.

4.1 ORR in Fuel Cells

Several factors determine the overall performance of fuel cells, a key factor being the catalysis of the reactions. The reduction of oxygen to water is the cathodic half-reaction of an operating fuel cell, whereas the hydrogen oxidation reaction (HOR) is the anodic half-reaction. Due to the more complex reaction pathways and the scaling relations of the involved intermediates, the ORR is much less facile than HOR. Consequently, the catalysis of the overall reaction is limited by the ORR. The $4e^-$-ORR reaction may proceed via a dissociative (seen in eqs. (4.3)) or an associative mechanism (seen in eqs. (4.4)). In the former, the O-O bond is split (O_2-dissociation) initially, whereas in the latter, the proton-electron transfer proceeds first. The dominating mechanism is dependent on oxygen coverage, applied potential and naturally the catalyst, and both mechanisms may proceed in parallel[33].

Dissociative Mechanism

$$O_2 + 2^* \longrightarrow 2O^* \tag{4.3a}$$
$$2O^* + 2H^+ + 2e^- \longrightarrow 2OH^* \tag{4.3b}$$
$$2OH^* + 2H^+ + 2e^- \longrightarrow 2H_2O + ^* \tag{4.3c}$$

Associative Mechanism

$$O_2 + ^* \longrightarrow O_2^* \tag{4.4a}$$
$$O_2^* + H^+ + e^- \longrightarrow OOH^* \tag{4.4b}$$
$$OOH^* + H^+ + e^- \longrightarrow O^* + H_2O \tag{4.4c}$$
$$O^* + H^+ + e^- \longrightarrow OH^* \tag{4.4d}$$
$$OH^* + H^+ + e^- \longrightarrow H_2O + ^* \tag{4.4e}$$

For catalysts that bind oxygen too weak, the limiting factor is splitting the O-O bond in case of the dissociative mechanism (4.3a) or the proton-electron transfer to O_2* (4.4b). For catalysts binding oxygen too strong, the proton-electron transfer to O* or OH* is the rate limiting step (4.3b, 4.3c)[33]. In line with Sabatier's principle, which was introduced earlier, this leads to a volcano-relationship of the catalytic activity with e.g. the oxygen binding strength as the descriptor - as was shown in figure 2.2. Platinum (Pt) has a near-optimal binding energy and therefore sits near the top of the activity volcano. This is a major reason why Pt-based materials are the best-performing $4e^-$-ORR catalysts. Nevertheless, even the best Pt-based catalyst require substantial overpotenials to catalyze the reaction. The reaction has multiple intermediates, whose binding energies are correlated through the linear scaling relations[32,33] and for this reason the binding energies cannot be optimized individually. The free energy diagram in figure 4.1 illustrates the issue: at equilibrium (1.23 V

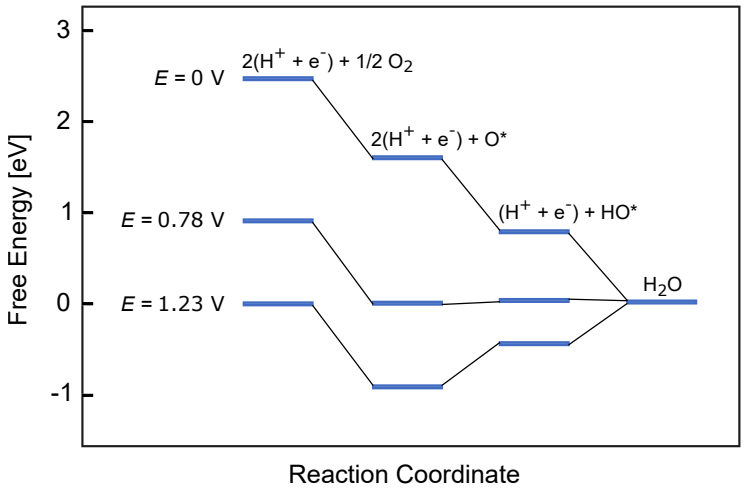

Figure 4.1: Free energy diagram for $4e^-$-ORR on Pt(111) based on DFT calculations. Three cases are represented: Equilibrium (E=1.23 V), high overpotential(E=0 V) and highest potential (lowest overpotential) where all intermediate steps are energetically favorable (E=0.78 V). Adapted with permission from [33]. Copyright 2004 American Chemical Society.

vs. RHE) the step toward the first intermediate is energetically downhill (which is favorable) but the opposite is true for the second step. Tuning the binding energy of one intermediate (moving it up or down) inevitably moves those of the other intermediates as well. By applying a larger overpotential, the driving force of the reaction is increased, as seen in the case of E=0 V, at the cost of energy efficiency. The minimum overpotential at which all intermediate steps become thermodynamically favorable is known as the *limiting potential*. In the case of the Pt(111) facet described by the free energy diagram in fig. 4.1, the limiting potential is computed via DFT to be at 0.78 V, thus even the best catalysts are quite far away from the equilibrium potential.[33] Figure 4.2 shows the two dimensional volcano plot of the limiting potential for ORR in a heat map with a line showing the scaling relation of oxygen intermediates. Unfortunately, the scaling line, which defines the parameter space in which catalysts can be tuned, does not pass through the top of the volcano (dark red area). This rationalizes why no better $4e^-$-ORR catalyst than the Pt-based ones have been found but also predicts that no such catalyst exists within these constraints. Thus, a major obstacle within $4e^-$-ORR (and other important reactions) is circumventing the scaling relations or finding more favorable ones.[58] In the context of the heat map in fig. 4.2 this would entail creating catalysts following a different scaling line, passing as close to the optimum as possible. In essence, being able to (de)stabilize a particular intermediate, while barely affecting other intermediates, is the challenge at hand. Several approaches of both intrinsic and extrinsic nature can be conceived, that might make this possible.[58] One such approach, receiving significant attention both within ORR and other reactions, is the development of single atom catalysts (SAC). This is the topic will be

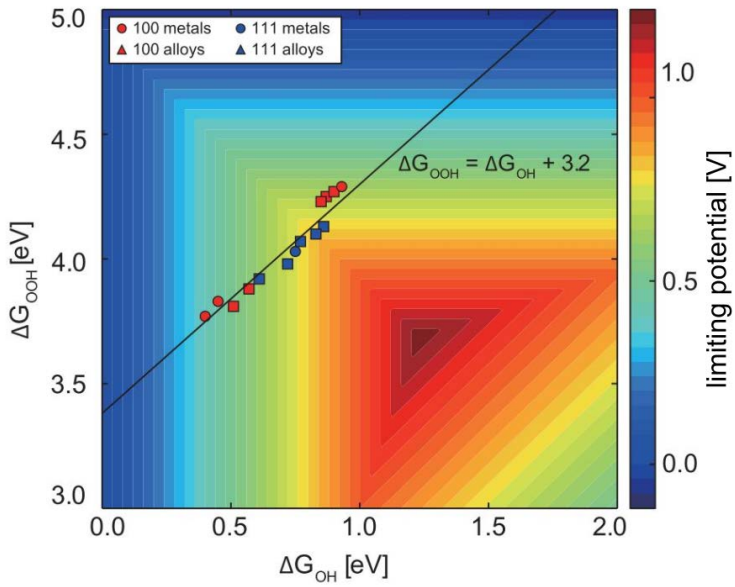

Figure 4.2: Linear scaling relations between Gibbs free energies of the OH and OOH intermediates of the 4-electron ORR. Reprinted from [58] under the CC-BY 4.0 license. Axis label for color scale added.

discussed further in chapter 6. Also for producing hydrogen peroxide via the $2e^-$-ORR, single atoms are of great interest, as will be discussed in the following.

4.2 Hydrogen Peroxide Synthesis via ORR

Hydrogen peroxide (H_2O_2) is an oxidizing agent with a wide range of application such as pulp and paper bleaching, waste-water treatment, as disinfectant, and within food, aquaculture and semiconductor industries[59–61]. Driven by it's usefulness and many possible applications the annual production has been drastically increasing over the past decades reaching a capacity of 5.5 million tonnes per year (in 2015) with an estimated market value of several billion $, with continued growth predicted[60]. The electrochemical synthesis of H_2O_2 is a promising alternative to the established methods. An efficient catalyst is, however, needed to drive the reaction. In the following section, these topic will be discussed.

4.2.1 Synthesis Methods for Hydrogen Peroxide

The current industrial method for producing H_2O_2 is via the anthraquinone auto-oxidation process. This batch process relies on the hydrogenation and subsequent oxidation of e.g. 2-ethylantraquinone, yeilding H_2O_2, which is then separated from the working solution and further distilled up to 70% wt. to

remove impurities[61]. The anthraquinone process has a high yield, but requires a centralized, large-scale plant to be viable[62] and comes with the additional disadvantages of needing to regenerate the working solution, the catalyst as well as the purification steps. The centralized production also necessitates transportation, stabilizers to prevent H_2O_2 from decomposing and in some cases dilution at the end-user.[59,61]

An alternative synthesis method is via the direct reaction of H_2 and O_2, but to stay below the explosive limit of this gas mixture, an inert gas must be used to dilute H_2 and O_2. The method might be suitable for production at the point of use, eliminating the need for transportation and unnecessary up-concentration and dilution steps[63]. Since the decomposition of H_2O_2 (or combustion of H_2 and O_2) into H_2O and O_2, as well as the further hydrogenation of H_2O_2 into H_2O, are also thermodynamically downhill processes, a key challenge is the selective formation and preservation of H_2O_2[59,64]. Pd-based catalyst have shown good performance in this regard and have been studied at length - for instance Pd-Au catalyst have proven active, both with core-shell structure[62] and alloyed[65]. The addition of Sn to Pd has also been shown to increase selectivity by suppressing the decomposition and hydrogenation reactions[66]. Similar observations have been made for the addition of Pt to Pd-Au[67]. In general, it has been found that the activity can be promoted both by additives to catalyst but also to the support material[63–65,68]. Operating under safe conditions with a high H_2O_2 yield are essential to the feasibility of this direct method, which has not yet matured to a commercial technology[64]. Although the direct reaction of H_2 and O_2 has been proven on the scale of a demonstration plant[69] the safety of operation and efficiency are still barriers in preventing a wider adoption of this method.[64,70,71]

Another route for producing H_2O_2 is the electrochemical synthesis, which is the method of the present work. Electrochemical synthesis of H_2O_2 can take place both by the oxidation of H_2O at an anode or reduction of O_2 at a cathode[71]. Only the oxygen reduction reaction (ORR) will be discussed here. The electrochemical synthesis route enables a decentralized production of dilute aqueous solutions of H_2O_2, thereby eliminating the need for transportation, purification, or handling of hazardous, concentrated solutions. In the following, the main focus will be on ORR in acidic media, as the alkaline ORR is easily catalyzed by glassy carbon, but the product is unstable[72]. Thereby, the alkaline conditions are best suited for purposes where the peroxide is used immediately. Furthermore, the alkaline conditions bring additional challenges, such as: The need to neutralize the solution for some applications, high Ohmic resistance due to the diaphragm used as separator, the carbonate formation in presence of CO_2 and the corrosive nature of the alkaline environment. Nevertheless, the Huron-Dow process based on this approach has been commercialized for bleaching pulp and paper[59]. Under acidic conditions, pure aqueous H_2O_2 can be produced using a proton exchange (PEM) membrane, potentially with a wider applicability. A key point for the development of electrochemical H_2O_2 synthesis is thereby finding an active and selective catalyst which is stable under acidic operating

conditions, preferably a cheap and earth-abundant material[48,59]. The process may be run as a PEM fuel cell (PEMFC) by oxidizing H_2 at the anode (HOR), so that electricity is generated simultaneously with the production of H_2O_2[73], but this requires supplying and separately handling H_2. On the other hand, the process can be run as an PEM electrolyzer requiring only water, electricity, O_2 (or simply air). In this case the oxidation of H_2O takes place at the anode, ensuring the supply of protons via the PEM as seen in the schematic in figure 4.3.

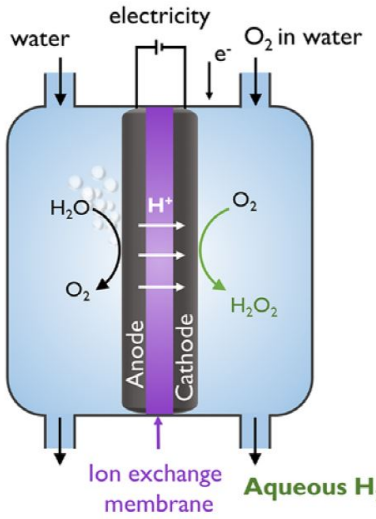

$$2H_2O \longrightarrow O_2 + 4H^+ + 4e^- \quad (4.5a)$$

$$O_2 + 2H^+ + 2e^- \longrightarrow H_2O_2 \quad (4.5b)$$

Figure 4.3: Schematic of PEM electrolyzer producing an aqueous solution of H_2O_2 from O_2, H_2O and electricity and the two half reactions. Figure adapted with permission from [59]. Copyright 2018, American Chemical Society.

4.2.2 Catalyzing the $2e^-$- ORR

The two-electron pathway of ORR seen in eq. (4.5b) proceeds via the OOH*-intermediate in the following steps (4.6) and (4.7)

$$O_2 + * + H^+ + e^- \longrightarrow OOH* \quad (4.6)$$

$$OOH* + H^+ + e^- \longrightarrow H_2O_2 + * \quad (4.7)$$

Yet the 4-electron ORR is still thermodynamically downhill, so the OOH may also be further reduced, for instance via the associative mechanism (4.4c). In fact, the competing $4e^-$-ORR reaction, having a more anodic equilibrium potential, is the main challenge for selectively catalyzing the $2e^-$-ORR. The produced H_2O_2 may also be chemically dissociated or further reduced by a proton/electron transfer. Like the direct synthesis method, the electrochemical methods also contends with the issue of selectivity, due to unwanted alternative

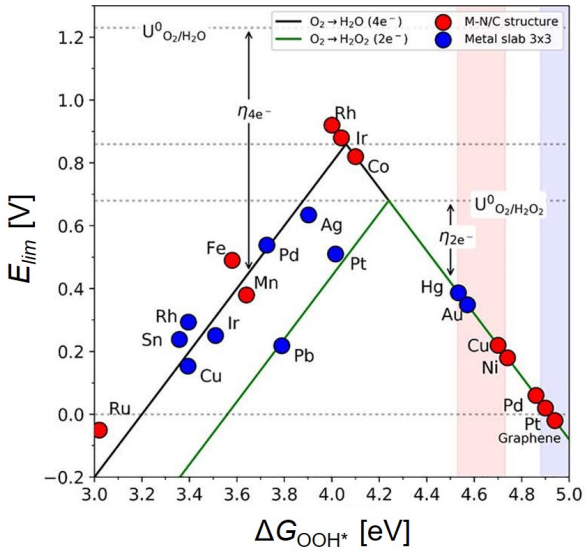

Figure 4.4: Volcano trend of theoretical limiting potential for $2e^-$-ORR (green line) and $4e^-$-ORR (black line). Red points indicated DFT calculations for M-N/C catalyst and blue points are for pure metals. Figure adapted with permission from [59]. Copyright 2018, American Chemical Society.

reaction pathways. In particular, the catalysts proclivity for breaking the O-O bond is determining for whether H_2O_2 or H_2O is produced, and is the result of two major factors at play, namely *electronic effects* and *geometric effects*.[48,59] Regarding the electronic effect the OOH^* is *the* intermediate of relevance for describing the $2e^-$-ORR mechanism. The optimal value of ΔG_{OOH^*} leads to a theoretical limiting potential which coincides with the standard potential (E^0) of the reaction at the apex of the volcano in figure 4.4. This means that for the optimal catalyst, the intermediate step is thermodynamically favorable from the onset, i.e. no extra overpotential must be applied to get the reaction going other than a slight pertubation of E. In contrast, the more complex scaling relation of the $4e^-$-ORR is less ideal. Not until $E \approx 0.9$ V are all the intermediate steps thermodynamically favorable, even at the optimal binding energy of OOH, so even the optimal catalyst imaginable within these scaling relations still requires an extra ≈300 mV overpotential. The simple scaling relation for the $2e^-$-ORR is favorable but in practice complicated by the coexistence of the $4e^-$-ORR pathway which has a somewhat overlapping volcano trend as seen in figure 4.4. On the strong binding side of the $2e^-$-ORR volcano (left leg) the further reduction of OOH is limiting, whereas on the weak binding side (right) the reduction of O_2 to OOH is limiting. In absence of the 4-electron pathway, the optimal $2e^-$-ORR catalyst would be at the apex of the green curve, but from this point and to the left of it, the $4e^-$-ORR has a more anodic limiting potential. Thereby, the driving force toward $4e^-$-ORR is greater in this region. The right leg of the $2e^-$-ORR volcano coincides with that for $4e^-$-ORR and

the two reactions thus have an equal driving force, making the H_2O_2 formation feasible although not necessarily preferential. Figure 4.4 shows that most pure metals considered (blue points) lie on the strong binding side (left) and thereby catalyze the formation of H_2O. On the other hand, Hg, Au and a handful of metal single atoms (red points) in porphyrin-like structures (M-N/C) fall on the weak binding side of the volcano, catalyzing the formation H_2O_2 to some extent. Given that $4e^-$-ORR involves breaking an O-O bond, the stability of the O* intermediate is of relevance for this pathway. If the O* intermediate is sufficiently destabilized, OOH* will not be dissociated further and the selectivity toward H_2O_2 will increase. Usually O* binds in hollow sites whereas OOH* binds on atop sites. In the absence of hollow sites, O* is destabilized compared to OOH*, which constitutes the geometrical effect - essentially a single catalytic site cannot split the O-O bond. For instance, porphyrin-like structures have no hollow sites an may thereby exhibit this geometric effect[74]. Figure 4.5 exemplifies the geometric effect by showing the shift in scaling lines of ΔG_{O*} versus ΔG_{OOH*} between pure metals (blue) and metal single atoms in porphyrin-like structures (red). For ΔG_{O*} above the horizontal stipulated line, the O* is less stable than H_2O_2 and H_2O_2 is thus thermodynamically more favorable. Several of the porphyrin-like catalyst inhabit this area of interest, namely M: Cu, Ni, Pt, Pd.[59] Generally speaking, the O* is destabilized when moving further to the right of the $2e^-$-volcano (figure 4.4), increasing selectivity but at the cost of activity. Perhaps the geometric effect might enable the design of a catalyst closer to the top of the volcano that still destabilizes O* thus achieving a high selectivity *and* activity. These considerations are based on a thermodynamic analyses and do not include kinetic barriers, electrolyte effects, catalyst stability etc. As such, the electronic and geometric effects act as guiding principles but not absolute predictors. Several classes of materials have been studied for the $2e^-$-ORR reaction, such as carbon-based catalysts with various dopants, metal-porphyrin-like structures (e.g. Co-N/C) and extended surfaces and nanoparticles of various alloys[59,71]. For instance, the selectivity and activity of Au-Pd nanoparticles has been reported for different compositions, showing structural sensitivity[75,76]. Among the porphyrin-based catalysts e.g. cobalt-porphyrin structure[77] has shown reasonable selectivity, however, porphyrin-like structures generally have low stability[78]. Using a DFT-screening to predict stable, selective and active alloys, Pt-Hg was found and experimentally tested, showing good performance[74]. The high activity and selectivity was rationalized by the near optimal ΔG_{OOH*} and the geometric effect stemming from the $PtHg_4$ structure in which single Pt-atoms are surrounded by Hg. Other transition metal alloys with Hg have also been tested, and in particular Pd-Hg displays state-of-the-art specific activity and high ($> 90\%$) selectivity toward H_2O_2[79].

4.2.3 Study of a Pd_1/N-C Catalyst

Inspired by the principles discussed in the precious sections of this chapter, a catalyst consisting of Pd single atoms anchored in a porphyrin-like structure (Pd_1/N-C) was synthesized, tested for the $2e^-$-ORR reaction, characterized

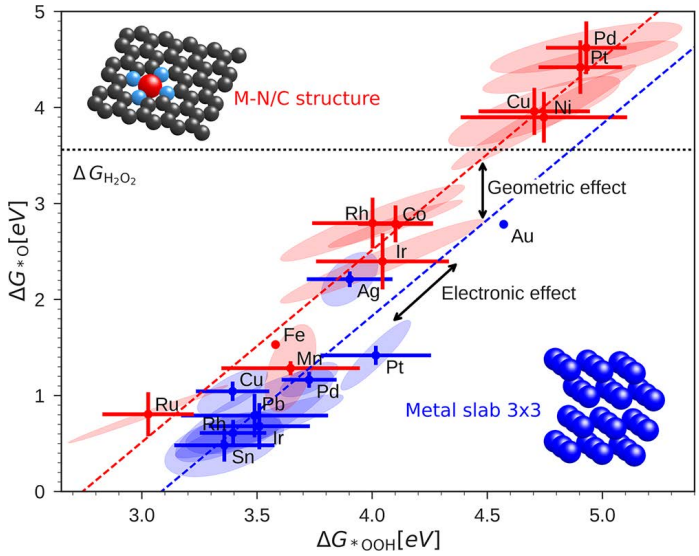

Figure 4.5: Shifted scaling relations of ORR-intermediates showing the geometric effect of isolated sites. Figure adapted with permission from [59]. Copyright 2018, American Chemical Society.

and theoretically modeled. The Pd_1/N-C catalyst proved active, selective and stable which was attributed to the single Pd atom anchored by the coordinating N-species. Highlights of the study will briefly be presented with a focus on the Pd_1/N-C catalyst. For more details see [48] in appendix A.

Synthesis

The synthesis of the Pd_1/N-C catalyst as well as the control samples follow a wet chemical-thermochemical process as shown in figure 4.6. Briefly, a template structure consisting of SiO_2-nanospheres was prepared[80] and subsequently covered with graphene oxide (GO)[81]. Next, the spheres were covered in either polydopamine (PDA, source of nitrogen) or amorphous carbon (AC) depending on the sample (but none for the Pd nanoparticle sample). Subsequently all samples were pyrolyzed and the silica spheres were etched away. Lastly, Pd was deposited except for the blank nitrogen doped carbon nanospheres (N-C). In summary, four different sample types were made, all supported on reduced graphene oxide (RGO). Two of these had nitrogen incorporated stemming from PDA, (N-C and Pd_1/N-C), the latter containing Pd. Third type (Pd_1/C) had Pd on amorphous carbon. The last type (Pd_{NP}/C) had Pd nanoparticles directly on the RGO.

Chracterization of Pd_1/N-C

Based on the measured X-ray absorption near edge structure (XANES), the valence of the Pd species is positive compared to a metallic Pd reference and

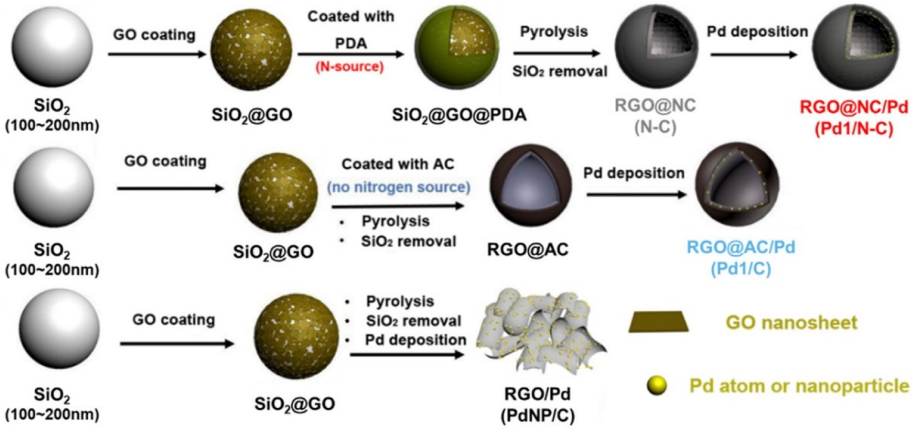

Figure 4.6: Synthesis procedures for Pd_1/N-C and the three control samples: N-C, Pd_1/C and Pd_{NP}/C. Adapted from [48].

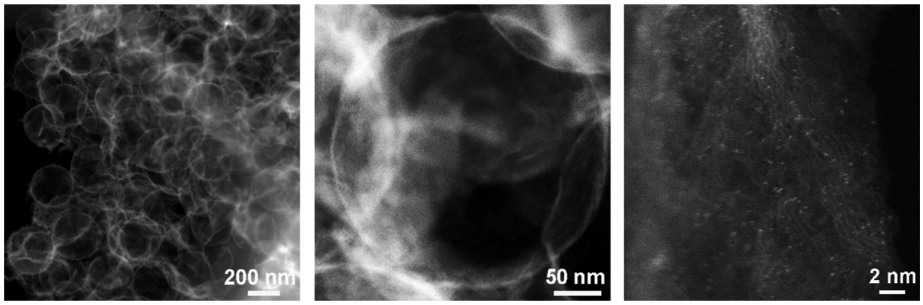

Figure 4.7: HAADF-STEM images of the Pd_1/N-C SAC showing the supporting carbon spheres (two left images) and bright dots ascribed to Pd single atoms (right image). Reprinted from [48].

the extended X-ray absorption fine structure (EXAFS) indicated that the Pd species was coordinated by N-atoms. The fitting of the EXAFS-data yielded a coordination number of ≈ 6 N with an average distance of ≈ 2.1 Å. Thereby, the structure of Pd_1/N-C was hypothesized to consist of Pd-single atoms coordinated by N-defects (e.g. pyridinic) in the carbon lattice. The existence of such N-sites is also consistent with the X-ray photoelectron spectroscopy (XPS) spectrum of N, showing significant ratios of pyridinic and pyrrolic N ($\approx 21\%$ each) although graphitic N ($\approx 54\%$) is prevalent while pyridinic-oxide is negligible (a visual overview of N-defects is given in figure 6.3 in chapter 6). The single atom dispersion of Pd is also seen as bright dots in the STEM image in figure 4.7 (right). The produced catalyst powders were suspended in a solution consisting of ethanol, Milli-Q H_2O and Nafion perfluorinated resin solution and then sonicated. The resulting inks were dropcasted on polished and cleaned glassy carbon electrodes used for RRDE-experiments as well as on gas diffusion

electrodes (GDEs) consiting of carbon cloth material, used for accumulation tests in a three-compartment cell.

Electrochemical Performance

The electrochemical performance of Pd_1/N-C and the reference samples was probed using RRDE-experiments to measure activity and selectivity. The selectivity here is given in terms of faradaic efficiency (FE), which is the percentage of the total measured current going toward producing H_2O_2. The three panels in figure 4.8(a) show (from top to bottom) the Faradaic efficiency, ring current and disk current density, all versus the disk potential. Evidently, all catalysts facilitate the $2e^-$-ORR to some degree, however, the selectivity and activity varies. The presence of Pd species in all cases enhance both selectivity and activity compared to the carbon based N-C catalyst (grey traces). The Pd_1/N-C (red traces) has the highest activity and selectivity, but interestingly the second best is not the other Pd SAC catalyst (Pd_1/C) but the Pd nanoparticles (Pd_{NP}/C). In general, the faradaic efficiencies also seem to vary somewhat with the applied potential and the Pd_1/N-C has a peak FE$\approx$ 80% at $E \approx 0.3$V. Regarding the activity, an intrinsic metric such as turnover frequency (TOF) is desirable but not always obtainable as it requires knowledge of the amount of active sites on the catalyst. If the electrochemically active surface area (ECSA) may be estimated, the current density normalized to ECSA may be used instead. This metric also requires the catalyst to be well-defined, and is not overly common in literature. Yet, in the case of extended crystalline surfaces, the analysis is straightforward, since $A_{ECSA} \approx A_{geo}$. By this metric of intrinsic activity, Pd_1/N-C is still surpassed by state-of-the-art Pt-Hg[74] and Pd-Hg[79] (see the manuscript in appendix A for comparison). On the other hand, the single atom dispersion of Pd_1/N-C allows for a high material utilization and consequently a high mass activity as seen in figure 4.8(b). While the mass activity is strictly speaking not an intrinsic measure, it may be a proxy in lieu of better alternatives, and furthermore it may have a techno-economic relevance. Here Pd_1/N-C performs on par with carbon supported Pd-Hg nanoparticles[79] and cobalt porphyrins[77,82–84], although there is some spread in the reported activities of the latter. Figure 4.8(c) shows that the selectivity of Pd_1/N-C compares reasonably well with other catalysts reported in literature, although it is not among the highest. For H_2O_2-generation in a PEM-electrolyzer running on water, the argument could be made, that a decreased selectivity essentially yields the same result as a lower activity, since the peroxide is effectively diluted in water. Therefore neither selectivity or activity alone, but their convolution is of importance. Additionally, the catalyst stability is of great significance of the viability on any such device. The stability of Pd_1/N-C was also evaluated using an accelerated degradation test, showing a somewhat reduced activity but with relatively stable selectivity[48]. However, more rigorous test are needed to evaluate the extent and origin of the degradation.

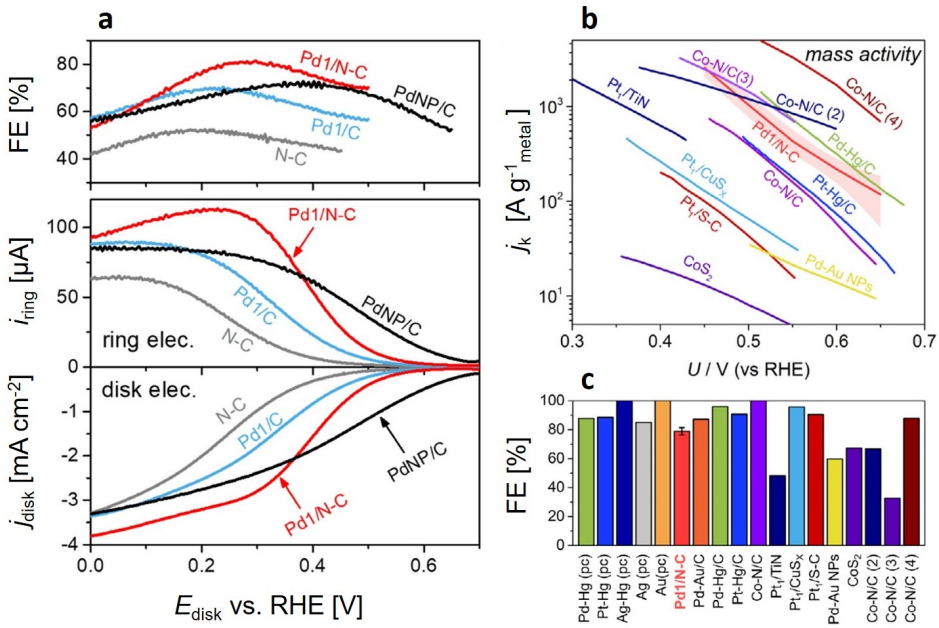

Figure 4.8: (a) RRDE measurements showing higher activity and selectivity of Pd_1/N-C (red curves) compared to reference samples. (b) mass activity of Pd_1/N-C compared to state-of-the-art catalysts (i.e. partial current density towards $2e^-$-ORR, corrected for mass-transport-limitations via Koutecký-Levich relation). (c) Faradaic efficiencies of various catalysts. RRDE-measurements performed in O_2-saturated 0.1 M $HClO_4$ with ν=50 mV/s, ω=1600 rpm and E_{ring}=1.4 V vs. RHE. Background scans in Ar-satruated electrolyte has been subtracted to minimize non-Faradaic currents. Figure adapted from [48].

To test the catalyst under more realistic conditions for H_2O_2-synthesis, GDEs were tested in a three-compartment cell for an extended time (until a total charge of 15 C was passed during chronoanperometry). In the three–compartment cell, the working electrode and counter electrode are located in two different compartments which are separated by a proton conducting membrane (Nafion 117). The separation ideally prevents H_2O_2 from reaching the anode and being oxidized, instead allowing it to accumulate in the working electrode compartment. The third compartment contains the reference electrode, which is connected via a ceramic frit to the working electrode chamber. The H_2O_2 yield versus passed charge can be seen in figure 4.9(a) for Pd_1/N-C and the reference measurements, while fig. 4.9(b) shows the corresponding partial current densities toward the H_2O_2 and H_2O products. Importantly, the trend in activity and selectivity differs from what was observed using RRDE-experiments. Particularly, the difference for Pd nanoparticles (Pd_{NP}/C) is significant: it now shows the lowest selectivity while the total current density is the highest. One might speculate that the Pd nanoparticles facilitate the further reduction and/or chemical dissociation of H_2O_2, but that the efficient transport

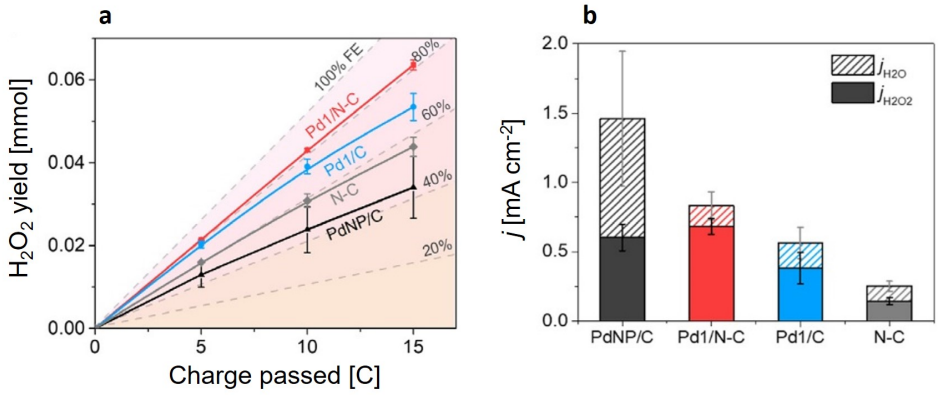

Figure 4.9: (a) Produced H_2O_2 quantified via titration with $KMnO_4$ versus the net passage of charge. (b) Partial current densities toward each reaction determined via the total current and the H_2O_2 yeild. Measured via chronoamperomerty at 0.2 V vs. RHE in O_2-saturated 0.1 M $HClO_4$. Adapted from [48].

of generated H_2O_2 away from the catalyst and the generally low concentration in RRDE-experiments suppresses this. In the test of GDEs, on the other hand, no forced convection carries products away and the accumulated H_2O_2 concentration may be significant. At any rate, the difference in performance between techniques underlines the necessity of also testing catalyst under conditions more relevant for scale-up. Nonetheless, the Pd_1/N-C catalyst is able to maintain the highest selectivity (FE $\approx$ 80%), and the highest partial current density toward H_2O_2.

Modelling the Impact of N-coordination with DFT

The M-N/C structure of Pd (where M: Pd, coordinated by 4 N) has previously been modeled by DFT, and was predicted to be selective, but not particularly active, given it's relatively week binding of OOH[59] (see red dot for Pd on the volcano plot in fig. 4.4). To rationalize the relatively high activity of Pd_1/N-C observed experimentally, DFT calculations were performed using more generalized M-N/C structures where Pd can be coordinated by up to 6 N and additional N may incorporated in the lattice in close proximity. This is in accordance with the coordination number found from EXAFS-fitting and the XPS spectrum showing a substantial fraction of graphitic N, as discussed above. Based on the DFT calculations for various coordination environments of Pd_1/N-C a volcano plot was constructed as seen in figure 4.10(a). The structures seen in fig.4.10(b) give significantly different values of ΔG_{OOH*} and by extension significant variations in activity and selectivity are predicted. For example, the 4 N structure sits furthest to the right on the weak-binding leg, whereas the (6+3) N and (6+2) N sit near the apex of the $4e^-$-ORR volcano. The green shaded area of the volcano plot indicates the region where O* is destabilized, which favors

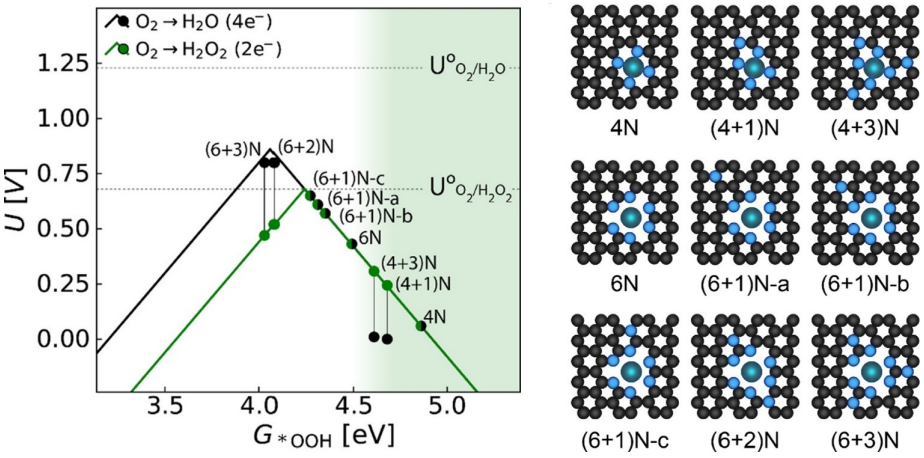

Figure 4.10: Volcano trend predicted by DFT calculations (left) for the various N-coordination environments of Pd_1/N-C (right). Adapted from [48].

the $2e^-$-pathway. In light of the DFT calculations, the relatively high activity *and* selectivity of Pd_1/N-C combined with the ≈ 6 N coordination indicated by EXAFS, it is feasible that the coordination environment of Pd_1/N-C is similar to one of the weak binding 6N-type structures seen in figure 4.10(b), e.g. 6 N or either of (6+1) N-(a,b,c). There is no compelling evidence that one specific type of site would preferentially be formed in the synthesis procedure, so it is likely that the Pd_1/N-C catalyst has a distribution of different site types similar to this (and perhaps other types as well to some extent). As shown in figure 4.8, some of the reported mass activities of Co-N/C are higher than for Pd_1/N-C. Assuming the mass activities to be representative of intrinsic activities, it is thus not obvious that Pd_1/N-C has achieved the optimal tuning of electronic and geometric effects - i.e. in terms of ΔG_{OOH*} and O* destabilization. Bearing in mind that the DFT calculations are thermodynamic in nature, kinetic barriers are not accounted for, hence relating the limiting potential calculated via DFT to an experimentally measured activity should not be expected to yield quantitative agreement. Considering the trend of the DFT calculations together with the difference in activity and selectivity of Pd_1/N-C and Pd_1/C (i.e. with and without N, respectively), the presence of N-coordination does, however, have a significant effect on the catalyst performance.

4.3 Conclusion

The ORR reactions are of interest both for fuel cells and in the synthesis of H_2O_2. For both reactions, tuning the catalysts toward better performance involves controlling the binding energies of intermediates, in which the scaling relations are a major challenge. The electrochemical synthesis of H_2O_2 is an interesting prospect, which among other factors require active, selective and

stable catalysts. In this regard single atom catalyst may be well-suited. From the electrochemical measurements the Pd_1/N-C catalyst was found to perform well in terms of activity and selectivity, although not surpassing state-of-the-art catalysts. In terms of stability, the system is not thoroughly characterized. In conjunction with structural characterization and DFT calculations the performances of Pd_1/N-C and reference samples were investigated. The high activity and selectivity of Pd_1/N-C toward $2e^-$-ORR was attributed to the single atom nature and N-coordination.

Chapter 5

Hydrogen Evolution Reaction (HER)

Platinum is the best HER catalyst known, but it is scarce and expensive. It is thus desirable to find cheaper and more abundant alternatives to replace Pt with for catalyzing the HER. The ongoing search for such alternatives continuously brings forth new catalysts, but none of which can compete with platinum. A direct comparison between catalysts of interest is often impossible, as intrinsic activities are rarely reported, and the experimental measurements are often subject to bad practice. These topics will be discussed in the present chapter. Firstly, a brief introduction will be given to the field of acidic HER catalysis, followed by some key points on the influence of mass-transport limitations and a summary of the common pitfalls in literature. This will qualify and motivate the subsequent presentation of a benchmark study of Pt nanoparticles.

This chapter is largely based on the paper *Is There Anything Better than Pt for HER?*[49] which was recently published in *ACS Energy Letters*. With this work we set out to perform a series of HER measurements of a well-defined Pt catalyst. The idea was to map out the activities over a large range of loadings for otherwise identical samples, thus creating an activity benchmark allowing easy comparison with other catalysts reported in the literature. The point was also to debunk the occasional "findings" of catalysts allegedly performing as well as platinum while emphasizing the guidelines for best-practice. These points are still essential, but the observation of the ever increasing intrinsic activity, with decreasing loading and the additional observation of a curious hysteresis phenomenon at ultra-low loadings, added another perspective to the study. I performed the electrochemical tests, contributed with ideas for the numerical modelling and the project in general and co-wrote the paper. Hector Prats performed the numerical simulations, supervised by Karen Chan. Niklas Secher and Karl Toudahl deposited and characterized the cluster source samples. Niklas also developed the simulation of particle overlap. The full manuscript is

included in appendix B.

5.1 HER Catalysis

The hydrogen evolution reaction is a two-electron reaction with one reaction intermediate, but several *reaction mechanisms* are possible, as described by eqs. (5.1). The same steps apply (in reverse) for the HOR. These steps may occur in a combination resulting in an overall reaction of $2H^+ + 2e^- \rightarrow H_2$, however, multiple reaction pathways may proceed in parallel. For example, step (5.1a) may be followed by either (5.1b) or (5.1c) for the Volmer-Heyrovský or Volmer-Tafel mechanism, respectively. Note, that the Tafel step is purely chemical.

$$H^+ + e^- + * \longrightarrow H^* \qquad \text{(Volmer)} \qquad (5.1a)$$

$$H^+ + e^- + H^* \longrightarrow H_2 + * \qquad \text{(Heyrovský)} \qquad (5.1b)$$

$$2H^* \longrightarrow H_2 + 2* \qquad \text{(Tafel)} \qquad (5.1c)$$

Regardless of the various reaction pathways, the adsorbed hydrogen (H^*) is the reaction intermediate. Thus, the hydrogen adsorption free energy ΔG_{H^*} is a relevant descriptor for catalyst activity, in line with Sabatiers principle dicussed earlier. So if a catalyst binds hydrogen too weakly, the Volmer step (adsorption) will limit the reaction, whereas a catalyst binding too strongly will be limited by the Heyrovský or Tafel step (desorption)[22]. An optimal catalyst should therefore have $\Delta G_{H^*} \approx 0$. Experimentally found HER activities for transition metals qualitatively fit the volcano-trend of this predictor[85,86], which was also shown in figure 2.2 in chapter 2.

During the past decade, transition metal sulfides (TMSs)[87–90] and transition metal phosphides (TMPs)[91–94] have been found to catalyze the HER reaction. The development of these catalyst was initiated by biomimicry of enzymes that can produce hydrogen (e.g. hydrogenase and nitrogenase) as well as known catalyst for the hydrodesulfurization process (HDS)[87,88,95]. In particular, catalysts inspired by MoS_2 have been studied at length. The HER activity of MoS_2 is due to the edge sites whereas the basal plane of the flat, layered structure is inert. Several steps have been taken to increase the overall activity of these catalysts, such as preferentially exposing edge sites[90] and synthesizing Mo-S nanoclusters with motifs similar to the active edge sites of MoS_2[89]. In addition, it has been shown that the basal plane can be activated by introducing strain and vacancies to optimize ΔG_{H^*}[96]. Similar to transition metals, TMSs and TMPs generally also follow a volcano-like trend in activity versus ΔG_{H^*}[93,96], however, their activities are several orders of magnitude lower. Thus $\Delta G_{H^*} \approx 0$ is a necessary condition for an active HER catalyst, but an insufficient predictor of absolute activity[22]. Another interesting class of HER catalyst is single atom catalysts (SACs) and other small entities, which are also discussed further in chapter 6. Both platinum group metals (PGMs)[97–99] and other transition metals[100–103]

have been studied for the HER reaction. Despite all these efforts, no reported catalyst can compete with Pt on any meaningful metric, although such claims occasionally arise. In fact, Pt is so active for HER in acid that it is limited by mass-transport even at ultra-low loadings and negligible overpotentials - one of the cardinal points of the present work. This has some interesting implications: Only a lower bound estimate of the true Pt activity can be obtained and if any alternative catalyst had comparable activity it would be impossible to discern which one is more active with current measurement techniques.[49]

5.2 Mass-Transport Limitations for HER/HOR

It is widely accepted that HOR can be completely limited by mass-transport due to the slow supply of the reactant species H_2 to the catalyst surface, owing to the low solubility of H_2 in the electrolyte (e.g. 0.59 mmol L^{-1} at 25 °C [104]). Although it is well described in literature, it is often overlooked that HER can be (and often is) mass-transport limited for a similar reason, namely the transport of H_2 away from the catalyst. Notably, for RDE measurements both HOR and HER is *completely* mass-transport limited for Pt-disks in acid[105,106]. Rewriting the Levich equation (3.1) in compact form specifically for the limiting current density of HOR yields eq. (5.2), where the $C^*_{H_2}$ is the bulk hydrogen concentration, ω is the RDE rotation speed and B is the Levich constant.

$$j_{\mathrm{l,HOR}} = B\, C_{\mathrm{H}^*_2}\, \omega^{1/2} \tag{5.2}$$

The experimental manifestation of this is easily observable, as the HOR current flattens out and reaches a potential-independent plateau at $j_{\mathrm{l,HOR}}$. For example at ω=1600 rpm, $j_{\mathrm{l,HOR}}$ is in the range of 2-3 mA cm^{-2} (depending on electrolyte)[105–108]. It is, however, important to note that the measured current density may be mass-transport limited well before this plateau. In the case where $j_0 \gg j_{l,a}, |j_{l,c}|$, the current-overpotential equation (2.16) simplifies to eq. (5.3), in which the measured current is the *diffusion limited* current density (j_{d}). Note that j_0 is gone and the equation now describes the so-called *diffusion overpotential* (also called *concentration overpotential*) and holds no kinetic information.

$$j_{\mathrm{d}} = \frac{1 - e^{-f\eta}}{\dfrac{1}{j_{\mathrm{l,a}}} - \dfrac{e^{-f\eta}}{j_{\mathrm{l,c}}}} \tag{5.3}$$

In the case of HOR/HER, $j_{l,a} = j_{\mathrm{l,HOR}}$ while $j_{\mathrm{l,c}} = j_{\mathrm{l,HER}}$ is the limiting cathodic current density governed by the transport rate of protons to the catalyst surface and is also given by the Levich equation. In strong acid, e.g. 0.5 M H_2SO_4, C_{H^+} is three orders of magnitude larger than C_{H_2} and consequently $j_{\mathrm{l,HER}}$ is three orders of magnitude greater than $j_{\mathrm{l,HOR}}$ (i.e. in the range of A cm^{-2}). Under the most common experimental conditions the measured current densities are much lower and therefore the proton supply poses no limitation in practice. A possible exception to this will be considered in the discussion

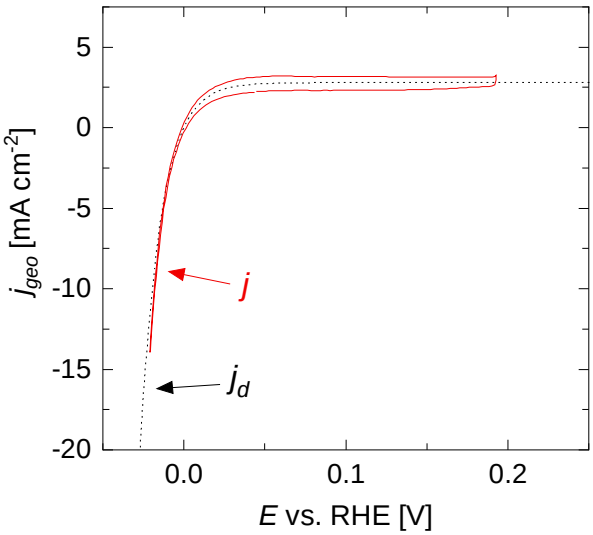

Figure 5.1: Concentration overpotential of Pt: Measured current density j of Pt/C coincides with the diffusion limited current density j_d. RDE-measurement done with 0.1 $\mathrm{mg_{Pt}cm^{-2}}$ on a GCE disk in H_2-saturated 0.5 M H_2SO_4 at ω=1600 rpm, ν= 10 mV s^{-1} and j_d calculated from eq. (5.3) with $j_{l,\mathrm{HOR}}$= 2.8 mA cm^{-2}, $j_{l,\mathrm{HER}}$= 3447 mA cm^{-2} at T = 298 K.

of hysteresis at ultra-low Pt loadings. In figure 5.1, the HER/HOR CV of Pt nanoparticles is shown together with the calculated j_d. The measured CV quickly reaches a plateau in the HOR branch, but furthermore it coincides with j_d over the entire potential range. Essentially, the HER branch is also limited by the slow H_2-diffusion. Since the measured HER current keeps increasing with more negative overpotentials it may not seem obvious at first, but it is diffusion limited and thus no reaction kinetics may be extracted from the CV. Tafel slopes are sometimes analyzed in order to obtain mechanistic information about the reaction, e.g. the rate limiting step. The Tafel slope analysis of a diffusion limited current yields an apparent slope of ∼30 mV/dec. This could erroneously be ascribed a mechanistic significance, e.g. the Tafel step (5.1c) being rate-limiting, but it's merely the slope of the concentration overpotential j_d.[105] The Tafel slope may also be extrapolated to $\eta = 0$ in an attempt to estimate the exchange current density j_0, but by extrapolating j_d (or any measured current coinciding with it), the limiting $j_{l,\mathrm{HOR}}$ rather than j_0 is found. Thereby highly active catalysts may be significantly underestimated with this approach.[109] More generally, Zalitis and Kucernak suggest that the entire concept of extrapolation of Tafel slopes and even fitting the micro-polarization region leads to flawed estimates of the exchange current density. Due to the mechanistic complexity of the possible reactions pathways and hydrogen coverage effects, the simplistic Butler-Volmer model is suggested to be unsuitable.[110] The RDE technique offers controllable and enhanced mass-transport rates compared to unstirred solutions[111], but even so the mass transport may evidently still be limited for

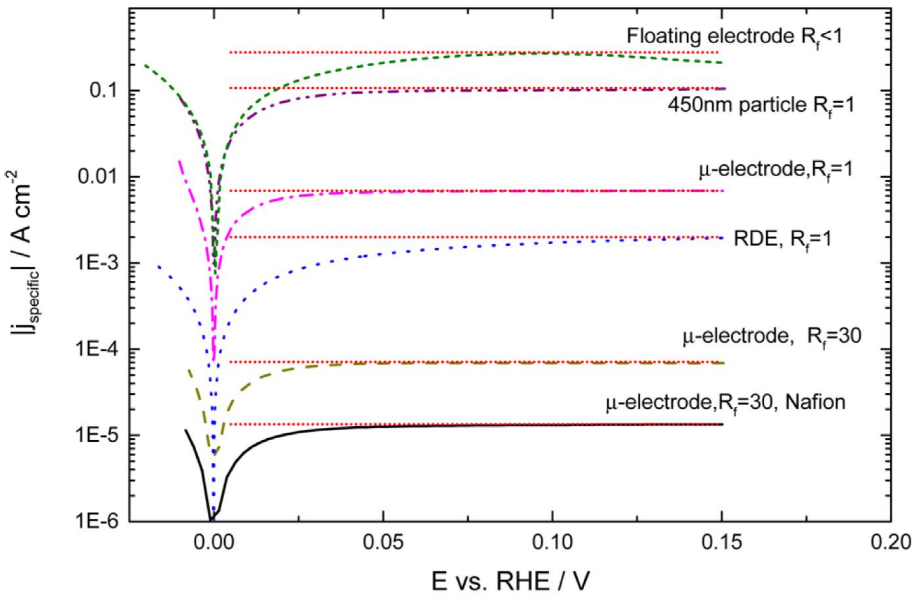

Figure 5.2: HER/HOR current densities of Pt in acidic solutions for various experimental techniques. Reprinted from [110] under the CC-BY 4.0 license.

highly active catalysts. Other methods such as the H_2-pump[109,112] and floating electrodes[113,114] techniques provide higher mass-transport rates compared to RDE for the HER/HOR reactions. Consequently, significantly higher estimates of the intrinsic activity of Pt can be made. In figure 5.2 specific HER/HOR-current densities are shown for a range of experimental techniques. For instance, the trend shows that floating electrodes can perform at current densities that are two orders of magnitude larger than for RDEs, ascribed to their superior H_2 mass-transport rate. Overall, it seems that the floating electrode outperforms the alternatives, but this is not equivalent of this technique being free of mass-transport limitations. As will be argued in the following presentation of our benchmark study, even the floating electrode and H_2-pump techniques may underestimate the intrinsic activity of Pt. In this regard it is worth observing that for *all* techniques the HOR-current reaches a plateau. One might argue that in the case of the floating electrode this could be due to the Tafel-step being rate-limiting and that the potential-independent current is in fact *kinetically* limited. On the other hand, one might also argue that the H_2-transport sets a limiting current density as for all the other techniques, albeit at a higher level.

5.3 The Need for a Benchmark

There are two overall catalyst development strategies: increasing the density of active sites on the catalyst (e.g. nanostructuring) or increasing the intrinsic activity of the sites. Both routes encompass a host of different methods aimed at increasing the overall catalyst performance.[22] Although large geometric current densities have been reported for earth-abundant catalysts, this has largely been accomplished by increasing the amount of active sites, often achieved simply by increasing the catalyst loading to make up for the much lower intrinsic activity.[23] This is not indicative of an enhanced catalyst, since neither intrinsic activity nor active site density is improved - only more catalytic material has been employed. Replacing Pt with an earth-abundant alternative of lower intrinsic activity only makes sense if the material price is correspondingly lower. Commonly the overpotential ($\eta_{10\,\mathrm{mA\,cm^{-2}}}$) needed to reach a geometric current density (j_{geo}) of 10 mA cm^{-2} is reported without regard for the applied catalyst loading.[115–117] While j_{geo} may be a relevant metric in the design and engineering of scaled-up devices (e.g. electrolyzers), it is not useful in the comparison of catalyst activities. Focus should be turned towards reporting intrinsic activities such as turnover frequency (TOF). Furthermore, the discussed influence of mass-transport limitations makes the estimation of intrinsic activity troublesome for highly active catalysts such as Pt, but also less active catalyst at sufficiently high loadings. In addition to this, there are some common pitfalls regarding acquisition and analysis of experimental data which are often seen in literature.[23] For example: lack of calibration of reference electrode; lack of H_2-saturation during HER experiments; comparison with subpar reference measurements and so on.[97,99,115] This can lead to false conclusions about the reported catalysts and generally limits the usefulness of the studies. Some of these pitfalls are summarized below.

5.3.1 Common Pitfalls

Lack of potential scale calibration: The reference electrode should be calibrated to the RHE scale in conjunction with each set of experiments to enable reproducible data. This requires a completely hydrogen saturated electrolyte and a Pt dummy electrode as described in section 3.4.4. Furthermore, complete hydrogen saturation must be maintained *during* HER experiments by continuous H_2-purging of the electrolyte. Neglecting to do so effectively gives an ill-defined Nernst-shift of the potential scale in favor of the HER.[105] It can often be seen when significant cathodic currents are drawn at potentials more positive than 0 V versus RHE, or when there is virtually no HOR current (given the lack of reactants).

Poor choice of counter electrode: When performing HER-experiments the counter electrode (CE) acts as the anode. Thus the CE should be electrochemically stable in this potential range and have a high electrochemically active surface are (ECSA) compared to the working electrode (WE). At high anodic

potentials, Pt may corrode and redeposit on the WE.[118–120] Even trace amounts of Pt may significantly alter the measured activity. Therefore, Pt is generally not suitable as CE - especially when the catalyst under investigation is significantly less active than Pt, which is almost always the case. Additionally, one may also place the anode and cathode in separate compartments in order to minimize the possible effect of redepositon.

Comparison to subpar measurements: Catalysts reported in literature are often compared to subpar measurements of reference samples, making the reported catalyst appear more attractive. A common fallacy is to apply a significantly higher loading of the reference sample (e.g. a commercial Pt/C catalyst) than of the studied catalyst. Given the mass-transport limitations of Pt in HER/HOR, the activity of the high loading reference sample will be severely underestimated. Upon normalizing the measured currents to the catalyst loadings, i.e. mass activity, the Pt/C reference sample will be artificially low compared to the studied catalyst, with the false conclusion that a better catalyst has been found. Catalysts should instead be compared to state-of-the-art measurements.

Lack of intrinsic activity assessment: Reporting geometric current densities with complete disregard for catalyst loading is another common and detrimental fallacy. Geometric current density and other extrinsic metrics do not properly represent the activity of a catalyst. For instance j_{geo} vs. η is easily changed for the same catalyst, simply by varying the catalyst loading. Since the catalytic process happens at specific sites, the number of these active sites is of utmost importance in assessing the merits of a catalyst.

Neglecting mass-transport limitations: Mass-transport limitations may complicate the assessment of activity, both intrinsic and otherwise. Although a measured HER current does not reach a plateau, like that of the HOR, the reaction may still be limited by mass transport. In these circumnstance kinetic analyses of e.g. Tafel slopes are meaningless. While there are practical boundaries for the rate mass-transport in any given setup, care should be taken to asses and minimize the relative impact of such mass-transport limitations.

In order to aid the scientific discussion and development of novel HER catalyst one might argue there is a need for a benchmark study for several reasons. Since the above mentioned pitfalls are frequently encountered in literature, it makes sense to highlight the best-practice procedures even though it seems trivial. Having a data set of a well-defined Pt catalyst over a large range of catalyst loading might furthermore serve as a useful basis for comparison in future studies. Finally, there is arguably a need for a better understanding of the implications of mass-transport limitations during HER. With these things in mind, we decided to conduct a benchmark study that would highlight the issues at hand.

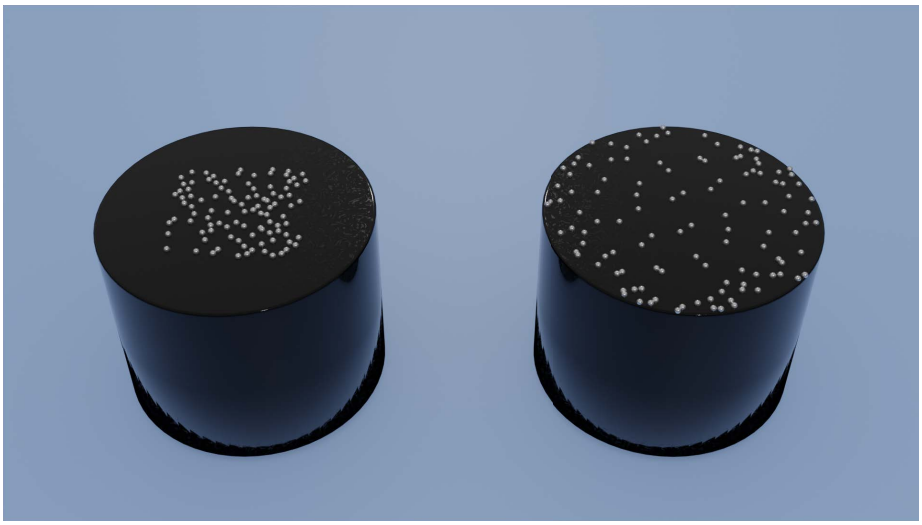

Figure 5.3: Schematic of Pt nanoparticles on GCE disks with small (left GCE) and large (right GCE) raster patterns. The difference in dispersion results in significantly different inter-particle distances for similar loading deposited.

5.4 Benchmark Study of Pt Nanoparticles

In this benchmark study a series of Pt nanoparticles were deposited using the cluster source system in order to gain a precise, controllable loading and uniform particle size. Furthermore, samples of a commercially available Pt/C catalyst were tested as well, to increase the achievable range of Pt loading toward the higher end and to generalize the study. In order to asses the intrinsic activity, CO-stripping experiments were used to quantify the number of active sites on each sample. Furthermore, a numerical diffusion model was used to study the mass-transport phenomena observed. All details on experimental procedures, characterization and numerical simulations can be found in the Supplementary Information (SI) of the paper[49], but all the main points will be discussed here. First, an overview of experimental procedures and the studied samples is given. Then, the main results will be discussed, with an emphasizes on why intrinsic activities are important. This naturally connects with the limitations set by mass-transport, also tying into the observed hysteresis phenomenon.

5.4.1 Sample Preparation

New glassy carbon electrode (GCE) disks ($\varnothing$ = 5.0 mm) were cleaned as described in section 3.3 and used as substrate for all samples. The cluster source (see chapter 6 for further description) was used to deposit mass-selected Pt nanoparticles (370k amu) corresponding to a particle size of 3.8 nm of loadings in the range L = 13-5000 ng cm^{-2} on the GCEs. The substrate cleanliness and the Pt depositions were verfied by ion scattering spectroscopy (ISS). To ensure

a uniform coverage, the samples were rastered during deposition using either a small 1×1 mm^2 or a large 4×4 mm^2 raster pattern giving a deposition area of ≈6.2 and ≈30 mm^2, respectively, due to the width of the beam profile. The small raster pattern thus gives a square coverage within the area of the GCE disk, whereas the large raster pattern covers the entire disk area. An illustration of this is seen in figure 5.3. A blank ink consisting of 7 mL Milli-Q H_2O, 18 mL isopropyl alcohol, 10 mL ethanol and 10 μL Nafion perfluorinated resin solution (5 wt.%) was prepared. A commercially available Pt/C catalyst powder (HiSPEC 9100, Johnson Matthey) was suspended in a portion of this ink. Approriate portions of the blank ink and aliquots of the concentrated catalyst suspension were mixed, creating a diluted suspension for each target loading. From each ink a 7 μL aliquot was dropcasted on a GCE disk, giving Pt/C samples in the range of 500-10^5 ng cm^{-2}. An overview of all samples is given in table 5.1.

5.4.2 Experimental Procedures

All experiments were carried out according to the methods outlined in section 3.3. In brief, the experiments were conducted in 0.5 M H_2SO_4 (Suprapur, Merck). Prior to each experiment the REF was calibrated using a dummy Pt electrode in the H_2-saturated electrolyte. Samples were introduced under potential control at +50 mV vs. RHE. HER/HOR CVs were recorded in H_2-saturated electrolyte using an RDE at ω= 1600 rpm. A scan speed of $\nu = 50$ mV s^{-1} was used for all HER/HOR CVs with the exception of the two highest loadings (0.5 and 1 $\times 10^5$ ng cm^{-2}), where $\nu = 10$ mV s^{-1} was necessary to minimize non-faradaic currents due to their high surface roughness. After each HER experiment, the uncompensated ohmic resistance was measured for each sample using the high frequency intercept of the EIS spectrum. This was used to post-correct all measured HER/HOR CVs. CO-stripping experiments were conducted on all samples using ν= 10 mV s^{-1} and ω= 200 rpm. A 15-minutes potential hold at +50 mV vs. RHE was used with CO-dosing for the first 2 minutes. A similar potential hold period was employed with no CO-dosing to obtain a cycle for background subtraction. An additional linear background was subtracted prior to the integration yielding $Q_{\mathrm{CO,tot.}}$.

5.4.3 Number of Active Sites Measured by CO-stripping

In order to estimate intrinsic catalytic activity, a quantification of the number of active sites and the reaction rate is needed. The reaction rate is given by the measured HER current (i) and the number of active sites via CO-stripping. This was used to estimate turnover frequencies, as will be shown in the following. CO-strip experiments were performed on all samples, and figure 5.4 shows the obtained strip peaks for the two most extreme cases, namely the samples with lowest (13 ng cm^{-2}) and highest (10^5 ng cm^{-2}) loading to the left and right, respectively. The black lines denote the background-subtracted strip-peaks. The

Table 5.1: Overview of sample loadings and selected metrics for 3.8 nm nanoparticles (370k amu) deposited with small and large raster pattern, respectively, and dropcasted commercial Pt/C.

	Loading [ng cm^{-2}]	**CO-strip charge** [C]	**TOF** [#H_2 $site^{-1}$ s^{-1}] at η=15 mV	η [mV] at 10 mA cm^{-2}
Small raster	13±1	3.0×10^{-7}	3.1×10^{2}	133
	19±1	4.6×10^{-7}	2.6×10^{2}	115
	50±3	1.4×10^{-6}	1.1×10^{2}	85
	100±5	2.6×10^{-6}	7.9×10^{1}	61
	17±1	4.2×10^{-7}	2.4×10^{2}	120
	50±3	1.6×10^{-6}	9.8×10^{1}	83
	100±5	3.1×10^{-6}	7.3×10^{1}	54
	200±10	6.7×10^{-6}	4.8×10^{1}	41
	200±10	5.0×10^{-6}	5.8×10^{1}	48
	500±25	1.6×10^{-5}	2.8×10^{1}	35
	500±25	1.5×10^{-5}	3.6×10^{1}	34
	1000±50	2.8×10^{-5}	2.2×10^{1}	29
	5000±250	1.1×10^{-4}	9.0	20
Large raster	565±28	1.9×10^{-5}	4.7×10^{1}	24
	1000±50	4.5×10^{-5}	2.4×10^{1}	21
	5000±250	1.5×10^{-4}	1.3×10^{1}	16
Commercial Pt/C	500±34	1.5×10^{-5}	4.0×10^{1}	30
	1000±67	3.6×10^{-5}	1.7×10^{1}	30
	5000±276	2.2×10^{-4}	5.0	21
	50000±2975	2.8×10^{-3}	3.0×10^{-1}	21
	100000±5150	3.3×10^{-3}	4.0×10^{-1}	18

dark green area under the stipulated green line shows the additional background subtracted. The linear background was chosen so that the end points enclosing the peak were at $\mathrm{d}i/\mathrm{d}E \approx 0$ or $i < 10$ nA, and both if possible. For consistency this approach was applied for all samples. Thereby the light green peak represents the area of integration. This lower bound value was used as the best estimate for the "true" $Q_{\mathrm{CO,tot.}}$ while the integration including the dark green background was used as an upper estimate. The scientific argumentation for the exact choice of integration limits and additional background subtraction is poor - except that a peak should be shaped like a peak, in the sense that applying a background subtraction should give a peak with $i \approx 0$ at both ends - hence the need for this, somewhat arbitrary, second background subtraction. For all but the ultra-low loading samples (less than 100 ng cm^{-2}), the difference and thus the estimated error is minuscule. For the lowest loading (left) the maximum relative error estimated is significant, but for the overall trends of this study it is inconsequential. An overview of integrated CO-strip charges can be seen in

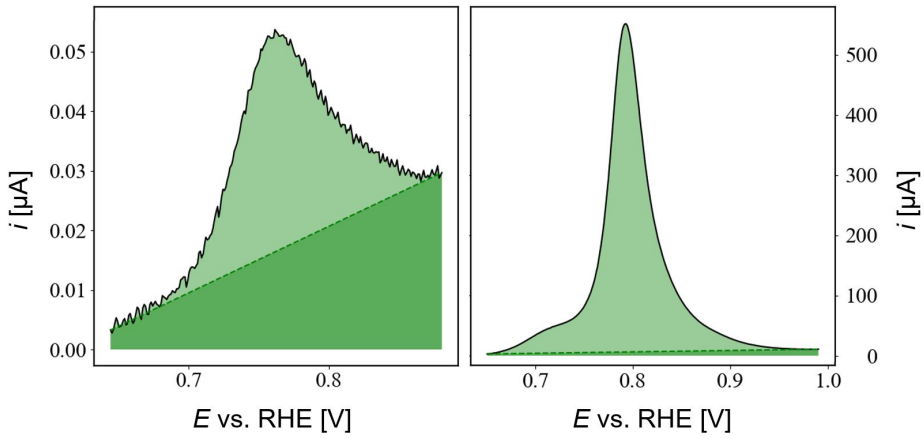

Figure 5.4: CO-strip peaks of 3.8 nm Pt nanoparticles with a loading of 13 ng cm^{-2} (left) and commercially available Pt/C with a loading of 0.1 mg cm^{-2} (right). The peaks (light green) are the strip peaks including background subtraction, giving a lower bound estimate on the number of active Pt sites. By including the entire background (the dark green region) an upper bound estimate is obtained. Figure adapted from [49].

table 5.1.

To validate the CO-strip procedure, the experimental results were compared with the deposited Pt loadings. In figure 5.5 the measured CO-strip charges are compared to the loading deposited either via the cluster source (blue: small raster, green: large raster) or via dropcasting (red). The loading range up to 5000 ng cm^{-2} is seen in 5.5(a), where also a simulation, a linear fit and a spherical approximation are co-plotted. The entire range of loading is plottet in (b). For the present analysis, focus will be on the nanoparticles with small raster pattern, since the ones with large raster pattern and particularly the commercial Pt/C cannot be expected to follow the same trend line. In the region of 0-200 ng cm^{-2} (inset) where particle-particle overlap is expected to be minimal, a linear fit was made. The linear fit is in good agreement with the data points for the small raster pattern up to 1000 ng cm^{-2}, after which the measured strip charge vs. loading tapers off, ascribed to increased particle-particle overlap causing loss of surface area. Notably, the three green points for large raster pattern have slightly higher strip-charge than their equivalent loadings with small raster pattern, consistent with a higher dispersion leading to less particle-particle overlap.

Spherical Approximation

The expected strip charge $Q_{\mathrm{CO,tot.}}$ as a function of loading (L, i.e. ng cm^{-2}) can be estimated via eq. (5.4), where the deposition area is given by A_{geo}, r_{particle} is the radius of a single nanoparticle (i.e. 1.9 nm), ρ_{Pt} is the mass density of Pt

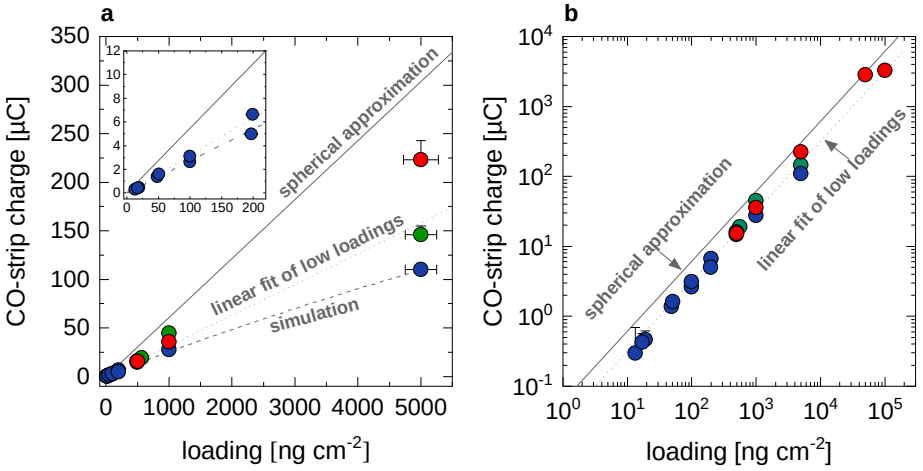

Figure 5.5: (a) CO-strip charge versus Pt loading: Low loading range including simulated values, spherical approximation and a linear fit for low loadings (line fitted at 13-200 ng cm^{-2}, seen in inset). (b) The entire range of loadings. Red dots denote commercial Pt/C while blue and green dots denote 3.8 nm Pt nanoparticle deposited with small and large raster patterns, respectively. Figure adapted from [49].

and $\sigma_{\mathrm{CO,Pt}}$ is the surface charge density of CO adsorbed on Pt.

$$Q_{\mathrm{CO,tot.}}(L) = \frac{3\,\sigma_{\mathrm{CO,Pt}}\,L\,A_{\mathrm{geo}}}{\rho_{\mathrm{Pt}}\,r_{\mathrm{particle}}} \tag{5.4}$$

The expression is derived with the underlying assumption that particles are completely spherical and well dispersed and thus have no loss of surface area due to overlap nor increase of surface area due to facets. The requirement about dispersion may in fact be relaxed, but the spheres should then required to be "hard", so that no adjacent spheres suffer any loss of area from agglomeration. Since this relation includes no area loss due to particle overlap with other paticles or with the substrate, it is expected to be an upper bound of $Q_{\mathrm{CO,tot.}}$ versus L, consistent with what is seen in figure 5.5. For the spherical approximation plotted here, the theoretical value of $\sigma_{\mathrm{CO,Pt}} = 420\ \mu\mathrm{C\ cm}_{\mathrm{Pt}}^{-2}$ is used. This value may, however, vary with the potential under which CO adsorbs, the electrolyte, and the Pt surface structure and is realistically somewhat lower.[53,55,57]

Particle-Overlap Simulation

A more realistic prediction of $Q_{\mathrm{CO,tot.}}$ was obtained with a simulation taking area loss due to overlap into account. The details of the simulation can be seen in the SI. In brief, a number of particles are randomly distributed within a deposition area, characterized by a set of spatial (X, Y)-coordinates (in correspondance with L). If a particle lands at a set of (X, Y)-coordinates sufficiently close to another particle (overlapping by more than 0.3 nm) it is moved up

(Z-coordinate) until the two particles are only tangent (edge to edge distance is zero). Assuming identical, spherical particles, a total surface area is found. All neighboring particles within a certain distance (0.5 nm) of each other, based on their (X, Y, Z)-coordinates, are ascribed a loss of surface area which emulates the particle-particle overlap. Furthermore, all particles at Z=0 are ascribed a loss of area due to particle-substrate overlap. To find appropriate values for the area lost due to the two types of overlap, the simulation is initially fitted to the data. In the region 0-200 ng cm^{-2} the particle-substrate area-parameter is found, as this loss dominates here. Conversely, particle-particle overlap dominates at higher coverages and thus the particle-particle area-parameter is found by fitting to this region. For consistency the simulation is only performed for the samples with small raster pattern.

Unsurprisingly, the simulation matches somewhat better than the linear fit, but the difference would presumably be even clearer at loadings higher than 5000 ng cm^{-2}. However, since no cluster source samples with higher loadings were made, simply extending the simulation region would be highly speculative and outside the scope of the investigation. The observed $Q_{\mathrm{CO,tot.}}$ vs. L behaves quite linearly even up to ≈1000 ng cm^{-2} (roughly half a monolayer with the small raster pattern), which could indicate that the particles act somewhat like "hard" objects. The spherical approximation clearly overestimates $Q_{\mathrm{CO,tot.}}$ already from the lowest loadings. This could be ascribed to $\sigma_{\mathrm{CO,Pt}} = 420$ μC cm^{-2} being on the high side or that particle-substrate overlap is non-negligible, or perhaps both. The Pt/C samples consists of Pt particles dispersed on a high surface area carbon support and are thus expected to suffer little from from particle-particle overlap even at high loadings, consistent with what can be seen in figure 5.5. In summary, the CO-strip charge and the deposited Pt loading are internally consistent, especially for the well-defined cluster source samples. At loadings below ≈1000 ng cm^{-2} the linear fit offers a good approximation, whereas the particle-overlap simulation can additionally also account for the $Q_{\mathrm{CO,tot.}}$ of the highest loading considered.

5.4.4 HER Activity & Mass-Transport Limitations

With all the legwork done, the experimental results are now to be discussed. First up, the shortcomings of extrinsic activity metrics will be exemplified. Hereafter the intrinsic activities will be assessed and used to argue for the superiority of Pt over all other HER catalyst, despite still being mass-transport limited.

Extrinsic Activity Metrics

To demonstrate the fallacy of reporting $\eta_{10\ \mathrm{mA\ cm^{-2}}}$ without consideration for loading, figure 5.6(a) shows the CVs for a representative set of Pt loadings. Both samples of 3.8 nm nanoparticles with small raster pattern (blue lines) and commercial Pt/C (red lines) are shown here. As seen from the figure, the over-

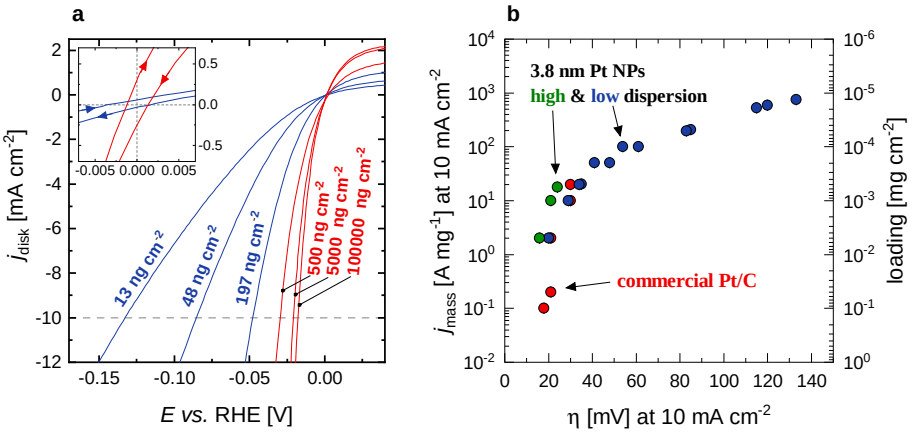

Figure 5.6: (a) Cathodic scan of HER CVs for a representative subset of samples showing that a lower overpotential at a certain current density can be obtained by a higher catalyst loading. Blue lines correspond to 3.8 nm nanoparticles (small raster pattern) and red is commercial Pt/C. The inset shows both anodic and cathodic scans with a negligible spread around (0,0) indicating correct potential scale calibration and a negligible contribution from non-faradaic currents. (b) Overview of all samples showing how an overpotential required to reach a certain geometric current density (η on horizontal axis) can be lowered by applying a higher catalyst loading. When approaching the limit of j_{d} for a full-sized disk then η, however, is not reduced further but j_{mass} keeps dropping. In fact, a higher loading (right vertical axis) at a fixed j_{geo} necessarily leads to a lower mass-activity in general. Figure adapted from [49].

potential $\eta_{10\,\mathrm{mA\,cm^{-2}}}$ can easily be reduced simply by increasing the loading, for exactly the same catalyst. This underlines that the geometric current density alone is not a useful measure for activity. For instance, $\eta_{10\,\mathrm{mA\,cm^{-2}}}$ varies by almost 0.1 V between 13 and 197 ng cm^{-2}, which are otherwise identical. It is worth noting that the geometric current density here is denoted j_{disk} as the current here is normalized to the geometric area of the entire GCE disk. The small raster pattern over which the Pt nanoparticles are dispersed is, however, considerably smaller than the disk. Thereby j_{disk} somewhat underestimates the actual geometric current density of samples with the small raster pattern. For the Pt/C samples this normalization is more accurate, provided that the dropcasted ink is well-dispersed over the entire disk, although, this might not always be the case. The inset shows CVs of the lowest and highest loading, which at appropriate scan speeds (50 and 10 mV s^{-1}, respectively) have a negligible spread between the anodic and cathodic sweep around (0,0).

Figure 5.6(b) shows an overview of all samples in this study, given as a map of mass activity (j_{mass}, i.e. current normalized by Pt mass deposited) vs. η at the point where j_{disk}=10 mA cm^{-2}. Again, red denotes Pt/C while blue and green represent the nanoparticles deposited with small and large raster patterns, respectively. This plot also confirms the trend, that $\eta_{10\,\mathrm{mA\,cm^{-2}}}$ can be reduced by increasing Pt loading - again the reason is obviously that the number of catalytically active sites is what matters. Another point is also exemplified here:

Decreasing the overpotential comes with a cost of a lower mass activity. In the case where mass activity is assessed at a fixed current density, this is a natural consequence of their mutual connection, that is $j_{\mathrm{mass}} = j_{\mathrm{geo}}\, L^{-1}$.

On another note, the commercial Pt/C samples have a larger particle size-distribution than the samples deposited using the cluster source. Furthermore, the Pt nanoparticles in the Pt/C catalyst are dispersed on a high surface area carbon support. This can be seen in the STEM-image in figure 5.7(b) where the dense Pt particles are seen and the less dense carbon support is not. In this image the particle sizes vary in the range of ∼1-5 nm. This essentially means that the samples are not quite like the mass-selected nanoparticles. Nevertheless, the Pt/C and mass-selected samples with small raster pattern overlap quite well at the points L=(500, 1000 and 5000) ng cm^{-2}, as depicted in figure 5.6(b). The three samples deposited with a large raster pattern (green points) show a lower overpotential, than their counter parts with smaller raster pattern but of comparable loading. This enhanced performance could be attributed to a smaller loss of electrochemically active surface area (ECSA), since more dispersed nanoparticles might suffer less from particle-particle overlap. While this might be a contributing factor, it will in the following section be demonstrated that it is not the main reason. This is an example where j_{mass} fails as an activity metric (although it is still better than j_{geo}) - it does not account for dispersion of the catalyst nor intrinsic activity of the catalyst.

Given two arbitrary samples of same loading and intrinsic activity, but differing particle sizes, the j_{mass} would asses the catalyst of smaller particles size as superior, given the higher ECSA per mass. In terms of intrinsic activity, this is naturally a false conclusion. There is, however, another more practical perspective worth considering: a redeeming quality of j_{mass} is it's techno-economic relevance. Since the catalyst material must be paid for in e.g. \$ g^{-1}, a high mass activity could be argued as an important metric when considering technology scale-up. But for any meaningful comparison, the measured j_{mass} must be free of mass-transport limitations, a fact often neglected c.f. the common pitfalls. Although it is well documented that acidic HER measured with RDE is completely mass-transport limited for extended surfaces (or high loadings) of Pt[105,106], novel catalyst reported in literature are often compared to "reference samples" of e.g. Pt/C.[97,99] When normalizing both the novel catalyst (typically of lower loading) and the mass-transport limited Pt/C, the novel catalyst may exhibit a j_{mass} comparable or better to that of Pt/C. By extension the false conclusion is made, that a catalyst on par with Pt is found. This "reference-sample fallacy" is exemplified in figure 5.7(a), where two otherwise identical Pt samples of different loading show a vastly differing j_{mass}, in favor of the low loading sample.

In cases where an estimate of intrinsic activity is for some reason unattainable, the mass activity may still be somewhat useful for comparison. For this purpose figure 5.6(b) provides a measure of j_{mass} for samples spanning four orders of

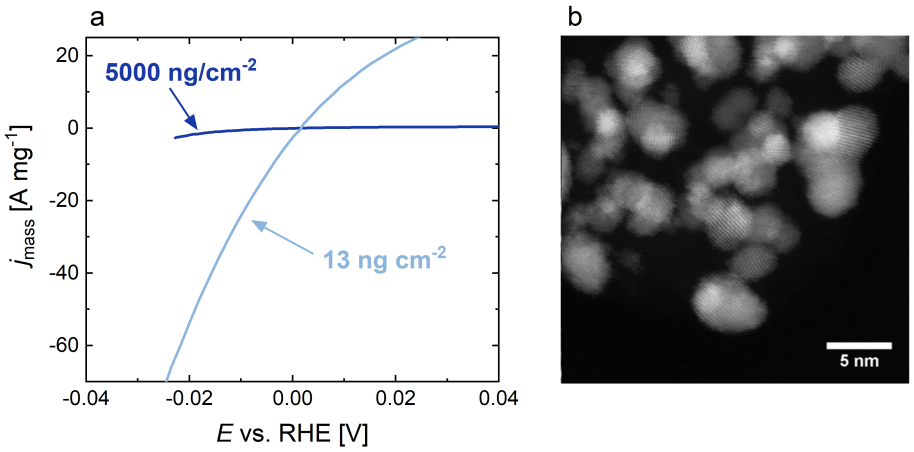

Figure 5.7: (a) Mass-activity of two samples of 3.8 nm Pt nanoparticles deposited with a small raster pattern, which are identical except for their loading. Due to mass-transport limitations and possibly loss of ECSA due to overlap, this assessment of activity is biased, favoring the low-loading sample. The large difference in j_{mass} exemplifies the "reference-sample fallacy", whereby any sample can be made to appear more active than a mass-transport limited Pt sample of high loading. (b) STEM image (300 kV) of Pt nanoparticles in a commercial Pt/C catalyst, where a broad size distribution of ∼1-5 nm is observed. Figures adapted from [49].

magnitude in loading. Thereby a sample of any loading can be compared to a Pt sample of a similar loading. This does not eliminate the issue of mass-transport limitations for high loadings, but gives a more direct comparison in which the relative impact of this should matter less. Even better is the current density normalized by ECSA (j_{ECSA}). This is essentially an intrinsic measure and an alternative to TOF, but may rely on indirect estimates of ECSA. In the case ECSA can be measured precisely, by extension the number of sites are most likely known too, and TOF may then be used instead.

Intrinsic Activity & Mass-Transport Limitations

As mentioned already, Pt is completely limited for HER (and HOR) in acid at high loadings/coverages - but what happens if the applied loading is decreased? The net amount of H_2 produced and H^+ consumed should go down (reverse for HOR), which is also indicated by the lower j_{geo} in the CVs shown back in figure 5.6. Following this reasoning, samples of lower loading should then be less limited by mass transport. This is the key argument for depositing samples with ultra-low Pt loadings for this study.

The turnover frequency (TOF) is *the* metric for intrinsic activity of a catalyst and describes how many reactions (e.g. H_2 molecules evolved) happen per time per catalytically active site[122]. The reaction rate is given via the HER current (i) measured in a CV and the charge transfer involved in each process (q_{HER}). The number of active sites can be found using a CO-stripping experiment as

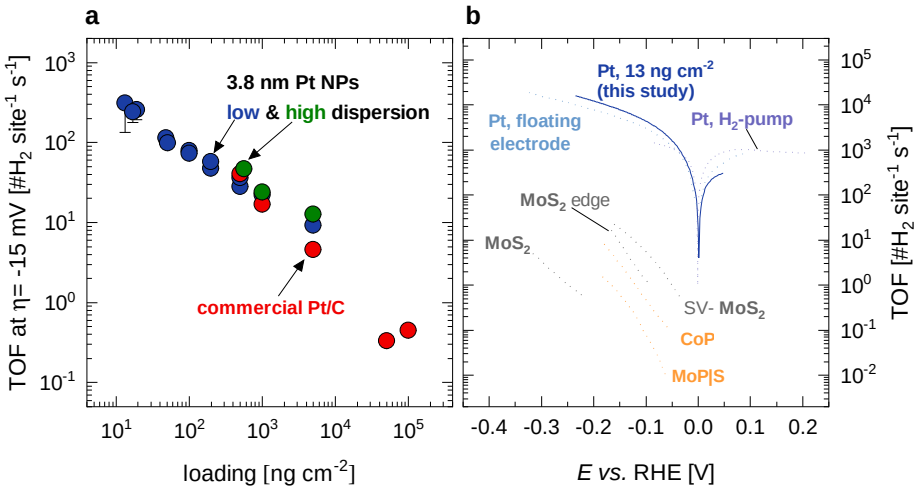

Figure 5.8: (a) TOF at η = -15 mV for every samples. The TOF increases with decreasing loading, indicating mass-transport limitation all the way down to the lowest loading. Lower error bars on the TOF is estimated from the upper bound of $Q_{\mathrm{CO,tot.}}$ and are within the marker size for all but the three lowest loadings. (b) TOF vs. potential plottet for the lowest loading (13 ng cm^{-2}) together with literature data. The lowest loading sample performs at the same level or better than Pt in high mass-transport setups such as the H_2-pump and floating electrode techniques. Some representative non-noble catalyst are co-plottet showing at least three orders of magnitude lower activities. Data adapted from: floating electrode[113], H_2-pump[109], MoS_2 edge[88,121], MoS_2[96], SV-MoS_2[96], CoP[121], MoP|S[94]. Figure adapted from [49].

previously discussed. The total integrated charge ($Q_{\mathrm{CO,tot.}}$) of a CO-strip peak and the charge transfer involved in each process (q_{CO}) gives the number of sites. Since both HER and CO-stripping are two-electron processes, the TOF is simply given by the HER current and the integrated strip charge, as seen in eq. (5.5).

$$\mathrm{TOF} = \frac{\#\mathrm{H_2}}{\mathrm{site^{-1}s^{-1}}} = \frac{i/q_{\mathrm{HER}}}{Q_{\mathrm{CO,tot.}}/q_{\mathrm{CO}}} = \frac{i}{Q_{\mathrm{CO,tot.}}} \tag{5.5}$$

Using the CO-strip the TOF is thereby found for each sample, and is plotted versus loading at the potential η= 15 mV in figure 5.8(a). The TOF drastically increases for decreasing loadings despite the same driving force for the reaction is applied, which indicates a significant mass-transport limitation. For the samples of Pt loadings roughly corresponding to a Pt monolayer or more ($\approx$ 2000 ng cm^{-2} and above for small raster pattern), this is expected given the previously discussed diffusion overpotential. Nevertheless, the trend continues in the same manner all the way to the lowest loading of 13 ng cm^{-2}, corresponding to less than 1% of a monolayer Pt. This has some significant implications: By decreasing the loading (and thus the number of active sites) the *relative* impact of mass-transport can be decreased. This approach might be advantageous both for RDE measurements and other techniques. The purely diffusion limited current of an RDE scales with $\omega^{1/2}$, and since there are practical limitations to

how high ω can be, decreasing the catalyst loading is an additional knob to turn. Furthermore, since no obvious limit is reached for the TOF at ultra-low loadings, there is no reason to believe that the influence of mass-transport is eliminated here - so even in this extreme limit, HER on platinum is still too fast to be measured with an RDE. Given the slightly higher TOFs for the large raster samples (green) compared to the small raster samples (blue) of comparable loading, it seems that the higher dispersion enhances the performance. This is ascribed to a relatively more efficient mass-transport for dispersed particles, analogous with the loading-effect. It is likely that the dispersion over a greater area simply allows a larger net rate of transport (similar to what would be expected by increasing the area of Pt disk) even though the local coverage might be less than a monolayer within this area. One can eliminate that this slightly enhanced performance stems from large raster samples suffering less from a loss of ECSA due to particle overlap, since the TOF is explicitly normalized by the number of active sites.

In figure 5.8 (b) TOF versus E for the lowest loading cluster source sample (13 ng cm^{-2}) is plotted along with other reported measurements of Pt activity using high mass-transport techniques, namely the floating electrode[113] and H_2-pump[109] techniques. Remarkably, this low loading sample, measured with RDE, shows higher HER activity than both of the high mass-transport techniques. Thus it is perhaps the highest intrinsic Pt activity ever measured at room temperature in any experimental setup. This measurement is likely still limited by mass-transport, given the observations in figure 5.8 (a), giving rise to some important points: Firstly, even the high mass-transport techniques must still be limited by mass-transport and as a consequence, the true intrinsic activity of Pt is still underestimated. The floating electrode and H_2-pump techniques, however, still perform better in the HOR region, presumably due to the overall higher transport rate of H_2 to the catalyst. Secondly, a representative selection of TOFs for earth-abundant catalyst are also plotted, showing that these catalysts generally have activities that are at least three orders of magnitude below that of Pt. This important point is not conveyed when reporting e.g. j_{geo} and $\eta_{10\,\text{mA}\,\text{cm}^{-2}}$, underlining the need for reporting intrinsic activities. It would be interesting to try the approach of gradually decreasing the Pt loading to the H_2-pump and floating electrode techniques, since the total mass-transport rate of these are higher than for an RDE. Perhaps, the true intrinsic activity of Pt might then be found, in which case a plot like the one in fig. 5.8(a) should reach a plateau at some sufficiently low loading. It is also worth considering the more general application of this: less active catalyst may also suffer from mass-transport limitations if their loading (and hence their net reaction rate) is sufficiently high. At least for high-coverage samples approaching the diffusion overpotential curve it would be fruitful to test the extent of mass-transport limitation - either by this loading approach or by other means.

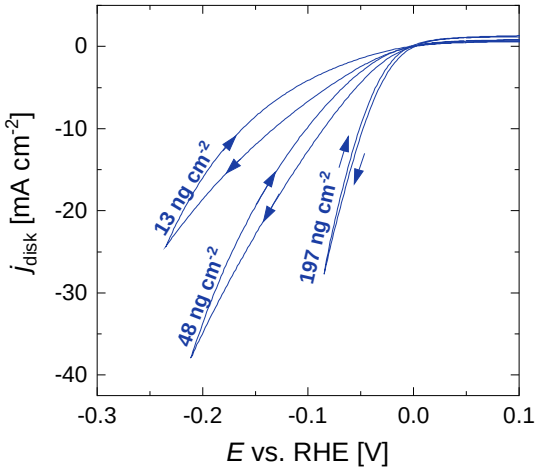

Figure 5.9: Hysteresis in the HER region for low Pt loadings of 3.8 nm nanoparticles deposited with small raster pattern. Arrows indicate the denote of CV scans, indicating the activity during the return sweep (anodic) is lower than the cathodic sweep. The effect seems lager with lower loadings, but the cathodic scan limit also differs, likely playing a role. Figure adapted from [49].

5.4.5 Hysteresis During HER

For the samples with ultra-low Pt loading (around 100 ng cm^{-2} or less) a hysteresis phenomenon of the HER CVs was observed, whereby the current in the anodic scan was lower than the previous cathodic scan, as seen in figure 5.9. The significant difference in activity is primarily seen well into the HER region which together with the low sample roughness means this phenomenon is not due to double layer charging. The effect also seems most pronounced for low loadings, although this hypothesis has not been rigorously tested. The cathodic (E_c) and anodic (E_a) vertex potentials also influence the degree of hysteresis, although the effect is not fully understood yet. The hypothesized cause of the hysteresis is that some effect reduces the net reaction rate by impeding the mass-transport, for instance by hydrogen build up and oversaturation. The argument for this is that the low-loading samples operate at extremely high TOFs, and hence a large local H_2-concentration could be imagined. This could presumably result in slowing down the removal of H_2 and supply of H^+ or lead to micro bubbles blocking active sites.[105,106,123] A high concentration of H_2 could also lead to a Nernst shift, decreasing the HER current. It could also be a sign of trace contaminants adsorbing and blocking sites, which at very low loadings could potentially have a significant impact. Despite rigorous cleaning of glassware and other equipment this is not easily ruled out without further studies, perhaps including ICP-MS measurements. The high activity and hysteresis of low-loading samples has been observed to have a transient nature, in that the current (and hysteresis) may decrease over a few cycles. This has practically been prevented by setting E_a= 1.0 V vs. RHE, at which

the HER performance is stable over multiple cycles. Decreasing to E_a= 0.2 V vs. RHE results in a gradually decreasing performance for the lowest loadings - i.e. the *anodic* potential limit influences the subsequent *cathodic* current. This is consistent with a H_2-buildup, since a longer time at anodic potentials allows more H_2 to be removed, either via HOR or by transport. The dependence on anodic limit could, however, also be consistent with trace contaminats gradually adsorbing and hence blocking active sites. Upon scanning sufficiently anodic the adsorbated might be stripped off, which could explain why the high E_a limit yeilds stable HER currents but the lower E_a does not. It is plausible that additional experiments such as potential steps or combined CV-CA might further elucidate the cause. Even though the exact cause it not yet known, the hysteresis phenomenon has been qualitatively investigated with simulations using a numerical diffusion model.

Hysteresis Model

The simulation revolves around the general Butler-Volmer equation (5.6) where the surface concentrations C^s of H_2 and H^+ are included. This formulation is equivalent to eq. (2.15), but written here in terms of the electrode potential (E) and the standard equilibrium potential $E^0_{\text{eq.}}$. The activity is given in terms of a geometric current density, since the mass-transport is essentially a flux of species to and from the projected area (A_{geo}) of the Pt in this planar diffusion approach. Furthermore, $f = F/RT$, n=2, k^0_{geo} is the intrinsic rate constant and α is the symmetry coefficient.

$$j_{\text{geo}} = nFk^0_{\text{geo}} \left(C^s_{\text{H}_2} e^{\alpha n f (E - E^0_{\text{eq.}})} - C^s_{\text{H}^+} e^{-(1-\alpha) n f (E - E^0_{\text{eq.}})} \right) \tag{5.6}$$

Since the model seeks to capture a time-dependent phenomenon, hypothesized to be concentration related, the crucial part of the model is the time-dependence on the concentrations at the surface (C^s_i), which is balanced by the reaction rates and mass-transport rates given by eqs. (5.7, 5.8).

$$\frac{dC^s_{\text{H}_2}}{dt} = \frac{1}{h_{\text{H}_2}} \left(-\frac{j_{\text{geo}}}{2F} - k_{d,\text{H}_2} (C^s_{\text{H}_2} - C^*_{\text{H}_2}) \right) \tag{5.7}$$

$$\frac{dC^s_{\text{H}^+}}{dt} = \frac{1}{h_{\text{H}^+}} \left(\frac{j_{\text{geo}}}{F} - k_{d,\text{H}^+} (C^s_{\text{H}^+} - C^*_{\text{H}^+}) \right) \tag{5.8}$$

The mass-transport rates $k_{d,i}$ of species i are given by the Levich equation (3.1) and contain the dependence on diffusion coefficients (D_i) and rotation rate (ω); C^*_i are the bulk concentrations and h_i are the characteristic diffusion length scales (see SI of [49] for details). These coupled differential equations are solved numerically with the potential $E(t)$ varying like a CV and with the initial conditions: $C^s_{\text{H}_2}(t=0) = C^*_{\text{H}_2}$, $C^s_{\text{H}^+}(t=0) = C^*_{\text{H}^+}$ and $E(t=0) = 0$.

For the samples presenting hysteresis, the Pt coverage is significantly smaller than a monolayer and the raster area is smaller than the GCE disk. For these

reasons neither A_{disk}, nor the ECSA can be expected to accurately represent A_{geo}. Therefore, the limiting density of the HOR branch was used to estimate the effective A_{geo} of each sample, given by eq. (5.9), where $i_{l,\text{HOR}}$ is the measured limiting current at 0.2 V vs. RHE for each sample and $j_{l,\text{HOR}}$ is the limiting current density of a full sized Pt disk.

$$A_{\text{geo}} = \frac{i_{l,\text{HOR}}}{j_{l,\text{HOR}}} \tag{5.9}$$

Using this normalization, the experimentally measured j_{geo} vs. E is shown in figure 5.10(a) for the samples considered together with concentration overpotential (j_{d}, black line). At 5000 ng cm^{-2}, the CV shows no hysteresis in the HER branch and follows the predicted diffusion limited current j_d, which is expected given the projected Pt coverage in the monolayer range. Already at 498 ng cm^{-2}, the CV bends off from the trend of j_d, exhibiting a lower current density. The same can be observed with an increasing degree for the lower loadings (100, 48 and 13 ng cm^{-2}). The degree of hysteresis also increases with lower loading but the difference in the cathodic vertex potential to which they are scanned may also play a role.

In figure 5.10(b) the simulations of CVs going to the same vertex potential as the experimental samples of the same color are shown. From highest to lowest loading, all curves coincide with the concetration overpotential of j_d. Note that the simulations for the two lowest loadings actually reach the limiting HER current density due to the extremely high values of j_{geo} predicted for these applied overpotentials, hence the flattening of the CVs. Although the experimental CVs do taper off, they do not reach a plateau, contrary to this prediction. This means the experiments deviate from the expected concentration overpotential and actually perform at a slower rate than expected. The inset shows the hydrogen concentration at the catalyst surface during the time of the CV scan. The concentration goes significantly beyond the soluble concentration, e.g. roughly three orders of magnitude above for the simulations of the two lowest loadings. Nevertheless, there is no hysteresis predicted within this parameter space.

The bulk diffusion coefficients are valid for dilute concentrations, but whether they apply at high concentrations of H_2 is to my knowledge not known. If in fact supersaturation of H_2 or micro bubbles is the origin of the hysteresis, it is conceivable that the diffusion coefficient might be lowered due to this. It is also plausible that it is not the actual diffusion coefficient that is lowered, but that the effect (whatever it may be) is equivalent. Thus the prospect of scaled (effective) diffusion coefficients was investigated. Figure 5.10 (c) shows the simulation when scalings of the diffusion coefficients are applied giving lower effective diffusion coefficients, specifically the bulk values are scaled down with a factor (a). The stipulated lines show the concentration overpotential predicted for each value of a and the full lines show the numerical simulations. Now hysteresis is observed in the HER: the smaller a is and hence the effective diffusion coefficient of H_2 and H^+, the larger the hysteresis. With these

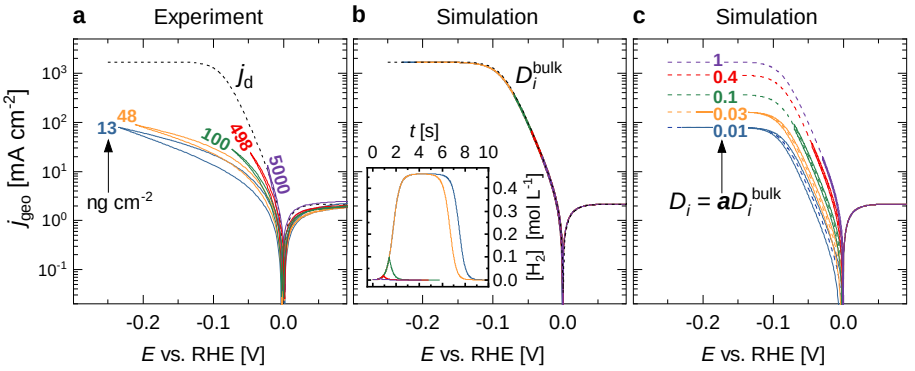

Figure 5.10: Numerical model of hysteresis in HER region: (a) A selection of experimental CVs showing hysteresis. The sample with 5000 ng cm^{-2} follows j_d, but for decreasing loadings j_{geo} tapers off and shows hyseresis. (b) Simulation showing that the low loading samples should in practice reach the limiting $j_{l,HER}$ under the experimental conditions. (c) Simulation employing lower effective diffusion coefficients. This results in hysteresis and lower limiting current densities, but do not quantitatively fit the experiments. Figure adapted from [49].

simulations some of the experimentally observed tendencies can be reproduced by choosing suitable calues of a: namely the simulated current densities which can become much lower than the unpertubed j_d, the hysteresis, and to some degree the bending of the CVs at high overpotentials. Regarding the first point, it is no surprise that lower diffusion coefficients lead to lower diffusion-limited current densities. Regarding the hysteresis, the simulations predict that an effective lowering of mass-transport rates (obtained here by decreasing diffusion coefficients) can to some degree reproduce the experimental phenomenon. This is not conclusive evidence that the actual coefficients are lowered during these extreme experimental conditions (although it seems feasible) but rather an example showing that a slower mass transport *could* lead to hysteresis. Regarding the shape of the CVs it is clear that the simulated ones deviate notably from the experimental one, which could have a wealth of possible explanations. One possible explanation could be as follows: The diffusion coefficients are supposedly concentration-dependent, but should initially be at their standard values given the initial equilibrium condition. As $C^s_{H_2}$ during HER grows faster than the rate of transport can carry H_2 away, the effective coefficients D_{H_2} and D_{H^+} should then *gradually* decrease rather than artificially be scaled down from the start. This gradual transition would presumably give a smoother shape of the CV, more similar to the experimentally observed ones. Including this in the numerical model, would either require specific knowledge of the concentration dependencies of the D_i parameters, which are not presently known, or an educated guess. A power-law model for the concentration dependence on D_i was used for a simulation as well, but provided results only slightly more aligned with the experimentally measured ones (details in SI of [49]). Another explanation could be that proton transport is largely unaffected by the buildup of

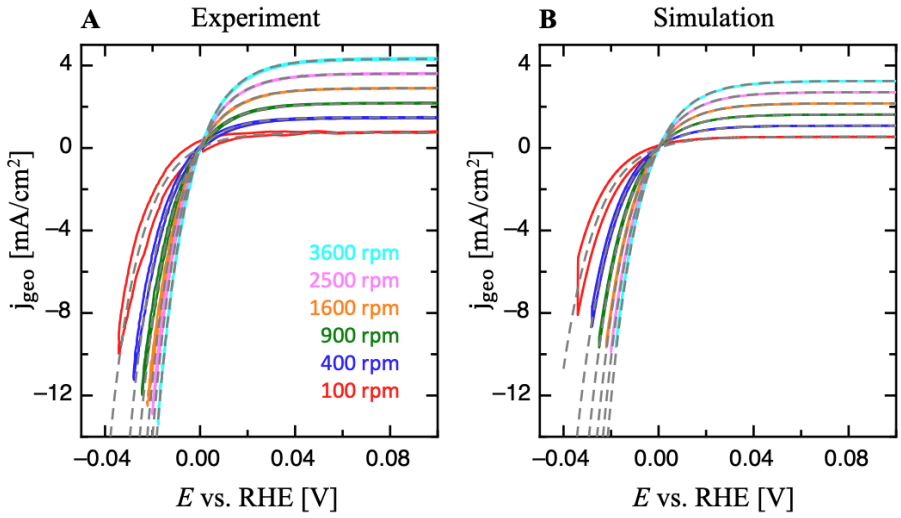

Figure 5.11: Benchmark of the numerical simulation against experimental RDE-data for poly-crystalline Pt disk. (A) Experimentally observed hysteresis of HER CVs varies with ω on a poly-crystalline Pt disk in H_2-saturated 0.1 M $HClO_4$, co-plotted here with j_d for each ω.(B) The numerical simulation reproduces the same hysteresis trend when ω is varied. Notably, a lower rotation rate leads to a higher degree of hysteresis, consistent with the idea that hysteresis is caused by slow mass-transport. Experimental data fro/m [105], courtesy of Bingjun Xu. Figure adapted from [49].

hydrogen and thus only D_{H_2} effectively decreases during HER. This would presumably also eliminate the very abrupt transition to a limiting cathodic current density.

Additionally, the numerical model was benchmarked against data from RDE-experiments reported in literature, in which a poly-crystalline Pt disk showed hysteresis of the HER, which was dependent on the RDE rotation rate.[105] The numeric simulations were performed for the same set of rotation rates (ω, which is contained in $k_{d,i}$). As seen in figure 5.11 the trend of the experiments is qualitatively captured by the numerical model. The slight quantitative discrepancies are attributed to the uncertainties in the parameters $C^*_{H_2}$, $D^*_{H_2}$, $D^*_{H^+}$ and kinematic viscosity (ν_{kin}) pertaining to the electrolyte used in the study (0.1 M $HClO_4$), which were approximated by the ones known for 0.5 M H_2SO_4.[104,108] The numerical model thereby seems to have a predictive quality that is more general than what can be obtain when artificially scaling the diffusion coefficients. This does, however, not confirm the validity of scaling the diffusion coefficients, but it does support the notion that mass-transport limitations could result in hysteresis.

5.5 Conclusion & Outlook

Some of the common pitfalls in HER literature have been pointed out, in particular those concerned with neglecting mass-transport limitations or reporting e.g. $\eta_{10\,\mathrm{mA\,cm^{-2}}}$ without regard for the catalyst loading. By testing Pt catalysts at a large range of loadings and measuring the intrinsic activity several interesting points are observed: decreasing the catalyst loading and hence the number of active sites is shown to be an effective way of limiting the relative impact of mass-transport limitations. The lowest loading studied had a TOF on par (or higher) than high-mass techniques. Still the present RDE measurements can not be shown to be free of mass-transport limitations. This in turn indicates the true intrinsic activity of Pt for HER in acid is still underestimated. Decreasing loadings may be useful in trying to map out the true intrinsic activity of Pt, in particular with high mass-transport techniques such as the floating electrode or H_2-pump. It has also been rationalized that catalyst of lower intrinsic activity may suffer from mass-transport limitations at sufficiently high loadings. It therefore seems prudent to asses the extent of this if the measured j vs. η lies close to the concentration overpotential curve - and if need be, decrease loading. Nevertheless, it has been demonstrated that Pt has at least three orders of magnitude higher intrinsic activity than non-noble alternatives. This also underlines that ΔG_{H} is not a sufficient predictor for HER activity. For ultra-low loadings a hysteresis phenomenon of the HER CVs was observed. Although the exact origin of the effect has not been elucidated it has been argued that it could be related to slow mass-transport and possibly a H_2 oversaturation.

Chapter 6

Developing a Model System for Small Entities

Taking catalysis to the single atom scale is the ultimate limit in several ways: in terms of tuning selectivity, activity and utilizing materials to the fullest extent, small entities appear to show great potential. But in conjunction with this lies a multitude of scientific and technical challenges to be solved. For this reason the work with small catalytic entities is perhaps the most difficult and exciting project I have been working on during my PhD. The work presented in this chapter, both concepts and experiments, is the product of a collaboration between several people primarily from SurfCat but also other groups, to whom credit is due. I have been working on this project throughout my time at SurfCat. From the beginning, I have been working closely with Niklas Mørch Secher, soon joined by Karl Krøjer Toudahl. While they have been working on the cluster source depositions and the associated characterization methods (ISS and XPS), I have worked on the electrochemical measurements on the prepared samples. More recently, Rikke Plougmann and Julius Lucas Needham have joined the cluster-source team as well. Furthermore, Niklas has done STEM-microscopy and XPS data treatment on the synchrotron data which was obtained at the ASTRID2 (Matline) beamline at Aarhus University, thanks to Zheshen Li. Arlette Sohanfo Ngankeu (and initially Miriam Galbiati) have conducted the STM experiments. Arlette's STM experiments have been conducted in Aarhus, made possible by the help of Jill Miwa, Marco Bianchi, Lutz Lammich and Federico Andreatta. Hector Prats Garcia and Sudarshan Vijay from the CatTheory group have performed the STM simulations. Furthermore, Degenhart Hochfilzer and I have designed a modified "sniffer cell" for the electrochemistry-mass spectrometry setup which he is in charge of.

It is evident from the preliminary results (and lack of conclusive results) that this project is very much *unfinished business*. Consequently, I have written this chapter in a manner reflecting it, focusing on the collaborative process

of developing our understanding, the challenges and the opportunities ahead. First, a brief introduction and motivation for single atom catalysts (SACs), and more generally small entities, is due. Then, I will focus on discussing the development of our *model system* and the preliminary results it has led to. Subsequently, I will give an outlook on the future perspectives of the project.

6.1 Small Entities in Brief

For the purpose of the present discussion, *small entities* shall be defined as entities ranging in size from a single atom to a small cluster consisting of a countable number of atoms. The experimental results reported here pertain to single atoms, dimers and trimers (clusters of two and three atoms, respectively), hence a more rigorous definition on the upper size bound is not strictly necessary.

6.1.1 Motivation & Challenges

As pointed out in chapters 2 and 4 small entities such as single atom catalysts (SACs) show interesting properties of relevance for electrochemical energy conversion and synthesis of sustainable chemicals. Especially single atoms, and to some extent dimers, have recently attracted a lot of attention as potential catalysts for various reactions such as ORR (both $2e^-$ and $4e^-$), OER, CO2RR and HER[48,84,102,124–127]. Single atoms have complete material utilization, since all atoms are exposed as active sites. Since catalyst cost may be a major obstacle in the scale-up of technologies, the cost-effectiveness of SACs and small entities is highly desirable[23,30]. Additionally, SACs have a uniform type of active sites as opposed to nanoparticles, which display various facets, edges and kinks. This potentially allows for optimizing the properties of all active sites simultaneously, as they are identical. This could lead to more active catalysts. Small entities may display finite-size effects, differing from what is observed for larger particles, which effectively act as extended surfaces. In this size regime, the clusters are molecular in nature, as they have more discrete electronic energy levels. They may show strong size-dependence on the binding energy of adsorbates, correlated to the coordination number of the binding site. Since small entities are more under-coordinated than larger particles, they generally bind adsorbates stronger.[42,128,129] A key point of interest is to circumvent the known linear scaling relations which impose significant limitations on multiple reactions of interest. In practice, this entails finding catalysts which follow new, more favorable scaling relations, as it is not known whether the scaling relations can be *broken* per se.[32,58] Along the same lines, the selectivity towards desired products may also be optimized, not only via electronic effects but via geometric effects. For instance, breaking the O_2-bond is unfavorable on the Pd SAC described in chapter 4, thus favoring the two-electron pathway of ORR and hence the selectivity toward generating H_2O_2. A primary obstacle in developing such catalysts is stabilizing the small entities. Due to their high surface energy, single atoms, for instance, easily migrate and aggregate into particles. Provid-

ing suitable sites for *anchoring* the atoms is thus essential for maintaining the atomic dispersion.[130] Moreover, since all active sites are in direct contact with the support for small entities, such as single atoms, the support is of major importance for the performance in general[131,132]. Due to this required specificity and the small size scale, thorough characterization is essential but may also be correspondingly more challenging.

6.1.2 Current Strategies

A host of different synthesis methods are employed to achieve these stabilized SACs. Syntheses of single atoms and clusters using UHV-methods have been reported[43,44,46], but in particular for SACs the prevalent synthesis method is via wet-chemical approaches[130]. There are several classifications for SACs and their respective synthesis routes. While the terminology is not universally agreed upon (and in some cases ambiguous), some of the main synthesis strategies are: spatial confinement, defect engineering and coordination design.[130–132] The confinement strategy utilizes porous structures such as zeolites, metal organic frameworks (MOFs) or covalent organic frameworks (COFs) to spatially confine and stabilize single atoms. Typically, a framework of e.g. a MOF is pyrolysed together with precursors and subsequently acid leached giving the SAC confined in a backbone structure. Defect engineering typically relies on oxygen vacancies in metal-oxides to stabilize single atoms, for instance Au in TiO_2 defects[133]. A similar approach has also been reported, where sulfur vacancies in MoS_2 were used to anchor Pt single atoms[134]. Expanding the definition a bit, MoS_2 edge sites have been decorated with Ni single atoms too[102]. The coordination design often relies on a carbon framework where dopants (or defects) such as sulfur, oxygen or nitrogen constitute the coordination environment stabilizing the single atom.[98,131]. These overall strategies allow a large variation of catalysts to be synthesized, however, the resulting structures are often highly complex, and thus detailed characterization is necessary. Multiple complementary techniques are often needed to elucidate the structure.[130,131]

6.2 A Model System - Motivation & Definition

For small entities, the difference of a single atom may completely alter the catalyst characteristics[43,44] and similarly the support material greatly influences the performance.[131] Having a model system with a uniform type of active sites and a high degree of parameter control might lead to better fundamental understanding of SACs. The typical wet-chemical approach relies on a series of complicated reaction steps with multiple precursors, which results in a complex structure requiring extensive characterization. Even so, it is conceivable that the type of active sites is not uniform, e.g. due excess precursor materials remaining in the structure. It might also not be straightforward to identify the number of active sites given the synthesis procedure. Hence, an estimate of intrinsic activity is unattainable unless the number of sites can be accurately

measured experimentally. The alternative to this is a *model system*, which is to some degree the inverse approach. The idea is to have a system with a precise control of parameters within a broad parameter space, allowing experimental findings to be deconvoluted and in turn systematically understood. In the ideal case, one might directly choose to study only the exact parameter of interest, rather than settling for or discarding the entire set of parameters given by a complex synthesis process. Inspired by Niklas' definition of a model sytem[135] I here define a set of key requirements for a model system:

(i) controllable density and preferential synthesis of one type of specified small entity as active species, ideally applicable for a range of relevant materials

(ii) controllable density of anchoring defect sites, ideally with the option to tune the type of site via controlled parameters

(iii) the substrate is highly uniform and characterizable with relevant techniques

(iv) the substrate material(s) and geometry should be compatible with electrochemical methods

Note that the definition coined here is primarily given in terms of the catalyst (active site, defects and support), but it is very much related to having well-controlled and clean methods to synthesize, characterize and test the catalyst. We aimed to start with the simplest conceivable model system, so going for small Pt entities for catalyzing the HER reaction seemed like a sound choice. Nevertheless, the hope was to build a framework of experimental procedures and fundamental understanding, which could be useful for expanding into other future catalyst systems as well. Based on the work of the Nakamura group, we figured that a graphite material with nitrogen defects might provide the appropriate sites for anchoring small Pt entities.[136,137] For generating the small Pt entities, the in-house cluster source was the obvious choice. Hence, we set out to study a model system consisting of platinum single atoms, dimers and trimers (Pt_{1-3}) on highly oriented pyrolytic graphite (HOPG) with incorporated nitrogen defects.

6.2.1 Mass-Selected Clusters

A cluster source system enables deposition of mass-selected cluster and particles of a controllable mass with a narrow distribution.[36,43,44,118,138] The cluster source at our lab is the foundation for creating the small entities such as single atoms, dimers and trimers, which are studied in this project. The term cluster source is here used for the entire ultra-high vacuum (UHV) system used for generating and depositing mass-selected species.

The Cluster Source

An overview of the cluster source system is seen in figure 6.1, showing the main steps of a deposition (from left to right): magnetron sputtering and aggregation

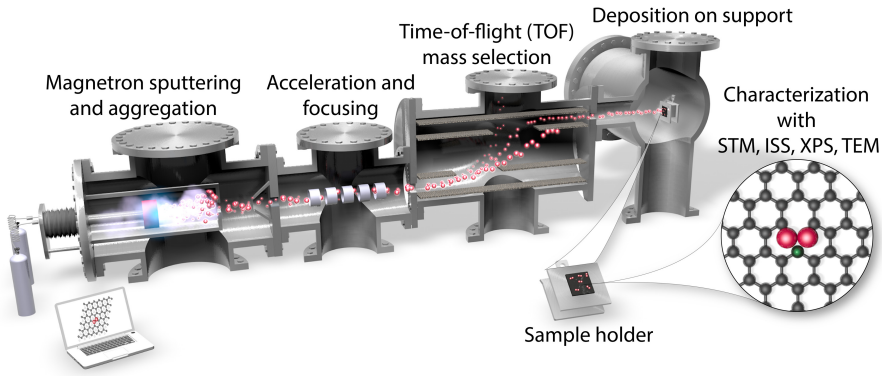

Figure 6.1: Schematic of the cluster source UHV system. From left to right is the: Magnetron sputtering of target and aggregation of the sputtered species, acceleration and focusing of particle beam, time-of-flight mass-selection according to mass/charge ratio and finally deposition on substrate. The system also includes characterization techniques such as ISS and XPS. Figure courtesy of Jakob Kibsgaard.

into clusters, focusing and acceleration of ion beam, mass selection of species and finally deposition onto a substrate. In the first stage, a target of the material desired for deposition undergoes magnetron sputtering and gas-phase aggregation.[139–141] A flow of Ar is applied and a plasma is sparked and sustained in the vicinity of the target surface, leading to a continuous flux of Ar^+ onto the target. This bombardment sputters off atoms from the target which may then undergo a gas-phase aggregation. A flow of He facilitates the aggregation of the entities sputtered off. A differential pressure ensures a gas flow that carries the generated clusters out off the aggregation zone. Next, the clusters are supersonically expanded into the next chamber. A fraction of these are charged and a lens system is used to focus the beam. In the connecting chamber, a time-of-flight (TOF) mass selection is then used to filter the incoming beam[142]. Here electric fields are applied in short pulses whereby charged species experience an acceleration proportional to their mass-to-charge ratio (m/q). By applying pulses of opposing electric field with a short interval the clusters are laterally spread out according to their m/q while maintaining their horizontal velocity. Thereby, only the clusters of the desired m/q exit through the aperture at the end of the TOF-chamber. Finally, the clusters are then deposited onto the substrate. Since a majority of the charged clusters will be singly ionized($q = \pm e$), clusters of a specified mass can then effectively be deposited. Due to the charge carried by the clusters, their deposition onto the substrate may be measured as a current, giving accurate measurements of the deposited loading. Furthermore, the sample may be rastered in a controlled pattern to ensure a homogeneous coverage of clusters over the substrate. Addtionally, it is possible to heat and sputter the substrate with e.g. Ar or NH_3. In conjunction with these synthesis capabilities, the UHV system includes several characterization techniques such as ion scattering spectroscopy (ISS), X-ray photo-electron spectroscopy (XPS)

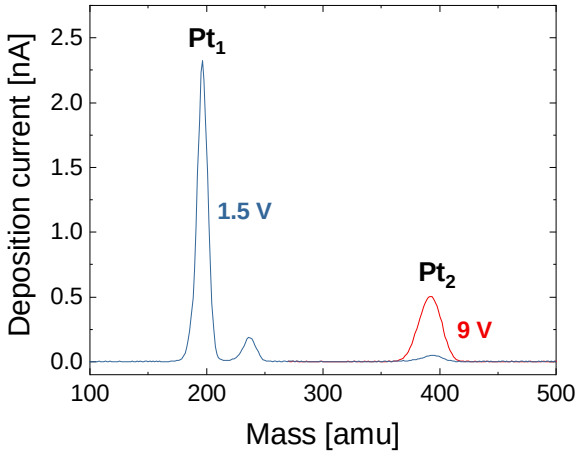

Figure 6.2: Mass scan of Pt_1 and Pt_2 generated in the cluster source. A higher sample bias (9 V) is needed to achieve sufficient deposition currents for Pt_2. The feature at ≈235 amu is a Pt_1Ar cluster.

and CO temperature-programmed desorption (CO-TPD).

Preparation of Samples

Square plates of HOPG (7×7×2 mm^3 SPI-2) are used as substrates. The deposition of Pt in the cluster source uses the following main steps, where the details may vary depending on the purpose.

(i) the HOPG substrate is cleaved multiple times prior to being loaded into the UHV-system, ensuring a clean and atomically flat surface.

(ii) light NH_3-sputtering of the HOPG substrate acting as source of N doping

(iii) the N-doped HOPG is annealed

(iv) either Pt_1, Pt_2 or Pt_3 entities are deposition

Figure 6.2 shows two superimposed mass-scans in the cluster source. By tuning the system parameters, the deposition current for each Pt entity is optimized (maximized). During the deposition all but the chosen m/q ratio is filtered out via the TOF mass filter giving the desired deposition. The Pt-deposition is performed with rastering over a mask ($\varnothing$ = 5 mm orifice), ensuring uniform coverage over a well-defined area of the HOPG.

6.2.2 A Suitable Substrate

Based on the criteria outlined we opted to try graphite-based substrates. Graphite-structures have a good electrical conductivity and may in some cases be highly uniform. It has earlier been reported that nitrogen doping of graphite based

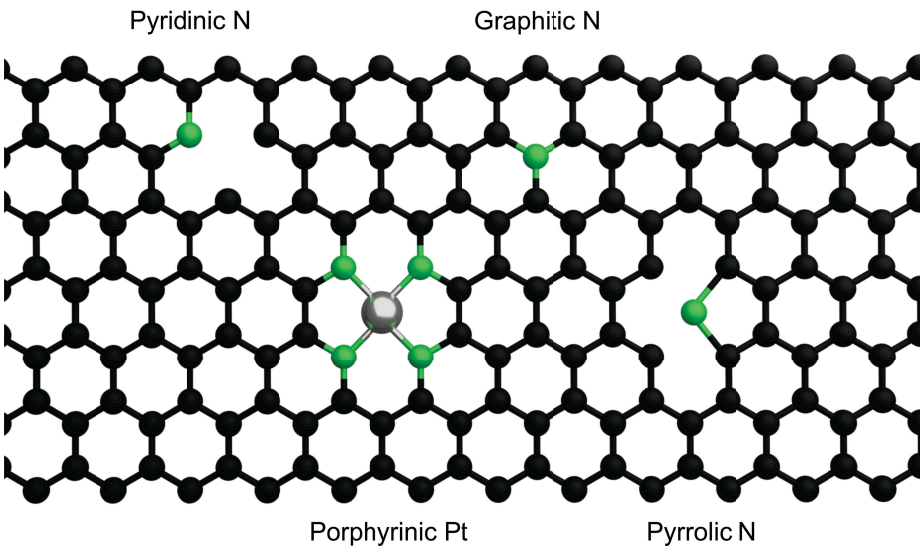

Figure 6.3: Nitrogen defects in hexagonal carbon lattice. Green denotes N-atoms showing pyridinic, graphitic and pyrrolic sites. Furthermore a Pt atom is shown in a porphyrin-like site where it has a four fold pyridinic N coordination.

materials can create structural motifs which by themselves are catalytically active,[143] or which can act as anchoring points for small catalytic entities.[130,136,144] It was therefore originally decided to attempt using graphene, i.e. a single graphite layer, as a substrate. This could potentially combine the possibilities of a graphite-based substrate with the desired range of characterization techniques - in particular TEM/STEM. Working with graphene proved to be challenging already at the first step: obtaining a clean, piece of graphene of a useful size. The attempts using a transfer method to obtain sheets of graphene will be discussed in section 6.3.1. While the possibility of using graphene (for some purposes) is not dropped, focus was turned to an analogous, more robust system: highly oriented pyrolytic graphite (HOPG). Graphene and HOPG are similar insofar they are both crystalline forms of carbon sitting in a hexagonal lattice, where HOPG simply has multiple stacked layers. The term "highly oriented" refers to the fact that the mosaic spread angle between stacked layers is small ($< 1°$ for HOPG). The Nakamura group has reported that well-defined N-defects can be obtained via N_2-sputtering and subsequent annealing and that Pt clusters could be stabilized via N-defects.[136,137] This aligns well with our system of choice and the capabilities of the cluster source, and it was therefore decided to use NH_3-sputtering to generate nitrogen defects in HOPG substrates. N-doping HOPG might lead to a number of different defects. The hope for our approach was that one defect type could preferentially be generated, and that it would be able to stabilize a small Pt entity, be it single atom, dimer or trimer. Figure 6.3 shows some fundamental N-defects of a graphene lattice, namely:

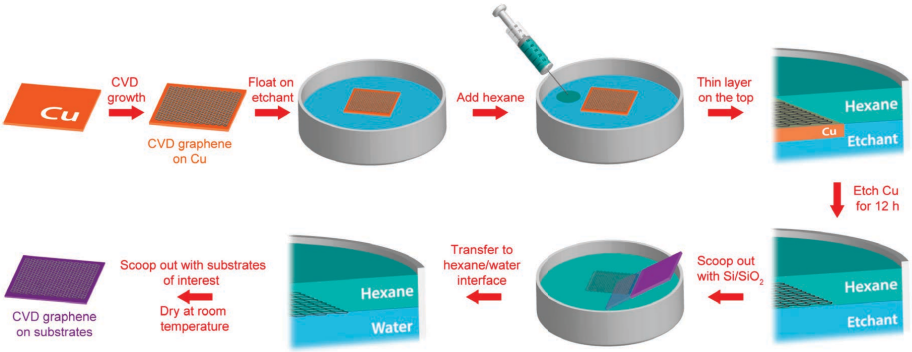

Figure 6.4: Graphene transfer process using the biphasic interface method. A monolayer graphene grown via CVD on a Cu substrate is floating in the interface between ammonium persulfate and hexane. After the Cu substrate is etched away the graphene layer may be scooped up with e.g. a piece of Si. Reprinted with permission from [146]. Copyright 2016 American Chemical Society.

pyridinic, graphitic and pyrrolic nitrogen. Furthermore, four adjacent pyridinic N may create a porphyrin-like structure into which a single atom may be anchored. This is a single-atom coordination environment, which is frequently reported in literature as the active site.[78,98,132,145]

6.3 Developing the Model System

6.3.1 Graphene Transfer

In search of a suitable substrate for a model system, graphene was considered from an early stage. Although the attempts at using graphene as a substrate did not prove successful, it might be worth giving some extra thought. Therefore, I will describe the attempted graphene transfer process and qualify how graphene might compliment the possibilities of the current HOPG-based system. Niklas had previously done TEM-imaging of commercially available grids with monolayer graphene, but found that these substrates were dominated by amorphous carbon and only very small patches of clean graphene could be observed. The in-situ cleaning procedures did not significantly change this, making the use of these substrates pointless.[135] This promted our investigation into alternative options, including the graphene transfer described below. The goal was to transfer monolayers of graphene onto Au TEM grids in a clean manner, which could then act as support for Pt single atoms and dimers deposited using the cluster source and subsequently be imaged using TEM/STEM. The polymer-free graphene transfer method described in [146] was therefore attempted. The method essentially employs a biphasic interface between two liquids where the graphene may be separated from it substrate and transferred to another substrate of choice - without the use polymer capping layers that tend to contaminate the graphene. A schematic overview of the procedure can be seen in figure

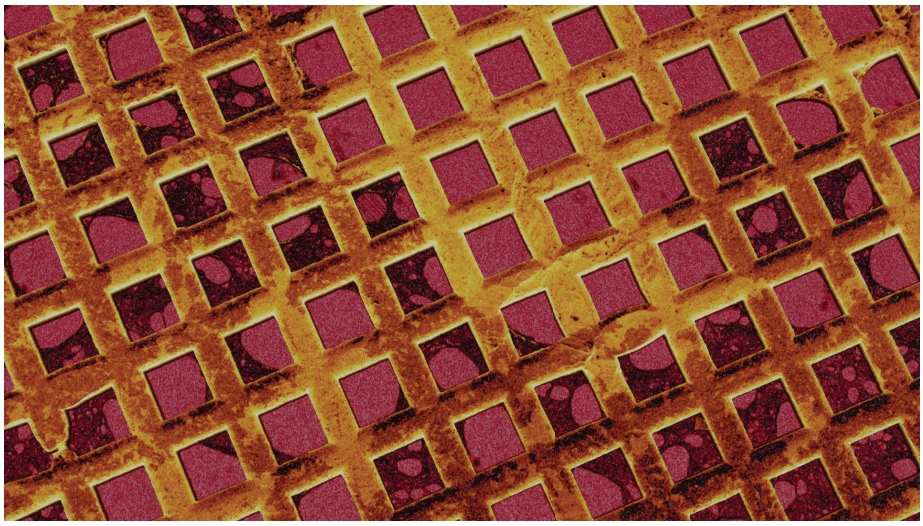

Figure 6.5: SEM image of graphene lifted onto Au grid. For clarity artificial colors were added based on image contrast. The deposited carbon sustance (seen in black) is damaged and not covering the grid (golden color) in a uniform manner. SEM imaging by Niklas.

6.4 and goes as follows. The starting point is a Cu substrate with a monolayer graphene grown by chemical vapor deposition (CVD). The Cu-graphene sheet is placed in an etchant solution (0.1 M ammonium persulfate, $(NH_4)_2S_2O_8$) with the graphene side facing up. Hexane is then carefully added onto the etchant solution where it floats on top and encapsulates the Cu-graphene sheet at the immiscible interface of the liquids. After $\approx$ 12 hours the Cu is etched away and a freestanding graphene layer now lies at the interface. This may gently be scooped out with a piece of Si and transferred to a hexane-water interface to remove debris from the etching process. The role of hexane is to lower the surface tension to prevent the graphene layer from ripping apart. Finally the graphene sheet may then be scooped out with the substrate of choice onto which it adheres.[146]

I attempted this procedure several times using commercially available CVD-grown graphene on Cu sheets (1×1 cm^2, Graphenea). The glass beakers used were thoroughly cleaned in piranha in advance. The Cu-graphene sheets were placed onto the etchant solution and hexane was slowly added with a syringe. Typically after a few hours most of the Cu would already be etched away (as opposed to the expected 12 hours). Most often the graphene layer would be visibly torn already at this stage. Upon scooping up the graphene sheet with either a Si substrate or directly with an Au TEM grid, it generally degraded further. The transfer of an intact sheet of graphene was never accomplished. One of the most "successful" attempts can be seen in the SEM image in figure 6.5. The graphene (black) is ripped apart so that a sheet is no longer identifi-

able on the Au grid (golden color). The cause of the discrepancy between the obtained results and what was reported in [146] was not found. Since the the torn graphene was observed already before the Cu was completely etched, one might speculate that the graphene sheet was of low quality (in terms of grain size) already from the start. It could perhaps also be an uneven etch rate of Cu leading to a strain on some areas of the graphene. If resolved, the method could prove to be a facile way to obtain clean graphene substrates. This could prove useful, since graphene satisfies the criteria set for a substrate, namely points (iii) and (iv) in the definition of a model system: it is compatible with electrochemical methods. Naturally the graphene must be supported on an appropriate material, e.g. a grid, to allow handling. There are RDE-like tips with the ability to support such substrates, although they may be slightly more challenging to work with than conventional RDEs. Furthermore, graphene has a highly uniform and well characterized structure. It is also a common substrate for electron microscopy, which may provide a good contrast to denser elements. In fact, this is where graphene may compliment HOPG, which due to it's typical thickness is not suitable for TEM or STEM. These techniques offer a useful way of characterizing and visualizing the deposited single atoms, dimers and trimers, which is the reason we looked into graphene substrates in the first place. Given the overall similarities between graphene and HOPG, it could therefore be fruitful to make comparable samples on both HOPG and graphene in parallel and then characterize the samples with the techniques appropriate for each of the substrates.

6.3.2 Characterization of Deposited Pt

Given the challenges of working with graphene, focus was shifted toward using HOPG as a substrate. Quite harsh NH_3-sputtering conditions were initially used to generate N-defects in the HOPG. This allowed a sufficient amount of nitrogen to be doped into the carbon lattice to be easily detectable with XPS. An analysis of the N 1s peak of HOPG exposed to 1 keV NH_3-sputtering for 10 minutes showed that the dominating coordination type of N was pyridinic (48%) and pyrrolic (41%) and to a lesser extent graphitic and oxidic N.[135] A similar procedure had also been used with subsequent Pt_1 depositing on a N-doped graphene substrate for STEM imaging. In figure 6.6a the Pt single atoms can be seen as white dots dispersed over the graphene support. This indicates that Pt_1 is somewhat stable on a carbon support with N-defects. The desire to study the coordination environment more in depth called for STM experiments, but we learned that the harsh sputtering roughened the HOPG surface too much to obtain atomic resolution with STM. Following this, milder sputtering conditions (150 eV) were implemented. Sample preparation for STM has been varied depending on the purpose, whereas for samples to be subjected to electrochemical tests, the standard procedure is as follows: cleaving of HOPG substrate, NH_3-sputtering (150 eV), annealing in vacuum (700 °C, 1 hour) and then either left as "blank" or deposition with Pt_1 or Pt_2. The sputtering times were tuned so that coverages of $\approx$ 3% N and $\approx$ 1% Pt were obtained relative

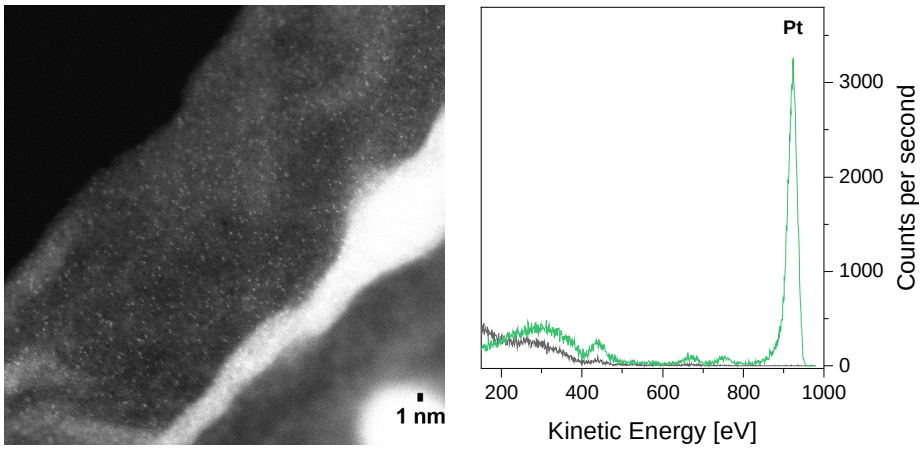

(a) STEM on Pt_1

(b) ISS Pre/post-deposition of N and Pt_1

Figure 6.6: (a) STEM image of 1% Pt_1 on graphene (supported by TEM grid) sputtered with NH_3 (1 keV, 30 minutes). STEM image by Niklas Secher.[135] (b) ISS spectra of blank, freshly cleaved HOPG (gray) and 1% Pt_1, 3% N on HOPG (green). N-doping of HOPG with 150 eV NH_3-sputtering.

to the number of C atoms in the HOPG layer. The argument for having relatively more N than Pt is to ensure that the (potential) anchoring of Pt in e.g. porphyrin sites is not limited by lack of N-defects, potentially resulting in Pt agglomeration. Even lower coverages (both Pt and N) were initially attempted for the electrochemical experiments, but in order to increase the measured signals and minimize the relative impact of potential trace contaminant this was abandoned. Figure 6.6b shows the ISS spectra of a freshly cleaved HOPG (gray) and of 1% Pt_1, 3% N on HOPG (green). The HOPG show the typical broad feature rising slightly above the baseline below $\approx$ 400 eV, which is attributable to carbon, and the otherwise flat spectrum indicates a pristine surface. The deposition of merely 1% Pt_1 gives a significant peak, so the smaller features of the spectrum may for all practical purposes be disregarded. While the ISS measurement (unsurprisingly) corroborates the presence of Pt on the HOPG, a further characterization is needed to elucidate the structure. To this end a series of STM-measurments was performed. The results of this will primarily be discussed in the next section, but one point should be mentioned here. To test the anchoring effect that N-defects are hypothesized to have on Pt, both Pt_1 samples with and without N-defects were made. Figure 6.7a displays an STM image of a HOPG sample with 1% Pt. Without NH_3-sputtering the surface looks pristine, like that of a blank HOPG as seen in figure 6.7b. There is no trace of Pt on the planes of HOPG grains. At the edges, however, lumps of varying sizes appear, which could be agglomerated Pt. It therefore seems that small Pt single atoms are not stable in the absence of N-defects. Whether they in fact are stable in the presence of N-defects is yet to be determined.

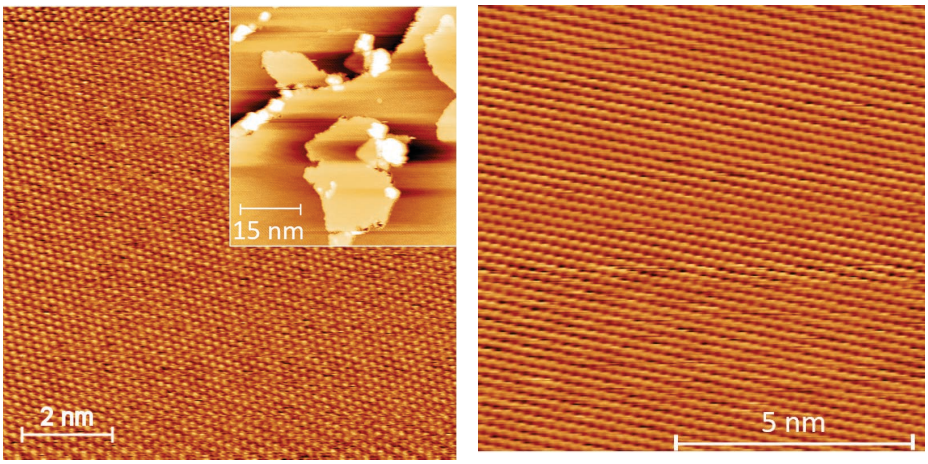

(a) HOPG with 1% Pt.

(b) Blank HOPG

Figure 6.7: (a) STM images showing the effect of anchoring sites. In the absence of NH_3-sputtering the HOPG planes looks pristine. (inset) The bright areas at the edges of HOPG flakes could be due to Pt-agglomeration. STM image by Arlette Ngankeu (b) Blank HOPG (no N). STM image by Miriam Galbiati.

6.3.3 N-doping of HOPG

Some insights and tentative conclusions about the N-defects arising from NH_3-sputtering were brought about by a series of STM-experiments. Figure 6.8 displays STM images of a HOPG sample with 1% Pt_1 and 3% N. After degassing in the STM for 10 minutes at 150 °C the surface displays vague round features, as seen in fig. 6.8a. These structures are ascribed to be the result of NH_3-sputtering, and could perhaps be blisters or domes due to implanted NH_3. After annealing the sample (700 °C, 2 hours) more distinct features emerge, as shown in fig 6.8b. These triangular or star-like defects are consistent with pyridinic N-defects in the carbon lattice, however, graphitic N-defects have a quite similar fingerprint.[137] Graphitic N substitutes a C atom in the lattice, and thus the rotational symmetry is preserved. Although pyridinic N breaks the symmetry, the experimental distinction is not easily seen. Furthermore, the observed fingerprint varies with the imaging conditions, making the analysis tricky.[137] Based on the difference between figures 6.8a and 6.8b it seems that an annealing step is necessary to create the N-defects, possibly in order to overcome the energy barrier of incorporating the nitrogen in a specific coordination. This seems plausible since the distribution of N-defect types have been reported to change as a consequence of an annealing step, although in this case the amount of pyridinic defects was relatively unchanged, whereas the amount of graphitic and pyrrolic defects went up and down, respectively.[137]

To analyze this further, scanning tunneling spectroscopy (STS) can be useful. With STS the density of states (DOS) can be measured as a function of energy

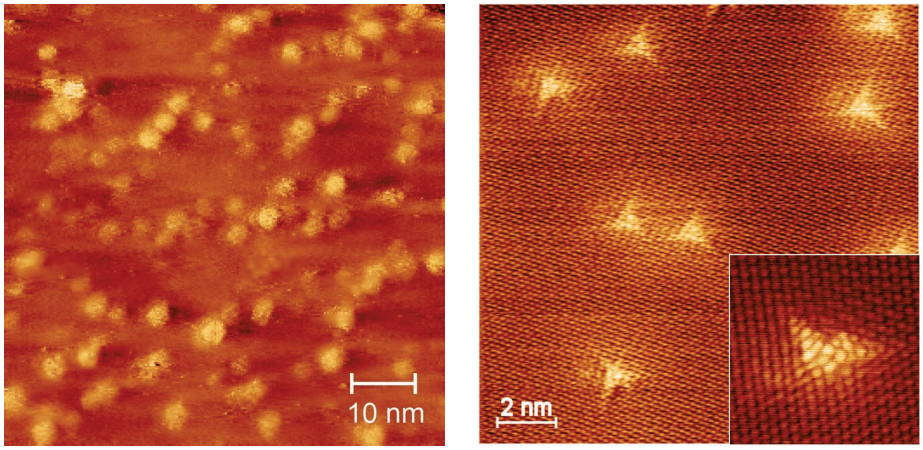

(a) 150 °C, 10 minutes (b) 700 °C, 2 hours

Figure 6.8: STM images of 1% Pt_1 on HOPG with 3% N showing the effect of annealing. (a) After only degassing the sample (150 °C, 10 minutes) it shows relatively large, round features, perhaps blisters or sputtering damage from NH_3. (b) More distinct structures appear after annealing to 700 °C for 2 hours. The triangular structures are consistent with N-defects in the carbon lattice, but their appearance varies with imaging conditions. Images leveled by mean plane subtraction. STM experiments by Arlette Ngankeu.

(applied bias) at the exact point of the defect. As the DOS over a pyridinic and graphitic N-defect differ, STS could potentially yield a more conclusive result. In addition to STM, Arlette has also done STS experiments, and while the results so far are inconclusive, it is still a point of interest. The sample discussed here was deposited with Pt_1, but similar defects were observed in STM experiments for samples deposited with dimers (Pt_2) and trimers (Pt_3), both N-doped, as well as N-doped HOPG without Pt. This does not rule out that small Pt entities could be incorporated in some of the defects on the Pt-deposited samples, but it does show that the defects occur in the absence of Pt. Consequently, they must first and foremost be N-defects. To get an idea of what an STM image of Pt_1 in a N-defect *might* look like, if encountered, various coordination geometries were simulated by Hector and Sudarshan. Initial attempts to simulate Pt_1 coordinated with a single pyridininc N-defect yielded a large, round "blob" over the Pt atom, extending significantly over several neighboring atoms. This is not consistent with anything observed experimentally. Furthermore, structures consisting of two graphene layers with Pt_1 sitting on top and surrounded between 0-4 N atoms were simulated. This also resulted in a set of STM-images, none of which resembled the experimentally observed images. This can be seen in figure C.3 in appendix C. The hypothesized structures might naturally be different than the simulated ones, and at any rate the interpretation of the simulated images is perhaps not easily applicable, since experimental imaging conditions may vary. A comparison of experimental and simulated STS might be easier to interpret.

The N-defects can in principle also be identified using XPS, but the low N coverage of these HOPG samples makes it a challenge. For this reason the synchrotron facility in Aarhus was used to obtain sufficiently intense signals. The obtained nitrogen spectra did, however, not match the the peaks expected from literature.[147] The spectrum was a convolution of peaks spanning a larger spectrum than expected, specifically toward the low binding energies. It was therefore not possible to assign the peaks to any structural motifs. This issue is possibly due to a technical problem at the beamline, which is now being investigated. The N 1s spectra can be seen in figures C.1 and C.2 in appendix C. The nitrogen coordination may prove difficult to identify by XPS alone, as the peaks are sensitive to the "long-range" neighboring atoms. For instance substantial peak shifts between isolated graphitic N and multiple graphitic N's in the vicinity of each other have been reported.[147] In this regard a model system with a controllable defect density comes in handy. Along these lines, the ability to tune the nitrogen content in the HOPG samples has also been tested. By varying the NH_3-sputtering time, the estimated N-content was varied between 0.1-1 % for a range of samples. Subsequent STM-measurements showed that the amount of star-like defects present after annealing varied accordingly, although the defect density generally varies somewhat over the surface of each sample.

6.3.4 Custom HOPG-RDE Design

The HOPG substrates were only found to be commercially available in square dimensions, which made the electrochemical RDE-experiments a challenge. Early on, we attempted to stamp out disks of HOPG that could fit in a standard RDE tip. It proved to be possible but not a feasible way forward, as the brittle HOPG would often crack or flakes would peel off. Given the low success rate, this method was abandoned. In order to accommodate the square HOPG substrates, I designed a customized RDE holder instead. The idea was to have a screw-cap assembly compatible with an RDE shaft of standard dimensions, which could be used with the available RDE rotator. This allowed the same well-defined samples both to be prepared and characterized with various UHV techniques and to be subjected to electrochemical tests, however some practical challenges ensued. The design of the HOPG-RDE and the main challenges will be described in the following section.

An overview of the latest iteration of this RDE-HOPG assembly is seen in figure 6.9. The HOPG substrate (black square) is located between two PTFE gaskets (pale sheets) on either side to ensure a conforming fit around the substrate upon assembly. The HOPG and square gasket fit in the square slot of the base piece, while the round gasket and screw cap are mounted on top. The base piece and screw cap are made of PCTFE to ensure chemical resistance against electrolytes and solutions used for cleaning while still being accurately machinable. A cylindrical bore with threading goes through the center of the base piece so that an RDE shaft can be screwed in place. The spring loaded gold

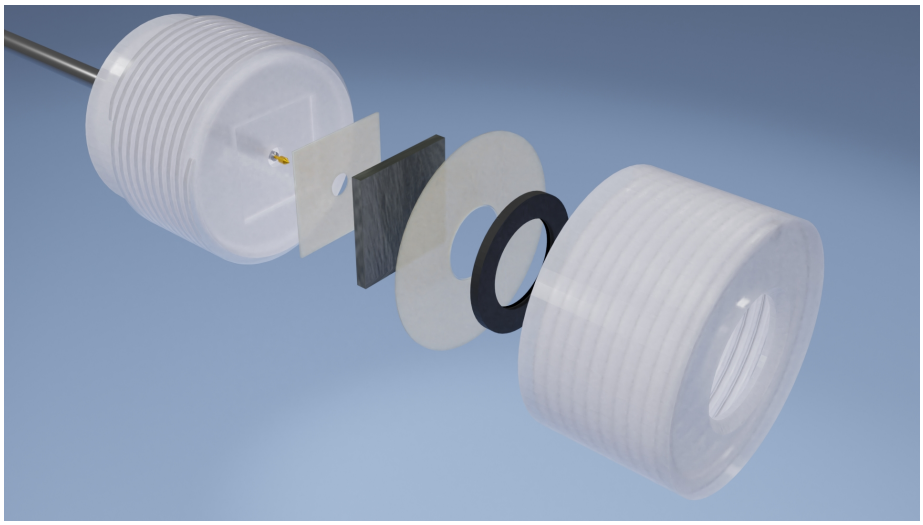

Figure 6.9: HOPG-RDE assembly: The substrate (black square, center of figure) sits between PTFE gaskets on either side. This stack is locked in place in between the base piece and screw cap. Electrical contact to the substrate is ensured by screwing an RDE shaft through the base piece (seen from top left corner) and a leak tight fit is ensured by compressing a Kalrez O-ring between the screw cap and circular PTFE gasket.

tip of the RDE shaft protrudes from the base piece and makes electrical contact with the back of the HOPG substrate. The front side of the HOPG substrate is exposed through the circular holes in the screw cap and top gasket. An additional Kalrez O-ring (FFKM perfluorelastomer) was later added in between these to ensure a more gas-tight fit, to address the issue of trace residual gas described below. The O-ring is seen in black in the figure.

The Effect of Residual Gas

Throughout several initial HOPG-RDE experiments, indications of trace amounts of unwanted gas was observed: long equilibration times when switching from one gas to another (e.g. H_2, Ar and O_2) as well as continuous CO-poisoning and multiple CO-oxidation peaks over several cycles during CO-strip experiments. These issues were not always present, making it difficult to identify the problem and subsequently troubleshoot it. In hindsight the variation in what was observed was most likely due to a difference in how well the compression of the sample worked out for each measurement. While HOPG is atomically flat over each grain it is not so on a macro scale. Ensuring a tight fit by pressing a gasket to this slightly uneven surface proved difficult. For example, a CO-strip experiment was performed on 1% Pt_1, 3% N on HOPG, giving a measurable oxidation peak. Observing a CO-strip on single atoms is interesting in it own right, however, the measurement showed indicated continuous presence of trace amount of CO. Presumably a less-than-ideal compression against the sample allows tiny

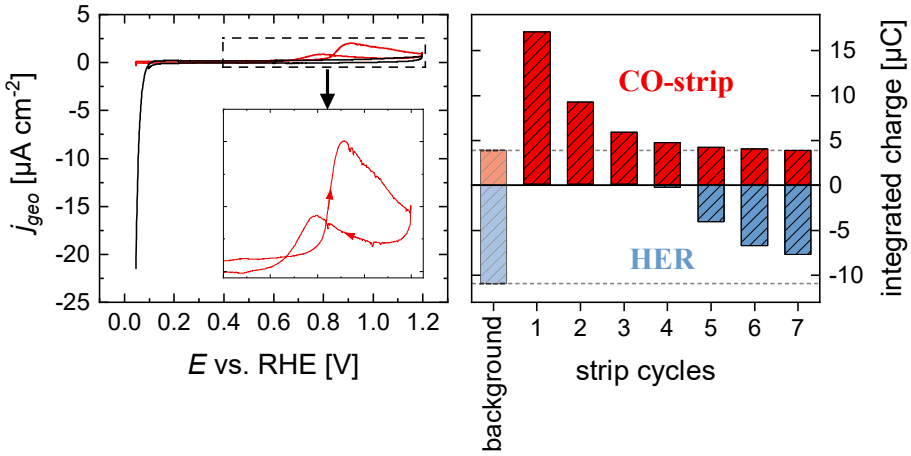

Figure 6.10: Excess CO-oxidation during a CO-strip on Pt single atoms in the HOPG-RDE assembly. Left figure shows CV's under Ar saturation with one cycle prior to 15 min. potential hold including 2 min. CO dosing (black) and the first cycle after (red) displaying HER activity and CO-strip, respectively. Right figure shows the continuous but diminishing presence of CO over multiple cycles and the effect on HER in terms of the integrated charge. Sample: 1% Pt_1, 3% N on HOPG in 0.1 M $HClO_4$.

dead volumes of gas to fill with e.g. CO, which then takes exceptionally long to get rid of or dilute sufficiently (in some cases many hours instead of a few minutes, being the normal). The issue of continuous CO-poisoning/stripping is shown in figure 6.10. The left plot shows the background cycle (black) and the CO-strip cycle (red), which has an oxidation peak both in the forward and reverse scan, shown in the inset. This feature is similar to that seen for bulk CO-oxidation.[50] Furthermore, no cathodic current is seen in the strip cycle when returning to the cathodic vertex potential after these two oxidation peaks, indicating either complete catalyst degradation, continuous site blocking from CO or perhaps a combination of the two. Notably, the same dual peak feature in the CO-strip region repeated itself in the following cycles at a slowly decreasing extent. Figure 6.10 (right) shows the integrated charge associated with the CO-strip (sum of both peaks) and the subsequent HER for each cycle. The background values are plotted as the leftmost bars, and the non-zero charge for the CO-strip background is due to the double layer capacitance in the region of integration, which could not be accurately subtracted. During strip cycles 1-4, clear oxidative peaks occur, but diminish for each cycle, although the HER is still completely blocked. At cycles 5-7 the oxidative features approach the background level, and the HER activity rises simultaneously. The presence of this dual peak over multiple cycles exemplifies the issue of trace amounts of residual gas, in this case CO. Attempts were made to mitigate this by shorter CO-dose time, longer potential hold and Ar-purge time and slower potential scan speed. These actions had little or no effect. Since there is no obvious reason that the electrolyte and the headspace above it should take longer time to be purged

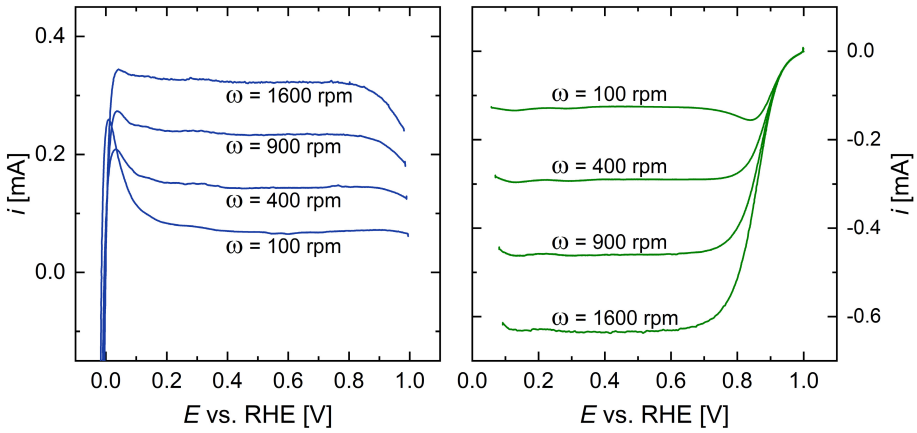

Figure 6.11: Mass-transport limited currents of HOR (left) and ORR (right) on Pt foil in the HOPG-RDE assembly. For HOR the anodic sweep is shown, for ORR the cathodic, for varying rotation rates. $\nu = 50$ mV/s, 0.1 M $HClO_4$.

and equilibrate with a new gas compared to usual RDE experiments, the issue was concluded to stem from the HOPG-RDE holder itself. Specifically, the sealing between screw cap, PTFE-gasket and HOPG was suspected not to be completely gas tight, potentially allowing trace amounts of gas leaking in and out of the internal volume of the RDE-tip during experiments. This prompted the addition of the Kalrez O-ring to the assembly, to provide a better sealing. This practically resolved the issue.

Benchmarking the Mass-Transport

In addition to the issue of a non gas-tight assembly some other effects, perhaps related to some degree, were observed. Faradaic current, for instance during HER experiments, were often seen to degrade over several cycles, some times even rapidly. While this could be an issue related to a degrading catalyst, the effect most often correlated with the formation of bubbles blocking the electrode surface. Any sample mounted in the HOPG-RDE is placed behind the screw-cap, and thus an electrolyte volume directly above the sample ($\sim$60 μL) is indented compared to the rest of the rotating end plane of the cylindrical tip. The opening of the screw-cap defining the geometric area of the sample has a tapered profile to enhance the radial flux of electrolyte and better allow bubbles to escape, however, it was not clear whether this was sufficient to ensure a reasonable mass transport. This prompted an investigation of the mass-transport characteristics of the HOPG-RDE (including the Kalrez O-ring) using a Pt foil as working electrode. Figure 6.11 shows HER/HOR (left) and ORR (right) experiments performed with the RDE-tip at varying rotation rates. The HER/HOR CV has a peak-like feature at the onset of HOR rather than a gradual transition towards i_l, especially at the lowest rotation speed ($\omega =$ 100 rpm). Apart from this, the limiting current scales proportionally with $\omega^{1/2}$

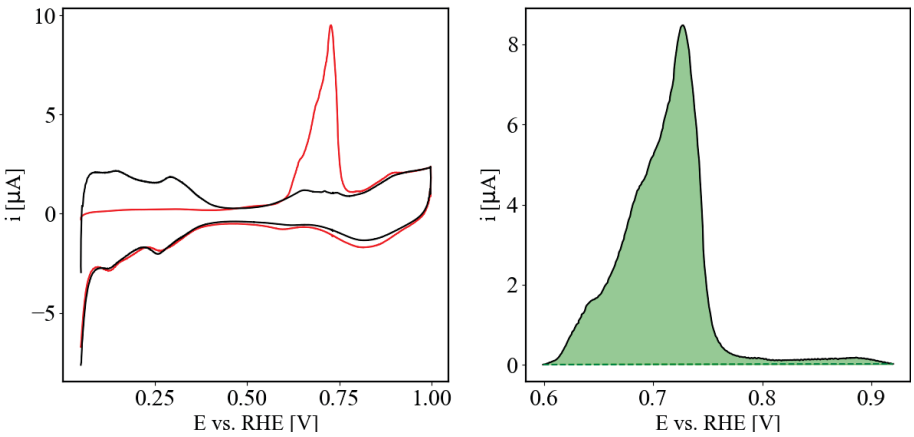

Figure 6.12: CO-strip experiment on a polycrystalline Pt-foil in HOPG-RDE-holder. (left) CO-strip cycle (red) and cycle used for background subtraction (black). (right) Background-subtracted CO-strip peak, which integrates to 5.53×10^{-5} C. CVs acquired in Ar-saturated 0.1 M $HClO_4$ with $\nu = 10$ mV s^{-1}, $\omega = 200$ rpm using a 15 minutes potential hold at +50 mV vs. RHE (with a CO-dose time of 1 min). A cleaned glassy carbon plate (1×1 cm^2) was used as backing plate on the backside of the Pt foil.

as described by the Levich equation (3.1), which agrees reasonably well with both the HOR and ORR plateaus observed here. In fact, this allows for a direct comparison with the performance of a regular RDE. The inner diameter of the Kalrez O-ring ($\varnothing_{in}$=4.2 mm) defines the exposed area of the sample ($A_{geo} \approx 0.14$ cm^2) and thus the limiting current densities at 1600 rpm are $j_{l,HOR} = 2.3$ mA/cm^2 and $j_{l,ORR}$=4.5 mA/cm^2. In regular RDE setups values of 2.9-3.0 mA/cm^2 and 6.0 mA/cm^2 have been reported for HOR and ORR, respectively.[105–107] Thereby the limiting current densities measured with the HOPG-RDE are only 75-79% of the expected values given the estimated A_{geo}. To clarify whether this is due to a non-ideal mass-transport mode caused by the design, or simply a consequence of A_{geo} being slightly overestimated, CO-stripping experiments were performed as well.

In figure 6.12 the resulting CVs of the CO-strip and background cycle are shown (left) giving the net strip-peak shown in green (right). After the addition of the Kalrez O-ring, no extra CO-strip features were observed. Integration of the CO-strip peak yields $Q_{CO,tot.} = 5.53 \times 10^{-5}$ C. Using $\sigma_{CO,Pt} = 340$ and 420 μC cm^{-2} as lower and upper bound, respectively, A_{ECSA}=0.13-0.16 cm^2 is found. Using the A_{ECSA}/A_{geo} ratio a roughness factor in the range 0.9-1.1 is found. This is on the low side since an extended single crystal surface is expected to give at least 1, and somewhat more is expected for a visibly rough polycrystalline Pt foil. Since the CO-strip is not expected to suffer from any mass-transport limitations, the indication is that A_{geo} is somewhat underestimated. This in turn accounts for $j_{l,ORR}$ and $j_{l,HOR}$ being somewhat lower than expected - at least to a certain extent. The significant peak of the HOR current, in particular

at $\omega = 100$ rpm, cannot be explained by this. It is therefore still plausible that the cavity gives rise to non-ideal mass-transport effects. Returning to the issue of bubbles accumulating and blocking the sample, it appears that adding the Kalrez O-ring generally solved the problem, with one important exception: the HOPG-RDE tip can only be immersed into the electrolyte from a vertical angle. This almost always results in a bubble being stuck in the cavity right above the sample, due to the gas being trapped there during immersion. This has practically been handled by filling the cavity with electrolyte before immersion. The downside, on the other hand, is that this approach prevents potential control while exposing the sample. Whether this actually *is* cause for concern is yet unknown.

6.3.5 Preliminary Results: Pt_1 & Pt_2

The addition of the Kalrez O-ring to the HOPG-RDE assembly was only made recently, hence the following experimental data to some extent suffer from measurement artifacts and can only provide limited insight. They do, however, lay out a path forward and show some interesting features.

CO-stripping

Figure 6.13 shows a CO-strip on 1% Pt_1, 3% N on HOPG. This comes from the same experiment shown in fig. 6.10, where continuous presence of CO gives rise to a series of CO-strip peaks. Although this drastically limits the data quality, perhaps some meaningful analysis can still be made. In lieu of a single well-defined peak, the peak for present analysis was chosen to be the one from the first cycle after CO-dosing showing no additional peak in the reverse (cathodic) scan. This cycle is shown in red. The argument is that any peak in the return scan indicates continuous CO-oxidation, corresponding to more than one CO per Pt atom, which would lead to an overestimation of $Q_{\mathrm{CO,tot.}}$ upon integration. Note, however, that even so $i > 0$ on the return scan all the way until $E \approx 0.75$ V. On the other hand, it is not possible to attribute this to residual CO with certainty, since the background cycle (black) is also slanted in a similar fashion. By integration of the peak an estimated $Q_{\mathrm{CO,tot.}} = 4.5 \times 10^{-7}$ C is found. In terms of CO molecules oxidized, this corresponds to $n_{\mathrm{CO}} \approx 1.4 \times 10^{12}$. This is roughly equivalent to the amount of Pt_1 deposited ($n_{\mathrm{Pt}} = 6.8 \times 10^{12}$ at 1% coverage). The exposed A_{geo} is, however, slightly smaller than the area over which the Pt_1 is deposited, approximately 71%. So the effective number of Pt_1 sites exposed to the electrolyte is expected to be $n^*_{\mathrm{Pt}} \approx 4.8 \times 10^{12}$. The slightly lower n_{CO} estimated could be due to agglomeration of Pt or degradation by other means, however, the uncertainties of this particular experiment makes such conclusions quite speculative. It is nonetheless interesting to observe a CO-strip on a Pt single atom sample. Whether the Pt is indeed still dispersed as single atoms during the electrochemical tests is still an open question. This could potentially be assessed with future CO-stripping experiments, now the issue of residual CO lingering is resolved. For instance an accurate observation

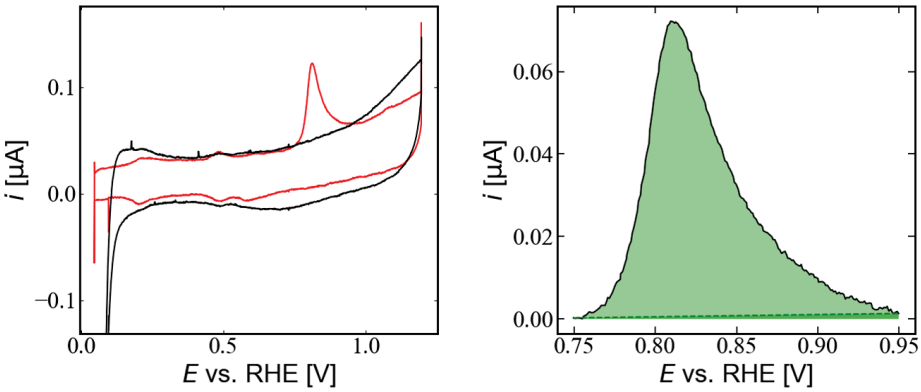

Figure 6.13: CO-strip on 1% Pt_1, 3% N on HOPG. (left) first strip cycle (red trace) where the return scan shows no additional peak. Approximated background cycle (black): After CO-dosing no suitable background cycle was achievable due to trace amounts of CO remaining and continuously adsorbing under potential hold. In stead a regular cycle before CO-dosing is used as background. (right) CO-strip peak with background subtraction gives $Q_{CO,tot.} = 4.5 \times 10^{-7}$ C. Experiment done in 0.1 M $HClO_4$ with ν=10 mV/s and ω= 600 rpm.

of $n_{CO} \approx n^*_{Pt}$ would indicate that all Pt sites are exposed and thus rule out agglomeration where a significant loss of ECSA would be expected (except for the case of agglomoreration into islands of monolayer thickness). One might hope to gain an accurate correspondence between a set of deposited loadings and measured $Q_{CO,tot.}$, like demonstrated for Pt nanoparticles in figure 5.5 in chapter 5. This could especially be interesting for a set of samples with a fixed Pt coverage but a varying N coverage, given the hypothesis that N-defects are required to prevent agglomeration. Naturally, an accurate measurment of the number of active sites is also a prerequisite for estimating intrinsic activities of the reactions investigated. From a mechanistic point of view, it could also be interesting to investigate whether Pt_2 effectively provides two sites per dimer during a CO-strip. Furthermore, differing peak potential could be of interest as an indicator of binding strength. By now it is worth mentioning that CO-stripping experiments have also been performed on Pt_2 samples, but suffered from the same issues as discussed above. Apart from the point that a CO-strip feature was also observed, a further comparison is pointless before the measurements are redone.

HER

Figure 6.14 (left) shows HER CVs for Pt_1 and Pt_2 (both 1% coverage on 3% N-doped HOPG) as well as 3% N-doped HOPG without Pt. Both Pt samples show clear HER activity, whereas the blank reference measurement does not. As discussed in chapter 5, the turnover frequency or a similar intrinsic metric is the key point of interest, but given the lack of a precise CO-strip, the activity is given here in terms of geometric current density. Note that the samples are still internally comparable, given their similar coverage. Both the Pt_1 and Pt_2

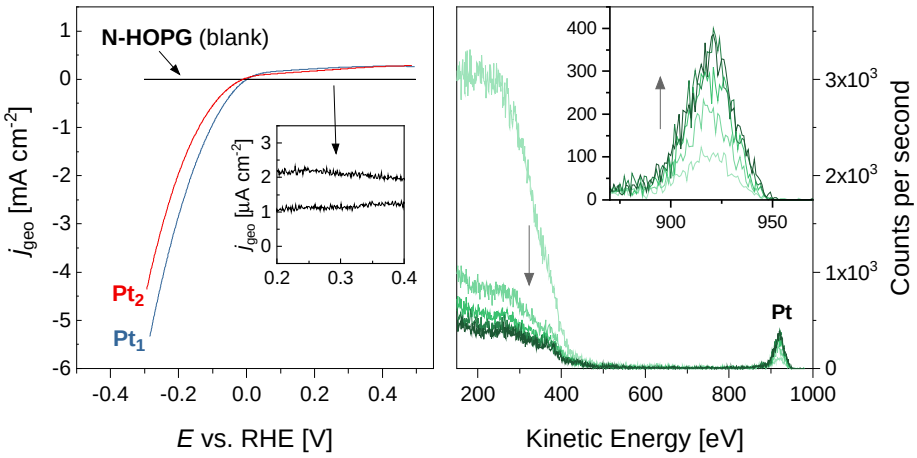

Figure 6.14: (left) CVs of Pt_1 and Pt_2 (both 1% coverage on 3% N-doped HOPG) showing HER activity (cathodic scan shown). A 3% N on HOPG (blank) for comparison shows no activity. CVs recorded in 0.1 M $HClO_4$, ω=600 rpm, ν=50 mV/s. (right) Post-electrochemistry ISS spectrum of 1% Pt_2, 3% N on HOPG: Five scans with 6 minutes 1 keV He^+ sputtering between each are shown. The large, broad feature below $\sim$ 550 eV is attributable to trace adventitious adsorbates of low atomic mass, which are gradually sputtered off for each cycle. The Pt peak signal (starting at 950 eV) simultaneously grows and then stabilizes.

samples presented here, and other similar samples generally showed somewhat unstable and/or irreproducible activities. This in part due the effect of bubbles accumulating and blocking the sample surface. With that issue resolved it should be possible to obtain comparable measurements moving forward, in order to elucidate to what extent catalyst degradation plays a role. In addition to electrochemical measurements, this assessment could possibly also include e.g. post-characterization of the samples with STM and ICP-MS analysis of the used electrolyte. The extremely surface-sensitive ISS method may also provide insight in this regard. Figure 6.14 (right) shows a series of ISS spectra of 1% Pt_2, 3% N on HOPG taken in a row, after electrochemical tests. For each scan (starting from light green toward darker green) the broad, low-energy feature attributable to trace adsorbates of light elements decreases and stabilizes. On the other hand, the peak attributable to Pt gradually increases and then stabilizes. This shows a clearly detectable amount of Pt remains on the surface of the HOPG. While an exact quantification is not readily available from this experiment alone, it does provide evidence that the Pt dimer sample is stable against dissolution to some degree. Judging by the remaining part of the spectrum, there is no evidence of unexpected elements on the HOPG surface, such as trace metal contaminants.

6.3.6 Additional Developments

Some additional techniques could provide valuable insight on the model system. The technical solutions for implementing the HOPG samples with these techniques is currently being developed. A brief perspective on what these techniques might contribute with is in order.

Electrochemistry-Mass Spectrometry

Coupling electrochemical experiments with real-time detection of products can provide valuable insight, not just on the small Pt entities discussed here but for future catalyst model systems too. One promising path for doing this is via the in-house developed *sniffer setup*, which is a coupled electrochemistry-mass spectrometry (EC-MS) method. The sniffer setup allows real-time, in-situ product detection of volatiles species by interfacing a stagnant thin-layer electrochemical cell with a UHV system (including a mass-spectrometer) by using a silicon micro-fabiracted membrane chip.[148] The EC-MS data allows correlation of electrochemical observables (e.g. via CVs) to mass-spec signals of generated/consumed species. This can, for example, be used in isotope-labeling experiments or for product detection when multiple reaction mechanisms are possible[149]. For the present model system it might be interesting to do isotope-labeled CO-stripping experiments to deconvolute the (potential) oxidation of the HOPG substrate from the observed CO-strips. The high sensitivity of this system might enable a more accurate estimate of number of active sites, compared to the CO-strips in the HOPG-RDE. In order to make these experiments possible, a new sniffer cell has been designed in order to accommodate the HOPG-samples. The system is soon to be tested.

CO-Temperature Programmed Desorption

Another interesting perspective is CO-temperature programmed desorption (CO-TPD), which is roughly speaking a UHV-analog of electrochemical CO-stripping. This technique allows estimating trends in binding energies from the observed desorption features. This may for example act as a fingerprint distinguishing single atoms from clusters.[150] The UHV-system hosting the cluster source also has the capabilities for CO-TPD. Sample holders for HOPG have been made and the system is currently being tested. It might be interesting to perform CO-TPD experiments on the small Pt entities deposited with the cluster source, without breaking vacuum in between. The comparison of Pt species at various size ranges, e.g. Pt_1, Pt_2, Pt_3 and Pt nanoparticles might be insightful.

6.4 Discussion of The Model System

To evaluate if the progress made so far aligns with our requirements, the points (i-iv) of the model system definition are considered again. The cluster source is an obvious choice for the precise synthesis of small entities. In this work,

so far only Pt single atoms, dimers and trimers are have been synthesized, but small entities of other transition metals could be deposited in a similar fashion. This fits well with requirement (i) of a model system. Whether the dispersion as small entities after deposition is maintained is, however, not demonstrated yet. A shortcoming of the cluster source is that the deposition current is relatively low (cf. fig. 6.2) and thus the obtainable catalyst coverages (equvalently loadings) are also low. There is naturally a balance between depositing sufficiently low loading to avoid interaction or overlapping of active sites, while still having sufficiently high coverage to enable accurate characterization and electrochemical tests. It is thus conceivable that the cluster source could present a limitation, in particular when going beyond single atoms, since the deposition current drops. On the other hand, there are no better alternatives for creating precisely mass-selected clusters. A more likely limitation is perhaps that the deposition is limited to two-dimensional substrates. While this is not a problem for samples to be characterized in STM, it does put a limitation on the possible materials that can be used as substrates in general. For instance there is currently no way of depositing on porous substrates suitable for high mass-transport techniques, e.g. gas diffusion electrodes or floating electrodes. In case a highly active catalyst is developed, this compatibility could be desirable.

Concerning requirement (ii) about defects, it has been shown that the density of N-defects could be varied with the sputtering time of NH_3 in a controllable manner. It was also shown that an annealing step after sputtering was necessary to observe the defects. Regarding the nature of the N-defects, there is no clear conclusion yet. Initial XPS measurements, after harsh sputtering, conditions showed that pyridinic and pyrrolic nitrogen constituted the main defects present. To observe defects in STM, milder sputtering and subsequent annealing was required, and so the STM results are not directly comparable with the initial XPS. Nonetheless, the STM-experiments indicate pyridinic and graphitic, but the exact distinction has proven difficult. To this end, STS measurements could bring new insight. Synchrotron XPS measurements on comparable samples indicate that multiple types of N-defects are present, although one seems to be prevalent. A reliable conclusion on which type has not yet been achieved. Whether the N-defect act as anchoring sites for small Pt entities is also yet unknown. From STM experiments it is indicated that a lack of N-defects leads to Pt agglomerating at grain boundaries of HOPG, but there is no conclusive evidence to determine whether N-defects actually prevent this agglomeration or not. The STEM imaging of the sample prepared with different sputtering conditions did, however, indicate atomic dispersion of Pt. So although the site density is controllable, the uniformity and anchoring capability required in point (ii) is still in question.

The requirement of point (iii) has been satisfied by HOPG, which has provided a clean, highly uniform substrate as seen in e.g. STM and ISS experiments. For STEM experiments graphene is necessary as an analogous substrate. It has proven difficult to obtain large areas of clean graphene supported on TEM grids

as a commercially available product. Partly due to this, it has been challenging to obtain STEM images. A graphene-transfer procedure has been tried as an alternative route for obtaining clean graphene, but has not yet proven successful. In order to make full use of STEM, a viable solution to this problem is needed. There might thus be a trade-off between which characterization procedures are possible given a certain substrate preparation.

In terms of compatibility with electrochemical methods, point (iv), the HOPG substrate poses a challenge. The substrates found to be commercially available do not fit the standard dimensions of RDE tips. The brittle structure of HOPG has so far prohibited machining or stamping the substrates to the desired dimensions. To resolve this issue a custom HOPG-RDE was designed. While this has enabled RDE-measurements of the synthesized HOPG samples, several measurement artifacts have been encountered. An update of the HOPG-RDE design has seemingly fixed this, but reproducible results on small Pt entities is yet to be demonstrated. If control over mass transport is not a key objective, one could think of alternatives ways to interface the HOPG samples with an electrochemical environment. In order to enable HOPG substrates in the sniffer setup, a new cell design was also necessary. While these issues are mainly technical challenges that can be overcome, it would be practical to use a substrate available in suitable dimensions rather than modifying everything else.

6.5 Conclusion & Outlook

Small entities show interesting catalytic properties and both clusters consisting of several atoms but in particular SACs have already garnered much attention. Due to the effective material utilization and the prospect of high catalytical performance, small entities are already investigated for several reactions. In addition to the active site, suitable support materials are of paramount importance to anchor the active species, due to their tendency to agglomerate. Various synthesis strategies are often reported as viable ways to achieve this. These are predominantly based on wet-chemical approaches, which may lack the specificity to systematically deconvolute the important parameters at play. As an alternative approach, a model system is suggested and discussed both as a general concept and with a specific example. In particular, small Pt entities anchored on N-doped HOPG have been synthesized, characterized and tested for the HER reaction. Although a lot of open questions remain, it has been demonstrated how single parameters might be altered independently to provide fundamental insight, which is essentially the strong suit of a model system. Activity for the HER reaction has been observed for N-doped HOPG samples deposited with Pt_1 and Pt_2 and specifically correlated with the presence of Pt, although the single atom and dimer structures, respectively, have not been verified. This can presumably be elucidated by further studies employing the characterization techniques discussed. A couple of suggestions have also been given for how the analysis of the model system could be expanded using EC-MS

and CO-TPD measurements. It is not set in stone, that the synthesis conditions currently used are optimal. For instance the sputtering and annealing procedure might be scrutinized further. It is plausible that an annealing step is needed after Pt deposition to overcome energy barriers to form the N-coordinated Pt sites - similar to how annealing was needed to generate the N-defects. Another interesting aspect to explore is the generation of the small entities: it might be feasible to directly generate small Pt-N entities with reactive N-sputtering. This could potentially allow a higher degree of control over the sites structure generated, provided the chosen entity is stable upon impact. Once a better understanding of the present model system is achieved, it might be interesting to use the same framework to study other small catalytic entities, e.g. other transition metal single atoms. This might be particularly interesting for the ORR reactions, given the connection between the geometric effect and reaction selectivity of SACs.

Chapter 7

Conclusion & Outlook

The goal of the work presented in this thesis was to gain insight on fundamental properties affecting catalytic performance, and by extension the development of novel catalysts. The focus of my work has been on activity measurement and auxiliary electrochemical experiments, but has here been presented in a broader context.

In chapter 4 the challenges synthesizing H_2O_2 via $2e^-$-ORR was discussed, focusing on the issues of selectivity and activity. In this regard, single atom catalysts are interesting due to the geometric effect of the isolated site. A single atom palladium atom catalyst, consisting of Pd coordinated in an N-defect carbon structure (Pd_1/N-C) was synthesized, characterized and tested for the $2e^-$-ORR. Although this SAC does not surpass state-of-the-art catalysts, it demonstrated high mass-activity and selectivity toward H_2O_2. The catalyst also performed well when tested in a GDE, and the need for such test was highlighted by comparison with reference samples. Various characterization techniques indicated the single-atom dispersion and N-coordination. Via DFT-models it was rationalized that this structure (likely with surrounding N-doping) was the reason for the high activity and selectivity.

In chapter 5 a benchmark study on Pt nanoparticles for HER was presented. The study highlights some of the common pitfalls in HER literature. The cluster source was used to produce well-defined samples of a large range of Pt loading, which was extended further by using commercially available Pt/C. Using CO-stripping experiments, the intrinsic activity was mapped out over the entire range of loadings, allowing the pervasive impact on mass-transport to be observed. It was indicated that the true intrinsic activity of Pt is underestimated and that decreasing catalyst loading is a practical way to minimize the relative impact of mass-transport limitations. Furthermore an observed hysteresis phenomenon at ultra-low loadings was suggested to be caused by a mass-transport limitation.

In chapter 6 a brief overview was given on the motivation and challenges of developing SACs and other small-entity catalysts. The current synthesis strategies were highlighted and used to motivate catalytic model systems to gain fundamental insight on small entities. The development of a model system consisting of Pt_{1-3} on N-doped HOPG is presented. The preliminary results indicate that NH_3-sputtering produces a range of N-defects in the HOPG. While the specific defect types are not yet determined, it is indicated that pyridinic and graphitic N-defects might be present. Electrochemical experiments show HER activity for the small Pt entities on N-doped HOPG and post characterization corroborates the presence of Pt. The active site structure is yet undetermined, pending further investigations. Several strategies for further development are outlined.

In summary, the common denominator for these projects has been the multidisciplinary approach taken, in order to gain new knowledge. The combination of experiments, characterization and theoretical modeling offers complementary means for obtaining a more complete understanding.

7.1 Outlook

The contrasts in the topics presented herein are worth noting: while new frontiers of e.g. single atom catalyst are being explored, there is still unanswered questions within well-studies systems like HER on Pt. For instance, how high is the intrinsic HER activity of Pt actually? The pursuit of these novel perspectives ought not to come at the expense of getting the fundamentals in order. This entails being able to estimate intrinsic activities and evaluate the impact of mass-transport while adhering to the best practices. Rigorous scrutiny of "well-known" systems might contribute to new, valuable insights which in turn, directly or indirectly, could aid the further development of novel systems. Furthermore, model systems might also help bridge the gap between highly exploratory studies and rigorous step-by-step procedures. For example, the high activity and selectivity of the Pd single atom catalyst for $2e^-$-ORR was rationalized to stem from the coordination with N-defects - not only the direct coordination, but possibly also from additional N-doping in the surrounding lattice. Such effects might be studied further in a model system akin to the one described for small Pt entities on N-doped HOPG. Given the tunable amount of N-defects demonstrated with NH_3-sputtering on HOPG, one might study the effect this has on Pd single atoms in a controlled manner. Furthermore, it may in some cases be necessary to deposit ultra-low catalyst loadings, as it was seen for the benchmark study of HER. While this is also possible, for instance by dilution of an ink, the cluster source offers a more precise approach, where also the dispersion is controllable via rastering. Such approaches might be useful in the further development of catalyst, finding use in a broad range of reactions relevant in a sustainable energy landscape.

Bibliography

[1] D. M. Etheridge, L. P. Steele, R. L. Langenfelds, R. J. Francey, J. M. Barnola, and V. I. Morgan, "in atmospheric the last 1000 years from air in Antarctic ice and firn," *Journal Of Geophysical Research-Atmospheres*, vol. 101, no. D2, pp. 4115–4128, 1996, ISSN: 0148-0227.

[2] K. W. Thoning and P. P. Tans, "Atmospheric carbon dioxide at Mauna Loa Observatory. 2. Analysis of the NOAA GMCC data, 1974-1985," *Journal of Geophysical Research*, vol. 94, no. D6, pp. 8549–8565, 1989, ISSN: 2156-2202. DOI: 10.1029/JD094iD06p08549.

[3] C. D. Keeling, R. B. Bacastow, and A. E. Bainbridge, "Atmospheric carbon dioxide variations at Mauna Loa Observatory, Hawaii," *Tellus*, vol. 28, no. 6, pp. 538–551, 1976, ISSN: 00402826. DOI: 10.3402/tellusa.v28i6.11322.

[4] S. Manabe and R. T. Wetherald, "Thermal Equilibrium of the Atmosphere with a Given Distribution of Relative Humidity," *Journal of the Atmospheric Sciences*, vol. 24, no. 3, pp. 241–259, May 1967, ISSN: 0022-4928. DOI: 10.1175/1520-0469(1967)024<0241:TEOTAW>2.0.CO;2. [Online]. Available: http://journals.ametsoc.org/doi/10.1175/1520-0469(1967)024%7B%5C%%7D3C0241:TEOTAW%7B%5C%%7D3E2.0.CO;2.

[5] J. Cook, D. Nuccitelli, S. A. Green, M. Richardson, B. Winkler, R. Painting, R. Way, P. Jacobs, and A. Skuce, "Quantifying the consensus on anthropogenic global warming in the scientific literature," *Environmental Research Letters*, vol. 8, 2013. DOI: 10.1088/1748-9326/8/2/024024.

[6] B. D. Santer, K. E. Taylor, T. M. L. Wigley, T. C. Johns, P. D. Jones, D. J. Karoly, J. F. B. Mitchell, A. H. Oort, J. E. Penner, V. Ramaswamy, M. D. Schwarzkopf, R. J. Stouffer, and S. Tett, "A search for human influences on the thermal structure of the atmosphere," *Nature*, vol. 382, no. 6586, pp. 39–46, Jul. 1996, ISSN: 0028-0836. DOI: 10.1038/382039a0. [Online]. Available: http://www.nature.com/articles/382039a0.

[7] G. C. Hegerl, H. V. Storch, K. Hasselmann, B. D. Santer, U. Cubasch, and P. D. Jones, "Detecting Greenhouse-Gas-Induced Climate Change with an Optimal Fingerprint Method," *American Meteorological Society*, vol. 9, pp. 2281–2306, 1996.

[8] S. Levitus, J. I. Antonov, T. P. Boyer, O. K. Baranova, H. E. Garcia, R. A. Locarnini, A. V. Mishonov, J. R. Reagan, D. Seidov, E. S. Yarosh, and M. M. Zweng, "World ocean heat content and thermosteric sea level change (0 – 2000 m), 1955 – 2010," *Geophysical Research Letters*, vol. 39, pp. 1–5, 2012. DOI: 10.1029/2012GL051106.

[9] R. S. Nerem, B. D. Beckley, J. T. Fasullo, B. D. Hamlington, D. Masters, and G. T. Mitchum, "Climate-change–driven accelerated sea-level rise detected in the altimeter era," *PNAS*, vol. 0, pp. 2022–2025, 2018. DOI: 10.1073/pnas.1717312115.

[10] IPCC, *Climate Change 2014 Synthesis Report*, Geneva, 2014.

[11] NASA, *Global Climate Change - Vital Sign of the Planet*. [Online]. Available: https://climate.nasa.gov/evidence/ (visited on 03/04/2021).

[12] J. Cook, N. Oreskes, P. T. Doran, W. R. L. Anderegg, B. Verheggen, E. W. Maibach, J. S. Carlton, S. Lewandowsky, A. G. Skuce, S. A. Green, D. Nuccitelli, P. Jacobs, M. Richardson, B. Winkler, R. Painting, and K. Rice, "Consensus on consensus : a synthesis of consensus estimates on human-caused global warming," *Environmental Research Letters*, vol. 11, no. 4, pp. 1–7, 2016. [Online]. Available: http://dx.doi.org/10.1088/1748-9326/11/4/048002.

[13] D. L. Floch, B. Bereiter, T. Blunier, J.-M. Barnola, U. Siegenthaler, D. Raynaud, J. Jouzel, H. Fischer, K. Kawamura, and T. Stocker., *Dome C 800,000-year record*, 2012. [Online]. Available: https://cdiac.ess-dive.lbl.gov/trends/co2/ice%7B%5C_%7Dcore%7B%5C_%7Dco2.html (visited on 03/05/2021).

[14] P. Tans and R. Keeling, *Trends in Atmospheric Carbon Dioxide - Mauna Loa CO2 annual mean data*, 2020. [Online]. Available: https://www.esrl.noaa.gov/gmd/webdata/ccgg/trends/co2/co2%7B%5C_%7Dannmean%7B%5C_%7Dmlo.txt (visited on 03/04/2021).

[15] D. Etheridge, L. Steele, R. Langenfelds, R. Francey, J.-M. Barnola, and V. Morgan, *Historical CO2 record from the Law Dome DE08, DE08-2, and DSS ice cores*, 1998. [Online]. Available: https://cdiac.ess-dive.lbl.gov/ftp/trends/co2/lawdome.combined.dat (visited on 03/04/2021).

[16] H. Ritchie and M. Roser, *Energy*, 2020. [Online]. Available: https://ourworldindata.org/energy-production-consumption (visited on 03/04/2021).

[17] Gapminder, *Understand a Changing World*. [Online]. Available: https://www.gapminder.org/ (visited on 03/05/2021).

[18] "World population prospects 2019: Highlights," Tech. Rep., 2019. [Online]. Available: http://www.ncbi.nlm.nih.gov/pubmed/12283219.

[19] Lawrence Livermore National and Laboratory, *Estimated U.S. Energy ConsUmption in 2019*, 2019. [Online]. Available: https://flowcharts.llnl.gov/content/assets/images/energy/us/Energy%7B%5C_%7DUS%7B%5C_%7D2019.png.

[20] IEA, "Projected Costs of Generating Electricity 2020," Paris, Tech. Rep. December, 2020. [Online]. Available: www.iea.org/reports/projected-costs-of-generating-electricity-2020.

[21] EnergiNet, *Vedvarende Energi*, 2021. [Online]. Available: https://energinet.dk/Gron-omstilling/Noegletal-om-den-gronne-omstilling%7B%5C#%7Dvedvarende (visited on 03/05/2021).

[22] Z. W. She, J. Kibsgaard, C. F. Dickens, I. Chorkendorff, J. K. Nørskov, and T. F. Jaramillo, "Combining theory and experiment in electrocatalysis: Insights into materials design," *Science*, vol. 355, no. 6321, 2017, ISSN: 10959203. DOI: 10.1126/science.aad4998.

[23] J. Kibsgaard and I. Chorkendorff, "Considerations for the scaling-up of water splitting catalysts," *Nature Energy*, vol. 4, pp. 430–433, 2019, ISSN: 2058-7546. DOI: 10.1038/s41560-019-0407-1. [Online]. Available: http://www.nature.com/articles/s41560-019-0407-1.

[24] IEA, "The Future of Hydrogen," Tech. Rep., 2019. [Online]. Available: https://www.iea.org/reports/the-future-of-hydrogen.

[25] European Commission, "A Clean Planet for all: A European strategic long-term vision for a prosperous, modern, competitive and climate neutral economy.," Tech. Rep., 2018. [Online]. Available: https://eur-lex.europa.eu/legal-content/EN/TXT/PDF/?uri=CELEX:52018DC0773%7B%5C&%7Dfrom=EN.

[26] X. Zou and Y. Zhang, "Noble metal-free hydrogen evolution catalysts for water splitting," *Chemical Society Reviews*, vol. 44, no. 15, pp. 5148–5180, Aug. 2015, ISSN: 14604744. DOI: 10.1039/c4cs00448e.

[27] X. Zhang, S. H. Chan, H. K. Ho, S. C. Tan, M. Li, G. Li, J. Li, and Z. Feng, "Towards a smart energy network: The roles of fuel/electrolysis cells and technological perspectives," *International Journal of Hydrogen Energy*, vol. 40, no. 21, pp. 6866–6919, 2015, ISSN: 03603199. DOI: 10.1016/j.ijhydene.2015.03.133. [Online]. Available: http://dx.doi.org/10.1016/j.ijhydene.2015.03.133.

[28] O. Schmidt, A. Gambhir, I. Staffell, A. Hawkes, J. Nelson, and S. Few, "Future cost and performance of water electrolysis: An expert elicitation study," *International Journal of Hydrogen Energy*, vol. 42, no. 52, pp. 30 470–30 492, 2017, ISSN: 03603199. DOI: 10.1016/j.ijhydene.2017.10.045. [Online]. Available: https://doi.org/10.1016/j.ijhydene.2017.10.045.

[29] M. Carmo, D. L. Fritz, J. Mergel, and D. Stolten, "A comprehensive review on PEM water electrolysis," *International Journal of Hydrogen Energy*, vol. 38, no. 12, pp. 4901–4934, 2013, ISSN: 03603199. DOI: 10.1016/j.ijhydene.2013.01.151.

[30] P. C. Vesborg and T. F. Jaramillo, "Addressing the terawatt challenge: Scalability in the supply of chemical elements for renewable energy," *RSC Advances*, vol. 2, no. 21, pp. 7933–7947, 2012, ISSN: 20462069. DOI: 10.1039/c2ra20839c.

[31] E. Kemppainen, A. Bodin, B. Sebok, T. Pedersen, B. Seger, B. Mei, D. Bae, P. C. Vesborg, J. Halme, O. Hansen, P. D. Lund, and I. Chorkendorff, "Scalability and feasibility of photoelectrochemical H2evolution: the ultimate limit of Pt nanoparticle as an HER catalyst," *Energy and Environmental Science*, vol. 8, no. 10, pp. 2991–2999, 2015, ISSN: 17545706. DOI: 10.1039/c5ee02188j.

[32] F. Abild-Pedersen, J. Greeley, F. Studt, J. Rossmeisl, T. R. Munter, P. G. Moses, E. Skúlason, T. Bligaard, and J. K. Nørskov, "Scaling Properties of Adsorption Energies for Hydrogen-Containing Molecules on Transition-Metal Surfaces," *Physical Review Letters*, vol. 99, no. 1, p. 016 105, Jul. 2007, ISSN: 0031-9007. DOI: 10.1103/PhysRevLett.99.016105. [Online]. Available: https://link.aps.org/doi/10.1103/PhysRevLett.99.016105.

[33] J. K. Nørskov, J. Rossmeisl, A. Logadottir, L. Lindqvist, J. R. Kitchin, T. Bligaard, and H. Jónsson, "Origin of the Overpotential for Oxygen Reduction at a Fuel-Cell Cathode," *The Journal of Physical Chemistry B*, vol. 108, no. 46, pp. 17 886–17 892, Nov. 2004, ISSN: 1520-6106. DOI: 10.1021/jp047349j. [Online]. Available: http://pubs.acs.org/doi/abs/10.1021/jp047349j.

[34] E. Skúlason, V. Tripkovic, M. E. Björketun, S. Gudmundsdóttir, G. Karlberg, J. Rossmeisl, T. Bligaard, H. Jónsson, and J. K. Nørskov, "Modeling the electrochemical hydrogen oxidation and evolution reactions on the basis of density functional theory calculations," *Journal of Physical Chemistry C*, vol. 114, no. 42, pp. 18 182–18 197, 2010, ISSN: 19327447. DOI: 10.1021/jp1048887.

[35] I. Chorkendorff and J. W. Niemantsverdriet, *Concepts of Modern Catalysis and Kinetics*. Wiley, Oct. 2003, ISBN: 9783527305742. DOI: 10.1002/3527602658. [Online]. Available: https://onlinelibrary.wiley.com/doi/book/10.1002/3527602658.

[36] P. Hernandez-Fernandez, F. Masini, D. N. McCarthy, C. E. Strebel, D. Friebel, D. Deiana, P. Malacrida, A. Nierhoff, A. Bodin, A. M. Wise, J. H. Nielsen, T. W. Hansen, A. Nilsson, I. E. Stephens, and I. Chorkendorff, "Mass-selected nanoparticles of PtxY as model catalysts for oxygen electroreduction," *Nature Chemistry*, vol. 6, no. 8, pp. 732–738, 2014, ISSN: 17554349. DOI: 10.1038/nchem.2001.

[37] J. Jirkovský, H. Hoffmannová, M. Klementová, and P. Krtil, "Particle Size Dependence of the Electrocatalytic Activity of Nanocrystalline RuO[sub 2] Electrodes," *Journal of The Electrochemical Society*, vol. 153, no. 6, E111, 2006, ISSN: 00134651. DOI: 10.1149/1.2189953.

[38] M. Haruta, S. Tsubota, T. Kobayashi, H. Kageyama, M. J. Genet, and B. Delmon, *Low-temperature oxidation of CO over gold supported on TiO2, α-Fe2O3, and Co3O4*, 1993. DOI: 10.1006/jcat.1993.1322.

[39] M. Haruta, "Size- and support-dependency in the catalysis of gold," *Catalysis Today*, vol. 36, no. 1, pp. 153–166, 1997, ISSN: 09205861. DOI: 10.1016/S0920-5861(96)00208-8.

[40] R. Reske, H. Mistry, F. Behafarid, B. Roldan Cuenya, and P. Strasser, "Particle size effects in the catalytic electroreduction of CO2 on Cu nanoparticles," *Journal of the American Chemical Society*, vol. 136, no. 19, pp. 6978–6986, 2014, ISSN: 15205126. DOI: 10.1021/ja500328k.

[41] L. Li, A. H. Larsen, N. A. Romero, V. A. Morozov, C. Glinsvad, F. Abild-Pedersen, J. Greeley, K. W. Jacobsen, and J. K. Nørskov, "Investigation of catalytic finite-size-effects of platinum metal clusters," *Journal of Physical Chemistry Letters*, vol. 4, no. 1, pp. 222–226, 2013, ISSN: 19487185. DOI: 10.1021/jz3018286.

[42] J. Kleis, J. Greeley, N. A. Romero, V. A. Morozov, H. Falsig, A. H. Larsen, J. Lu, J. J. Mortensen, M. Dułak, K. S. Thygesen, J. K. Nørskov, and K. W. Jacobsen, "Finite Size Effects in Chemical Bonding: From Small Clusters to Solids," *Catalysis Letters*, vol. 141, no. 8, pp. 1067–1071, Aug. 2011, ISSN: 1011-372X. DOI: 10.1007/s10562-011-0632-0. [Online]. Available: http://link.springer.com/10.1007/s10562-011-0632-0.

[43] A. Beniya, S. Higashi, N. Ohba, R. Jinnouchi, H. Hirata, and Y. Watanabe, "CO oxidation activity of non-reducible oxide-supported mass-selected few-atom Pt single-clusters," *Nature Communications*, vol. 11, no. 1, pp. 1–10, 2020, ISSN: 20411723. DOI: 10.1038/s41467-020-15850-4. [Online]. Available: http://dx.doi.org/10.1038/s41467-020-15850-4.

[44] E. C. Tyo and S. Vajda, "Catalysis by clusters with precise numbers of atoms," *Nature Nanotechnology*, vol. 10, no. 7, pp. 577–588, 2015, ISSN: 17483395. DOI: 10.1038/NNANO.2015.140.

[45] A. Sanchez, S. Abbet, U. Heiz, W. D. Schneider, H. Häkkinen, R. N. Barnett, and U. Landman, "When Gold Is Not Noble: Nanoscale Gold Catalysts," *Journal of Physical Chemistry A*, vol. 103, no. 48, pp. 9573–9578, 1999, ISSN: 10895639. DOI: 10.1021/jp9935992.

[46] S. Abbet, A. Sanchez, U. Heiz, W. D. Schneider, A. M. Ferrari, G. Pacchioni, and N. Rösch, "Acetylene cyclotrimerization on supported size-selected Pd(n) clusters (1 n 30): One atom is enough!" *Journal of the American Chemical Society*, vol. 122, no. 14, pp. 3453–3457, 2000, ISSN: 00027863. DOI: 10.1021/ja9922476.

[47] L. R. Faulkner and A. J. Bard, *Electrochemical Methods: Fundamentals and Applications*, Second. New York: John Wiley & Sons, Inc., 2001.

[48] J. Xi, S. Yang, L. Silvioli, S. Cao, P. Liu, Q. Chen, Y. Zhao, H. Sun, J. Novak Hansen, J.-P. B. Haraldsted, J. Kibsgaard, J. Rossmeisl, S. Bals, S. Wang, and I. Chorkendorff, "Highly active, selective, and stable Pd single-atom catalyst anchored on N-doped hollow carbon sphere for electrochemical H2O2 synthesis under acidic conditions," *Journal of Catalysis*, vol. 393, pp. 313–323, 2020, ISSN: 00219517. DOI: 10.1016/j.jcat.2020.11.020. [Online]. Available: https://doi.org/10.1016/j.jcat.2020.11.020.

[49] J. N. Hansen, H. Prats, K. K. Toudahl, N. Mørch Secher, K. Chan, J. Kibsgaard, and I. Chorkendorff, "Is There Anything Better than Pt for HER?" *ACS Energy Letters*, vol. 6, pp. 1175–1180, Mar. 2021, ISSN: 2380-8195. DOI: 10.1021/acsenergylett.1c00246. [Online]. Available: https://pubs.acs.org/doi/10.1021/acsenergylett.1c00246.

[50] N. M. Marković, B. N. Grgur, C. A. Lucas, and P. N. Ross, "Electrooxidation of CO and H2/CO mixtures on Pt(111) in acid solutions," *Journal of Physical Chemistry B*, vol. 103, no. 3, pp. 487–495, 1999, ISSN: 10895647. DOI: 10.1021/jp983177c.

[51] T. Binninger, E. Fabbri, R. Kotz, and T. J. Schmidt, "Determination of the Electrochemically Active Surface Area of Metal-Oxide Supported Platinum Catalyst," *Journal of the Electrochemical Society*, vol. 161, no. 3, H121–H128, Dec. 2014, ISSN: 0013-4651. DOI: 10.1149/2.055403jes. [Online]. Available: http://jes.ecsdl.org/cgi/doi/10.1149/2.055403jes.

[52] G. Samjeské, K. I. Komatsu, and M. Osawa, "Dynamics of CO oxidation on a polycrystalline platinum electrode: A time-resolved infrared study," *Journal of Physical Chemistry C*, vol. 113, no. 23, pp. 10 222–10 228, 2009, ISSN: 19327447. DOI: 10.1021/jp900582c.

[53] S. Rudi, C. Cui, L. Gan, and P. Strasser, "Comparative Study of the Electrocatalytically Active Surface Areas (ECSAs) of Pt Alloy Nanoparticles Evaluated by Hupd and CO-stripping voltammetry," *Electrocatalysis*, vol. 5, no. 4, pp. 408–418, Oct. 2014, ISSN: 1868-2529. DOI: 10.1007/s12678-014-0205-2. [Online]. Available: http://link.springer.com/10.1007/s12678-014-0205-2.

[54] E. G. Ciapina, S. F. Santos, and E. R. Gonzalez, "Electrochemical CO stripping on nanosized Pt surfaces in acid media: A review on the issue of peak multiplicity," *Journal of Electroanalytical Chemistry*, vol. 815, no. February, pp. 47–60, 2018, ISSN: 15726657. DOI: 10.1016/j.jelechem.2018.02.047. [Online]. Available: https://doi.org/10.1016/j.jelechem.2018.02.047.

[55] A. Cuesta, A. Couto, A. Rincón, M. Pérez, A. López-Cudero, and C. Gutiérrez, "Potential dependence of the saturation CO coverage of Pt electrodes: The origin of the pre-peak in CO-stripping voltammograms. Part 3: Pt(poly)," *Journal of Electroanalytical Chemistry*, vol. 586, no. 2, pp. 184–195, Jan. 2006, ISSN: 15726657. DOI: 10.1016/j.jelechem.2005.10.006. [Online]. Available: http://linkinghub.elsevier.com/retrieve/pii/S0022072805005036.

[56] P. Urchaga, S. Baranton, C. Coutanceau, and G. Jerkiewicz, "Evidence of an Eley-Rideal mechanism in the stripping of a saturation layer of chemisorbed CO on platinum nanoparticles," *Langmuir*, vol. 28, no. 36, pp. 13 094–13 104, 2012, ISSN: 07437463. DOI: 10.1021/la302388p.

[57] T. Binninger, E. Fabbri, R. Kötz, and T. J. Schmidt, "Determination of the Electrochemically Active Surface Area of Metal-Oxide Supported Platinum Catalyst," *Journal of The Electrochemical Society*, vol. 161, no. 3, H121–H128, 2014, ISSN: 0013-4651. DOI: 10.1149/2.055403jes.

[58] A. Vojvodic and J. K. Nørskov, "Special Topic : Catalysis — Facing the Future New design paradigm for heterogeneous catalysts," *National Science Review*, vol. 2, no. August, pp. 140–143, 2015.

[59] S. Yang, A. Verdaguer-Casadevall, L. Arnarson, L. Silvioli, V. Čolić, R. Frydendal, J. Rossmeisl, I. Chorkendorff, and I. E. Stephens, "Toward the Decentralized Electrochemical Production of H2O2: A Focus on the Catalysis," *ACS Catalysis*, vol. 8, no. 5, pp. 4064–4081, 2018, ISSN: 21555435. DOI: 10.1021/acscatal.8b00217.

[60] R. Ciriminna, L. Albanese, F. Meneguzzo, and M. Pagliaro, "Hydrogen Peroxide: A Key Chemical for Today's Sustainable Development," *ChemSusChem*, vol. 9, no. 24, pp. 3374–3381, 2016, ISSN: 1864564X. DOI: 10.1002/cssc.201600895.

[61] J. M. Campos-Martin, G. Blanco-Brieva, and J. L. Fierro, "Hydrogen peroxide synthesis: An outlook beyond the anthraquinone process," *Angewandte Chemie - International Edition*, vol. 45, no. 42, pp. 6962–6984, 2006, ISSN: 14337851. DOI: 10.1002/anie.200503779.

[62] J. K. Edwards, B. E. Solsona, P. Landon, A. F. Carley, A. Herzing, C. J. Kiely, and G. J. Hutchings, "Direct synthesis of hydrogen peroxide from H2 and O2 using TiO2-supported Au-Pd catalysts," *Journal of Catalysis*, vol. 236, no. 1, pp. 69–79, 2005, ISSN: 00219517. DOI: 10.1016/j.jcat.2005.09.015.

[63] J. K. Edwards, S. J. Freakley, R. J. Lewis, J. C. Pritchard, and G. J. Hutchings, "Advances in the direct synthesis of hydrogen peroxide from hydrogen and oxygen," *Catalysis Today*, vol. 248, pp. 3–9, 2015, ISSN: 09205861. DOI: 10.1016/j.cattod.2014.03.011. [Online]. Available: http://dx.doi.org/10.1016/j.cattod.2014.03.011.

[64] E. Ghedini, F. Menegazzo, M. Signoretto, M. Manzoli, F. Pinna, and G. Strukul, "Mesoporous silica as supports for Pd-catalyzed H2O2 direct synthesis: Effect of the textural properties of the support on the activity and selectivity," *Journal of Catalysis*, vol. 273, no. 2, pp. 266–273, 2010, ISSN: 00219517. DOI: 10.1016/j.jcat.2010.06.003. [Online]. Available: http://dx.doi.org/10.1016/j.jcat.2010.06.003.

[65] F. Menegazzo, M. Manzoli, M. Signoretto, F. Pinna, and G. Strukul, "H2O2 direct synthesis under mild conditions on Pd-Au samples: Effect of the morphology and of the composition of the metallic phase," *Catalysis Today*, vol. 248, pp. 18–27, 2015, ISSN: 09205861. DOI: 10.1016/j.cattod.2014.01.015. [Online]. Available: http://dx.doi.org/10.1016/j.cattod.2014.01.015.

[66] S. J. Freakley, Q. He, J. H. Harrhy, L. Lu, D. A. Crole, D. J. Morgan, E. N. Ntainjua, J. K. Edwards, A. F. Carley, A. Y. Borisevich, C. J. Kiely, and G. J. Hutchings, "Palladium-tin catalysts for the direct synthesis of H2O2 with high selectivity," *Science*, vol. 351, no. 6276, pp. 965–968, Feb. 2016, ISSN: 0036-8075. DOI: 10.1126/science.aad5705. [Online]. Available: https://onlinelibrary.wiley.com/doi/abs/10.1002/cctc.201900100%20https://www.sciencemag.org/lookup/doi/10.1126/science.aad5705.

[67] R. J. Lewis, K. Ueura, Y. Fukuta, S. J. Freakley, L. Kang, R. Wang, Q. He, J. K. Edwards, D. J. Morgan, Y. Yamamoto, and G. J. Hutchings, "The Direct Synthesis of H 2 O 2 Using TS-1 Supported Catalysts," *ChemCatChem*, vol. 11, no. 6, pp. 1673–1680, 2019, ISSN: 18673899. DOI: 10.1002/cctc.201900100.

[68] S. Wang, K. Gao, W. Li, and J. Zhang, "Effect of Zn addition on the direct synthesis of hydrogen peroxide over supported palladium catalysts," *Applied Catalysis A: General*, vol. 531, pp. 89–95, 2017, ISSN: 0926860X. DOI: 10.1016/j.apcata.2016.10.023. [Online]. Available: http://dx.doi.org/10.1016/j.apcata.2016.10.023.

[69] *United States Environmental Protection Agency (EPA)*, 2007. [Online]. Available: https://www.epa.gov/greenchemistry/presidential-green-chemistry-challenge-2007-greener-reaction-conditions-award (visited on 02/18/2021).

[70] Y. Yi, L. Wang, G. Li, and H. Guo, "A review on research progress in the direct synthesis of hydrogen peroxide from hydrogen and oxygen: Noble-metal catalytic method, fuel-cell method and plasma method," *Catalysis Science and Technology*, vol. 6, no. 6, pp. 1593–1610, 2016, ISSN: 20444761. DOI: 10.1039/c5cy01567g.

[71] S. C. Perry, D. Pangotra, L. Vieira, L. I. Csepei, V. Sieber, L. Wang, C. Ponce de León, and F. C. Walsh, "Electrochemical synthesis of hydrogen peroxide from water and oxygen," *Nature Reviews Chemistry*, vol. 3, no. 7, pp. 442–458, 2019, ISSN: 23973358. DOI: 10.1038/s41570-019-0110-6. [Online]. Available: http://dx.doi.org/10.1038/s41570-019-0110-6.

[72] Z. Qiang, J. H. Chang, and C. P. Huang, "Electrochemical generation of hydrogen peroxide from dissolved oxygen in acidic solutions," *Water Research*, vol. 36, no. 1, pp. 85–94, 2002, ISSN: 00431354. DOI: 10.1016/S0043-1354(01)00235-4.

[73] K. Otsuka and I. Yamanaka, "One step synthesis of hydrogen peroxide through fuel cell reaction," *Electrochimica Acta*, vol. 35, no. 2, pp. 319–322, 1990, ISSN: 00134686. DOI: 10.1016/0013-4686(90)87004-L.

[74] S. Siahrostami, A. Verdaguer-Casadevall, M. Karamad, D. Deiana, P. Malacrida, B. Wickman, M. Escudero-Escribano, E. A. Paoli, R. Frydendal, T. W. Hansen, I. Chorkendorff, I. E. Stephens, and J. Rossmeisl, "Enabling direct H2O2 production through rational electrocatalyst design," *Nature Materials*, vol. 12, no. 12, pp. 1137–1143, 2013, ISSN: 14764660. DOI: 10.1038/nmat3795.

[75] E. Pizzutilo, O. Kasian, C. H. Choi, S. Cherevko, G. J. Hutchings, K. J. Mayrhofer, and S. J. Freakley, "Electrocatalytic synthesis of hydrogen peroxide on Au-Pd nanoparticles: From fundamentals to continuous production," *Chemical Physics Letters*, vol. 683, pp. 436–442, 2017, ISSN: 00092614. DOI: 10.1016/j.cplett.2017.01.071. [Online]. Available: http://dx.doi.org/10.1016/j.cplett.2017.01.071.

[76] J. S. Jirkovský, I. Panas, E. Ahlberg, M. Halasa, S. Romani, and D. J. Schiffrin, "Single atom hot-spots at Au-Pd nanoalloys for electrocatalytic H 2O 2 production," *Journal of the American Chemical Society*, vol. 133, no. 48, pp. 19 432–19 441, 2011, ISSN: 00027863. DOI: 10.1021/ja206477z.

[77] I. Yamanaka, R. Ichihashi, T. Iwasaki, N. Nishimura, T. Murayama, W. Ueda, and S. Takenaka, "Electrocatalysis of heat-treated cobalt-porphyrin/carbon for hydrogen peroxide formation," *Electrochimica Acta*, vol. 108, pp. 321–329, 2013, ISSN: 00134686. DOI: 10.1016/j.electacta.2013.06.072. [Online]. Available: http://dx.doi.org/10.1016/j.electacta.2013.06.072.

[78] C. W. B. Bezerra, L. Zhang, K. C. Lee, H. S. Liu, A. L. B. Marques, E. P. Marques, H. J. Wang, and J. J. Zhang, "A review of Fe-N/C and Co-N/C catalysts for the oxygen reduction reaction," English, *Electrochimica Acta*, vol. 53, no. 15, pp. 4937–4951, 2008. DOI: 10.1016/j.electacta.2008.02.012.

[79] A. Verdaguer-Casadevall, D. Deiana, M. Karamad, S. Siahrostami, P. Malacrida, T. W. Hansen, J. Rossmeisl, I. Chorkendorff, and I. E. L. Stephens, "Trends in the Electrochemical Synthesis of H2O2: Enhancing Activity and Selectivity by Electrocatalytic Site Engineering," *Nano Letters*, vol. 14, no. 3, pp. 1603–1608, 2014, ISSN: 1530-6984. DOI: 10.1021/nl500037x. [Online]. Available: http://pubs.acs.org/doi/10.1021/nl500037x.

[80] W. Stöber, A. Fink, and E. Bohn, "Controlled growth of monodisperse silica spheres in the micron size range," *Journal of Colloid and Interface Science*, vol. 26, no. 1, pp. 62–69, Jan. 1968, ISSN: 00219797. DOI: 10.1016/0021-9797(68)90272-5. [Online]. Available: https://linkinghub.elsevier.com/retrieve/pii/0021979768902725.

[81] W. S. Hummers and R. E. Offeman, "Preparation of Graphitic Oxide," *Journal of the American Chemical Society*, vol. 80, no. 6, p. 1339, 1958, ISSN: 15205126. DOI: 10.1021/ja01539a017.

[82] J. Gao, H. bin Yang, X. Huang, S.-F. F. Hung, W. Cai, C. Jia, S. Miao, H. M. Chen, X. Yang, Y. Huang, T. Zhang, and B. Liu, "Enabling Direct H2O2 Production in Acidic Media through Rational Design of Transition Metal Single Atom Catalyst," *Chem*, vol. 6, no. 3, pp. 658–674, 2020, ISSN: 24519294. DOI: 10.1016/j.chempr.2019.12.008. [Online]. Available: https://doi.org/10.1016/j.chempr.2019.12.008.

[83] Y. Sun, L. Silvioli, N. R. Sahraie, W. Ju, J. Li, A. Zitolo, S. Li, A. Bagger, L. Arnarson, X. Wang, T. Moeller, D. Bernsmeier, J. Rossmeisl, F. Jaouen, and P. Strasser, "Activity-Selectivity Trends in the Electrochemical Production of Hydrogen Peroxide over Single-Site Metal-Nitrogen-Carbon Catalysts," *Journal of the American Chemical Society*, vol. 141, no. 31, pp. 12 372–12 381, 2019, ISSN: 15205126. DOI: 10.1021/jacs.9b05576.

[84] E. Jung, H. Shin, B. H. Lee, V. Efremov, S. Lee, H. S. Lee, J. Kim, W. Hooch Antink, S. Park, K. S. Lee, S. P. Cho, J. S. Yoo, Y. E. Sung, and T. Hyeon, "Atomic-level tuning of Co–N–C catalyst for high-performance electrochemical H2O2 production," *Nature Materials*, vol. 19, no. 4, pp. 436–442, 2020, ISSN: 14764660. DOI: 10.1038/s41563-019-0571-5. [Online]. Available: http://dx.doi.org/10.1038/s41563-019-0571-5.

[85] J. K. Nørskov, T. Bligaard, A. Logadottir, J. R. Kitchin, J. G. Chen, S. Pandelov, and U. Stimming, "Trends in the Exchange Current for Hydrogen Evolution," *Journal of The Electrochemical Society*, vol. 152, no. 3, J23, 2005, ISSN: 00134651. DOI: 10.1149/1.1856988.

[86] I. Roger, M. A. Shipman, and M. D. Symes, "Earth-abundant catalysts for electrochemical and photoelectrochemical water splitting," *Nature Reviews Chemistry*, vol. 1, 2017, ISSN: 23973358. DOI: 10.1038/s41570-016-0003.

[87] B. Hinnemann, P. G. Moses, J. Bonde, K. P. Jørgensen, J. H. Nielsen, S. Horch, I. Chorkendorff, and J. K. Nørskov, "Biomimetic hydrogen evolution: MoS2 nanoparticles as catalyst for hydrogen evolution," *Journal of the American Chemical Society*, vol. 127, no. 15, pp. 5308–5309, 2005, ISSN: 00027863. DOI: 10.1021/ja0504690.

[88] T. F. Jaramillo, K. P. Jørgensen, J. Bonde, J. H. Nielsen, S. Horch, and I. Chorkendorff, "Identification of active edge sites for electrochemical H2 evolution from MoS2 nanocatalysts," *Science*, vol. 317, no. 5834, pp. 100–102, 2007, ISSN: 00368075. DOI: 10.1126/science.1141483.

[89] J. Kibsgaard, T. F. Jaramillo, and F. Besenbacher, "Building an appropriate active-site motif into a hydrogen-evolution catalyst with thiomolybdate [Mo3S13]2- clusters," *Nature Chemistry*, vol. 6, no. 3, pp. 248–253, 2014, ISSN: 17554330. DOI: 10.1038/nchem.1853. [Online]. Available: http://dx.doi.org/10.1038/nchem.1853.

[90] J. Kibsgaard, Z. Chen, B. N. Reinecke, and T. F. Jaramillo, "Engineering the surface structure of MoS2 to preferentially expose active edge sites for electrocatalysis," *Nature Materials*, vol. 11, no. 11, pp. 963–969, 2012, ISSN: 14764660. DOI: 10.1038/nmat3439.

[91] E. J. Popczun, J. R. McKone, C. G. Read, A. J. Biacchi, A. M. Wiltrout, N. S. Lewis, and R. E. Schaak, "Nanostructured nickel phosphide as an electrocatalyst for the hydrogen evolution reaction," *Journal of the American Chemical Society*, vol. 135, no. 25, pp. 9267–9270, 2013, ISSN: 00027863. DOI: 10.1021/ja403440e.

[92] E. J. Popczun, C. G. Read, C. W. Roske, N. S. Lewis, and R. E. Schaak, "Highly Active Electrocatalysis of the Hydrogen Evolution Reaction by Cobalt Phosphide Nanoparticles," *Angewandte Chemie*, vol. 126, no. 21, pp. 5531–5534, 2014, ISSN: 0044-8249. DOI: 10.1002/ange.201402646.

[93] J. Kibsgaard, C. Tsai, K. Chan, J. D. Benck, J. K. Nørskov, F. Abild-Pedersen, and T. F. Jaramillo, "Designing an improved transition metal phosphide catalyst for hydrogen evolution using experimental and theoretical trends," *Energy and Environmental Science*, vol. 8, no. 10, pp. 3022–3029, 2015, ISSN: 17545706. DOI: 10.1039/c5ee02179k.

[94] J. Kibsgaard and T. F. Jaramillo, "Molybdenum phosphosulfide: An active, acid-stable, earth- Abundant catalyst for the hydrogen evolution reaction," *Angewandte Chemie - International Edition*, vol. 53, no. 52, pp. 14 433–14 437, 2014, ISSN: 15213773. DOI: 10.1002/anie.201408222.

[95] R. R. Chianelli, M. H. Siadati, M. P. De la Rosa, G. Berhault, J. P. Wilcoxon, R. Bearden, and B. L. Abrams, "Catalytic properties of single layers of transition metal sulfide catalytic materials," *Catalysis Reviews - Science and Engineering*, vol. 48, no. 1, pp. 1–41, 2006, ISSN: 01614940. DOI: 10.1080/01614940500439776.

[96] H. Li, C. Tsai, A. L. Koh, L. Cai, A. W. Contryman, A. H. Fragapane, J. Zhao, H. S. Han, H. C. Manoharan, F. Abild-Pedersen, J. K. Nørskov, and X. Zheng, "Activating and optimizing MoS2 basal planes for hydrogen evolution through the formation of strained sulphur vacancies (Nature Materials (2016) 15 (48-53))," *Nature Materials*, vol. 15, no. 3, p. 364, Jan. 2016, ISSN: 14764660. DOI: 10.1038/nmat4564. [Online]. Available: www.nature.com/naturematerials.

[97] L. Zhang, R. Si, H. Liu, N. Chen, Q. Wang, K. Adair, Z. Wang, J. Chen, Z. Song, J. Li, M. N. Banis, R. Li, T. K. Sham, M. Gu, L. M. Liu, G. A. Botton, and X. Sun, "Atomic layer deposited Pt-Ru dual-metal dimers and identifying their active sites for hydrogen evolution reaction," *Nature Communications*, vol. 10, no. 1, Dec. 2019, ISSN: 20411723. DOI: 10.1038/s41467-019-12887-y.

[98] Q. Q. Yan, D. X. Wu, S. Q. Chu, Z. Q. Chen, Y. Lin, M. X. Chen, J. Zhang, X. J. Wu, and H. W. Liang, "Reversing the charge transfer between platinum and sulfur-doped carbon support for electrocatalytic hydrogen evolution," *Nature Communications*, vol. 10, no. 1, 2019, ISSN: 20411723. DOI: 10.1038/s41467-019-12851-w. [Online]. Available: http://dx.doi.org/10.1038/s41467-019-12851-w.

[99] N. Cheng, S. Stambula, D. Wang, M. N. Banis, J. Liu, A. Riese, B. Xiao, R. Li, T. K. Sham, L. M. Liu, G. A. Botton, and X. Sun, "Platinum single-atom and cluster catalysis of the hydrogen evolution reaction," *Nature Communications*, vol. 7, no. 1, pp. 1–9, Nov. 2016, ISSN: 20411723. DOI: 10.1038/ncomms13638. [Online]. Available: http://dx.doi.org/10.1038/ncomms13638%20www.nature.com/naturecommunications.

[100] L. Cao, Q. Luo, W. Liu, Y. Lin, X. Liu, Y. Cao, W. Zhang, Y. Wu, J. Yang, T. Yao, and S. Wei, "Identification of single-atom active sites in carbon-based cobalt catalysts during electrocatalytic hydrogen evolution," *Nature Catalysis*, vol. 2, no. 2, pp. 134–141, 2019, ISSN: 25201158. DOI: 10.1038/s41929-018-0203-5. [Online]. Available: http://dx.doi.org/10.1038/s41929-018-0203-5.

[101] W. Chen, J. Pei, C. T. He, J. Wan, H. Ren, Y. Wang, J. Dong, K. Wu, W. C. Cheong, J. Mao, X. Zheng, W. Yan, Z. Zhuang, C. Chen, Q. Peng, D. Wang, and Y. Li, "Single Tungsten Atoms Supported on MOF-Derived N-Doped Carbon for Robust Electrochemical Hydrogen Evolution," *Advanced Materials*, vol. 30, no. 30, pp. 1–6, 2018, ISSN: 15214095. DOI: 10.1002/adma.201800396.

[102] Q. Wang, Z. L. Zhao, S. Dong, D. He, M. J. Lawrence, S. Han, C. Cai, S. Xiang, P. Rodriguez, B. Xiang, Z. Wang, Y. Liang, and M. Gu, "Design of active nickel single-atom decorated MoS2 as a pH-universal catalyst for hydrogen evolution reaction," *Nano Energy*, vol. 53, no. July, pp. 458–467, 2018, ISSN: 22112855. DOI: 10.1016/j.nanoen.2018.09.003. [Online]. Available: https://doi.org/10.1016/j.nanoen.2018.09.003.

[103] M. D. Hossain, Z. Liu, M. Zhuang, X. Yan, G. L. Xu, C. A. Gadre, A. Tyagi, I. H. Abidi, C. J. Sun, H. Wong, A. Guda, Y. Hao, X. Pan, K. Amine, and Z. Luo, "Rational Design of Graphene-Supported Single Atom Catalysts for Hydrogen Evolution Reaction," *Advanced Energy Materials*, vol. 9, no. 10, pp. 1–10, 2019, ISSN: 16146840. DOI: 10.1002/aenm.201803689.

[104] R. M. Q. Mello, E. A. Ticianelli, D. Q. D. Sho, and C. Usp, "Kinetic study of the hydrogen oxidation reaction on platinum and Nafion@ covered platinum electrodes," *Electrochim. Acta*, vol. 42, no. 6, pp. 1031–1039, 1997.

[105] J. Zheng, Y. Yan, and B. Xu, "Correcting the Hydrogen Diffusion Limitation in Rotating Disk Electrode Measurements of Hydrogen Evolution Reaction Kinetics," *Journal of The Electrochemical Society*, vol. 162, no. 14, F1470–F1481, 2015, ISSN: 0013-4651. DOI: 10.1149/2.0501514jes.

[106] W. Sheng, H. A. Gasteiger, and Y. Shao-Horn, "Hydrogen oxidation and evolution reaction kinetics on platinum: Acid vs alkaline electrolytes," *Journal of the Electrochemical Society*, vol. 157, no. 11, pp. 1529–1536, 2010, ISSN: 00134651. DOI: 10.1149/1.3483106.

[107] C. Wei, R. R. Rao, J. Peng, B. Huang, I. E. Stephens, M. Risch, Z. J. Xu, and Y. Shao-Horn, "Recommended Practices and Benchmark Activity for Hydrogen and Oxygen Electrocatalysis in Water Splitting and Fuel Cells," *Advanced Materials*, vol. 31, no. 31, pp. 1–24, 2019, ISSN: 15214095. DOI: 10.1002/adma.201806296.

[108] N. M. Marković, B. N. Grgur, and P. N. Ross, "Temperature-dependent hydrogen electrochemistry on platinum low-index single-crystal surfaces in acid solutions," *Journal of Physical Chemistry B*, vol. 101, no. 27, pp. 5405–5413, 1997, ISSN: 10895647. DOI: 10.1021/jp970930d.

[109] J. Durst, C. Simon, F. Hasche, and H. A. Gasteiger, "Hydrogen oxidation and evolution reaction kinetics on carbon supported Pt, Ir, Rh, and Pd electrocatalysts in acidic media," *Journal of the Electrochemical Society*, vol. 162, no. 1, F190–F203, 2015, ISSN: 19457111. DOI: 10.1149/2.0981501jes.

[110] A. R. Kucernak and C. Zalitis, "General Models for the Electrochemical Hydrogen Oxidation and Hydrogen Evolution Reactions: Theoretical Derivation and Experimental Results under Near Mass-Transport Free Conditions," *Journal of Physical Chemistry C*, vol. 120, no. 20, pp. 10 721–10 745, 2016, ISSN: 19327455. DOI: 10.1021/acs.jpcc.6b00011.

[111] V. Levich, *Physicochemical Hydrodynamics*. Englewood Cliffs, N.J.: Prentice-Hall, 1962.

[112] K. C. Neyerlin, W. Gu, J. Jorne, and H. A. Gasteiger, "Study of the Exchange Current Density for the Hydrogen Oxidation and Evolution Reactions," *Journal of The Electrochemical Society*, vol. 154, no. 7, B631, 2007, ISSN: 00134651. DOI: 10.1149/1.2733987.

[113] C. M. Zalitis, D. Kramer, J. Sharman, E. Wright, and A. R. Kucernak, "Pt Nano-Particle Performance for PEFC Reactions at Low Catalyst Loading and High Reactant Mass Transport," *ECS Transactions*, vol. 58, no. 1, pp. 39–47, 2013, ISSN: 1938-6737. DOI: 10.1149/05801.0039ecst.

[114] C. Zalitis, J. Sharman, E. Wright, and A. Kucernak, "Properties of the hydrogen oxidation reaction on Pt/C catalysts at optimised high mass transport conditions and its relevance to the anode reaction in PEFCs and cathode reactions in electrolysers," *Electrochimica Acta*, vol. 176, pp. 763–776, Sep. 2015, ISSN: 00134686. DOI: 10.1016/j.electacta.2015.06.146. [Online]. Available: http://dx.doi.org/10.1016/j.electacta.2015.06.146%20http://linkinghub.elsevier.com/retrieve/pii/S0013468615300669.

[115] Y. Qu, M. Shao, Y. Shao, M. Yang, J. Xu, C. T. Kwok, X. Shi, Z. Lu, and H. Pan, "Ultra-high electrocatalytic activity of VS2 nanoflowers for efficient hydrogen evolution reaction," *Journal of Materials Chemistry A*, vol. 5, no. 29, pp. 15 080–15 086, 2017, ISSN: 20507496. DOI: 10.1039/c7ta03172f.

[116] J. Zhang, C. Zhang, Z. Wang, J. Zhu, Z. Wen, X. Zhao, X. Zhang, J. Xu, and Z. Lu, "Synergistic Interlayer and Defect Engineering in VS 2 Nanosheets toward Efficient Electrocatalytic Hydrogen Evolution Reaction," *Small*, vol. 14, no. 9, p. 1 703 098, Mar. 2018, ISSN: 16136810. DOI: 10.1002/smll.201703098. [Online]. Available: http://doi.wiley.com/10.1002/smll.201703098.

[117] Z. Li, J. Y. Fu, Y. Feng, C. K. Dong, H. Liu, and X. W. Du, "A silver catalyst activated by stacking faults for the hydrogen evolution reaction," *Nature Catalysis*, vol. 2, no. December, 2019, ISSN: 25201158. DOI: 10.1038/s41929-019-0365-9. [Online]. Available: http://dx.doi.org/10.1038/s41929-019-0365-9.

[118] D. J. Sandbeck, N. M. Secher, F. D. Speck, J. E. Sørensen, J. Kibsgaard, I. Chorkendorff, S. Cherevko, and S. Cherevko, "Particle Size Effect on Platinum Dissolution: Considerations for Accelerated Stability Testing of Fuel Cell Catalysts," *ACS Catalysis*, vol. 10, no. 11, pp. 6281–6290, 2020, ISSN: 21555435. DOI: 10.1021/acscatal.0c00779.

[119] D. J. Myers, X. Wang, M. C. Smith, and K. L. More, "Potentiostatic and Potential Cycling Dissolution of Polycrystalline Platinum and Platinum Nano-Particle Fuel Cell Catalysts," *Journal of The Electrochemical Society*, vol. 165, no. 6, F3178–F3190, 2018, ISSN: 0013-4651. DOI: 10.1149/2.0211806jes.

[120] A. Pavlišič, P. Jovanovič, V. S. Šelih, M. Šala, N. Hodnik, and M. Gaberšček, "Platinum Dissolution and Redeposition from Pt/C Fuel Cell Electrocatalyst at Potential Cycling," *Journal of The Electrochemical Society*, vol. 165, no. 6, F3161–F3165, 2018, ISSN: 0013-4651. DOI: 10.1149/2.0191806jes.

[121] T. R. Hellstern, J. D. Benck, J. Kibsgaard, C. Hahn, and T. F. Jaramillo, "Engineering Cobalt Phosphide (CoP) Thin Film Catalysts for Enhanced Hydrogen Evolution Activity on Silicon Photocathodes," *Advanced Energy Materials*, vol. 6, no. 4, pp. 1–8, 2016, ISSN: 16146840. DOI: 10.1002/aenm.201501758.

[122] M. Boudart, "Turnover Rates in Heterogeneous Catalysis," *Chemical Reviews*, vol. 95, no. 3, pp. 661–666, May 1995, ISSN: 0009-2665. DOI: 10.1021/cr00035a009. [Online]. Available: https://pubs.acs.org/doi/abs/10.1021/cr00035a009.

[123] P. J. Rheinländer, J. Herranz, J. Durst, and H. A. Gasteiger, "Kinetics of the Hydrogen Oxidation / Evolution Reaction on Polycrystalline Platinum in Alkaline Electrolyte Reaction Order with Respect to Hydrogen Pressure," *J. Electrochem. Soc.*, vol. 161, no. 14, F1448–F1457, 2014. DOI: 10.1149/2.0501414jes.

[124] H. Fei, J. Dong, Y. Feng, C. S. Allen, C. Wan, B. Volosskiy, M. Li, Z. Zhao, Y. Wang, H. Sun, P. An, W. Chen, Z. Guo, C. Lee, D. Chen, I. Shakir, M. Liu, T. Hu, Y. Li, A. I. Kirkland, X. Duan, and Y. Huang, "General synthesis and definitive structural identification of MN4C4 single-atom catalysts with tunable electrocatalytic activities," *Nature Catalysis*, vol. 1, no. 1, pp. 63–72, 2018, ISSN: 25201158. DOI: 10.1038/s41929-017-0008-y. [Online]. Available: http://dx.doi.org/10.1038/s41929-017-0008-y.

[125] Y. Cheng, S. Zhao, B. Johannessen, J. P. Veder, M. Saunders, M. R. Rowles, M. Cheng, C. Liu, M. F. Chisholm, R. De Marco, H. M. Cheng, S. Z. Yang, and S. P. Jiang, "Atomically Dispersed Transition Metals on Carbon Nanotubes with Ultrahigh Loading for Selective Electrochemical Carbon Dioxide Reduction," *Advanced Materials*, vol. 30, no. 13, pp. 1–7, 2018, ISSN: 15214095. DOI: 10.1002/adma.201706287.

[126] H. B. Yang, S. F. Hung, S. Liu, K. Yuan, S. Miao, L. Zhang, X. Huang, H. Y. Wang, W. Cai, R. Chen, J. Gao, X. Yang, W. Chen, Y. Huang, H. M. Chen, C. M. Li, T. Zhang, and B. Liu, "Atomically dispersed Ni(i) as the active site for electrochemical CO 2 reduction," *Nature Energy*, vol. 3, no. 2, pp. 140–147, 2018, ISSN: 20587546. DOI: 10.1038/s41560-017-0078-8. [Online]. Available: http://dx.doi.org/10.1038/s41560-017-0078-8.

[127] X. X. Wang, D. A. Cullen, Y.-T. Pan, S. Hwang, M. Wang, Z. Feng, J. Wang, M. H. Engelhard, H. Zhang, Y. He, Y. Shao, D. Su, K. L. More, J. S. Spendelow, and G. Wu, "Nitrogen-Coordinated Single Cobalt Atom Catalysts for Oxygen Reduction in Proton Exchange Membrane

Fuel Cells," *Advanced Materials*, vol. 1706758, p. 1 706 758, 2018, ISSN: 09359648. DOI: 10.1002/adma.201706758. [Online]. Available: http://doi.wiley.com/10.1002/adma.201706758.

[128] A. A. Peterson, L. C. Grabow, T. P. Brennan, B. Shong, C. Ooi, D. M. Wu, C. W. Li, A. Kushwaha, A. J. Medford, F. Mbuga, L. Li, and J. K. Nørskov, "Finite-size effects in O and CO adsorption for the late transition metals," *Topics in Catalysis*, vol. 55, no. 19-20, pp. 1276–1282, 2012, ISSN: 10225528. DOI: 10.1007/s11244-012-9908-x.

[129] L. Li, A. H. Larsen, N. A. Romero, V. A. Morozov, C. Glinsvad, F. Abild-Pedersen, J. Greeley, K. W. Jacobsen, and J. K. Nørskov, "Investigation of catalytic finite-size-effects of platinum metal clusters," *Journal of Physical Chemistry Letters*, vol. 4, no. 1, pp. 222–226, 2013, ISSN: 19487185. DOI: 10.1021/jz3018286.

[130] Y. Chen, S. Ji, C. Chen, Q. Peng, D. Wang, and Y. Li, "Single-Atom Catalysts: Synthetic Strategies and Electrochemical Applications," *Joule*, vol. 2, no. 7, pp. 1242–1264, 2018, ISSN: 25424351. DOI: 10.1016/j.joule.2018.06.019. [Online]. Available: https://doi.org/10.1016/j.joule.2018.06.019.

[131] R. Qin, P. Liu, G. Fu, and N. Zheng, "Strategies for Stabilizing Atomically Dispersed Metal Catalysts," *Small Methods*, vol. 2, no. 1, pp. 1–21, 2018, ISSN: 23669608. DOI: 10.1002/smtd.201700286.

[132] S. Mitchell, E. Vorobyeva, and J. Pérez-Ramírez, "The Multifaceted Reactivity of Single-Atom Heterogeneous Catalysts," *Angewandte Chemie - International Edition*, vol. 57, no. 47, pp. 15 316–15 329, 2018, ISSN: 15213773. DOI: 10.1002/anie.201806936.

[133] J. Wan, W. Chen, C. Jia, L. Zheng, J. Dong, X. Zheng, Y. Wang, W. Yan, C. Chen, Q. Peng, D. Wang, and Y. Li, "Defect Effects on TiO2Nanosheets: Stabilizing Single Atomic Site Au and Promoting Catalytic Properties," *Advanced Materials*, vol. 30, no. 11, pp. 1–8, 2018, ISSN: 15214095. DOI: 10.1002/adma.201705369.

[134] H. Li, S. Wang, H. Sawada, G. G. Han, T. Samuels, C. S. Allen, A. I. Kirkland, J. C. Grossman, and J. H. Warner, "Atomic Structure and Dynamics of Single Platinum Atom Interactions with Monolayer MoS2," *ACS Nano*, vol. 11, no. 3, pp. 3392–3403, 2017, ISSN: 1936086X. DOI: 10.1021/acsnano.7b00796.

[135] N. M. Secher, "Mass-Selected Model Systems in Catalysis: From Nanoparticles to Single Atoms," Ph.D. dissertation, Technical University of Denmark, 2020.

[136] T. Kondo, T. Suzuki, and J. Nakamura, "Nitrogen doping of graphite for enhancement of durability of supported platinum clusters," *Journal of Physical Chemistry Letters*, vol. 2, no. 6, pp. 577–580, 2011, ISSN: 19487185. DOI: 10.1021/jz200077y.

[137] T. Kondo, S. Casolo, T. Suzuki, T. Shikano, M. Sakurai, Y. Harada, M. Saito, M. Oshima, M. I. Trioni, G. F. Tantardini, and J. Nakamura, "Atomic-scale characterization of nitrogen-doped graphite: Effects of dopant nitrogen on the local electronic structure of the surrounding carbon atoms," *Physical Review B - Condensed Matter and Materials Physics*, vol. 86, no. 3, pp. 1–6, 2012, ISSN: 10980121. DOI: 10.1103/PhysRevB.86.035436.

[138] E. Kemppainen, A. Bodin, B. Sebok, T. Pedersen, B. Seger, B. Mei, D. Bae, P. C. Vesborg, J. Halme, O. Hansen, P. D. Lund, and I. Chorkendorff, "Scalability and feasibility of photoelectrochemical H2 evolution: the ultimate limit of Pt nanoparticle as an HER catalyst," *Energy and Environmental Science*, vol. 8, no. 10, pp. 2991–2999, 2015, ISSN: 17545706. DOI: 10.1039/c5ee02188j.

[139] Y. Huttel, L. Martínez, A. Mayoral, and I. Fernández, "Gas-phase synthesis of nanoparticles: Present status and perspectives," *MRS Communications*, vol. 8, no. 3, pp. 947–954, 2018, ISSN: 21596867. DOI: 10.1557/mrc.2018.169.

[140] H. Haberland, M. Karrais, M. Mall, and Y. Thurner, "Thin films from energetic cluster impact: A feasibility study," *Journal of Vacuum Science & Technology A: Vacuum, Surfaces, and Films*, vol. 10, no. 5, pp. 3266–3271, 1992, ISSN: 0734-2101. DOI: 10.1116/1.577853.

[141] H. Hahn and R. S. Averback, "The production of nanocrystalline powders by magnetron sputtering," *Journal of Applied Physics*, vol. 67, no. 2, pp. 1113–1115, Jan. 1990, ISSN: 0021-8979. DOI: 10.1063/1.345798. [Online]. Available: http://aip.scitation.org/doi/10.1063/1.345798.

[142] B. Von Issendorff and R. E. Palmer, "A new high transmission infinite range mass selector for cluster and nanoparticle beams," *Review of Scientific Instruments*, vol. 70, no. 12, pp. 4497–4501, 1999, ISSN: 00346748. DOI: 10.1063/1.1150102.

[143] D. Guo, R. Shibuya, C. Akiba, S. Saji, T. Kondo, and J. Nakamura, "Active sites of nitrogen-doped carbon materials for oxygen reduction reaction clarified using model catalysts," *Science*, vol. 351, no. 6271, pp. 361–365, 2016, ISSN: 0036-8075. DOI: 10.1126/science.aad0832. [Online]. Available: http://www.sciencemag.org/cgi/doi/10.1126/science.aad0832.

[144] Y. C. Lin, P. Y. Teng, C. H. Yeh, M. Koshino, P. W. Chiu, and K. Suenaga, "Structural and Chemical Dynamics of Pyridinic-Nitrogen Defects in Graphene," *Nano Letters*, vol. 15, no. 11, pp. 7408–7413, 2015, ISSN: 15306992. DOI: 10.1021/acs.nanolett.5b02831.

[145] Q. Li, W. Chen, H. Xiao, Y. Gong, Z. Li, L. Zheng, X. Zheng, W. Yan, W. C. Cheong, R. Shen, N. Fu, L. Gu, Z. Zhuang, C. Chen, D. Wang, Q. Peng, J. Li, and Y. Li, "Fe Isolated Single Atoms on S, N Codoped Carbon by Copolymer Pyrolysis Strategy for Highly Efficient Oxygen

Reduction Reaction," *Advanced Materials*, vol. 30, no. 25, pp. 1–6, 2018, ISSN: 15214095. DOI: 10.1002/adma.201800588.

[146] G. Zhang, A. G. Güell, P. M. Kirkman, R. A. Lazenby, T. S. Miller, and P. R. Unwin, "Versatile Polymer-Free Graphene Transfer Method and Applications," *ACS Applied Materials and Interfaces*, vol. 8, no. 12, pp. 8008–8016, 2016, ISSN: 19448252. DOI: 10.1021/acsami.6b00681.

[147] K. Artyushkova, "Misconceptions in interpretation of nitrogen chemistry from x-ray photoelectron spectra," *Journal of Vacuum Science & Technology A*, vol. 38, no. 3, p. 031 002, May 2020, ISSN: 0734-2101. DOI: 10.1116/1.5135923.

[148] D. B. Trimarco, S. B. Scott, A. H. Thilsted, J. Y. Pan, T. Pedersen, O. Hansen, I. Chorkendorff, and P. C. K. Vesborg, "Enabling real-time detection of electrochemical desorption phenomena with sub-monolayer sensitivity," *Electrochimica Acta*, 2018.

[149] S. B. Scott, J. Kibsgaard, P. C. Vesborg, and I. Chorkendorff, "Tracking oxygen atoms in electrochemical CO oxidation - Part II: Lattice oxygen reactivity in oxides of Pt and Ir," *Electrochimica Acta*, vol. 374, p. 137 844, 2021, ISSN: 00134686. DOI: 10.1016/j.electacta.2021.137844. [Online]. Available: https://doi.org/10.1016/j.electacta.2021.137844.

[150] G. S. Parkinson, "Single-Atom Catalysis: How Structure Influences Catalytic Performance," *Catalysis Letters*, vol. 149, no. 5, pp. 1137–1146, 2019, ISSN: 1572879X. DOI: 10.1007/s10562-019-02709-7. [Online]. Available: http://dx.doi.org/10.1007/s10562-019-02709-7.

Appendices

Appendix A

Paper I

Highly active, selective, and stable Pd single-atom catalyst anchored on N-doped hollow carbon sphere for electrochemical H_2O_2 synthesis under acidic conditions

Jiangbo Xi, Sungeun Yang, Luca Silvioli, Sufeng Cao, Pei Liu, Qiongyang Chen, Yanyan Zhao, Hongyu Sun, Johannes Novak Hansen, Jens-Peter B. Haraldsted, Jakob Kibsgaard, Jan Rossmeisl, Sara Bals, Shuai Wang, Ib Chorkendorff

Journal of Catalysis, Volume 393, 2021, Pages 313-323

https://doi.org/10.1016/j.jcat.2020.11.020

Cited as reference [48] in present thesis

Journal of Catalysis 393 (2021) 313–323

Contents lists available at ScienceDirect

Journal of Catalysis

journal homepage: www.elsevier.com/locate/jcat

Highly active, selective, and stable Pd single-atom catalyst anchored on N-doped hollow carbon sphere for electrochemical H_2O_2 synthesis under acidic conditions

Jiangbo Xi [a,i,1], Sungeun Yang [b,j,1], Luca Silvioli [c,d,1], Sufeng Cao [e,1], Pei Liu [f], Qiongyang Chen [f], Yanyan Zhao [g], Hongyu Sun [h], Johannes Novak Hansen [b], Jens-Peter B. Haraldsted [b], Jakob Kibsgaard [b], Jan Rossmeisl [c], Sara Bals [f], Shuai Wang [a,*], Ib Chorkendorff [b,*]

[a] Key Laboratory of Material Chemistry for Energy Conversion and Storage, Ministry of Education, School of Chemistry and Chemical Engineering, Huazhong University of Science and Technology, Wuhan 430074, PR China
[b] Department of Physics, Technical University of Denmark, DK-2800 Kongens Lyngby, Denmark
[c] Nano-Science Center, Department of Chemistry, University of Copenhagen, Copenhagen Ø DK-2100, Denmark
[d] Seaborg Technologies ApS, Titangade 11, Copenhagen DK-2200, Denmark
[e] Department of Chemical and Biological Engineering, Tufts University, Medford, MA 02155, United States
[f] Electron Microscopy for Materials Science, University of Antwerp, Groenenborgerlaan 171, 2020 Antwerp, Belgium
[g] Department of Chemistry, Merkert Chemistry Center, Boston College, Chestnut Hill, MA 02467, United States
[h] Department of Micro- and Nanotechnology, Technical University of Denmark, DK-2800 Kongens Lyngby, Denmark
[i] School of Chemistry and Environmental Engineering, Key Laboratory of Green Chemical Engineering Process of Ministry of Education, Wuhan Institute of Technology, Wuhan 430205, China
[j] Center for Energy Materials Research, Korea Institute of Science and Technology (KIST), Hwarangno 14-gil 5, Seongbuk-gu, Seoul 02792, South Korea

ARTICLE INFO

Article history:
Received 31 August 2020
Revised 29 October 2020
Accepted 13 November 2020
Available online 26 November 2020

Keywords:
Single-atom catalyst
Nitrogen doped carbon
Hydrogen peroxide
Electrochemical synthesis
Density functional theory

ABSTRACT

Single-atom catalysts (SACs) have recently attracted broad scientific interests due to their unique structural feature, the single-atom dispersion. Optimized electronic structure as well as high stability are required for single-atom catalysts to enable efficient electrochemical production of H_2O_2. Herein, we report a facile synthesis method that stabilizes atomic Pd species on the reduced graphene oxide/N-doped carbon hollow carbon nanospheres (Pd1/N-C). Pd1/N-C exhibited remarkable electrochemical H_2O_2 production rate with high faradaic efficiency, reaching 80%. The single-atom structure and its high H_2O_2 production rate were maintained even after 10,000 cycle stability test. The existence of single-atom Pd as well as its coordination with N species is responsible for its high activity, selectivity, and stability. The N coordination number and substrate doping around Pd atoms are found to be critical for an optimized adsorption energy of intermediate *OOH, resulting in efficient electrochemical H_2O_2 production.

1. Introduction

Hydrogen peroxide, H_2O_2, is an environmentally friendly oxidant with annual production over 5 million tons and its wide usage covers bleaching, chemicals synthesis, and waste water treatment [1,3,4]. Current production of H_2O_2 is limited by the anthraquinone process which is a viable batch process that requires a centralized plant [4]. Centralized production requires additional costs for distillation, transportation, and dilution at the point of use [1]. Thermal catalysis for H_2O_2 synthesis has potential for the decentralized production with high yields in batch reactors, but developments in flow reactors remain a challenge in this technology's applicability [2,5–12]. Electrochemical synthesis of H_2O_2 by the oxygen reduction reaction in acidic conditions holds promise for decentralized, on-site production, where the electrochemical device requires only water, air, and electricity [1,13–16]. Designing a selective and active cathode catalyst with high stability in acidic conditions is critical for realizing electrochemical H_2O_2 production [17]. Single atom catalysts (SACs), particularly single metal atoms stabilized in a porphyrin-like support, are promising as selective, active, and stable catalysts for various electrochemical reactions including the oxygen reduction reaction (ORR) resulting in the scalable electrochemical production of H_2O_2 [15,18–21].

* Corresponding authors.
E-mail addresses: chmsamuel@hust.edu.cn (S. Wang), ibchork@fysik.dtu.dk (I. Chorkendorff).
[1] These authors contributed equally.

https://doi.org/10.1016/j.jcat.2020.11.020
0021-9517/

Acidic conditions have an advantage over alkaline conditions for H_2O_2 production. In alkaline conditions, H_2O_2 can be easily produced by using a glassy carbon electrode, but the product HO_2^-, is unstable, thus its applicability is limited to processes where the H_2O_2 must be used immediately. In contrast, acidic conditions stabilize H_2O_2, and allow the use of durable proton-exchange membranes resulting in the production of pure aqueous H_2O_2 solution, which has broader applications. The overall reactions of oxygen reduction and their thermodynamic equilibrium potentials versus reversible hydrogen electrode (RHE) in acidic conditions are as follows:

$$O_2 + 2H^+ + 2e^- \rightarrow H_2O_2$$

$$(U_0 = +0.7 \text{ V vs RHE}) \quad (1)$$

$$O_2 + 4H^+ + 4e^- \rightarrow 2H_2O$$

$$U_0 = +1.23 \text{ V vs RHE}) \quad (2)$$

The oxygen reduction reaction can either produce H_2O_2 *via* 2-electron (2e) pathway (1) or H_2O *via* 4-electron (4e) pathway (2). Efficient catalyst for electrochemical H_2O_2 production should produce H_2O_2 *via* the 2e pathway with high selectivity at a high rate. Adsorption energies of reaction intermediates are often good descriptors to rationalize given catalytic reaction. The only intermediate in the 2e pathway is *OOH, and the 4e pathway has additional intermediates *OH and *O. There are two principles determining catalytic performance for electrochemical H_2O_2 production. The first principle is *electronic effect*. Adsorption energy of the intermediate *OOH is tuned by the electronic structure of catalyst, and it should neither be too strong nor too weak, as stated in the Sabatier principle. A weak affinity for the reaction intermediates is preferred to inhibit O-O bond dissociation, limiting the 4e pathway that yields H_2O production. The second principle is *geometric effect*. On a metal surface, the most stable adsorption site for *OOH and *OH is on-top, while *O prefer to sit in a hollow site. On single site catalysts, isolated atoms cannot provide a hollow adsorption site, therefore *O is forced to bind on-top site, weakening its adsorption energy as compared to the other reaction intermediates. The selective destabilization of *O as compared to *OOH is the reason why single site catalysts are frequently studied for the 2e pathway [1,16,22].

Single-atom catalysts (SAC) have the potential to provide optimal active site structures for state-of-the-art electrochemical H_2O_2 production in acidic conditions [1,13–15]. Siahrostami *et al.* (2013) provided a rational background for designing new catalysts for electrochemical H_2O_2 production by alloying a strong oxygen adsorbing element, Pt, with a weaker oxygen adsorbing element, Hg. Alloying these two elements resulted in the isolation of a single active Pt atom surrounded by less active Hg atoms, providing an optimized electronic structure, electronic effect, and geometric effect [22]. Following this idea, Verdaguer-Casadevall et al. (2014) examined a set of Metal-Hg surfaces and Pd-Hg was found to be the best catalyst providing the highest activity up to this date [16]. A similar strategy was applied for Pd-Au alloy [23,24], cobalt-porphyrin (Co-N_4) like structures [13,15,25,26], and more recently sulfide type catalysts, Pt_1-CuS_x [27] and CoS_2 [28], have been proposed where S atoms serving as weak *OOH adsorbing element. Atomically dispersed active sites satisfy the geometric requirements; and maximized utilization of noble metal atoms may dramatically reduce the materials cost. Previous work reported that Pt single-atoms on TiN [29], TiC [30], S doped carbon [31] provided high selectivity for 2e pathway with appreciable activity. Tuning the electronic structure of single-atom catalysts (SAC) can lead to even higher activity through an optimized electronic effect.

The anchoring site plays a crucial role in improving the activity, stability and selectivity of the SAC *via* a direct coordination effect between atomic metal and support [30,32,33]. The metal-coordination not only alters the electronic effect, but also, very importantly, determines the stability of the atomic structure. The interaction between support and metal atom can be strengthened by modifying support materials and introducing coordination sites for atomic metal [34–36]. Recent findings also showed that selectivity can be tuned through electronic effect and/or heteroatoms (e.g., N, O, S) electron donation between metal and heteroatom containing supports [37–39]. In line with this, a suitable support material that provides anchoring sites and coordination environment for single atoms are important to achieve satisfactory catalytic performance.

In this work, we propose a strategy to overcome the stability issue and improve the activity and the selectivity of SACs by introducing suitable coordination sites for Pd single-atoms. Pd atoms are anchored by doped N species on a hollow carbon nanosphere *via* dative coordination. We have previously synthesized hollow carbon nanospheres by taking a graphene oxide (GO) shell and coated it with amorphous carbon. These nanospheres anchored Pd single-atom sites and exhibited high stability towards 4-nitrophenol reduction reaction [40]. In this work we introduced N sites into the carbon support to further modify the coordination environment for Pd single-atom. Here we present the preparation of Pd single-atoms anchored on N-doped hollow carbon nanospheres (Pd1/N-C) and its enhanced electrochemical performance for the oxygen reduction reaction. The mass activity of Pd1/N-C was comparable to the best performing catalysts with 78.9 ± 2.5% faradaic efficiency. Single-atom dispersion of Pd1/N-C was maintained even after 10,000 cycle "on-off" test with little activity degradation showing its exceptional stability. The Pd single site surrounded by six coordinating pyridinic N atoms and moderate additional graphitic N doping was suggested as a possible explanation of the observed high activity by density functional theory (DFT) calculations.

2. Experimental section

2.1. The detailed fabrication process of Pd1/N-C SAC

2.1.1. Synthesis of GO wrapped SiO_2 (SiO_2@GO) spheres

SiO_2 spheres (100–200 nm) were synthesized as templates by the Stöber method [41]. GO was prepared according to a modified Hummers method [42]. In a typical synthesis, 0.2 g of SiO_2 spheres were firstly dispersed in 100 mL ethanol by sonication for 20 min. Next, 1 mL of 3-aminopropyltrimethoxysilane was added and refluxed for 5 h to obtain amine-functionalized SiO_2 nanospheres. After the products were centrifugated and re-dispersed in 100 mL DI water, 30 mL of 0.2 mg/mL GO aqueous solution was added and stirred vigorously for 1 h. During this process, the amino-functionalized SiO_2 nanospheres were tightly wrapped by a graphene oxide (GO) nanosheets through electrostatic reaction and hydrogen bonds between the amino group and the oxygen-containing groups on GO sheets (step 1 in Fig. S4) [43]. Finally, the products were collected by centrifugation, washed with water several times, and then dried at 60 °C overnight.

2.1.2. Synthesis of N-C

The surface of the SiO_2@GO nanospheres was further coated by polydopamine [44]. Typically, 200 mg of as-prepared SiO_2@GO spheres were dispersed in 100 mL of 2 mg mL^{-1} dopamine Tris solution (pH 8.5, 10 mM Tris buffer) and allowed to react for 36 h under stirring at room temperature. The resultant SiO_2@GO@PDA was separated and collected, and subsequently washed

for 5 cycles and dried by freeze-drying. After that, the resulting powder was carbonized at 900 °C for 3 h under inert atmosphere. Finally, the as-prepared SiO_2@N-C spheres were then transformed into N-C hollow carbon nanospheres by etching the SiO_2 cores with HF solution (≈2%) for two times.

2.1.3. Synthesis of Pd1/N-C SAC

50 mg of N-C composites were dispersed in 50 mL DI water. Then, 0.5 mg of K_2PdCl_4 was added to the suspension and stirred for 2 h in an ice bath. During this process, Pd atoms were deposited on the confined interface of N-C support, leading to the formation of Pd1/N-C SAC. Afterwards, the reaction mixture was filtered and washed three times with pure water to remove the remaining reagents. Finally, the resulting solid Pd1/N-C catalysts were collected and dried by freeze-drying.

2.2. Electrochemical measurements details

All electrochemical measurements were conducted in a conventional three electrode electrochemical cell with a potentiostat or a bi-potentiostat (VMP2, Bio-Logic). A graphite rod (Grade 1, Ted Pella) was used as a counter electrode, and a mercury-mercurous sulphate reference electrode (SI Analytics) was used as the reference electrode. The electrolyte was 0.1 M $HClO_4$ prepared from 70% $HClO_4$ (Merck Suprapur) purged with either O_2 (5N5, AGA) or Ar (5N5, AGA). All measurements were performed at room temperature, 25 ± 1 °C. All potentials reported in this study are referred to the reversible hydrogen electrode (RHE) scale. The RHE was calibrated by performing hydrogen evolution and oxidation reactions in a H_2-purged electrolyte using a Pt wire. The catalyst ink was composed of 5 mg of catalyst dispersed in a solution containing 3.75 mL of ethanol (≥99.8%, Fluka Analytical), 1.25 mL of ultrapure water (18.2 MΩ cm, Millipore Synergy uV water purification system), and 15 μl of Nafion solution (5% in lower aliphatic alcohols, Sigma-Aldrich). The ink was ultrasonicated in an ultrasonic bath for at least 30 min before drop casting.

2.2.1. Rotating ring disk electrode measurements

Rotating ring disk electrode (ChangeDisk, Pine Research Inst.) with a glassy carbon disk electrode (Pine Research Inst.) and a platinum ring electrode was used for RRDE measurements. Glassy carbon electrode was polished before use with alumina slurry suspension (Buehler), first with 0.3 μm and then with 0.05 μm particle size. The electrode was cleaned between the two polishing steps by ultra-sonicating in ultrapure water and in isopropyl alcohol (EMSURE, Merck). After polishing with 0.05 μm silica powder, the electrode was cleaned by ultra-sonicating in ultrapure water and in isopropyl alcohol, three times repetitively. The ink was drop casted on to the glassy carbon electrode with a loading amount of 15 μg catalyst on to 5 mm diameter glassy carbon electrode. The ink was dried at room temperature. The Ohmic drop was measured by electrochemical impedance spectroscopy and compensated manually after the measurements. Before performing RRDE measurements, platinum ring electrode was activated by cycling between 0.05 V and 1.6 V for 100 cycles with a scan rate of 500 mV s^{-1} in an Ar-saturated 0.1 M $HClO_4$. The ORR was conducted by performing cyclic voltammetry between −0.2 V to 0.7 V in an O_2-saturated 0.1 M $HClO_4$ solution with a scan rate of 50 mV/s and a rotating rate of 1600 rpm. First few cycles of ORR show low activity with small double layer capacitance region due to poor wetting of the electrode. After ~5 cycles of CVs catalyst coated glassy carbon electrode becomes completely wet and shows higher activity with larger double layer capacitance region. Blank CV was also measured in an Ar-saturated 0.1 M $HClO_4$ to subtract the double layer capacity region from ORR CVs. The potential of the Pt ring electrode was maintained at 1.4 V during the ORR measurement to oxidize H_2O_2 produced. Accelerated durability tests were performed by cycling potential between 0.05 V and 0.7 V for 10,000 cycles with a scan rate of 500 mV s^{-1} and a rotating rate of 400 rpm in an O_2-saturated 0.1 M $HClO_4$. The electrolyte was changed after the durability test to minimize the effect of H_2O_2 produced during the course of durability test on the forthcoming ORR measurement.

2.2.2. 3-compartment cell measurements

Gas diffusion electrode submerged in 0.1 M $HClO_4$ in three compartments set-up. The catalyst ink, described above, was drop-casted with a loading of 0.1 mg cm^{-2} on a gas diffusion layer (H15, Freudenberg) substrate placed on a 60 °C hot plate on an area of approximately 2 cm^2. This gas diffusion electrode (GDE) was used as a working electrode for the H_2O_2 accumulation tests.

A conventional three-electrode electrochemical cell was used. Catalyst casted GDE was used as a working electrode, a graphite rod as a counter electrode, and a mercury-mercurous sulphate reference electrode as a reference electrode. The working electrode was separated from the counter electrode by Nafion 117 membrane. The Ohmic drop was measured by electrochemical impedance spectroscopy and compensated by 85% using automatic compensation (EC-Lab, BioLogic). Three electrode experiments with stagnant electrode were conducted at a potential of 0.2 V for up to 15 C of accumulated charge in an O_2-saturated 0.1 M $HClO_4$. Resulting hydrogen peroxide was quantified by permanganate titration method using 0.02 M $KMnO_4$ (Titripur, EMD Millipore).

2.3. Computational details

All ground state DFT calculations were performed at the GGA level with the Grid-based Projected Augmented Wave (GPAW) program [45,46] and the Atomic Simulation Environment (ASE) package [47]. We used finite difference mode with the BEEF-vdW exchange and correlation functional [48], sampling the Brillouin zone with a 2 × 2 × 1 Monkhorst-Pack *k*-point set and a grid spacing of h = 0.18 Å. All structures were relaxed to a force below 0.05 eV/Å. The unit cell for all structure is periodic in x and y directions, while we applied a vacuum of 8 Å to each side of the catalyst plane along the z-axis. To evaluate the Gibbs free energy contribution, the entropy and zero point energy corrections were added to the DFT energies [49]. For all the structures calculated, we added solvation corrections to take into account water induced stabilization of the reaction intermediates [50]. After publication, all structures with total energies will be available on Jan Rossmeisl' group homepage at the URL: http://nano.ku.dk/english/research/theoretical-electrocatalysis/katladb/.

3. Results and discussion

3.1. Preparation of catalysts

Pd1/N-C along with three control samples were prepared and tested for electrochemical H_2O_2 production. Synthesis of Pd1/N-C consists of four steps: (1) GO coating of SiO_2 nanospheres, SiO_2@-GO; (2) dopamine polymerization and coating, SiO_2@GO@polydopamine (SiO_2@GO@PDA); (3) post carbonization and etching of SiO_2 template; (4) Pd deposition *via* the direct adsorption of Pd species (Fig. 1a and d) [40]. The additional three control samples were prepared to elucidate the effect of individual parameters: single-atom, N-dopant species, and carbon support. Pd nanoparticle deposited on reduced graphene oxide (RGO) (PdNP/C, Fig. 1c and d) was prepared as a control sample for the single-atom dispersion parameter. Pd single-atom on non-N-doped hollow amor-

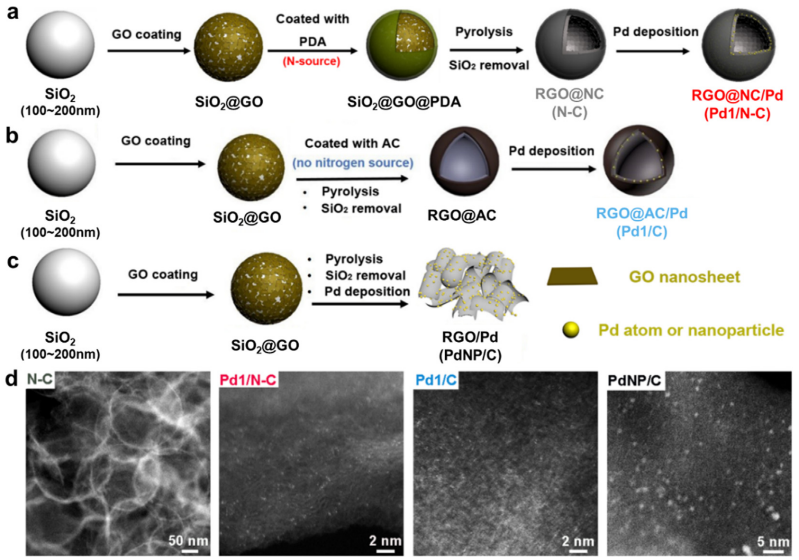

Fig. 1. Schematic illustration of the preparation steps and representative images. Schematic illustration of the preparation of (a) N-doped hollow carbon nanospheres without Pd (N-C) and Pd single-atom anchored at N-doped hollow carbon nanospheres (Pd1/N-C), (b) Pd single-atom at non-doped hollow AC nanospheres (Pd1/C), (c) Pd nanoparticles deposited on RGO (PdNP/C), and representative HAADF-STEM images of the catalysts.

phous carbon (AC) nanospheres (Pd1/C, Fig. 1b and d) was prepared as a control sample for the N-dopant species parameter. N-doped hollow carbon nanospheres without Pd (N-C, Fig. 1a and d) was prepared as a control sample for the carbon support parameter. Weight percent of Pd was controlled to 0.3 wt% except for N-C catalyst, and same catalyst amount was tested. Detailed description of the catalysts will be discussed later.

3.2. Electrochemical production of H_2O_2

Electrochemical H_2O_2 production using Pd1/N-C was first characterized with rotating ring-disk electrode (RRDE) measurements (Fig. 2). RRDE permits easy and fast determination of catalytic activity for oxygen reduction reaction as well as selectivity towards H_2O_2. As seen in Fig. 2d, oxygen is reduced to either H_2O_2 or H_2O at the surface of the disk electrode with the catalyst of interest. Radial convection introduces the H_2O_2 product to the ring electrode where H_2O_2 is oxidized back to O_2. Catalytic activity and selectivity for H_2O_2 production is determined by measuring and comparing the reductive current of the disk electrode and the oxidative current of the ring electrode. In this article, we refer to selectivity in terms of faradaic efficiency, i.e., the ratio between electrons used for H_2O_2 production and the total current used in the oxygen reduction reaction

Pd1/N-C SAC (Fig. 1a) was compared with the state-of-the-art catalyst surfaces measured by RRDE in the form of Tafel plots in Fig. 2a and b.[1,13,15,16,22–29,31,51] Peak faradaic efficiencies of each catalyst is plotted in Fig. 2c. Fig. 2a presents Tafel plots showing specific activity of different catalyst surfaces using polycrystalline surfaces (pc); the plot compares intrinsic activities of catalyst surfaces. To accurately benchmark the intrinsic activity of Pd1/N-C with polycrystalline surfaces, we have controlled the density of active atoms on the electrode to 2.15 $nmol_{Pd}$ cm^{-2}_{geo}, which is in the range of low index surfaces of precious metals such as Pt, Pd, Au, and Ag (2.00–2.53 $nmol_{PM}$ cm^{-2}_{geo}). Intrinsic activity of Pd1/N-C per site is slightly higher than Ag(pc) and Ag-Hg(pc) and lower than Pt-Hg(pc) and Pd-Hg(pc). The merit of SAC is its high utilization, that is high mass activity. The mass activity is compared in Fig. 2b. The mass activity of Pd1/N-C is comparable to the best reported catalysts, Pd-Hg/C and various Co-N/C catalysts. Since Pd is heavier atom, higher atomic mass, than Co, we replotted Fig. 2b into activity per mole for more precise comparison in Fig. S1. In this new plot, Pd1/N-C is more active than Co-N/C (2) and Co-N/C (3) catalysts in most of the potential range. Use of mercury, Hg, might draw concerns from end-users, making Pd1/N-C and Co-N/C catalysts the best candidates for electrochemical H_2O_2 production in terms of activity.

The Pd1/N-C catalyst sample (Fig. 1a) and three additional control samples were compared in a RRDE set-up (Fig. 3). Pd1/N-C showed the highest faradaic efficiency of 78.9 ± 2.5% as well as highest H_2O_2 production rate, shown by the highest ring current. The three control samples were prepared to elucidate the effects of individual parameters of the Pd1/N-C catalyst. The N-doped hollow carbon nanospheres without Pd single-atom (N-C, Fig. 1a), showed the lowest activity, suggesting insignificant effects from the support. The Pd-nanoparticles catalyst (PdNP/C) was prepared (Fig. 1c) to test the effects of the single atom parameter. PdNP/C had a lower faradaic efficiency towards H_2O_2. As expected and in contrast to single atom sites, a nanoparticle structure with continuous active sites facilitates the 4e pathway to H_2O due to the presence of hollow sites. A single atom Pd catalyst without N-doping (Pd1/C) was prepared (Fig. 1b) to test the effects of the N-dopant. Pd1/C had less activity as well as less selectivity towards H_2O_2 in comparison to Pd1/N-C. This suggests that the N-dopant coordinates with the Pd single-atom to increase the activity and selectivity. In addition, Pd1/C had a selectivity comparable to the PdNP/C, challenging the effect of the single atom site parameter, in RRDE set-up.

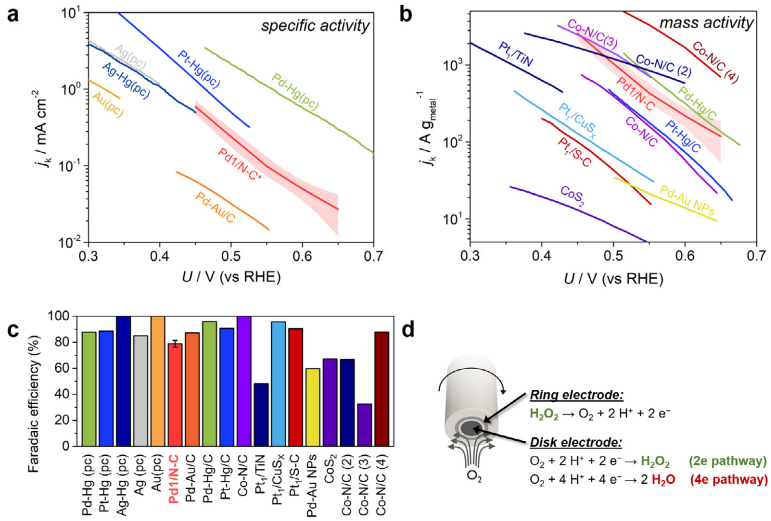

Fig. 2. Comparison of state-of-the-art catalysts and present work for electrochemical production of H_2O_2 using RRDE measurements. Tafel plots of mass-transport corrected kinetic current densities for electrochemical H_2O_2 production in acidic media based on RRDE measurements for (a) specific activity, and (b) mass activity. Red line and pale red bands of Pd1/N-C indicate mean and standard deviation of three independent measurements. (c) Peak faradaic efficiency towards H_2O_2. (d) Schematic of RRDE measurement. Data adapted from Ref. [22] for Pt–Hg(pc, polycrystalline) and Pt–Hg/C; Ref. [16] for Pd–Hg(pc) and Pd–Hg/C; Ref. [1] for Ag(pc), and Ag-Hg(pc); Ref. [23] for Pd–Au NPs; Ref. [51], for Au(pc); Ref. [24] for Pd–Au/C; Ref. [26] for Co–N/C; Ref. [29] for Pt_1/TiN; Ref. [31] for Pt_1/S–C; Ref. [27] for Pt_1/CuS_X; Ref. [28] for CoS_2; Ref. [13] for Co-N/C (2); Ref. [15] for Co-N/C (3); Ref. [25] for Co-N/C (4). Data noted with asterisk, *, have been normalized with the geometric surface area of the working electrode.

The most critical issue in SACs is its low stability and obtaining stable SACs is a key challenge for the development of SACs [40,52–54]. The operating potential of electrochemical production of H_2O_2 is below 1.0 V vs RHE, where electrochemical oxidation of carbon support is not significant. However, H_2O_2 is highly oxidizing chemical and known to oxidize carbon supports chemically even below 1.0 V vs RHE [55,56]. The durability of the prepared catalysts was assessed by adopting "on–off" accelerated durability test. The potential was cycled between 0.05 V and 0.7 V for 10,000 cycles and H_2O_2 was accumulated in the electrolyte solution over time. The potential range represents "off-condition" at 0.7 V where no H_2O_2 is being produced, and "on-condition" at 0.05 V where H_2O_2 is being produced with limiting current density for all four catalysts. Oxygen reduction reaction RRDE measurements were performed before and after the "on-off" cycling and compared in Fig. 4a. When the production rate of H_2O_2 were compared, Pd1/N-C was far better than other 3 samples after 10,000 cycles "on-off" test. The H_2O_2 production current, depicted by the ring current curve, was only slightly shifted negatively for Pd1/N-C, while the peak current and selectivity remained almost the same before and after the stability test. This suggests that although 2e pathway deactivated to a certain extent, 4e pathway also deactivated to a similar or to a greater extent after 10,000 cycles "on-off" test. We note that if the selectivity is maintained, the decrease in the activity can be easily compensated by slightly increasing the applied voltage. H_2O_2 production currents decreased for other three samples after the stability tests. This accentuates the improved stability of Pd1/N-C compared to other samples. All four samples showed similar extent of activity degradation for oxygen reduction reaction, shown in disk currents. Potentials where current density reaches −1.5 mA cm^{-2}, half-wave potential for 2e pathway, were compared before and after the stability tests. Potential difference was 0.05 V (0.40–0.35 V) for Pd1/N-C, which was similar or better than 0.06 V (0.33–0.27 V) for Pd1/C, 0.05 V (0.26–0.21 V) for N-C, and 0.1 V (0.45–0.35 V) for PdNP/C. Interestingly, PdNP/C showed the poorest stability. Even after 10,000 cycle "on-off" test, Pd1/N-C showed no obvious sign of aggregation observed by HAADF-

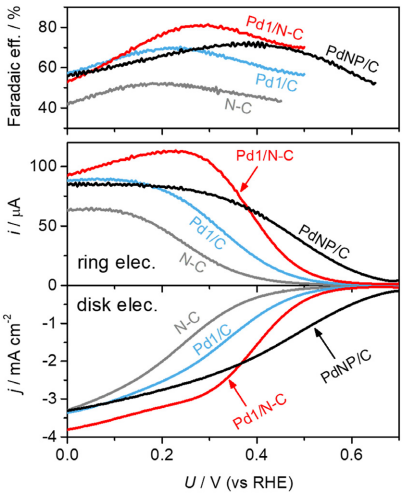

Fig. 3. Comparison of Pd1/N–C with control samples, electrochemical production of H_2O_2 using RRDE measurements. Oxygen reduction reaction on different catalysts using rotating ring-disk electrode. From bottom to top: current density plot from the disk electrode showing total oxygen reduction current, current from oxidation of H_2O_2 at the ring electrode, and Faradaic efficiency towards H_2O_2 production. Measurements in O_2-saturated 0.1 M $HClO_4$ with a rotating rate of 1600 rpm at room temperature.

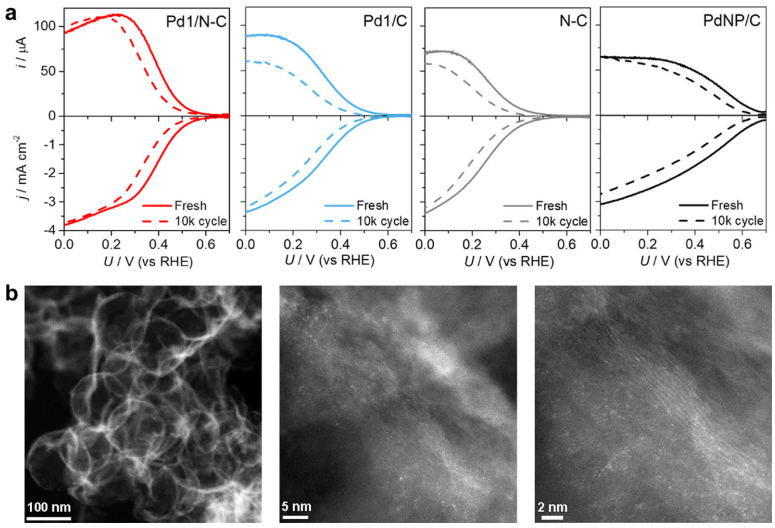

Fig. 4. Electrochemical durability assessment by 10,000 cycle "on-off" test. (a) Oxygen reduction reaction on different catalysts using a rotating ring-disk electrode before and after 10,000 cycle "on-off" durability test. Measurements in O_2-saturated 0.1 M $HClO_4$ with a rotating rate of 1600 rpm at room temperature. "On-off" durability test was performed by potential cycling between 0.05 V and 0.7 V with a scan rate of 500 mV s^{-1} in O_2-saturated 0.1 M $HClO_4$ with a rotating rate of 400 rpm at room temperature. (b) Aberration-corrected HAADF-STEM image of Pd1/N-C SAC and enlarged HAADF-STEM image after 10,000 cycle "on-off" test.

STEM, Fig. 4b. No nanometer sized metal cluster was observed at lower magnification and only the single-atoms and few sub-nanometer Pd clusters were observed at higher magnification. Preservation of atomically dispersed Pd single-atoms was key to retain high selectivity after the stability test.

While RRDE measurements are a convenient and widely practiced tool to benchmark electrochemical production of H_2O_2, they have limitations in determining the selectivity of catalysts. As we have discussed in our earlier perspective article, RRDE measurements only provide an upper-bound selectivity [1]. A thin catalyst layer on the disk electrode coupled with forced convection by rotating the electrode shortens the residence time of produced H_2O_2. As a result, further reduction of H_2O_2 to H_2O is poorly represented in RRDE measurements in comparison to more realistic scalable set-ups. For this reason, some catalysts that showed high selectivity in RRDE measurements fail to perform in more realistic set-ups with higher local concentrations of H_2O_2 and slower mass transport [1]. It is therefore imperative to test H_2O_2 production catalysts in more realistic conditions. We have adopted a three-compartment set-up where a catalyst-deposited gas diffusion electrode (GDE) is submerged into the O_2-purged electrolyte and the working electrode potential is held at 0.2 V vs RHE (Fig. 5a and Fig. S2). During testing, there was no forced convection other than the bubbling of O_2 gas and over 100 ppm of H_2O_2 accumulated in the electrolyte, where the H_2O_2 was quantified by permanganate titration using a 0.02 M $KMnO_4$ titrant. At concentrations over 100 ppm without forced convection, further reduction of H_2O_2 to H_2O is no longer negligible. In these conditions, the Pd1/N-C catalyst again had the highest partial current density for H_2O_2 (Fig. 5c) and maintained faradaic efficiencies of over 80% across experiments with an accumulated total charge of 15 C (Fig. 5b). Again, the N-doped hollow carbon nanospheres without Pd single-atom (N-C), showed the lowest activity. PdNP/C catalyst had an improved overall oxygen reduction activity but with lower selectivity towards H_2O_2, than both N-C and Pd1/C, which is different from the RRDE results. Pd1/C had less activity as well as less selectivity towards H_2O_2 in comparison to Pd1/N-C. This is the same as the RRDE results and reconfirms that the N-dopant coordinates with the Pd single-atom to increase the activity and selectivity. We conclude that coordinating Pd single-atoms to N-doped carbon is successful strategy for preparing an efficient catalyst for the selective electrochemical production H_2O_2 in realistic applied set-ups. It should also be noted that the selectivity of Pd1/C was higher than PdNP/C, confirming the effects of the single atom site parameter. These observations reinforce our arguments for benchmarking H_2O_2 production using a more realistic scalable set-up in addition to RRDE measurements. The performance of the Pd1/N-C catalyst in a scalable set-up stresses the impact of this catalyst.

3.3. Characterization of Pd1/N-C SAC and control samples.

A templating method was employed in the synthesis of the N-C nanospheres as shown in Fig. 1a. Fig. S3 and Fig. S4, show hollow nanosphere structure. Hollow structured spherules with the shell thicknesses of ~10 nm, can be used as support of nano-reactor in heterogeneous catalysis. The morphology of Pd1/N-C SACs and PdNP/C composites were initially characterized by scanning electron microscopy (SEM) and aberration-corrected high-angle annular dark-field scanning transmission electron microscopy (HAADF-STEM). As can be seen from the SEM images, the Pd1/N-C atomic catalysts demonstrate spherical structure (Supplementary Fig. S3), while PdNP/C composite exhibited a randomly-stacked sheet-like morphology (Supplementary Fig. S5), indicating that the outer PDA-derived carbon coating facilitates the resulting hollow carbon nanosphere structure. Tomography results (Fig. S6, S7, Supplementary Movie 1 and Movie 2) further indicate a hollow nanosphere structure. However, the contrast of the initial RGO coating and the subsequent N-doped amorphous carbon coating is indistinguishable. It can be speculated that there is a double carbon shell present from the connection of two tangent spheres

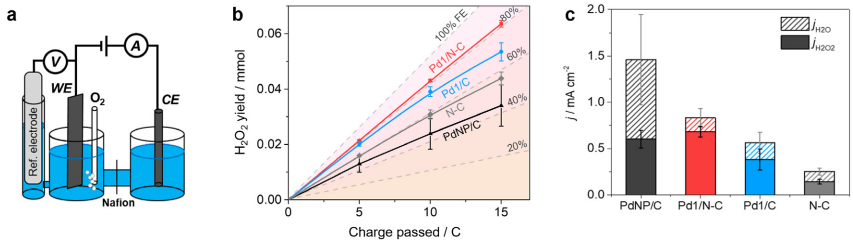

Fig. 5. Electrochemical production of H_2O_2 using three compartments set-up with stagnant electrolyte. (a) Schematic of three compartment set-up. (b) H_2O_2 yield over charge accumulated up to 15 C. Potential of working electrode was held at 0.2 V vs RHE in 0.1 M $HClO_4$. Dashed lines indicate corresponding lines for given faradaic efficiencies. (c) Partial current densities of measurements in (b).

(Fig. S6a) and the orthoslice showing a partially peeled off RGO layer (Fig. S7c).

In addition, Raman spectroscopy was used to study the structural defects of the N-C and RGO supports. The higher I_D/I_G value of N-C can be attributed to the higher N-doping content, which creates more defects than that for RGO supports (Supplementary Fig. S8). Supplementary Fig. S9a and S9c exhibits the N_2 adsorption/desorption isotherms of N-C and RGO support materials. The respective specific surface areas (SSA) for N-C and RGO supports are 635.7 $m^2\ g^{-1}$ and 460.9 $m^2\ g^{-1}$, which are calculated by Brunauer-Emmett-Teller (BET) method. As can be seen from pore size distribution, N-C shows a characteristic microporous property, which mainly originates from numerous micropores with a maximum peak at *ca.* 1.9 nm (Supplementary Fig. S9b and d). Notably, the micropore ratio of N-C was slightly higher than that of RGO support.

The detailed morphology of Pd1/N-C was characterized by electron tomography and aberration-corrected HAADF-STEM. Fig. 6 shows HAADF-STEM images of Pd1/N-C with different magnification. Notably, no Pd nanoparticle or cluster was observed in the low magnification images of the Pd1/N-C SAC. At higher magnification, Fig. 6 shows that the bright dots (Pd) were well dispersed with an average size of 3–4 Å, which matches the van der Waals diameter of a single Pd atom [57]. In comparison, many Pd clusters were observed in HAADF-STEM images for the PdNP/C (0.4–3 nm, 0.312 wt%) composite (Supplementary Fig. S10). According to the energy dispersive X-ray spectroscopy (EDS) analysis (Fig. S11), C, O, and N were uniformly distributed over the entire spherical architecture of Pd1/N-C (Fig. S11b), confirming the successful N doping of N-C. However, Pd signal is too weak to be identified due to the low content of Pd species.

To elucidate coordination environment and chemical state of the Pd single-atom of Pd1/N-C, X-ray absorption near edge structure (XANES) and extended X-ray absorption fine structure (EXAFS) were conducted. As can be seen from Fig. 7a, the chemical valence of Pd in Pd1/N-C SAC was positive, which can be determined by its higher white line intensity and higher edge energy compared to Pd foil from XANES spectra. In the EXAFS spectra (Fig. 7b), electron-riched N atoms (with lone-pairs) was found to be coordinated with Pd, further confirming that Pd species existed as isolated atoms and anchored by N doped carbon support. The coordination configurations for the Pd-N_x moieties in Pd1/N-C SAC were then investigated by quantitative least-squares EXAFS curve-fitting analysis. Findings demonstrate that the number of coordinating N atoms of Pd is around six and the mean N-Pd bond length was 2.13 Å. To further validate 6 coordination number (CN) of Pd-N, another common CN of Pd-N, 4, has also been investigated by EAXFS fitting, with the CN set as 4. The 0.047 R factor from this fitting is not acceptable for EXAFS fitting, which rules out the possibility of 4 CN of Pd-N (Supplementary Table 1). These N atoms act as anchoring sites and could adjust electron density of Pd *via* coordination, which may lead to an improved catalytic performance [58,59].

X-ray photoelectron spectroscopy (XPS) was employed to investigate the surface composition and oxidation states of the Pd1/N-C SAC. The survey scan (Fig. S12) and Pd 3d scan (Fig. 7d) reveal the existence of C, O, N (*ca.* 3.8 at.%), and Pd, which is consistent with the element composition of Pd1/N-C. The high-resolution XPS spectrum for N 1s could be deconvoluted into four peaks centered at the binding energy of 398.5, 400.1, 401.3 and 403.0 eV, which were assigned to pyridinic-N, pyrrolic-N, graphitic-N and pyridinic oxide, respectively (Fig. 7c), while Pd was entirely oxidic, Pd^{2+} (Fig. 7d) [60]. The dominant N species in Pd1/N-C was graphitic-N (54.2%), pyridinic-N (21.0%) and pyrrolic-N (20.7%), which could serve as anchoring sites for Pd single-atoms and lead to the formation of heterojunction between incorporated N atoms and Pd species [59]. The doped N atoms might donate electron density to Pd^{2+}, and enhance binding strength with the Pd species, resulting in an enhanced stability.

3.4. DFT modeling

To rationalize the observed activity of Pd SAC towards the 2e pathway, we investigated the nature of the Pd active site by means of DFT. The computational details are found in the Supplementary Information. In our previous works, we calculated the activity of 10 different metal atoms coordinated with four pyridinic N (4 N) [1,61]. The results predicted very low activity for Pd/N-C in such coordination site, due to severe limitations of weak binding of the oxygen intermediates [1]. Co/N-C showed instead the highest computed activity for 2e ORR, being the closest to the top of 2e volcano [1]. In this report, we investigate the origin of Pd site activity in relation to our previous understanding, creating a set of model catalysts using inputs from material characterization of Pd1/N-C. Through the ORR associative pathway mechanism [63], we calculated the limiting potential for the ORR on each structure and presented it in a volcano plot relationship (Fig. 8a) [64]. Specifically, we incorporated the EXAFS fitting result modeling structures with a six-fold coordination geometry of pyridinic N atoms (6 N). As XPS result indicated a significant amount of graphitic N in the N-C substrate, we also studied the effect of graphitic N doping around the coordination site. We modelled various N-doped 6 N structures (Fig. 8b) where the total amount of N (coordinating + doping) was varied from ~12% [(6 + 1)N-a,b,c] to ~16% [(6 + 3)N] atomic concentration. To evaluate the N-doping effect on our previously published structural motif, we also reported four-fold pyridinic coordinated catalysts (4 N), varying the overall atomic concentra-

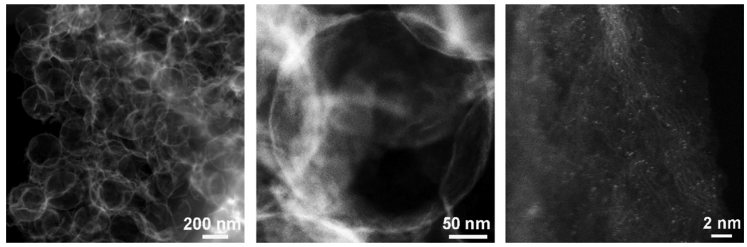

Fig. 6. Atomic structure characterizations of Pd1/N-C SAC by HAADF-STEM. Aberration-corrected HAADF-STEM images of Pd1/N-C SAC; images revealing hollow structure of N-C hollow carbon nanospheres, and high density of Pd atoms (bright dots) deposited on N-C.

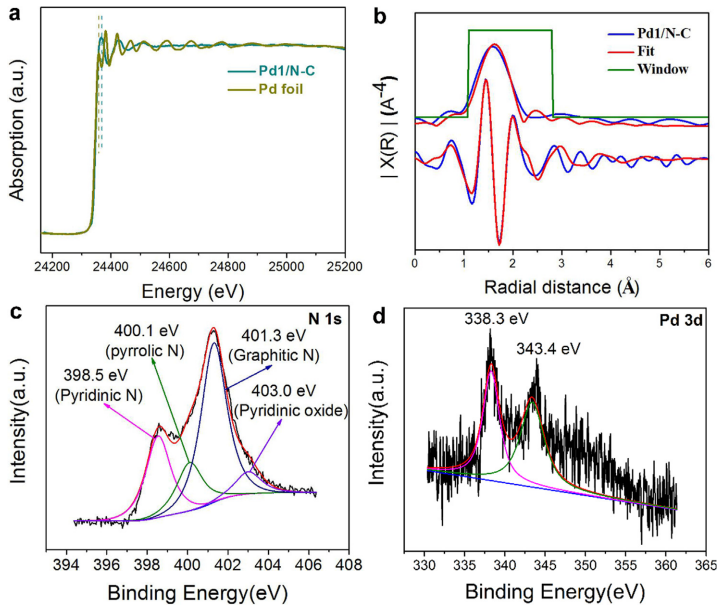

Fig. 7. (a) Characterizations of Pd1/N-C SAC by X-ray absorption spectroscopy and X-ray photoelectron spectroscopy (XPS). (a) Pd K X-ray absorption near edge structure (XANES) spectra of Pd1/N-C SAC and Pd foil; (b) EXAFS functions and the fittings of Pd1/N-C SAC. XPS spectra of the Pd1/N-C SAC; (c) N 1s, (d) Pd 3d.

tion of N from 5% to 12%. All the model structures are reported in Fig. 8b for visual clarity.

In Fig. 8a, the 2e and 4e pathway volcano lines are shown in green and black, respectively. The structures computed limiting potential are presented with dots following the same color coding. The green background in the plot indicates the area where the computed selectivity to peroxide for single site catalysts is 100%, from purely thermodynamic perspective and taking into account the specific geometric effect on single sites (*O destabilization relative to H_2O_2 reversible potential), faded at the boundary to account for the inherent uncertainty in ground state DFT predictions. A detailed explanation of this selectivity area can be found in the Supplementary Information.

We recently proved the 4 N model structure to be an accurate approximation to study catalytic trends in single site transition metal catalysts [13,62], demonstrating the positive structural effects of single site catalysis for 2e ORR altogether. However, in the present study a discrepancy between the 4 N model and the observed catalytic performance for Pd SAC emerges. Within the 4 N coordination, Pd was predicted to be a very weak binder for *OOH – a selective but inactive catalyst. Notably, when the coordination number is switched from 4 N to 6 N (always within pyridinic coordination, see 6 N in Fig. 8b), we observed an increase in computed activity, due to a stronger interaction between the active site and the reaction intermediates. The stronger interaction originates from the wider graphene vacancy, which host a six-fold N coordination geometry. With the Pd center at greater distance from the N ligands, we predicted a decreasing inductive electronic effect as compared to 4 N, even though two more N ligands are coordinating the metal atom. The addition of graphitic N in the graphene sheet further reduces the electron donation from the coordinating N, enhancing the binding strength of the Pd metal center.

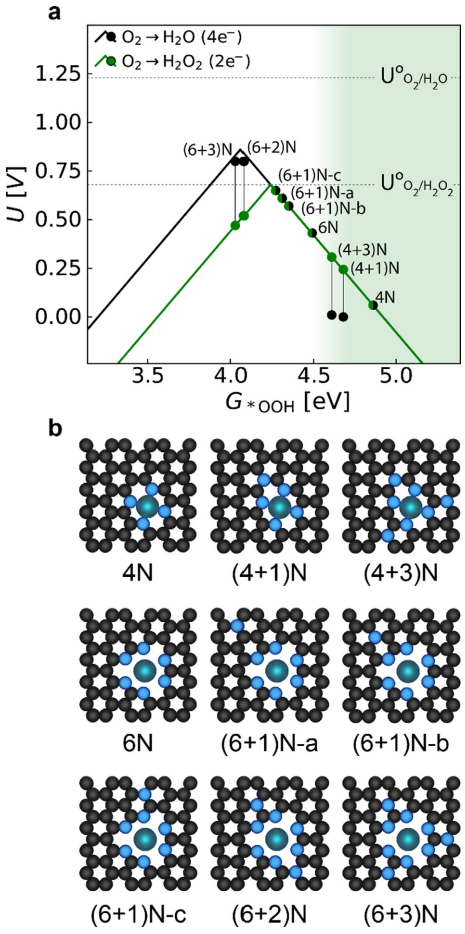

Fig. 8. DFT modeling results. (a) Computational Sabatier volcano plot. The calculated onset potential is plotted as function of the descriptor G*OOH (*OOH formation free energy). Each structure has an onset potential for 2e (green dots) and 4e (black dots), connected by a black vertical line for readability. If these potentials coincide, the dot is half-green, half-black. The green area represents the theoretical 100% H_2O_2 selectivity threshold. (b) Unit cell rendering for the Pd-SAC structures modelled. Black, teal and light blue spheres represent C, Pd and N atoms, respectively.

For its electron withdrawing nature, graphitic N engages part of the electronic density that pyridinic N uses for the dative coordination with the Pd atom. Fig. S13 shows the progressive loss of electron density around Pd upon increasing amount of doped graphitic N. Beyond 16% overall N atomic concentration (structure (6 + 3)N, Fig. 8b), we found the coordination site is unable to stabilize the metal center. Pd migrates at the defect edge, coordinating only to two N, yielding structures severely limited by ORR intermediates strong retention (Fig. S14). The binding strength of Pd is increased by the doping of graphitic N and, regardless of the exact position, one graphitic N at the surroundings of the coordinating center [(6 + 1)N-a,b,c] determines increased computed activity. In fact, structures (6 + 1)N-a, b or c approach the ideal G_{*OOH} to reach the top of the 2e volcano, where rate of 2e ORR is highest. Further N- doping with 2 and 3 graphitic N yields model catalysts even more active, which lie at the top of the 4e volcano. Their computed rate deviate from experimental observations, as Pd SAC shows high selectivity to H_2O_2. In fact, for these two catalysts the 2e rate is significantly lower than the 4e rate, as evidenced by the y-axis gap between black and green dots in Fig. 8a. Notably, also the N-doping on the 4 N structure determines increased affinity of Pd for the ORR intermediates. Despite being activated, (4 + 1)N and (4 + 3)N model catalysts possess a lower 4e activity than the reference Pd 4 N catalyst, as the 4e pathway rate limiting step becomes the reduction *OOH → *O. However, the 2e rate is defined only by the thermodynamics of a single intermediate, *OOH. Hence, we observe an onset potential gap in favor of the 2e reaction for (4 + 1)N and (4 + 3)N, i.e. a higher reaction rate for the peroxide formation than for the full reduction.

By comparing experimental results with DFT calculations, we suggest that the high activity of Pd1/N-C stems from 6 N coordinating environment, possibly sustained by additional graphitic N-doping around the coordinating site. The optimal doping in the immediate surroundings of the metal center is predicted between one and two graphitic N, which still secures good stability to the Pd site. Table S2 reports the sites reduction potential referenced to fcc bulk Pd, showing higher thermodynamic stability toward oxidative leaching for the sites proposed as active and selective, compared to the standard reduction potential of palladium. Table S2 further shows that an excessive N doping results in lower reduction potential thus lower Pd atom retention in the coordination site. As we have presented above, the intrinsic activity of Pd1/N-C still does not match the highly selective Pd-Hg(pc) catalyst, although we show how site coordination and moderate doping potentially enable catalytic activities close to thermodynamic limit for peroxide production. This thermodynamic model is useful to qualitatively determine the features of a real catalytic surface, however, it does not necessarily represent accurately the synthesized catalyst, which is likely a mixture of differently coordinated Pd active sites. Also other kinetic limitations could play a major role. Nonetheless, we indicate how the control on N content in the substrate could be a key to enable creation of highly active sites, achieving even higher activity for electrochemical H_2O_2 production using Pd SAC.

4. Conclusion

Pd single-atoms on N-doped hollow carbon nanosphere, Pd1/N-C, exhibited excellent catalytic performance for electrochemical H_2O_2 production owing to its optimized electronic and geometric structure. Presence of single-atom active sites and coordination effect of Pd single-atom with N-species are main reasons for high activity and selectivity. Pd1/N-C also showed improved stability of Pd1/N-C after 10,000 cycle "on-off" test. DFT calculations suggests that 6 N coordinating environment with additional doping of graphitic N can explain the high catalytic activity. The method for benchmarking electrochemical H_2O_2 synthesis requires more attention. Comparison of measurements from RRDE and three compartment set-up exhibited the effect of mass transport and H_2O_2 concentration on the catalysis. For example, PdNP/C could have been considered as a promising candidate when RRDE measurement is considered, but in a more realistic set-up PdNP/C failed to produce H_2O_2 with reasonable selectivity. SACs have unique potential in heterogeneous catalysis field as shown in the case of Pd1/N-C for H_2O_2 synthesis. The proposed synthesis strategy could be adopted to other SAC systems if the active atom has coordination strength with N species. Carbon substrate doping could be fur-

ther investigated, also with other well-known dopant species (O, B, S, *etc.*). Controlling the coordinating sphere of active atoms via controlled synthesis of coordination sites, as well as control over site proximity dopants could be a key for successful development of other single-atom catalysts of this kind.

Author contributions

J. B. X. performed the synthesis, most of the structural characterizations. S. Y., J. N. H., J. –P. B. H., J. K., and I. C. designed and performed the electrochemical tests. S. F. C. and Y. Y. Z. performed the XAFS measurement and analyzed the EXAFS and XANES data. H. Y. S and P. L. conducted the HAADF-STEM characterization. L. S. and J. R. designed and performed the computational modeling. P. L., Q. Y. C, and S. B. conducted the 3D tomography characterization. The paper was co-written by J. B. X., S. Y., L. S., S. F. C. and P. L. The research was supervised by S. W. and I. C. All authors discussed the results and commented on the manuscript. J. B. X., S. Y., L. S. and S. F. C. contributed equally.

Declaration of Competing Interest

The authors declare that they have no known competing financial interests or personal relationships that could have appeared to influence the work reported in this paper.

Acknowledgements

This research was financially supported by the National Natural Science Foundation of China (No. 51772110), Natural Science Foundation of Hubei Province (No. 2019CFB539), Danmarks Innovationsfond within the ProActivE project (5160-00003B), Villum Foundation V-SUSTAIN grant 9455 to the Villum Center for the Science of Sustainable Fuels and Chemicals, the Carlsberg Foundation grant CF18-0435, the Institutional Research Program (2E30220) of the Korea Institute of Science and Technology (KIST), Shenzhen Science and Technology Plan under Grant (JCYJ20170818160751460) and the Open Project of Key Laboratory of Green Chemical Engineering Process of Ministry of Education (No. GCP20200205). The authors would like to acknowledge the Analytical and Testing Center of Huazhong University of Science and Technology and the Wuhan National Laboratory for Optoelectronics for SEM, TEM, Raman and XPS measurements.

Appendix A. Supplementary material

Supplementary data to this article can be found online at https://doi.org/10.1016/j.jcat.2020.11.020.

References

[1] S. Yang, A. Verdaguer-Casadevall, L. Arnarson, L. Silvioli, V. Colic, R. Frydendal, J. Rossmeisl, I. Chorkendorff, I.E. Stephens, ACS Catal. 8 (2018) 4064–4081.
[2] S.J. Freakley, Q. He, J.H. Harrhy, L. Lu, D.A. Crole, D.J. Morgan, E.N. Ntainjua, J.K. Edwards, A.F. Caraley, A.Y. Borrisevich, C.J. Kiely, G.J. Hutchings, Science 351 (2016) 965–968.
[3] R. Ciriminna, L. Albanese, F. Meneguzzo, M. Pagliaro, ChemSusChem. 9 (2016) 3374–3381.
[4] J.M. Campos-Martin, G. Blanco-Brieva, J.L. Fierro, Angew. Chem. Int. Ed. 45 (2006) 6962–6984.
[5] J.K. Edwards, B.E. Solsona, P. Landon, A.F. Carley, A. Herzing, C.J. Keily, G.J. Hutchings, J. Catal. 236 (2005) 69–79.
[6] R.J. Lewis, K. Ueura, Y. Fukuta, S.J. Freakley, L.Q. Kuang, R. Wang, Q. He, J.K. Edwards, D.J. Morgan, Y. Yamamoto, G.J. Hutchings, ChemCatChem 11 (2019) 1673–1680.
[7] J.K. Edwards, S.J. Freakley, R.J. Lewis, J.C. Pritchard, G.J. Hutchings, Catal. Today 248 (2015) 3–9.
[8] S.L. Wang, K.G. Gao, W. Li, J.L. Zhang, Appl. Catal. A- Gen. 531 (2017) 89–95.
[9] E. Ghedini, F. Menegazzo, M. Signoretto, M. Manzoli, F. Pinna, G. Strukul, J. Catal. 273 (2010) 266–273.
[10] F. Menegazzo, M. Manzoli, M. Signoretto, F. Pinna, G. Strukul, Catal. Today 248 (2015) 18–27.
[11] A. Pashkova, L. Greiner, U. Krtschil, C. Hofmann, R. Zapf, Appl. Catal. A- Gen. 464 (2013) 281–287.
[12] T. Ishihara, R. Nakashima, Y. Ooishi, H. Hagiwara, M. Matsuka, S. Ida, Catal. Today 248 (2015) 35–39.
[13] Y.Y. Sun, L. Silvioli, N.R. Sahraie, W. Ju, J.K. Li, A. Zitolo, S. Li, A. Bagger, L. Arnarson, X.L. Wang, T. Moeller, D. Bernsmeier, J. Rossmeisl, F. Jaouen, P. Strasser, J. Am. Chem. Soc. 141 (2019) 12372–12381.
[14] X.Y. Guo, S.R. Lin, J.X. Gu, S.L. Zhang, Z.F. Chen, S.P. Huang, ACS Catal. 9 (2019) 11042–11054.
[15] E. Jung, H. Shin, B.H. Lee, V. Efremov, S. Lee, H. Seok Lee, J. Kim, W.H. Antink, S. Park, K.S. Lee, S.P. Cho, J.S. Yoo, Y.E. Sung, T. Hyeon, Nat. Mater. 19 (2020) 436–442.
[16] A. Verdaguer-Casadevall, D. Deiana, M. Karamad, S. Siahrostami, P. Malacrida, T.W. Hansen, J. Rossmeisl, I. Chorkendorff, I.E. Stephens, Nano Lett. 14 (2014) 1603–1608.
[17] C.H. Choi, H.K. Lim, M.W. Chung, G. Chon, N.R. Sahraie, A. Altin, M.T. Sougrati, L. Stievano, H.S. Oh, E.S. Park, F. Luo, P. Strasser, G. Dražić, K.J.J. Mayrhofer, H. Kim, F. Jaouen, Energy Environ. Sci. 11 (2018) 3176–3182.
[18] H.B. Yang, S.F. Hung, S. Liu, K.D. Yuan, S. Miao, L.P. Zhang, X. Huang, H.Y. Wang, W.Z. Cai, R. Chen, J.J. Gao, X.F. Yang, W. Chen, Y.Q. Huang, H.M. Chen, C.M. Li, T. Zhang, B. Liu, Nat. Energy 3 (2018) 140–147.
[19] J.Z. Li, M.J. Chen, D.A. Cullen, S. Hwang, M.Y. Wang, B.Y. Li, K.X. Liu, S. Karakalos, M. Lucero, H.G. Zhang, C. Lei, H. Xu, G.E. Sterbinsky, Z.X. Feng, D. Su, K.L. More, G.F. Wang, Z.B. Wang, G. Wu, Nat. Catal. 1 (2018) 935–945.
[20] A. Zitolo, V. Goellner, V. Armel, M.T. Sougrati, T. Mineva, L. Stievano, E. Fonda, F. Jaouen, Nat. Mater. 14 (2015) 937–942.
[21] H.L. Fei, J.C. Dong, Y.X. Feng, C.S. Allen, C.Z. Wan, B. Volosskiy, M.F. Li, Z.P. Zhao, Y.L. Wang, H.T. Sun, P.F. An, W.X. Chen, Z.Y. Guo, C. Lee, D.L. Chen, I. Shakir, M.J. Liu, T.D. Hu, Y.D. Li, A.I. Kirkland, X.F. Duan, Y. Huang, Nat. Catal. 1 (2018) 63–72.
[22] S. Siahrostami, A. Verdaguer-Casadevall, M. Karamad, D. Deiana, P. Malacrida, B. Wickman, M. Escudero-Escribano, E.A. Paoli, R. Frydendal, T.W. Hansen, I. Chorkendorff, I.E.L. Stephens, J. Rossmeisl, Nat. Mater. 12 (2013) 1137–1143.
[23] E. Pizzutilo, O. Kasian, C.H. Choi, S. Cherevko, G.J. Hutchings, K.J.J. Mayrhofer, S. J. Freakley, Chem. Phys. Lett. 683 (2017) 436–442.
[24] J.S. Jirkovsky, I. Panas, E. Ahlberg, M. Halasa, S. Romani, D.J. Schiffrin, J. Am. Chem. Soc. 133 (2011) 19432–19441.
[25] J.J. Gao, H.B. Yang, X. Huang, S.F. Hung, W.C. Cai, C.M. Jia, S. Miao, H.M. Chen, X. F. Yang, Y.Q. Huang, T. Zhang, B. Liu, Chem 6 (2020) 1–17.
[26] I. Yamanaka, R. Ichihashi, T. Iwasaki, N. Nishimura, T. Murayama, W. Ueda, S. Takenaka, Electrochim. Acta 108 (2013) 321–329.
[27] R.A. Shen, W.X. Chen, Q. Peng, S.Q. Lu, L.R. Zheng, X. Cao, Y. Wang, W. Zhu, J.T. Zhang, Z.B. Zhuang, C. Chen, D.S. Wang, Y.D. Li, Chem. 5 (2019) 2099–2110.
[28] H.Y. Sheng, E.D. Hermes, X.H. Yang, D.W. Ying, A.N. Janes, W.J. Li, J.R. Schmidt, S. Jin, ACS Catal. 9 (2019) 8433–8442.
[29] S. Yang, J. Kim, Y.J. Tak, A. Soon, H. Lee, Angew. Chem. Int. Ed. 55 (2016) 2058–2062.
[30] S. Yang, Y.J. Tak, J. Kim, A. Soon, H. Lee, ACS Catal. 7 (2017) 1301–1307.
[31] C.H. Choi, M. Kim, H.C. Kwon, S.J. Cho, S. Yun, H.T. Kim, K.J. Mayrhofer, H. Kim, M. Choi, Nat. Commun. 7 (2016) 10922.
[32] S. Mitchell, E. Vorobyeva, J. Pérez-Ramírez, Angew. Chem. Int. Ed. 57 (2018) 15316–15329.
[33] S.W. Li, J.J. Liu, Z. Yin, P.J. Ren, L.L. Lin, Y. Gong, C. Yang, X.S. Zheng, R.C. Cao, S.Y. Yao, Y.C. Deng, X. Liu, L. Gu, W. Zhou, J.F. Zhu, X.D. Wen, B.J. Xu, D. Ma, ACS Catal. 10 (2020) 907–913.
[34] R.H. Lin, D. Albani, E. Fako, S.K. Kaiser, O.V. Safonova, N. López, J. Pérez-Ramírez, Angew. Chem. 131 (2019) 514–519.
[35] R. Jiang, L. Li, T. Sheng, G.F. Hu, Y.G. Chen, L.Y. Wang, J. Am. Chem. Soc. 140 (2018) 11594–11598.
[36] P.Q. Yin, T. Yao, Y.E. Wu, L.R. Zheng, Y. Lin, W. Liu, H.X. Ju, J.F. Zhu, X. Hong, Z.X. Deng, G. Zhou, Angew. Chem. Int. Ed. 55 (2016) 10800–10805.
[37] G.X. Chen, C.F. Xu, X.Q. Huang, J.Y. Ye, L. Gu, G. Li, Z.C. Tang, B.H. Wu, H.Y. Yang, Z.P. Zhao, Z.Y. Zhou, G. Fu, N.F. Zheng, Nat. Mater. 15 (2016) 564–569.
[38] Y.J. Chen, S.F. Ji, Y.G. Wang, J.C. Dong, W.X. Chen, Z. Li, R.A. Shen, L.R. Zheng, Z.B. Zhuang, D.S. Wang, Y.D. Li, Angew. Chem. Int. Ed. 56 (2017) 6937–6941.
[39] H.C. Tao, C. Choi, L.X. Ding, Z. Jiang, Z.S. Han, M.W. Jia, Q. Fan, Y.N. Gao, H.H. Wang, A.W. Robertson, S. Hong, Y. Jung, S.Z. Liu, Z.Y. Sun, Chem. 5 (2019) 204–214.
[40] J.B. Xi, H.Y. Sun, D. Wang, Z.Y. Zhang, X.M. Duan, J.W. Xiao, F. Xiao, L.M. Liu, S. Wang, Appl. Catal. B: Environ. 225 (2018) 291–297.
[41] W. Stöber, A. Fink, E. Bohn, J. Colloid Interface Sci. 26 (1968) 62–69.
[42] W.S. Hummers Jr, R.E. Offeman, J. Am. Chem. Soc. 80 (1958) 1339.
[43] J.S. Lee, K.H. You, C.B. Park, Adv. Mater. 24 (2012) 1084–1088.
[44] H. Lee, S.M. Dellatore, W.M. Miller, P.B. Messersmith, Science 318 (2007) 426–430.
[45] A.H. Larsen, J. Jørgen Mortensen, J. Blomqvist, I.E. Castelli, R. Christensen, M. Dułak, J. Friis, M.N. Groves, B. Hammer, C. Hargus, E.D. Hermes, P.C. Jennings, P. B. Jensen, J. Kermode, J.R. Kitchin, E.L. Kolsbjerg, J. Kubal, K. Kaasbjerg, S. Lysgaard, J.B. Maronsson, T. Maxson, T. Olsen, L. Pastewka, A. Peterson, C. Rostgaard, J. Schiøtz, O. Schütt, M. Strange, K.S. Thygesen, T. Vegge, L. Vilhelmsen, M. Walter, Z.H. Zeng, K.W. Jacobsen, J. Phys. Condens. Matter. 29 (2017) 273002.
[46] J.J. Mortensen, L.B. Hansen, K.W. Jacobsen, Phys. Rev. B. - Condens. Matter Mater. 71 (2005) 1–11.

[47] S.R. Bahn, K.W. Jacobsen, Comput. Sci. Eng. 4 (2002) 56–66.
[48] J. Wellendorff, K.T. Lundgaard, A. Møgelhøj, V. Petzold, D.D. Landis, J.K. Nørskov, T. Bligaard, K.W. Jacobsen, Phys. Rev. B. - Condens. Matter Mater. Phys. 85 (2012) 32–34.
[49] J. Rossmeisl, Z.W. Qu, H. Zhu, G.J. Kroes, J.K. Nørskov, J. Electroanal. Chem. 607 (2007) 83–89.
[50] F. Calle-Vallejo, J.I. Martínez, J. Rossmeisl, Phys. Chem. Chem. Phys. 13 (2011) 15639–15643.
[51] J.S. Jirkovský, M. Halasa, D.J. Schiffrin, Phys. Chem. Chem. Phys. 12 (2010) 8042–8053.
[52] J. Kim, C.W. Roh, S.K. Sahoo, S. Yang, J. Bae, J.W. Han, H. Lee, Adv. Energy Mater. 8 (2018) 1–8.
[53] H.J. Qiu, Y. Ito, W.T. Cong, Y.W. Tan, P. Liu, A. Hirata, T. Fujita, Z. Tang, M.W. Chen, Angew. Chem. Int. Ed. 54 (2015) 14031–14035.
[54] J. Jones, H.F. Xiong, A.T. DeLaRiva, E.J. Peterson, H. Pham, S.R. Challa, G.S. Qi, S. Oh, M.H. Wiebenga, X.I.P. Hernández, Y. Wang, A.K. Datye, Science 353 (2016) 150–154.
[55] A.M. Chaparro, N. Mueller, C. Atienza, L. Daza, J. Electroanal. Chem. 591 (2006) 69–73.
[56] S. Maass, F. Finsterwalder, G. Frank, R. Hartmann, C. Merten, J. Power Sources 176 (2008) 444–451.
[57] G. Vilé, D. Albani, M. Nachtegaal, Z.P. Chen, D. Dontsova, M. Antonietti, N. López, J. Pérez-Ramírez, Angew. Chem. Int. Ed. 54 (2015) 11265–11269.
[58] P.X. Liu, N.F. Zheng, Natl. Sci. Rev. 5 (2018) 1–3.
[59] Y.J. Chen, S.F. Ji, C. Chen, Q. Peng, D.S. Wang, Y.D. Li, Joule 2 (2018) 1242–1264.
[60] S.Q. Zhou, L. Shang, Y.X. Zhao, R. Shi, G.I.N. Waterhouse, Y.C. Huang, L.R. Zheng, T.R. Zhang, Adv. Mater. 31 (2019) 1900509.
[61] P.F. Zhang, Y.T. Gong, H.R. Li, Z.R. Chen, Y. Wang, Nat. Commun. 4 (2013) 1593.
[62] W. Ju, A. Bagger, G.P. Hao, A.S. Varela, I. Sinev, V. Bon, B.R. Cuenya, S. Kaskel, J. Rossmeisl, P. Strasser, Nat. Commun. 8 (2017) 944.
[63] J.K. Nørskov, J. Rossmeisl, A. Logadottir, L. Lindqvist, J.R. Kitchin, T. Bligaard, H. Jónsson, J. Phys. Chem. B 108 (2004) 17886–17892.
[64] V. Viswanathan, H.A. Hansen, J. Rossmeisl, J.K. Nørskov, J. Phys. Chem. Lett. 3 (2012) 2948–2951.

Appendix B

Paper II

Is There Anything Better than Pt for HER?
Johannes Novak Hansen, Hector Prats, Karl Krøjer Toudahl, Niklas Mørch Secher, Karen Chan, Jakob Kibsgaard, Ib Chorkendorff
ACS Energy Letters, Volume 6, 2021, Pages 1175-1180

https://pubs.acs.org/doi/10.1021/acsenergylett.1c00246
 Cites as reference [49] in present thesis

ACS Energy LETTERS

http://pubs.acs.org/journal/aelccp

PERSPECTIVE

Is There Anything Better than Pt for HER?

Johannes Novak Hansen, Hector Prats, Karl Krøjer Toudahl, Niklas Mørch Secher, Karen Chan, Jakob Kibsgaard,* and Ib Chorkendorff*

Cite This: *ACS Energy Lett.* 2021, 6, 1175−1180

ABSTRACT: **The search for cheap and abundant alternatives to Pt for the hydrogen evolution reaction (HER) has led to many efforts to develop new catalysts. Although the discovery of promising catalysts is often reported, none can compete with Pt in intrinsic activity. To enable true progress, a rigorous assessment of intrinsic catalytic activity is needed, in addition to minimizing mass-transport limitations and following best practices for measurements. Herein, we underline the importance of measuring intrinsic catalytic activities, e.g., turnover frequencies (TOFs). Using mass-selected, identical Pt nanoparticles at a range of loadings, we show the pervasive impact of mass-transport limitations on the observed activity of Pt in acid. We present the highest TOF measured for Pt at room temperature. Since our measurements are still limited by mass transport, the true intrinsic HER activity for Pt in acid is still unknown. Using a numerical diffusion model, we suggest that hysteresis in cyclic voltammograms arises from H_2 oversaturation, which is another indicator of mass-transport limitations.**

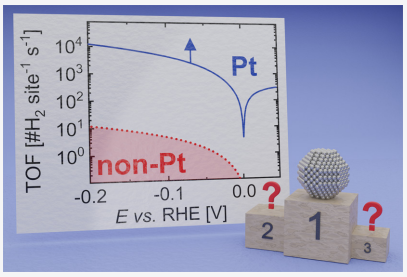

Novel hydrogen evolution reaction (HER) catalysts are often reported in the literature without regard for the applied catalyst loading, intrinsic activities, or possible mass-transport limitations. Much effort has been put into achieving high geometric current densities by increasing mass loading and the corresponding active surface area.[1] However, the geometric current density, while important from the applied perspective, does not reflect the intrinsic catalytic activity that arises from tuning the electronic structure of the catalyst. The only metric of intrinsic activity is the turnover frequency (TOF), which is defined as the number of molecules (e.g., H_2) produced per second per site.[2] Furthermore, there are some common pitfalls which limit the quality and usefulness of the reported measurements in the literature, for instance: lacking potential scale calibration, lack of hydrogen saturation when performing HER, poor choice of counter electrode, and comparison to subpar measurements.[1] Often, catalysts are claimed to have record-breaking activities or to surpass the performance of commercially available Pt/C. In general, a closer inspection shows this not to be the case, due to one or more of the aforementioned pitfalls.[3−5]

In this work, we study the influence of mass transport on the intrinsic Pt HER activity with rotating disk electrode (RDE) measurements and report benchmark values of the specific activities. We investigate identical, mass-selected Pt nanoparticles at a range of Pt loading as well as commercial Pt/C samples, which together spans 4 orders of magnitude in Pt loading. We show that decreasing catalyst loading is effective in mitigating mass-transport limitations of HER (and HOR, the hydrogen oxidation reaction), but even at ultra-low loading, HER/HOR is mass-transport-limited on Pt in acid, and the resultant TOFs are only lower bounds on the intrinsic activity. By varying deposition area (using a small and a large raster pattern) of the mass-selected particles, we show that particle dispersion also influences TOF. To our knowledge, the TOF we report for the lowest Pt loading is the highest ever reported at room temperature regardless of the measurement technique. We furthermore find that the intrinsic activity of Pt exceeds that of any existing earth-abundant HER catalyst by at least 3 orders of magnitude. We also observe hysteresis in the cyclic voltammograms (CVs) at ultra-low Pt loadings, which we investigate using a time-dependent coupled kinetic-transport model. This model suggests that the displayed hysteresis is a marker for mass-transport limitations, since it arises from H_2 buildup.

WHY SITES MATTER

We emphasize, first, that turnover frequencies are *the only metric that reflects the intrinsic activity of a catalyst*. Figure 1

Received: February 3, 2021
Accepted: March 3, 2021

https://dx.doi.org/10.1021/acsenergylett.1c00246
ACS Energy Lett. 2021, 6, 1175−1180

The intrinsic activity of Pt exceeds that of any existing earth-abundant HER catalyst by at least 3 orders of magnitude.

The turnover frequency should be reported whenever possible, as it is the relevant scientific metric for comparing intrinsic activity.

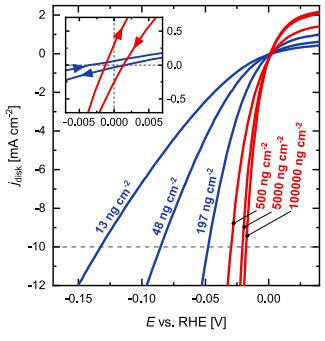

Figure 1. Cathodic sweeps of HER cyclic voltammograms for a representative set of Pt loadings exemplify how a lower overpotential to reach a certain geometric current density can be achieved by increasing catalyst loading. Blue lines correspond to 3.8 nm Pt nanoparticles deposited with the cluster source over a small raster pattern, while red lines correspond to commercially available Pt/C catalyst. Note that for 3.8 nm nanoparticles, j_{disk} is a lower bound on the real geometric current density, since the raster pattern area is smaller than the disk. (Inset) Anodic and cathodic sweeps for the lowest- and highest-loading samples are shown. Correct calibration ensures the CV passes (0,0) at low scan speeds or with a negligible spread to each side at higher scan speeds. It is necessary to calibrate the reference electrode vs RHE and maintain a completely H_2-saturated electrolyte throughout any HER/HOR experiment used for measuring catalytic activity. Failing to do so results in an ill-defined potential shift and consequently an invalid activity measurement.[9] CVs were recorded in H_2-saturated 0.5 M H_2SO_4 with a rotation rate of ω = 1600 rpm and are post-corrected for 100% of the ohmic drop as measured by EIS. A potential scan rate of ν = 50 mV s^{-1} was used for all samples except for the two highest loadings (50 000 (not shown in Figure) and 100 000 ng cm^{-2}), in which case 10 mV s^{-1} was used to minimize the influence of double-layer charging current arising from the relative high roughness.

shows the geometric current densities normalized by disk area (j_{disk}) for a representative subset of samples of Pt loading from 13 to 10^5 ng cm^{-2}. The overpotential (η_{10} mA cm^{-2}) needed to reach a geometric current density of 10 mA cm^{-2} is often reported in literature without consideration for the catalyst loading.[5−8] From Figure 1, it is obvious that the overpotential needed to reach a certain current density can be reduced simply by increasing the catalyst loading and hence the number of active sites. This is not equivalent to improved intrinsic catalytic activity. Between the lowest loading and the highest loading, 13 and 10^5 ng cm^{-2}, respectively, η_{10} mA cm^{-2} varies by more than 0.1 V, and it is therefore apparent why considering the active site density is crucial for any meaningful comparison of intrinsic activity.

The TOF should be reported whenever possible, as it is the relevant scientific metric for comparing intrinsic activity. Without the site density, j_{ECSA} (ECSA: electrochemically active surface area) may be used as an approximation of the TOF. If neither metric is available, the mass activity (j_{mass}) can be used as a stand-in metric for activity. While j_{mass} is by default not indicative of intrinsic activity, it can have some merit as a techno-economic metric, since the catalyst material is priced by mass. Considering this, it is only meaningful to replace platinum with a high mass loading of a catalyst of lower mass activity, if the catalyst price (e.g., \$ mg^{-1}) is correspondingly lower than that of platinum. The HER mass activity of platinum is several orders of magnitude higher than those of phosphide-based catalysts reported in the literature.[1] This may significantly limit the feasibility of simply increasing mass loading of abundant catalysts. As a benchmark for comparison of mass activity, j_{mass} versus η_{10} mA cm^{-2} is plotted for all loadings considered in Figure S3 in the Supporting Information (SI). Although j_{geo} can be useful from the practical perspective of the activity of a large-scale electrolyzer or photoelectochemical device, it is not useful in the comparison of intrinsic catalytic activity from a scientific point of view.

TRANSPORT LIMITATIONS ARE UBIQUITOUS IN RDE MEASUREMENTS OF Pt IN ACID

Figure 2A shows the corresponding TOFs at −15 mV overpotential for all samples. While the j_{disk} increases with loading, the TOF decreases by 3 orders of magnitude. This dramatic reduction in TOF with increasing loading indicates that mass-transport limitations play a major role for all samples, as will be discussed in the following. Akin to what is observed for the mass activity, Figure 2A shows that highly dispersed 3.8 nm nanoparticles (green) also perform slightly better than their less dispersed counterparts (blue). It can be ruled out that the effect stems solely from the less dispersed samples suffering more from particle overlap and hence a loss in ECSA, since the activity metric is normalized per site. It is also worth noting that, although loss of ECSA at higher loadings is to be expected, the effect is moderate even at 5000 ng cm^{-2} (see Figure S2 for further details).

RDE experiments offer enhanced mass transport compared to electrodes submerged in an unstirred solution.[10] Even so, the kinetics of acidic HOR/HER on Pt are so facile that the measured currents in RDEs with Pt disk electrodes are entirely limited by mass transport of H_2 to (HOR) or away from (HER) the electrode.[9,11−13] Under these conditions, the intrinsic activity has no effect on the measured activity, and the frequently reported Tafel slope of 30 mV/dec for HER is just the apparent Tafel slope of the diffusion overpotential at room temperature.[9] From Figure 2A it is evident that, even in the limit of ultra-low Pt loading, the mass-transport limitation dominates, since no plateau for the TOF is reached. Similarly, less active non-Pt catalysts might also be affected by slow mass transport when loading is sufficiently high. Mass-transport limitations therefore prevent a genuine comparison of intrinsic activities. A common pitfall is to report and compare a catalyst to a reference measurement (typically Pt/C) of significantly higher loading.[4] Given the mass-transport limitation of Pt, the higher the loading applied, the lower the TOF (or j_{mass}) observed. The reported catalyst thus seems more active than

https://dx.doi.org/10.1021/acsenergylett.1c00246
ACS Energy Lett. 2021, 6, 1175−1180

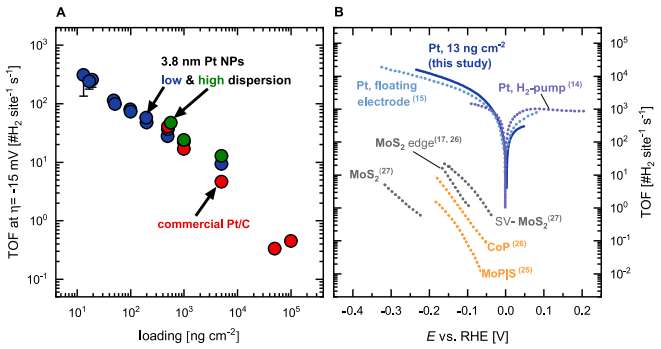

Figure 2. (A) TOF at $\eta = -15$ mV vs Pt loading for all samples in the present study. Blue and green dots correspond to 3.8 nm Pt nanoparticles deposited over a glassy carbon disk using small and large raster areas, respectively, while red dots correspond to commercially available Pt/C catalyst. The turnover frequency is calculated using the CO-strip charge of each sample, and all error bars are within the size of the markers except for the three lowest loadings (13, 17, and 19 ng cm^{-2}) as displayed. (B) TOFs corresponding to the cathodic scans for the lowest-loading sample in this study (solid blue line) and other Pt/C samples using fast mass-transport techniques: floating electrode (dotted light blue line) and H_2-pump (dotted purple line) taken from refs 15 and,14, respectively. A selection of transition metal sulfides and phosphides are added for comparison: MoPlS,[25] CoP,[26] MoS_2 (edge),[17,26] and (MoS_2, SV-MoS_2).[27] See section 4 in the SI for further details.

the reference measurement, leading to a false conclusion (see Figure S4 as an example).

Figure 2B compares the TOF for the lowest-loading sample in this study (i.e., 13 ng cm^{-2}) with the TOFs reported for other Pt samples using fast mass-transport techniques (i.e., H_2-pump method[14] and floating electrodes[15]). Note that our lowest-loading sample, along with the floating electrode technique of the Kucernak group,[15] gives the highest HER activity reported for Pt at room temperature. This result, along with the trend shown in Figure 2A, shows that decreasing the loading is a general strategy to evaluate and mitigate the impact of mass-transport effects in electrochemical reactions. However, since the TOF does not reach an obvious upper limit with decreasing loading, the lowest-loading sample gives a lower bound on HER activity. Therefore, the HER measurements using fast mass-transport techniques are most likely also limited by mass transport and thus do not display the true intrinsic activity. We find, from the micropolarization region, an apparent exchange current density of $j_0 = 140$ mA cm$_{Pt}^{-2}$ at room temperature (see section 5.2 in the SI), almost twice the value ($j_0 = 75$ mA cm$_{Pt}^{-2}$) reported from H_2-pump measurements.[14]

> Decreasing the loading is a general strategy to evaluate and mitigate the impact of mass-transport effects in electrochemical reactions.

Over the past decade, metal sulfides[16−19] and, more recently, metal phosphides[20−22] have proven to be active HER catalysts. The development of these classes of catalysts has been inspired by biomimicry and known catalysts for the hydrodesulfurization (HDS) process.[16,17] The hydrogen adsorption free energy (ΔG_H) has proven to be a good descriptor for rationalizing the measured activities of these catalysts,[16,23] which follow a volcano-like trend where $\Delta G_H \approx 0$ corresponds to the highest activity. Apart from Pt, metal sulfides and phosphides are located at the top of the volcano. However, as shown in Figure 2B, their intrinsic activities are at least 3 orders of magnitude lower for comparable room-temperature measurements. Thus, $\Delta G_H \approx 0$ is not a sufficient predictor for intrinsic catalytic activity. Kinetic barriers or coverage effects could be at play; these effects should be explored if alternative catalysts, which can compete with platinum on intrinsic activity, are to be developed.[22,24]

HYSTERESIS IN POLARIZATION CURVES ARISES FROM H_2 BUILDUP

Apart from the variation in specific activity with the loading, another indication that the measured currents are limited by mass transport is the presence of hysteresis in the HER branch. As shown in Figure 3A, the activity is higher in the cathodic scan than in the subsequent anodic-going scan (see also Figure S5). We evaluate this effect using a time-dependent numerical model that couples reaction kinetics and diffusion of H^+ and H_2, as detailed in section 5 in the SI. To validate the model, we benchmarked it against the data in ref 9, where the polarization curves for HOR/HER on a full-sized Pt disk in 0.1 M $HClO_4$ at different rotation rates (i.e., ranging from 100 to 3600 rpm) were reported to have varying degrees of hysteresis. As shown in Figure S9, simulated and experimental polarization curves are in nearly quantitative agreement. We furthermore include a parametric study in section 5.4 in the SI, which shows that the degree of hysteresis depends on the relative rate of mass transport determined by the rotation rate, the diffusion coefficients, and the scan rate.

The conditions of the present study are slightly more complex. The same scan rate (i.e., 50 mV s^{-1}) and rotation rate (i.e., 1600 rpm) are used to record the CVs. However, the loading is varied, and the low-loading samples are scanned to more negative potentials and present lower geometric current densities and more hysteresis. This trend may seem contradictory to the reaction being completely mass-transport-controlled and can be attributed to a slowdown in the effective diffusion coefficients in the HER branch at the lowest loadings, as shown in Figure 3B,C. Assuming uniform diffusion coefficients for all samples (i.e., valid in dilute solutions), the

https://dx.doi.org/10.1021/acsenergylett.1c00246
ACS Energy Lett. 2021, 6, 1175−1180

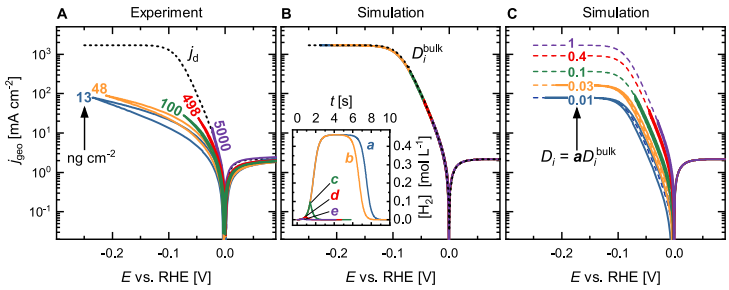

Figure 3. (A) *iR*-corrected polarization curves for HOR/HER on 3.8 nm Pt nanoparticles in H_2-saturated 0.5 M H_2SO_4 at a scan rate of 50 mV s^{-1}, a rotation rate of 1600 rpm, and different loadings: 13 ng cm^{-2} (blue), 48 ng cm^{-2} (orange), 100 ng cm^{-2} (green), 498 ng cm^{-2} (red), and 5000 ng cm^{-2} (purple). (B) Simulated polarization curves using bulk diffusion coefficient values, D_i^{bulk}. The inset shows the average surface concentration of H_2 as a function of time during the simulation (traces *a*−*e* correspond to 13, 48, 100, 498, and 5000 ng cm^{-2}, respectively). (C) Simulated polarization curves (solid lines) using scaled diffusion coefficients aD_i^{bulk} with $a \leq 1$. Dashed lines are the concentration overpotential curves for scaled diffusion coefficients, and $a = 1$ (purple) corresponds to bulk diffusion coefficients.

model predicts CVs for the different samples to all follow the *concentration overpotential curve* (black dashed line; discussed in section 6 in the SI). This curve corresponds to the Nernstian limit where the intrinsic kinetics play no role in the current density. However, the model reproduces qualitatively the experimental trends if the diffusion coefficients of H_2 and H^+ for low-loading samples in the HER branch are scaled by a factor $0 \leq 1$, as shown in Figure 3C.

We hypothesize the drastic reduction in the rate of mass transport at the interface to arise from a large, local H_2 buildup at the lowest loadings. The inset in Figure 3B suggests that the H_2 oversaturation in the HER branch can be larger than 400 mmol L^{-1} in the lowest-loading samples that are swept to the most negative potentials (more details in section 6 in the SI and Figure S16). This corresponds to an increase of up to 3 orders of magnitude with respect to saturation concentration at room temperature (i.e., 0.59 mmol L^{-1}).[28] For the lowest-loading samples, we expect this buildup to be more localized than suggested by the present mean-field model, since they operate at a much higher TOF and have a much lower active area (Figure 2A). This high buildup of evolved H_2 might lead to partial hindrance of incoming H^+ and outgoing H_2 species, as well as to the formation of H_2 microbubbles[9,13,29] that remain located on the catalyst surface, blocking active sites; both of these effects could lead to a reduction in the diffusion rate. We note that the formation of microbubbles at geometric current densities higher than 2−4 mA cm^{-2} has been suggested,[13,29] and as shown in Figure 3A, the geometric current densities recorded in this study for low-loading samples can reach 100 mA cm^{-2}. Our simple scaling approach does not account for the changes in diffusion coefficient with the changes in the concentration of H_2 buildup as the potential is swept; to our knowledge, there is no established relationship between diffusion coefficient and H_2 concentration. This is presumably why the experimental CVs show a smoother transition as the potential is swept, whereas the simulations have the down-scaled diffusion constant artificially imposed from the onset. The present scaling factors serve to heuristically illustrate the impact of a change in diffusion coefficient on the degree of hysteresis. Using a power-law function to describe the variation of the diffusion coefficients with H_2 concentration leads to a better agreement with the experimental CVs, albeit sacrificing simplicity (see Figure S12).

OPPORTUNITIES AND CHALLENGES

In summary, the mass-transport limitations of HER in acid make the assessment of true intrinsic activity of Pt an open challenge. Since we observe mass-transport limitations even at ultra-low Pt loading, but with an activity which is on par with fast mass-transport techniques, we conclude that the intrinsic activity of Pt is still underestimated. The presented activity may well be the highest ever reported at room temperature, but it remains only a lower bound estimate.

> The intrinsic activity of Pt is still underestimated.

We suggest that decreasing loading is a general strategy to evaluate and mitigate the influence of mass-transport effects in electrochemical reactions. For highly active catalysts, the combination of fast mass-transport techniques and ultra-low catalyst loading might be particularly useful. By combining experiments and numerical modeling, we illustrate that the presence of hysteresis in HER CVs at ultra-low catalyst loading is a further marker of mass-transport limitations. Observing similar phenomena in other setups and reactions could possibly help to identify relevant mass-transport limitations.

So is there anything better than Pt for HER? To our knowledge, no earth-abundant catalyst material comes even close to Pt in terms of intrinsic activity. Any claim of making a better catalyst should be supported by a rigorous characterization of intrinsic activity (TOF), with careful consideration of the impact of mass-transport limitations.

ASSOCIATED CONTENT

Supporting Information

The Supporting Information is available free of charge at https://pubs.acs.org/doi/10.1021/acsenergylett.1c00246.

Description of electrochemical methods, sample preparation (nanoparticle deposition and drop casting), general experimental procedures, additional experimental results, characterization (STEM and ISS), description of numerical simulation model, benchmarking of model, parametric study, and further discussion, including Figures S1−S16 and Tables S1−S13 (PDF)

https://dx.doi.org/10.1021/acsenergylett.1c00246
ACS Energy Lett. 2021, 6, 1175−1180

AUTHOR INFORMATION

Corresponding Authors

Jakob Kibsgaard − *SurfCat, Department of Physics, Technical University of Denmark, 2800 Kongens Lyngby, Denmark;* orcid.org/0000-0002-9219-816X; Email: jkib@fysik.dtu.dk

Ib Chorkendorff − *SurfCat, Department of Physics, Technical University of Denmark, 2800 Kongens Lyngby, Denmark;* orcid.org/0000-0003-2738-0325; Email: ibchork@fysik.dtu.dk

Authors

Johannes Novak Hansen − *SurfCat, Department of Physics, Technical University of Denmark, 2800 Kongens Lyngby, Denmark;* orcid.org/0000-0003-0142-3112

Hector Prats − *CatTheory, Department of Physics, Technical University of Denmark, 2800 Kongens Lyngby, Denmark;* orcid.org/0000-0003-4991-253X

Karl Krøjer Toudahl − *SurfCat, Department of Physics, Technical University of Denmark, 2800 Kongens Lyngby, Denmark*

Niklas Mørch Secher − *SurfCat, Department of Physics, Technical University of Denmark, 2800 Kongens Lyngby, Denmark*

Karen Chan − *CatTheory, Department of Physics, Technical University of Denmark, 2800 Kongens Lyngby, Denmark;* orcid.org/0000-0002-6897-1108

Complete contact information is available at: https://pubs.acs.org/10.1021/acsenergylett.1c00246

Notes

The authors declare no competing financial interest.

Biographies

Johannes Novak Hansen is currently a Ph.D. student in the SurfCat group, supervised by Ib Chorkendorff and Jakob Kibsgaard. He has B.Sc. and M.Sc. degrees in physics and nanotechnology from the Technical University of Denmark. His research interest is within electro-catalysis and its application for the sustainable synthesis of fuels and chemicals.

Hector Prats completed his doctoral studies in 2019 at the University of Barcelona. At present, he is a postdoctoral researcher at CatTheory, Technical University of Denmark, under the supervision of Dr. Karen Chan. His current research interest lies in understanding hydrogen redox reactions on the atomic scale.

Karl Krøjer Toudahl holds B.Sc. (2017) and a M.Sc. (2019) degrees in physics and nanotechnology from the Technical University of Denmark and is currently a Ph.D. student under the supervision of Professor Ib Chorkendorff and Associate Professor Jakob Kibsgaard. His research is focused on the synthesis and characterization of atomic clusters and nanoparticles, primarily for electrocatalytic reactions.

Niklas Mørch Secher received his Ph.D. in surface science and experimental catalysis from the Technical University of Denmark in 2020. He has specialized in synthesis and characterization of well-defined model catalysts for investigating the fundamentals of catalytic reactions. His work focuses on catalysis for reactions in sustainable energy technologies such as HER, ORR, and OER.

Karen Chan is an Associate Professor at the Technical University of Denmark at the CatTheory Center in the Department of Physics. Her research focuses on computational electrochemistry toward a sustainable carbon cycle. She was previously an Associate Staff Scientist at SUNCAT as part of the Joint Center for Artificial Photosynthesis.

Jakob Kibsgaard is an Associate Professor of Physics at the Technical University of Denmark. He received his Ph.D. from Aarhus University in 2008. His research focuses on the development and understanding of thermal and electro-catalysts for sustainable energy conversion. He is currently a Carlsberg Foundation Distinguished Fellow and ERC consolidator grantee.

Ib Chorkendorff is a Professor in heterogeneous catalysis at the Technical University of Denmark (DTU)-Physics. He has authored or co-authored more than 370 scientific papers, 22 patents, and one textbook. His research activities focus on finding new catalysts for improving energy production/conversion and for environmental protection. He is co-founder of three start-up companies.

ACKNOWLEDGMENTS

For funding of this work, we gratefully acknowledge the European Research Council (ERC) under the European Union's Horizon 2020 research and innovation program (CLUNATRA, Advanced Grant, PE4, ERC-2016-ADG), the Villum Foundation through grant no. 9455, and the Carlsberg Foundation grant CF18-0435. Finally, we thank Bingjun Xu for supplying the data[9] used in Figure S9, and we also thank Julien Durst and Hubert Gasteiger for supplying the H_2-pump data[14] used in Figure 2B.

REFERENCES

(1) Kibsgaard, J.; Chorkendorff, I. Considerations for the Scaling-up of Water Splitting Catalysts. *Nat. Energy* **2019**, *4* (6), 430−433.

(2) Boudart, M. Turnover Rates in Heterogeneous Catalysis. *Chem. Rev.* **1995**, *95* (3), 661−666.

(3) Cheng, N.; Stambula, S.; Wang, D.; Banis, M. N.; Liu, J.; Riese, A.; Xiao, B.; Li, R.; Sham, T. K.; Liu, L. M.; Botton, G. A.; Sun, X. Platinum Single-Atom and Cluster Catalysis of the Hydrogen Evolution Reaction. *Nat. Commun.* **2016**, *7* (1), 13638.

(4) Zhang, L.; Si, R.; Liu, H.; Chen, N.; Wang, Q.; Adair, K.; Wang, Z.; Chen, J.; Song, Z.; Li, J.; Banis, M. N.; Li, R.; Sham, T.-K.; Gu, M.; Liu, L.-M.; Botton, G. A.; Sun, X. Atomic Layer Deposited Pt-Ru Dual-Metal Dimers and Identifying Their Active Sites for Hydrogen Evolution Reaction. *Nat. Commun.* **2019**, *10* (1), 4936.

(5) Qu, Y.; Shao, M.; Shao, Y.; Yang, M.; Xu, J.; Kwok, C. T.; Shi, X.; Lu, Z.; Pan, H. Ultra-High Electrocatalytic Activity of VS2 Nanoflowers for Efficient Hydrogen Evolution Reaction. *J. Mater. Chem. A* **2017**, *5* (29), 15080−15086.

(6) Cao, L.; Luo, Q.; Liu, W.; Lin, Y.; Liu, X.; Cao, Y.; Zhang, W.; Wu, Y.; Yang, J.; Yao, T.; Wei, S. Identification of Single-Atom Active Sites in Carbon-Based Cobalt Catalysts during Electrocatalytic Hydrogen Evolution. *Nat. Catal.* **2019**, *2* (2), 134−141.

(7) Zhang, J.; Zhang, C.; Wang, Z.; Zhu, J.; Wen, Z.; Zhao, X.; Zhang, X.; Xu, J.; Lu, Z. Synergistic Interlayer and Defect Engineering in VS 2 Nanosheets toward Efficient Electrocatalytic Hydrogen Evolution Reaction. *Small* **2018**, *14* (9), 1703098.

(8) Li, Z.; Fu, J. Y.; Feng, Y.; Dong, C. K.; Liu, H.; Du, X. W. A Silver Catalyst Activated by Stacking Faults for the Hydrogen Evolution Reaction. *Nat. Catal.* **2019**, *2*, 1107−1114.

(9) Zheng, J.; Yan, Y.; Xu, B. Correcting the Hydrogen Diffusion Limitation in Rotating Disk Electrode Measurements of Hydrogen Evolution Reaction Kinetics. *J. Electrochem. Soc.* **2015**, *162* (14), F1470−F1481.

(10) Levich, V. G. *Physicochemical Hydrodynamics*; Prentice-Hall: Englewood Cliffs, NJ, 1962.

(11) Zalitis, C. M.; Kramer, D.; Kucernak, A. R. Electrocatalytic Performance of Fuel Cell Reactions at Low Catalyst Loading and High Mass Transport. *Phys. Chem. Chem. Phys.* **2013**, *15* (12), 4329−4340.

(12) Kucernak, A. R.; Zalitis, C. General Models for the Electrochemical Hydrogen Oxidation and Hydrogen Evolution Reactions: Theoretical Derivation and Experimental Results under Near Mass-Transport Free Conditions. *J. Phys. Chem. C* **2016**, *120* (20), 10721−10745.
(13) Sheng, W.; Gasteiger, H. A.; Shao-Horn, Y. Hydrogen Oxidation and Evolution Reaction Kinetics on Platinum: Acid vs Alkaline Electrolytes. *J. Electrochem. Soc.* **2010**, *157* (11), 1529−1536.
(14) Durst, J.; Simon, C.; Hasche, F.; Gasteiger, H. A. Hydrogen Oxidation and Evolution Reaction Kinetics on Carbon Supported Pt, Ir, Rh, and Pd Electrocatalysts in Acidic Media. *J. Electrochem. Soc.* **2015**, *162* (1), F190−F203.
(15) Zalitis, C. M.; Kramer, D.; Sharman, J.; Wright, E.; Kucernak, A. R. Pt Nano-Particle Performance for PEFC Reactions at Low Catalyst Loading and High Reactant Mass Transport. *ECS Trans.* **2013**, *58* (1), 39−47.
(16) Hinnemann, B.; Moses, P. G.; Bonde, J.; Jørgensen, K. P.; Nielsen, J. H.; Horch, S.; Chorkendorff, I.; Nørskov, J. K. Biomimetic Hydrogen Evolution: MoS2 Nanoparticles as Catalyst for Hydrogen Evolution. *J. Am. Chem. Soc.* **2005**, *127* (15), 5308−5309.
(17) Jaramillo, T. F.; Jørgensen, K. P.; Bonde, J.; Nielsen, J. H.; Horch, S.; Chorkendorff, I. Identification of Active Edge Sites for Electrochemical H2 Evolution from MoS2 Nanocatalysts. *Science (Washington, DC, U. S.)* **2007**, *317* (5834), 100−102.
(18) Kibsgaard, J.; Jaramillo, T. F.; Besenbacher, F. Building an Appropriate Active-Site Motif into a Hydrogen-Evolution Catalyst with Thiomolybdate [Mo3S13]2- Clusters. *Nat. Chem.* **2014**, *6* (3), 248−253.
(19) Kibsgaard, J.; Chen, Z.; Reinecke, B. N.; Jaramillo, T. F. Engineering the Surface Structure of MoS2 to Preferentially Expose Active Edge Sites for Electrocatalysis. *Nat. Mater.* **2012**, *11* (11), 963−969.
(20) Popczun, E. J.; McKone, J. R.; Read, C. G.; Biacchi, A. J.; Wiltrout, A. M.; Lewis, N. S.; Schaak, R. E. Nanostructured Nickel Phosphide as an Electrocatalyst for the Hydrogen Evolution Reaction. *J. Am. Chem. Soc.* **2013**, *135* (25), 9267−9270.
(21) Popczun, E. J.; Read, C. G.; Roske, C. W.; Lewis, N. S.; Schaak, R. E. Highly Active Electrocatalysis of the Hydrogen Evolution Reaction by Cobalt Phosphide Nanoparticles. *Angew. Chem.* **2014**, *126* (21), 5531−5534.
(22) Kibsgaard, J.; Tsai, C.; Chan, K.; Benck, J. D.; Nørskov, J. K.; Abild-Pedersen, F.; Jaramillo, T. F. Designing an Improved Transition Metal Phosphide Catalyst for Hydrogen Evolution Using Experimental and Theoretical Trends. *Energy Environ. Sci.* **2015**, *8* (10), 3022−3029.
(23) Nørskov, J. K.; Bligaard, T.; Logadottir, A.; Kitchin, J. R.; Chen, J. G.; Pandelov, S.; Stimming, U. Trends in the Exchange Current for Hydrogen Evolution. *J. Electrochem. Soc.* **2005**, *152* (3), J23.
(24) Seh, Z. W.; Kibsgaard, J.; Dickens, C. F.; Chorkendorff, I.; Nørskov, J. K.; Jaramillo, T. F. Combining Theory and Experiment in Electrocatalysis: Insights into Materials Design. *Science* **2017**, *355* (6321), eaad4998.
(25) Kibsgaard, J.; Jaramillo, T. F. Molybdenum Phosphosulfide: An Active, Acid-Stable, Earth- Abundant Catalyst for the Hydrogen Evolution Reaction. *Angew. Chem., Int. Ed.* **2014**, *53* (52), 14433−14437.
(26) Hellstern, T. R.; Benck, J. D.; Kibsgaard, J.; Hahn, C.; Jaramillo, T. F. Engineering Cobalt Phosphide (CoP) Thin Film Catalysts for Enhanced Hydrogen Evolution Activity on Silicon Photocathodes. *Adv. Energy Mater.* **2016**, *6* (4), 1501758.
(27) Li, H.; Tsai, C.; Koh, A. L.; Cai, L.; Contryman, A. W.; Fragapane, A. H.; Zhao, J.; Han, H. S.; Manoharan, H. C.; Abild-Pedersen, F.; Nørskov, J. K.; Zheng, X. Erratum: Activating and Optimizing MoS2 Basal Planes for Hydrogen Evolution through the Formation of Strained Sulphur Vacancies. *Nat. Mater.* **2016**, *15*, 48−53; *Nat. Mater.* **2016**, *15* (3), 364.
(28) Mello, R. M. Q.; Ticianelli, E. A. Kinetic Study of the Hydrogen Oxidation Reaction on Platinum and Nafion@ Covered Platinum Electrodes. *Electrochim. Acta* **1997**, *42* (6), 1031−1039.
(29) Rheinländer, P. J.; Herranz, J.; Durst, J.; Gasteiger, H. A. Kinetics of the Hydrogen Oxidation/Evolution Reaction on Polycrystalline Platinum in Alkaline Electrolyte Reaction Order with Respect to Hydrogen Pressure. *J. Electrochem. Soc.* **2014**, *161* (14), F1448−F1457.

https://dx.doi.org/10.1021/acsenergylett.1c00246
ACS Energy Lett. 2021, 6, 1175−1180

Appendix C

Additional Figures

C.1 Synchrotron XPS Fits

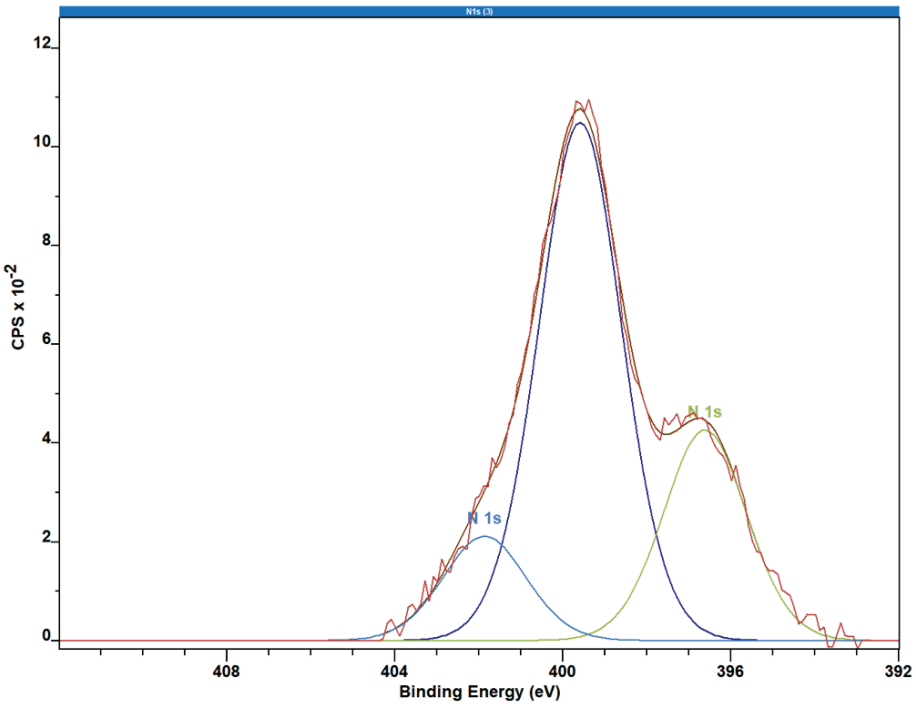

Figure C.1: N 1s XPS spectrum of 1% Pt_2 on HOPG with 3% N, annealed at 700 °C. Data obtained at the Matline endstation of the ASTRID2 beamline at Aarhus University by Zheshen Li. Fitting by Niklas Secher.

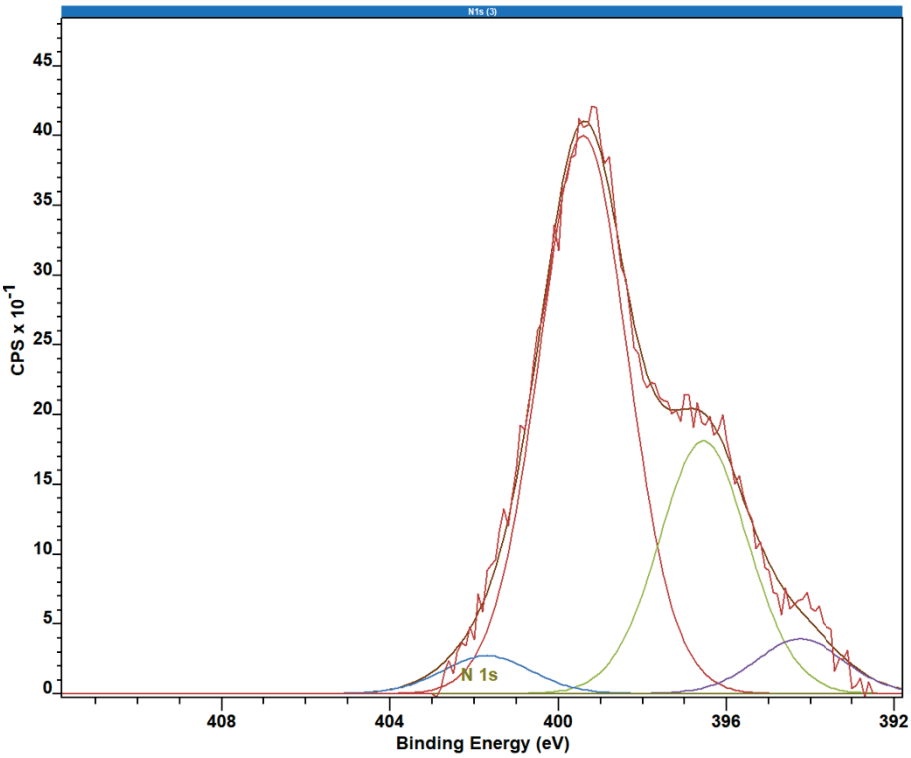

Figure C.2: N 1s XPS spectrum of HOPG with 3% N, annealed at 700 °C. Data obtained at the Matline endstation of the ASTRID2 beamline at Aarhus University by Zheshen Li. Fitting by Niklas Secher.

C.2 STM Simulations

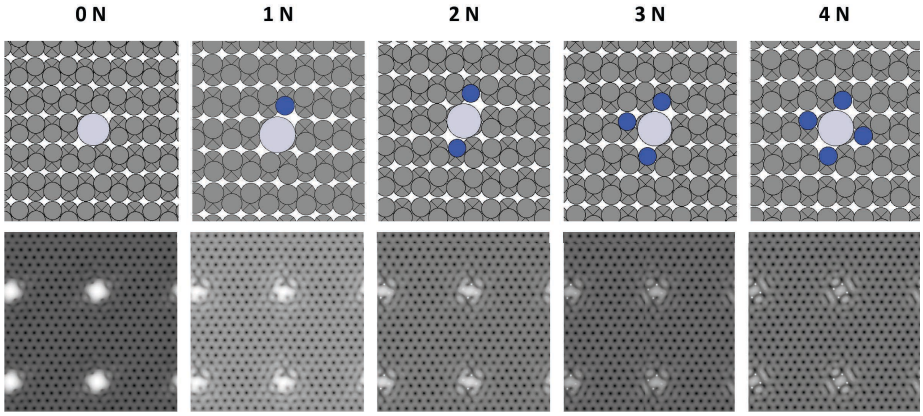

Figure C.3: STM simulations of Pt_1 on the surface of graphene with between 0 and 4 coordinating N atoms. (Top row) Optimized structures with the Pt atoms colored light gray and the N atoms clored blue. (Bottom row) Corresponding STM images simulated. STM simulations by Hector Prats and Sudarshan Vijay.